



HAL
open science

Uncertainty quantification and propagation in rapid dynamics : application to crash problem

Biswarup Bhattacharyya

► **To cite this version:**

Biswarup Bhattacharyya. Uncertainty quantification and propagation in rapid dynamics : application to crash problem. Mechanical engineering [physics.class-ph]. Université de Lyon, 2020. English. NNT : 2020LYSE1123 . tel-03712014

HAL Id: tel-03712014

<https://theses.hal.science/tel-03712014>

Submitted on 2 Jul 2022

HAL is a multi-disciplinary open access archive for the deposit and dissemination of scientific research documents, whether they are published or not. The documents may come from teaching and research institutions in France or abroad, or from public or private research centers.

L'archive ouverte pluridisciplinaire **HAL**, est destinée au dépôt et à la diffusion de documents scientifiques de niveau recherche, publiés ou non, émanant des établissements d'enseignement et de recherche français ou étrangers, des laboratoires publics ou privés.



N°d'ordre NNT : 2020LYSE1123

THESE de DOCTORAT DE L'UNIVERSITE DE LYON

opérée au sein de
l'Université Claude Bernard Lyon 1

Ecole Doctorale N° 162
Mécanique, Énergétique, Génie Civil et Acoustique

Spécialité de doctorat : Mécanique
Discipline : Génie Mécanique

Soutenue publiquement le 23/07/2020, par :
Biswarup Bhattacharyya

Quantification et propagation de l'incertitude en dynamique rapide : Application au problème du crash

Devant le jury composé de :

| | | | |
|---------------------|-----------------------|----------------------------------|----------------------------|
| ADHIKARI, Sondipon | Professeur | Swansea University | Rapporteur |
| GAYTON, Nicolas | Professeur | Université Clermont-Auvergne | Rapporteur |
| SARROUY, Emmanuelle | Maître de Conférences | École Centrale de Marseille | Examinatrice |
| RONEL, Sylvie | Professeure | Université Claude Bernard Lyon 1 | Examinatrice et Présidente |
| JACQUELIN, Eric | Professeur | Université Claude Bernard Lyon 1 | Directeur de thèse |
| BRIZARD, Denis | Chargé de recherche | Université Gustave Eiffel | Co-directeur de thèse |
| HELBERT, Céline | Maître de Conférences | Ecole Centrale de Lyon | Invitée |

Université Claude Bernard – LYON 1

| | |
|---|-------------------------|
| Président de l'Université | M. Frédéric FLEURY |
| Président du Conseil Académique | M. Hamda BEN HADID |
| Vice-Président du Conseil d'Administration | M. Didier REVEL |
| Vice-Président du Conseil des Etudes et de la Vie Universitaire | M. Philippe CHEVALLIER |
| Vice-Président de la Commission de Recherche | M. Jean-François MORNEX |
| Directeur Général des Services | M. Damien VERHAEGHE |

COMPOSANTES SANTE

| | |
|---|--|
| Faculté de Médecine Lyon-Est – Claude Bernard | Doyen : M. Gilles RODE |
| Faculté de Médecine et Maïeutique Lyon Sud Charles. Mérieux | Doyenne : Mme Carole BURILLON |
| UFR d'Odontologie | Doyenne : Mme Dominique SEUX |
| Institut des Sciences Pharmaceutiques et Biologiques | Directrice : Mme Christine VINCIGUERRA |
| Institut des Sciences et Techniques de la Réadaptation | Directeur : M. Xavier PERROT |
| Département de Formation et Centre de Recherche en Biologie Humaine | Directrice : Mme Anne-Marie SCHOTT |

COMPOSANTES & DEPARTEMENTS DE SCIENCES & TECHNOLOGIE

| | |
|---|--|
| UFR Biosciences | Directrice : Mme Kathrin GIESELER |
| Département Génie Electrique et des Procédés (GEP) | Directrice : Mme Rosaria FERRIGNO |
| Département Informatique | Directeur : M. Behzad SHARIAT |
| Département Mécanique | Directeur M. Marc BUFFAT |
| UFR - Faculté des Sciences | Administrateur provisoire : M. Bruno ANDRIOLETTI |
| UFR (STAPS) | Directeur : M. Yannick VANPOULLE |
| Observatoire de Lyon | Directrice : Mme Isabelle DANIEL |
| Ecole Polytechnique Universitaire Lyon 1 | Directeur : Emmanuel PERRIN |
| Ecole Supérieure de Chimie, Physique, Electronique (CPE Lyon) | Directeur : Gérard PIGNAULT |
| Institut Universitaire de Technologie de Lyon 1 | Directeur : M. Christophe VITON |
| Institut de Science Financière et d'Assurances | Directeur : M. Nicolas LEBOISNE |
| ESPE | Administrateur Provisoire : M. Pierre CHAREYRON |

Uncertainty Quantification and Propagation in Rapid Dynamics

Application to Crash Problem

A thesis submitted by
Biswarup Bhattacharyya
in partial fulfillment of the requirements for
the degree of
Doctor of Philosophy



Univ Lyon, Université Claude Bernard Lyon 1
Univ Gustave Eiffel, IFSTTAR
LBMC UMR_T 9406
F-69622, Lyon
France

Acknowledgement

I was fortunate enough to have two great supervisors during my Ph.D.: Prof. Eric Jacquelin and Dr. Denis Brizard. Although the Ph.D. started in October 2017, the journey started in February 2017 when Prof. Eric Jacquelin proposed this research topic. I was very excited to join as a Ph.D. student in the research area of ‘uncertainty quantification’. During my Ph.D. tenure, I have learned many technical pieces of knowledge and the application of several methodologies for uncertainty quantification from Prof. Eric Jacquelin. He always encouraged me to gain diverse knowledge in research. His advice was always fruitful to achieve a goal during my research period. He helped me in developing the main methodology presented in this thesis. I am also thankful to Dr. Denis Brizard for his invaluable advice. He helped me to learn LS-Dyna software and Python. His several tricks about Latex made my works easier and well organized. Both of my supervisors provided enormous support for writing papers and their suggestions were quite helpful for giving a proper shape of a paper. Besides the technical help, both of them helped me to settle down in France after my arrival.

Except for my supervisors, I would like to express my thankful gratitude to all the members of LBMC. Prof. Sylvie Ronel was one of them, who encouraged and motivated me always. I am thankful to the director of LBMC, Prof. David Mitton who always encouraged me and provided proper support whenever required in every step of my research. During my Ph.D., Marc Dagnino was the person who always stood next to me for any technical help with software and hardware. For the administrative works, I received enormous support from Brigitte Chimenton and Virginie Dupasquier.

I am thankful to Prof. Sondipon Adhikari and Prof. Nicolas Gayton for their useful comments on my research work. I am also thankful to my research monitoring committee members Dr. Francois Bermond and Prof. Thouraya Baranger for their invaluable suggestions about my research work.

I shared my laboratory cabin with several great researchers namely Ilias Theodorakos, Gengjian Qian, Li Peng, Jeanne Tondut, and Abdel-Aziz Ahmat Timan. I managed to spend some friendly times with the other researchers in my laboratory who are Tomas Janak, Mehdi Shirzadi, Julia Greenfield, Mingming Zhao, Mohamed Maamir, and Yuliia Sednieva. Except for my laboratory members, I am also thankful to my other friends from all over the world who always motivated me during my research: Subhadip Biswas, Dipaloke Majumder, Souvik Chakraborty, Tanmoy Chatterjee, Bibekananda Mandal, Sabyasachi Biswas, Arpita Saha and many more.

I am thankful to my wife Tanushree Bhattacharyya for her sacrifice and support all the period of my Ph.D. Without her support, it would not be possible to achieve this milestone. Finally, I am very thankful to my parents who provided me motivation and support throughout my life to make me a good human being.

Biswarup Bhattacharyya

Villeurbanne, France

Résumé

Lors d'un accident, dans le cas d'un choc frontal, une grande partie de l'énergie est généralement dissipée par la déformation et l'écrasement de dispositifs fusibles. L'énergie dissipée est alors incertaine car elle dépend de plusieurs paramètres incertains. Dans cette thèse, une crash box est étudiée en tenant compte des incertitudes.

Le but de cette thèse est de propager des paramètres incertains à travers un problème de crash. L'approche usuelle pour la quantification de l'incertitude (UQ) est la simulation de Monte Carlo (MCS). Or la MCS nécessite un grand nombre d'évaluations du modèle. Cela rend l'utilisation de cette approche très difficile dans le cadre d'un problème complexe, comme un problème de collision. Pour surmonter cette difficulté, l'approche par métamodèle est utilisée: on recherche alors un compromis entre précision et efficacité.

Pour notre problème dynamique, un premier métamodèle est développé : il combine le modèle de krigeage et le modèle NARX (Nonlinear Auto-Regressive with eXogenous input). Ce modèle, appelé KNARX creux, est généralement adapté à l'UQ des systèmes dynamiques non linéaires en utilisant un faible nombre d'évaluations du modèle. Il est cependant incapable d'estimer de façon satisfaisante les réponses d'un oscillateur simple impacté, représentatif d'un problème de crash (car comportement non régulier).

Un nouveau métamodèle, appelé POD-PCE, est alors formulé. Il découple respectivement le domaine temporel et le caractère aléatoire par l'utilisation d'une décomposition orthogonale (POD) et d'un développement en chaos polynomiaux (PCE). Les incertitudes d'un oscillateur impacté sont propagées à l'aide de ce modèle POD-PCE. Le modèle POD-PCE et le modèle PCE fonctionnent bien avec un nombre assez faible d'évaluations du modèle par rapport à l'approche MCS. L'approche POD-PCE est plus efficace que le modèle PCE parce que les coefficients du modèle PCE doivent être calculés à chaque pas de temps, alors que l'aspect temporel est pris en compte avec seulement quelques modes orthogonaux dans le cas du modèle POD-PCE. Toutefois, le modèle POD-PCE prédit parfois des forces de contact négatives non physiques, qui peuvent être réduites en utilisant des polynômes de degré élevé. L'utilisation d'un polynôme de degré élevé peut toutefois s'avérer prohibitive pour le modèle PCE car la détermination d'un nombre élevé de coefficients nécessite un grand nombre d'évaluations du modèle. C'est pourquoi un modèle PCE basée sur une inférence bayésienne variationnelle creuse (SVB) est proposé: il sélectionne les termes importants dans la base polynomiale et réduit ainsi les problèmes liés à un sur-ajustement, tout en utilisant un faible nombre d'évaluations du modèle. Il est observé que les forces négatives peuvent être réduites en utilisant le modèle POD-SVB-PCE.

En outre, il est important de formuler un cadre adaptatif pour la sélection du nombre d'évaluations du modèle et du degré polynomial. Pour cette raison, un modèle SVB-PCE adaptatif est formulé. Il a été également couplé à l'approche POD pour formuler un modèle POD-SVB-PCE adaptatif. Ce cadre adaptatif est finalement appliqué à une crash box écrasée

par une masse rigide impactante pour propager les différentes incertitudes du modèle et effectuer une analyse de sensibilité globale (GSA). Les exemples montrent que le modèle adaptatif POD-SVB-PCE a la capacité de prédire des résultats satisfaisants avec un faible nombre d'évaluations du modèle pour la plupart des réponses. Cependant, il est assez difficile d'obtenir une bonne précision pour la force de contact, même en utilisant le nombre maximum d'évaluations de modèle alloué ; la précision prédite pour la force de contact reste cependant acceptable. La GSA dépendante du temps est réalisée efficacement, sans coût de calcul supplémentaire, en post-traitant les paramètres du modèle adaptatif POD-SVB-PCE.

Mots-clés: Quantification des incertitudes, Développement en chaos polynomiaux, POD, Crash, Analyse de sensibilité globale.

Abstract

The safety of a car occupant depends on several factors during an accident such as the seatbelt condition, the number of occupants in the car, the structure of the car. Usually, in the case of a frontal crash, a large part of the initial kinetic energy is dissipated in the compression of the crash boxes and the dissipated energy may be uncertain due to several uncertain parameters. A crash box is investigated in this thesis considering several uncertain parameters.

The main challenging task for the thesis is the propagation of the uncertain parameters through a crash problem. The conventional approach for the uncertainty quantification (UQ) is the Monte Carlo simulation (MCS). However, MCS requires a large number of model evaluations which prohibits to apply this approach in a complex problem (i.e. a crash problem). To overcome this issue, the surrogate modeling approach is investigated in this thesis, which maintains a trade-off between accuracy and efficiency.

As the crash problem is a dynamic problem, a first surrogate model called sparse KNARX is developed in this thesis: it combines the Kriging model and a Nonlinear Auto-Regressive with eXogenous input (NARX) model. The sparse KNARX model performs very well for UQ of several nonlinear dynamical systems using low number of model evaluations. However, the sparse KNARX model is unable to identify an impact oscillator (a representative system for a crash problem) due to the non-smooth behavior.

For the impact problem, a new surrogate model is formulated, which decouples the time-domain and the randomness by the proper orthogonal decomposition (POD) and the uncertain parameters are propagated by the polynomial chaos expansion (PCE) approach: the resulting surrogate model is called POD-PCE model. Further, it is applied to an impact oscillator for UQ. The POD-PCE model and the PCE model perform well with quite low number of model evaluations as compared to the MCS approach. The PCE model is constructed only for the reduced number of proper orthogonal modes in case of the POD-PCE model whereas the coefficients must be computed at each time-step in case of the PCE model. Although the results are quite good, some non-physical negative contact forces are predicted by the POD-PCE model, which may be reduced by using a high degree polynomial. At the same time, the use of high degree polynomial is prohibitive for the PCE model as it requires a large number of model evaluations. For that reason, a sparse variational Bayesian (SVB) based PCE model is proposed in this thesis: it selects the important terms in the polynomial basis and subsequently reduces the chances of overfitting with a low number of model evaluations. It is observed that the non-physical negative forces can be reduced to some extent using the POD-SVB-PCE model. However, it is impossible to mitigate the non-physical forces due to the non-smooth behavior of the impact oscillator.

Further, it is important to formulate an adaptive framework such that the number of model evaluations and the polynomial degree are selected adaptively. For that reason, an adaptive SVB-PCE model is formulated and furthermore, it is coupled with the POD approach to

formulate an adaptive POD-SVB-PCE model. This adaptive framework is applied to a crash box under impact loading for UQ and global sensitivity analysis (GSA). The results show that the adaptive POD-SVB-PCE model has the capability to predict a good result with a low number of model evaluations for most of the responses. However, it is quite difficult to achieve a good accuracy for the contact force with the adaptive POD-SVB-PCE model even using the maximum allocated number of model evaluations; the predicted accuracy for the contact force remains however acceptable. The time-dependent GSA is performed by post-processing the adaptive POD-SVB-PCE model parameters which is quite efficient without any additional computational cost.

Keywords: Uncertainty quantification, Global sensitivity analysis, Polynomial chaos expansion, Proper orthogonal decomposition, Crash box

Contents

| | |
|---|--------------|
| Acknowledgement | vii |
| Résumé | ix |
| Abstract | xi |
| List of Figures | xvii |
| List of Tables | xxi |
| List of Algorithms | xxiii |
| Nomenclature | xxv |
| 1 Introduction | 1 |
| 1.1 Context | 1 |
| 1.2 Uncertainty quantification of dynamical systems | 2 |
| 1.3 Objectives of the research | 3 |
| 1.4 Outline of the thesis | 3 |
| 2 State-of-the-art review | 5 |
| 2.1 Monte Carlo simulation | 5 |
| 2.2 Sampling based approaches | 5 |
| 2.2.1 Latin hypercube sampling | 6 |
| 2.2.2 Sobol sequence | 6 |
| 2.3 Surrogate modeling approach | 6 |
| 2.3.1 General outline of intrusive surrogate model | 6 |
| 2.3.2 General outline of non-intrusive surrogate model | 7 |
| 2.4 Polynomial chaos expansion for dynamical systems | 8 |
| 2.4.1 Formulation of polynomial chaos expansion | 8 |
| 2.4.2 Computation of PCE coefficients by Galerkin projection | 9 |
| 2.4.3 Computation of PCE coefficients by a regression approach | 10 |
| 2.4.4 Post-processing of PCE results | 10 |
| 2.5 PCE models applied to dynamical systems: available approaches | 11 |
| 2.5.1 Intrusive approaches | 11 |
| 2.5.2 Non-intrusive approaches | 14 |
| 2.6 Kriging surrogate model | 16 |

| | | |
|----------|---|-----------|
| 2.6.1 | Construction of the model | 17 |
| 2.6.2 | Prediction | 18 |
| 2.7 | Radial basis function surrogate model | 19 |
| 2.8 | Support vector machine surrogate model | 19 |
| 2.9 | UQ of stochastic impact problems: Literature review | 20 |
| 2.10 | Need of the research | 22 |
| 3 | Kriging-NARX model for dynamical systems | 23 |
| 3.1 | Introduction | 23 |
| 3.2 | NARX model | 24 |
| 3.2.1 | Overview of NARX model | 24 |
| 3.2.2 | Model formulation and parameter estimation of the NARX model | 25 |
| 3.2.3 | Sparse NARX model | 25 |
| 3.3 | Kriging-NARX model | 27 |
| 3.4 | Numerical application to nonlinear dynamical systems | 28 |
| 3.4.1 | Duffing oscillator | 30 |
| 3.4.2 | Bouc-Wen oscillator | 37 |
| 3.4.3 | A 2-DOF dynamical system | 43 |
| 3.5 | Failure of the auto-regressive model for an impact oscillator | 46 |
| 3.5.1 | Linear auto-regressive model | 49 |
| 3.5.2 | Nonlinear AR model | 49 |
| 3.5.3 | Nonlinear wavelet AR model | 50 |
| 3.5.4 | Identification of an impact oscillator by AR models | 50 |
| 3.6 | Concluding remarks | 55 |
| 4 | Proper orthogonal decomposition based PCE model | 57 |
| 4.1 | Introduction | 57 |
| 4.2 | Proper orthogonal decomposition | 58 |
| 4.3 | POD-PCE model | 59 |
| 4.4 | Post-processing of POD-PCE results | 60 |
| 4.5 | Application to an impact oscillator | 61 |
| 4.5.1 | Case 1: Single impact oscillator | 61 |
| 4.5.2 | Case 2: Multiple impact oscillator | 68 |
| 4.6 | Concluding remarks | 78 |
| 5 | Variational Bayesian inference based sparse PCE model | 81 |
| 5.1 | Introduction | 81 |
| 5.2 | Bayesian inference in PCE model | 82 |
| 5.2.1 | Generalized Bayesian inference in PCE | 82 |
| 5.2.2 | Variational Bayesian inference | 83 |
| 5.2.3 | Factorized distribution | 84 |
| 5.3 | Variational Bayesian inference based PCE | 85 |
| 5.4 | Sparse VB-PCE model by automatic relevance determination | 87 |
| 5.5 | Proposed UQ framework by SVB-PCE model | 89 |
| 5.6 | UQ of test functions by SVB-PCE model | 91 |
| 5.6.1 | Ishigami function | 91 |
| 5.6.2 | High-dimensional function | 95 |

| | | |
|----------|--|------------|
| 5.6.3 | Observations | 97 |
| 5.7 | POD-SVB-PCE model | 98 |
| 5.8 | Application of POD-SVB-PCE model to impact oscillator | 98 |
| 5.8.1 | Contact force | 99 |
| 5.8.2 | Projectile displacement | 102 |
| 5.8.3 | Projectile velocity | 104 |
| 5.9 | Concluding remarks | 107 |
| 6 | Application to crash simulations | 109 |
| 6.1 | Introduction | 109 |
| 6.2 | Adaptive SVB-PCE model | 110 |
| 6.2.1 | Sequential experimental design | 110 |
| 6.2.2 | Adaptivity in the polynomial degree | 110 |
| 6.2.3 | Formulation of adaptive SVB-PCE model | 111 |
| 6.3 | Adaptive POD-SVB-PCE model | 113 |
| 6.4 | Numerical formulation of a crash box | 114 |
| 6.4.1 | Finite element model of a crash box | 114 |
| 6.4.2 | Finite element model of a quarter crash box | 116 |
| 6.4.3 | Deterministic analysis of crash boxes | 119 |
| 6.5 | Uncertainty quantification of quarter crash box | 119 |
| 6.5.1 | Problem definition | 119 |
| 6.5.2 | Uncertainty quantification of crash boxes | 123 |
| 6.6 | Global sensitivity analysis of the crash box model | 142 |
| 6.6.1 | Adaptive POD-SVB-PCE model for time-dependent sensitivity analysis | 142 |
| 6.6.2 | Global sensitivity analysis of the quarter crash boxes | 146 |
| 6.7 | Concluding remarks | 153 |
| 7 | Conclusions and future perspectives | 157 |
| 7.1 | Conclusions of the research | 157 |
| 7.2 | Limitations of the research | 159 |
| 7.3 | Future scope of research | 159 |
| A | Investigation of a dynamical system by TDgPCE | 161 |
| A.1 | Problem definition | 161 |
| A.2 | Case 1: $\bar{k} = 150 \text{ N m}^{-1}$ | 162 |
| A.3 | Case 2: $\bar{k} = 1500 \text{ N m}^{-1}$ | 163 |
| A.4 | Case 3: $\bar{k} = 15\,000 \text{ N m}^{-1}$ | 163 |
| A.5 | Discussion on failure of TDgPCE | 167 |
| B | Distribution for the prior and likelihood function | 169 |
| C | Computation of variational lower bound | 171 |
| D | Sobol' sensitivity indices | 173 |

| | |
|--|------------|
| E Long summary in French | 175 |
| E.1 Introduction | 175 |
| E.2 Examen de l'état de l'art | 176 |
| E.3 Modèle Kriging-NARX pour les systèmes dynamiques | 177 |
| E.4 Modèle PCE reposant sur une décomposition orthogonale en modes propres de type POD | 178 |
| E.5 Modèle PCE creux basé sur l'inférence bayésienne variationnelle | 179 |
| E.6 Application aux simulations de dynamique rapide | 180 |
| E.7 Conclusions | 182 |
| Bibliography | 185 |

List of Figures

| | | |
|------|---|----|
| 1.1 | Frame structure of a car body (www.cgtrader.com) | 2 |
| 3.1 | Displacement versus restoring force plot (blue curve) for the Duffing oscillator | 31 |
| 3.2 | Displacement versus restoring force plots (blue curves) of two different realizations for the Duffing oscillator | 32 |
| 3.3 | Statistical response characteristics of the Duffing oscillator | 34 |
| 3.4 | Comparison of instantaneous response characteristics for the Duffing oscillator at different time instances | 35 |
| 3.5 | Comparison of predicted $\max(y(t))$ for the Duffing oscillator | 36 |
| 3.6 | Statistical response characteristics for the displacement of the Bouc-Wen oscillator | 39 |
| 3.7 | Statistical response characteristics for the velocity of the Bouc-Wen oscillator | 39 |
| 3.8 | Prediction of instantaneous displacement characteristics for the Bouc-Wen oscillator at different times | 40 |
| 3.9 | Prediction of instantaneous velocity characteristics for the Bouc-Wen oscillator at different times | 41 |
| 3.10 | Comparison of predicted $\max(y(t))$ for the Bouc-Wen oscillator | 42 |
| 3.11 | Comparison of predicted $\max(\dot{y}(t))$ for Bouc-Wen oscillator | 42 |
| 3.12 | A 2-DOF dynamical system | 43 |
| 3.13 | Statistical response characteristics for displacement ($y_1(t)$) of the 2-DOF dynamical system | 45 |
| 3.14 | Statistical response characteristics for velocity ($\dot{y}_1(t)$) of the 2-DOF dynamical system | 45 |
| 3.15 | Prediction of instantaneous displacement characteristics for 2-DOF dynamical system at different time instances | 47 |
| 3.16 | Comparison of predicted $\max(y_1(t))$ for the 2-DOF dynamical system | 48 |
| 3.17 | Comparison of predicted $\max(\dot{y}_1(t))$ for the 2-DOF dynamical system | 48 |
| 3.18 | 2-DOF nonlinear impact oscillator | 51 |
| 3.19 | Deterministic contact force for the single impact oscillator | 52 |
| 3.20 | Identification of the response quantities for the single impact oscillator in time domain $[0\text{ s}, 10^{-3}\text{ s}]$ | 53 |
| 3.21 | Identification of the response quantities for the single impact oscillator in time domain $[0\text{ s}, 1.9 \times 10^{-4}\text{ s}]$ | 54 |
| 3.22 | Deterministic contact force for the multi-impact oscillator | 54 |
| 3.23 | Identification of the response quantities for the multi-impact oscillator | 54 |

| | | |
|------|---|-----|
| 4.1 | Evaluation of the mean relative errors of all the stochastic response quantities for the single impact oscillator | 63 |
| 4.2 | Time-dependent statistical moments of the stochastic response quantities for the single impact oscillator: MCS was performed using $N_{\text{MCS}} = 10^4$ model evaluations | 65 |
| 4.3 | Time-dependent errors for the statistical moments of the stochastic responses of single impact oscillator | 66 |
| 4.4 | Comparison of responses for single impact oscillator at 5 samples: $m_p \in \{342.71, 292.84, 365.62, 310.35, 373.82\}\text{g}$, $k_c \in \{13.97, 13.87, 14.61, 14.23, 13.63\} \times 10^3 \text{MN m}^{-3/2}$, $v_0 \in -\{11.32, 9.51, 9.96, 9.11, 10.95\}\text{m s}^{-1}$ | 68 |
| 4.5 | Evaluation of mean relative error for all the stochastic response quantities of the multiple impact oscillator | 70 |
| 4.6 | Time-dependent statistical moments of the stochastic responses for the multiple impact oscillator: MCS was performed using $N_{\text{MCS}} = 10^4$ model evaluations | 71 |
| 4.7 | Time-dependent errors for the statistical moments of the responses of multiple impact oscillator | 72 |
| 4.8 | Comparison of responses for the multiple impact oscillator at 5 samples: $m_p \in \{342.71, 292.84, 365.62, 310.35, 373.82\}\text{g}$, $k_c \in \{13.97, 13.87, 14.61, 14.23, 13.63\} \times 10^3 \text{MN m}^{-3/2}$, $v_0 \in -\{11.32, 9.51, 9.96, 9.11, 10.95\}\text{m s}^{-1}$ | 75 |
| 4.9 | Prediction of contact force at 5 samples with $p = 3$: —MCS, - · - · -PCE, - - -POD-PCE | 76 |
| 4.10 | Prediction of contact force at 5 samples with $p = 5$: —MCS, - · - · -PCE, - - -POD-PCE | 77 |
| 4.11 | Prediction of contact force at 5 samples with $N = 1000$ for different polynomial degrees: —MCS, - · - · -PCE, - - -POD-PCE | 79 |
| 5.1 | Graphical model representing the dependencies between the Bayesian model parameters | 83 |
| 5.2 | Flowchart of the SVB-PCE for UQ | 92 |
| 5.3 | Evaluation of PE for different polynomial degrees by the SVB-PCE and the LARS-PCE models | 93 |
| 5.4 | Evaluation of PE with the increase of sample points for the Ishigami function with $p = 8$ | 94 |
| 5.5 | PDF of the Ishigami function by MCS, LARS-PCE and SVB-PCE models | 94 |
| 5.6 | Evaluation of variational lower bound (VLB) for the Ishigami function using $N = 40$ and $p = 8$ | 95 |
| 5.7 | Evaluation of percentage error (PE) with the increase of sample points for the high-dimensional function | 96 |
| 5.8 | PDF of the high-dimensional function by MCS, LARS-PCE and SVB-PCE using $N = 85$ and $p = 2$ | 97 |
| 5.9 | Evaluation of variational lower bound (VLB) for the high-dimensional function using $N = 85$ and $p = 2$ | 98 |
| 5.10 | Evolution of the mean relative error and the PCE coefficients with the increase of polynomial degree p for the predicted contact force by the POD-PCE and the POD-SVB-PCE models with $N = 50$ | 100 |

| | | |
|------|--|-----|
| 5.11 | Evaluation of the mean relative error with the increase of sample point N for the predicted contact force by the POD-PCE and the POD-SVB-PCE model with $p = 10$ | 101 |
| 5.12 | Comparison of contact force at 5 samples predicted by the POD-PCE and the POD-SVB-PCE models with $N = 50$ (zoom view over the impact duration) . | 102 |
| 5.13 | Evolution of the mean relative error and the PCE coefficients with the increase of polynomial degree p for the predicted projectile displacement by the POD-PCE and the POD-SVB-PCE models with $N = 50$ | 103 |
| 5.14 | Evaluation of the mean relative error with the increase of sample point N for the predicted projectile displacement by the POD-PCE and the POD-SVB-PCE models with $p = 10$ | 104 |
| 5.15 | Evaluation of the mean relative error with the increase of polynomial degree p for the predicted projectile velocity by the POD-PCE and the POD-SVB-PCE models with $N = 50$ | 105 |
| 5.16 | Evaluation of the mean relative error with the increase of sample point N for the predicted projectile velocity by the POD-PCE and the POD-SVB-PCE models with $p = 10$ | 106 |
| 5.17 | Comparison of projectile velocity at 5 samples predicted by the POD-PCE and the POD-SVB-PCE models with $N = 50$ | 107 |
| 6.1 | Geometrical views of FE model of the full crash box | 117 |
| 6.2 | Plastic stress-strain diagram | 117 |
| 6.3 | Geometrical views of FE model of the quarter crash box | 118 |
| 6.4 | Failure shapes at different times for both crash boxes under impact loading . | 120 |
| 6.5 | Comparison of the response quantities for both crash boxes for deterministic analysis | 121 |
| 6.6 | The symmetrical quarter crash box with different end conditions | 122 |
| 6.7 | Failure shapes of CB2 at different time instances | 123 |
| 6.8 | Evolution of LOO error for the impactor displacement of crash boxes | 124 |
| 6.9 | Evolution of the POM number (a)-(c) and the total number of PCE coefficients (b)-(d) with the increase of the sample number for the impactor displacement of crash boxes | 125 |
| 6.10 | Comparison of statistical moments for the impactor displacement of crash boxes by different methods | 127 |
| 6.11 | Comparison of the impactor displacement predicted by the adaptive POD-SVB-PCE model with the MCS results at 3 samples (the samples were selected randomly) | 128 |
| 6.12 | Evolution of LOO error for the impactor velocity of crash boxes | 129 |
| 6.13 | Evolution of the POM number (a)-(c)-(e) and the total number of PCE coefficients (b)-(d)-(f) with the increase of the sample number for the impactor velocity of crash boxes | 130 |
| 6.14 | Comparison of statistical moments for the impactor velocity of crash boxes by different methods | 132 |
| 6.15 | Comparison of the impactor velocity predicted by the adaptive POD-SVB-PCE model with the MCS results at 3 samples (the samples were selected randomly) | 133 |
| 6.16 | Evolution of LOO error for the contact force of crash boxes | 134 |

| | | |
|------|---|-----|
| 6.17 | Evolution of the POM number (a)-(c)-(e) and the total number of PCE coefficients (b)-(d)-(f) with the increase of the sample number for the contact force of crash boxes | 136 |
| 6.18 | Comparison of statistical moments of the contact force for all crash boxes by different methods | 137 |
| 6.19 | Comparison of the contact force predicted by the adaptive POD-SVB-PCE model with the MCS results at 3 samples (the samples were chosen randomly) | 138 |
| 6.20 | Evolution of the modified LOO error and the number of selected PCE coefficients with the increase of the sample number for the maximum contact force of all the crash boxes | 140 |
| 6.21 | PDF of the maximum contact force for all the crash boxes by different approaches | 141 |
| 6.22 | Evolution of the modified LOO error and the number of selected PCE coefficients with the increase of sample number for the dissipated energy of all the crash boxes | 143 |
| 6.23 | PDF of the dissipated energy for all the crash boxes by different approaches . | 144 |
| 6.24 | Time-dependent GSA results for all the uncertain parameters obtained by the adaptive POD-SVB-PCE model considering contact force as the QoI | 148 |
| 6.25 | Time-dependent GSA results for all the uncertain parameters obtained by the adaptive POD-SVB-PCE model considering impactor velocity as the QoI . . | 150 |
| 6.26 | Evolution of LOO error for the kinetic energy | 151 |
| 6.27 | Time-dependent GSA results for all the uncertain parameters obtained by the adaptive POD-SVB-PCE model considering kinetic energy as the QoI | 152 |
| A.1 | SDOF dynamical system | 161 |
| A.2 | Statistical response characteristics of the linear SDOF system for $\bar{k} = 150 \text{ N m}^{-1}$ | 163 |
| A.3 | PDF of displacement at different time instances for $\bar{k} = 150 \text{ N m}^{-1}$ | 164 |
| A.4 | Statistical response characteristics of the linear SDOF system for $\bar{k} = 1500 \text{ N m}^{-1}$ | 164 |
| A.5 | PDF of displacement at different time instances for $\bar{k} = 1500 \text{ N m}^{-1}$ | 165 |
| A.6 | Statistical response characteristics of the linear SDOF system for $\bar{k} = 15\,000 \text{ N m}^{-1}$ | 165 |
| A.7 | PDF of displacement at different time instances for $\bar{k} = 15\,000 \text{ N m}^{-1}$ | 166 |

List of Tables

| | | |
|------|---|----|
| 2.1 | Type of orthogonal polynomials for different types of input random variables in PCE (Xiu and Karniadakis, 2002) | 9 |
| 3.1 | Algorithm for the sparse KNARX model | 29 |
| 3.2 | Uncertain parameters for the Duffing oscillator | 30 |
| 3.3 | The polynomials selected by the LARS algorithm for the Duffing oscillator | 32 |
| 3.4 | Accuracy of the surrogate models in predicting instantaneous response characteristics for the Duffing oscillator | 34 |
| 3.5 | Comparison of accuracy and efficiency of the surrogate models for the Duffing oscillator | 36 |
| 3.6 | Uncertain parameters for the Bouc-Wen oscillator | 37 |
| 3.7 | Accuracy of the surrogate models in predicting the instantaneous response characteristics for the Bouc-Wen oscillator | 39 |
| 3.8 | Accuracy and efficiency of the surrogate models in computing $\dot{y}(t)$ for the Bouc-Wen oscillator | 42 |
| 3.9 | Uncertain parameters for the 2-DOF dynamical system | 43 |
| 3.10 | Accuracy of sparse KNARX in predicting instantaneous response characteristics for the 2-DOF dynamical system | 46 |
| 3.11 | Accuracy and efficiency of sparse KNARX in computing $y_1(t)$ for the 2-DOF dynamical system | 46 |
| 3.12 | Parameters of the impact oscillator | 51 |
| 4.1 | Parameters of the uniformly distributed random variables for the impact oscillator | 61 |
| 4.2 | Accuracy of different surrogate models in assessing the stochastic response quantities for the single impact oscillator by $N = 20$ | 67 |
| 4.3 | Accuracy of different surrogate models in assessing the stochastic responses for the multiple impact oscillator using $N = 50$ | 73 |
| 5.1 | Statistical moments of the response for the Ishigami function using $N = 40$ and $p = 8$ | 93 |
| 5.2 | Percentage error (PE) and sparsity index (SI) for the Ishigami function using $N = 40$ and $p = 8$ | 95 |
| 5.3 | Statistical moments of the response for the high-dimensional function using $N = 85$ and $p = 2$ | 96 |
| 5.4 | Percentage error (PE) and sparsity index (SI) for the high-dimensional function using $N = 85$ and $p = 2$ | 97 |

| | | |
|-----|--|-----|
| 6.1 | Parameters of the uniformly distributed random variables for the crash boxes | 123 |
| 6.2 | Predicted mean relative error $\bar{\epsilon}$ and number of sample points N for the impactor displacement of the crash boxes with the obtained adaptive POD-SVB-PCE model | 126 |
| 6.3 | Predicted mean relative error $\bar{\epsilon}$ and number of sample points N for the impactor velocity of the crash boxes with the obtained adaptive POD-SVB-PCE model | 131 |
| 6.4 | Predicted mean relative error $\bar{\epsilon}$ and number of sample points N for the contact force of the crash boxes with the obtained adaptive POD-SVB-PCE model . | 139 |
| 6.5 | Predicted percentage error (PE) for the maximum contact force of the crash boxes by the obtained adaptive SVB-PCE model with $p_{\max} = 15$ | 139 |
| 6.6 | Predicted percentage error (PE) for the dissipated energy of the crash boxes by the obtained adaptive SVB-PCE model with $p_{\max} = 15$ | 142 |
| 6.7 | Time-independent GSA results for the maximum of the contact force obtained by the adaptive SVB-PCE model | 153 |
| 6.8 | Time-independent GSA results for the total dissipated energy obtained by the adaptive SVB-PCE model | 154 |
| A.1 | Different parameters used for the SDOF dynamical system | 162 |

List of Algorithms

| | | |
|-----|---|-----|
| 4.1 | Algorithm for the construction of POD-PCE model | 60 |
| 5.1 | Pseudo-code for VB inference based PCE formulation | 88 |
| 5.2 | Pseudo-code for the SVB-PCE model | 90 |
| 5.3 | Algorithm for the construction of POD-SVB-PCE model | 99 |
| 6.1 | Pseudo-code for the adaptive SVB-PCE model | 112 |
| 6.2 | Pseudo-code for the adaptive POD-SVB-PCE model | 115 |

Nomenclature

| | |
|-------------------------------|---|
| α | Hyper-prior for Bayesian model |
| $\bar{\epsilon}$ | Mean relative error |
| $\bar{\epsilon}_{\text{LOO}}$ | Mean relative LOO error |
| \bar{Y} | Time average of response |
| β | Coefficient vector for Kriging |
| ψ | Polynomial basis matrix for Kriging |
| \mathbf{a} | PCE coefficient matrix |
| \mathbf{a}^* | Sparse PCE coefficient matrix |
| \mathbf{c} | Parameter of SVM model |
| \mathbf{f} | Polynomial basis matrix for NARX model |
| \mathbf{V} | Proper orthonormal mode |
| \mathbf{a} | NARX coefficient matrix |
| δ | Kronecker delta |
| Δt | Time step |
| $\epsilon(t)$ | Time dependent error for statistical moment |
| ϵ_k | Relative error for k -th sample |
| ϵ_{LOO} | Relative LOO error |
| ϵ_{tol} | Threshold value for mean relative LOO error |
| η | Slake variable |
| γ | True strain |
| γ_{eff} | Effective strain |
| $\hat{\mu}$ | Predicted mean |
| $\hat{\sigma}$ | Predicted standard deviation |

| | |
|---------------|---|
| \hat{f} | Kernel density estimator |
| \hat{h} | Bandwidth |
| κ | Basis function for RBF model |
| Λ | Matrix having hyper-parameters |
| λ | Eigenvalue |
| \mathbb{E} | Expectation operator |
| \mathcal{C} | Parameter for SVM model |
| \mathcal{F} | Events |
| \mathcal{F} | Performance function for NARX model |
| \mathcal{L} | Variational lower bound |
| \mathcal{M} | Computational model |
| \mathcal{P} | Probability measure |
| \mathcal{R} | Auto-correlation function |
| \mathcal{L} | Differential operator |
| \mathcal{R} | Correlation matrix |
| Ω | Sample space |
| ω_x | Excitation frequency |
| Φ | Multivariate orthonormal polynomial basis matrix |
| ϕ | Multivariate orthogonal polynomial basis function |
| Φ^* | Sparse polynomial basis matrix |
| A | ARD value |
| a | NARX coefficient |
| Σ | Diagonal matrix for SVD |
| σ | Applied stress |
| σ_Z^2 | Gaussian process variance |
| Θ | Bayesian model parameter |
| θ | Hyper-parameter in Kriging |
| Υ | A multiplying constant |
| var | Variance operator |

| | |
|------------------------------|---|
| ε | Nonlinearity controller for Duffing oscillator |
| $\varepsilon(t)$ | NARX model residual error |
| ε_p | Residual error for PCE |
| ε_{LOO} | Relative LOO error |
| $\varepsilon_{\text{LOO}}^*$ | Modified LOO error |
| ε_{SVM} | An error for SVM model |
| ε_{res} | Residual error |
| φ | Univariate orthogonal polynomial basis function |
| ς | Prior for Bayesian model |
| ϑ_{tol} | Thresold value for LOO error in PCE |
| Ξ | Random variable matrix |
| ζ | Damping ratio |
| ζ_{st} | Damping ratio for impact oscillator |
| T | Transpose of matrix or vector |
| A | Excitation amplitude |
| a | Polynomial chaos expansion coefficient vector |
| a^* | Sparse PCE coefficient |
| A_0 | Gamma distribution parameter for ς |
| b | POD coefficient |
| B_0 | Gamma distribution parameter for ς |
| C | Correlation matrix |
| C_0 | Gamma distribution parameter for α |
| c_σ | Stress multiplying factor |
| c_{st} | Viscous damping for impact oscillator |
| d | Number of uncertain parameters |
| D_0 | Gamma distribution parameter for α |
| E | Elastic modulus |
| e | Resolution for ARD threshold value |
| E_{POD} | Threshold value for energy criterion in POD |

| | |
|--------------------|--|
| Err_{LOO} | LOO error |
| f | Polynomial basis function for NARX model |
| f_c | Contact force |
| f_s | Restoring force |
| g | Mathematical function |
| H | Crash box thickness |
| h | Constant for orthogonality condition in PCE |
| K | Kernel smoothing function |
| k_c | Nonlinear spring stiffness for impact oscillator |
| k_{st} | Linear spring stiffness for impact oscillator |
| l | Degree for excitation |
| M | Total number of terms in NARX model |
| m | Degree for response |
| M_1 | Reduced number of terms in NARX model |
| m_E | End mass |
| m_I | Impactor mass |
| m_p | Mass of projectile for impact oscillator |
| m_{st} | Mass of structure for impact oscillator |
| N | Number of samples or model evaluations |
| n | Number of terms in PCE |
| N_1 | Sample number |
| N_2 | Sample number |
| n_β | Number of terms in Kriging |
| n_{tot} | Total number of PCE coefficients |
| n_b | Number of POD modes |
| N_e | Number of elements in Bayesian model parameter |
| n_t | Number of time steps |
| n_x | Time lags for excitation |
| n_y | Time lags for response |

| | |
|-------------------|--|
| N_{\max} | Maximum number of model evaluations |
| n_{\max} | Maximum number of terms in sparse PCE model |
| N_{MCS} | Number of samples for MCS |
| N_{pred} | Number of samples for prediction |
| N_{incr} | Number of samples increased in each step |
| n_{x_m} | Maximum time lag for excitation |
| n_{y_m} | Maximum time lag for response |
| p | Maximum polynomial degree for PCE |
| p_{\max} | Maximum polynomial degree for PCE |
| p_{\min} | Minimum polynomial degree for PCE |
| Q | Degree of basis function |
| q | Variational distribution |
| r | Correlation matrix between new and initial samples |
| S | Partial sensitivity index |
| S_T | Total sensitivity index |
| T | Total time |
| t | Discretized or continuous time |
| $T_{\mathcal{L}}$ | Threshold value for VLB |
| T_A | Threshold value for ARD |
| V | Proper orthogonal mode |
| v | Impactor initial velocity |
| v_0 | Initial velocity for impact oscillator |
| w | Weighted coefficient |
| x | Excitation |
| Y | Matrix or vector of QoI |
| y | Stochastic response or QoI |
| y_p | Displacement of projectile for impact oscillator |
| y_{st} | Displacement of structure for impact oscillator |
| Z | Gaussian process |

| | |
|----------|---|
| z | Vector having lagged excitation and response |
| γ | Coefficient of RBF model |
| ω | Natural frequency |
| ξ | Vector having uncertain parameters |
| Ξ_0 | Prediction samples |
| ALS | Alternating least square |
| ANN | Artificial neural network |
| ANOVA | Analysis of variance |
| AR | Auto-regressive |
| ARD | Automatic relevance determination |
| ARX | Auto-regressive with exogenous input |
| BLUP | Best linear unbiased predictor |
| CB | Crash box |
| CV | Cross validation |
| DOF | Degree-of-freedom |
| EPC | Exponential-polynomial closure |
| FE | Finite element |
| FP | Fokker-Planck |
| FRF | Frequency response function |
| GSA | Global sensitivity analysis |
| KL | Kullback-Leibler |
| KNARX | Kriging-NARX |
| LARS | Least angle regression |
| LASSO | Least absolute shrinkage and selection operator |
| LHS | Latin hypercube sampling |
| LOO | Leave-one-out |
| MCS | Monte Carlo simulation |
| ME | Multi-element |
| MLE | Maximum likelihood estimation |

| | |
|--------|---|
| NAR | Nonlinear auto-regressive |
| NARX | Nonlinear auto-regressive with exogenous input |
| NID | Normally independent distributed |
| OLS | Ordinary least square |
| PCA | Principal component analysis |
| PCE | Polynomial chaos expansion |
| PDF | Probability density function |
| PE | Percentage error |
| POD | Proper orthogonal decomposition |
| POM | Proper orthogonal mode |
| PSI | Partial sensitivity index |
| QoI | Quantity of interest |
| RBDO | Reliability based design optimization |
| RBF | Radial basis function |
| SA | Sensitivity analysis |
| SDOF | Single degree of freedom |
| SI | Sparsity index |
| SIR | Sensitivity index ratio |
| SVB | Sparse variational Bayesian |
| SVD | Singular value decomposition |
| SVM | Support vector machine |
| TDgPCE | Time-dependent generalized polynomial chaos expansion |
| TSI | Total sensitivity index |
| UQ | Uncertainty quantification |
| VB | Variational Bayesian |
| VI | Vibro-impact |
| VLB | Variational lower bound |

Chapter 1

Introduction

1.1 Context

Car accident is one of the major issues concerning road safety. More than 25000 life losses were reported Commission (2019) in 2018 within the area of the European Union due to the road accidents. In the eventually of an accident, one way to mitigate life loss is to properly design the structure of the vehicle. Hence, safe design of a car components is a very important issue in the current scenario.

During an accident, the main concern is the safety of the occupants. Safety of a car passenger depends on several parameters such as design parameters of the car structure, seatbelt condition during an accident, number of occupants and direction of accident. One of the possible accident scenario is the accident due to a frontal impact. Usually, the kinetic energy propagates through its safeguard (which provides safety to the car structure) during an accident and the occupants get injured when the kinetic energy level is too high. Mainly, the ‘bumper’ installed in front of a car is affected first by a frontal accident. Then, the kinetic energy propagates in the car body through its several other protection devices. The mainly affected protections after the bumper are the crash boxes. A car body along with the crash boxes is shown in Figure 1.1. The kinetic energy dissipates through the crash boxes during a frontal accident. Less absorption of the kinetic energy is a possible cause of life loss during a frontal accident. Therefore, the design of the crash boxes is one of the important tasks for designing a safe car.

Analysis of a crash box considering all the possible design parameters is one of the most important criteria for the design of a safe car. Some of the important design parameters of the crash boxes are material properties, geometrical shape, thickness, velocity of the car during an accident, total mass of the car (including the occupants). Usually an impact dynamic analysis is performed considering these parameters deterministic (Abramowicz, 1983; Shaik Dawood et al., 2017; Dirgantara et al., 2013). Often some variability is noticed in the above-mentioned design parameters due to the workmanship, fabrication procedure, non-uniform plate thickness and the number of occupants. Therefore, deterministic analysis may produce non-robust results which ultimately may lead to failure of the crash box during a frontal accident. Therefore, a proper analysis of a crash box should be performed accounting the variability in the design parameters.

As already mentioned, impact dynamic analysis is performed for analyzing a crash box behavior during its design phase. Impact dynamic phenomenon has a quite complicated and

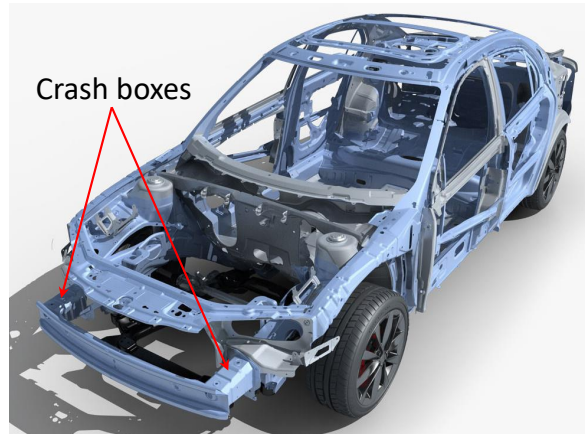


Figure 1.1: Frame structure of a car body (www.cgtrader.com)

nonlinear behavior. The failure and the responses of a crash box under impact loading can be investigated through an experiment. However, conducting an experiment requires a lot of auxiliary equipments, crash box specimen and workmanship. Therefore, performing an experiment is always a costly and destructive procedure. Now, if we consider the above-mentioned variability in the design parameters of a crash box then the experiment should be performed more than several thousand times to make a conclusion on the obtained results. On the contrary, a numerical approach doesn't need any of these cost intensive and destructive procedures, and still produces a similar results as the experiment (Zarei et al., 2008; Dirgantara et al., 2013; Shaik Dawood et al., 2017). Hence, accounting the variability in the design parameters would be much easier by the numerical modeling of a crash box under impact loading. The propagation of the variability through the numerical model allows for the quantification of the variability of the response quantities (e.g. kinetic energy). The impact phenomenon is a time-dependent behavior as the propagation of the kinetic energy through a crash box depends on time. Therefore, to obtain the actual variability in the response quantity, the variability in the design parameters should be propagated through a dynamical system and the time-dependent behavior of the response quantities should be investigated. The design parameters are the uncertain parameters and the propagation of the uncertain parameters through an impact dynamical system is the main challenge of this thesis. Along with this, all the design parameters may not contribute equally in the response quantity which can be measured by the sensitivity of a design parameter on the response quantity (Saltelli et al., 2010; Borgonovo and Plischke, 2016). For a dynamical system, the sensitivity of a design parameter may vary in time. Therefore, time-dependent sensitivity analysis is also necessary to know the contribution of a design parameter on a response quantity properly.

1.2 Uncertainty quantification of dynamical systems

The uncertainty quantification (UQ) of a dynamical system is generally performed through three main steps:

1. First of all, the uncertain parameters (e.g. design parameters in a crash box) are characterized. In this thesis, the uncertain parameters are modeled by a random variable or

random field. The uncertain parameters are then characterized either from an available large data-set or by expert's knowledge.

2. The second step is the propagation of the uncertain parameters through the dynamical system. In this step, the uncertain parameters are considered for the analysis of the physical system to produce the uncertain response quantities. The uncertainty propagation is a multi-step procedure which includes numerical formulation of the problem, computational cost, performing numerical integration etc. Therefore, properly propagating the uncertain parameters through a dynamical system is the main challenge.
3. In the third step, UQ is performed for the obtained uncertain response quantities. The uncertain response quantities are then characterized through some statistical quantities such as mean, standard deviation and probability density function (PDF). For a dynamical system, these quantities are time-dependent.

1.3 Objectives of the research

Inspired from the facts discussed in section 1.1, there are two main objectives of the present research work, which are listed below.

1. The first objective of the research is to propose an efficient approach for UQ of stochastic nonlinear dynamical systems in time domain.
 - Surrogate modeling approach is the most efficient way for UQ. Therefore, the first important aspect of the above-mentioned objective is to formulate a surrogate model which can be used to suitably propagate the uncertain parameters for a nonlinear dynamical system.
 - The second important aspect of a surrogate model is to formulate adaptivity in the number of model evaluations such that the number of model evaluations selected adaptively for a response quantity.
2. The second objective of the thesis is to quantify uncertainty and perform sensitivity analysis of the impact dynamical systems using the developed approach in the previous step.
 - UQ of an impact oscillator will be performed first.
 - Then, UQ of a crash box under impact loading will be conducted in the time domain.
 - Global sensitivity analysis of the crash problem will be performed to identify the influential uncertain parameters for the problem.

1.4 Outline of the thesis

This thesis is organized as follows:

Chapter 2 describes the available approaches for UQ of the dynamical systems. More specifically, an extensive review of the available surrogate models is conducted. Along with this, the more general approaches for UQ such as Monte Carlo simulation and the other

sampling based approaches are also discussed. The need of the present research work is identified from the extensive literature review.

Chapter 3 introduces a new approach for UQ of the nonlinear dynamical systems which decouples the time domain and the randomness by the Nonlinear Auto-Regressive with eXogenous input (NARX) model and the Kriging surrogate model, respectively. Applicability of the developed approach is investigated on different nonlinear dynamical systems in this chapter. The applicability of this approach is also discussed in the context of an impacted dynamical system. Finally, the concluding remarks of this chapter and the limitations of this approach are discussed which depict NARX is unable to capture the dynamics of an impact oscillator. To address this issue, a different kind of surrogate model is developed in the next chapter.

Chapter 4 introduces a different approach for the propagation of the uncertain input parameters and for UQ of the dynamical systems to address the limitations arisen in the previous chapter. Furthermore, UQ is performed for the impact oscillators using the developed approach. To reduce the number of coefficients in the PCE model, a sparse PCE model is developed in the next chapter.

Chapter 5 describes a method for the construction of a sparse PCE surrogate model based on variational Bayesian inference. This approach helps in propagating uncertainty using a reduced number of terms in the polynomial basis of a PCE model and it is used in the next chapter along with the POD approach.

Chapter 6 explains an adaptive framework for UQ of impact dynamical systems in time domain. UQ is performed for different uncertain response quantities of a crash box model. In addition, a global sensitivity analysis is also performed to identify the most influential uncertain input parameters for a particular response quantity.

Chapter 7 gives the concluding remarks of the present research work. The limitations of the present research work are also discussed. Finally, some future developments of this present research work are proposed to the research community.

Chapter 2

State-of-the-art review

Several approaches have been proposed in the literature for uncertainty propagation. Most of the available approaches for uncertainty propagation of uncertain (stochastic) dynamical systems are discussed in this chapter.

2.1 Monte Carlo simulation

Monte Carlo simulation (MCS) (Fishman, 1996; Caflisch, 1998; Rubinstein and Kroese, 2008) is a quite famous and simple approach for UQ of any systems. Let us consider a dynamical system having d uncertain parameters $\xi = \{\xi_1, \xi_2, \dots, \xi_d\} \in \mathbb{R}^d$, and the uncertain quantity of interest (QoI) is denoted by $y(\xi, t)$. t denotes the time and the uncertain parameters are assumed here independent of time. A large number of random samples is usually drawn for each of the d dimensional uncertain parameters according to probability distributions, and a deterministic simulation is performed for each sample to get the QoI. The usefulness of the MCS approach is that it can predict accurate results for UQ. MCS was applied to propagate uncertainty for stochastic dynamical system (Papadrakakis and Papadopoulos, 1996) in finite element (FE) model. Furthermore, MCS approach has been used extensively for the stochastic dynamical systems (Pradlwarter and Schuëller, 1997; Hurtado and Barbat, 1998). MCS has been used for obtaining the stationary and the non-stationary PDF of non-linear oscillators (Muscolino et al., 1997), and for nonlinear stochastic dynamical systems excited with the stationary Poisson white noise (Muscolino et al., 2003).

Often the analytical results are not available for a given uncertain response quantity and MCS computed results are considered as the reference solution in that case. However, the convergence rate of the MCS approach is approximately proportional to $\frac{1}{\sqrt{N_{\text{MCS}}}}$ (Mai, 2016) where N_{MCS} is the number of samples. Hence, the convergence rate is quite slow for the MCS. Often, in practice, the number of model evaluation (N_{MCS}) is at least 10^6 , which may lead to a prohibitive computational cost depending on the cost of one model evaluation.

2.2 Sampling based approaches

MCS is based on the possibility of generating samples. Different methods for obtaining samples are presented in the following sub-sections.

2.2.1 Latin hypercube sampling

Latin hypercube sampling (LHS) approach (McKay et al., 1979; Stein, 1987; Helton and Davis, 2003) is commonly used to generate samples. LHS generates samples in the d -dimensional unit hypercube $[0, 1]^d$ uniformly. Usually, the domains of the random variables are divided in N_{MCS} equal intervals and the samples are placed randomly at a single position in each of the intervals. The usefulness of the LHS scheme is that the convergence rate is quite high using this approach as compared to the random sampling based MCS approach. The computer code for generating the LHS points can be found in (Iman and Conover, 1980). However, the LHS points can also be generated using the Matlab function *lhsdesign*: it is utilized in this thesis for generating LHS points.

2.2.2 Sobol sequence

Sobol sequence (Sobol, 1967, 1990), the so-called quasi-Monte Carlo (QMC) method is another sampling based approach, which can be used for the MCS. Sobol sequence is also called as the quasi-random low discrepancy sequence (Niederreiter, 1992; Dick and Pillichshammer, 2010). In Sobol sequence, the samples are generated in the d -dimensional unit hypercube $[0, 1]^d$ uniformly. It tries to minimize the intersite distance and the projected distance such that most of the space in the unit hypercube can be filled. Hence, the convergence of the QMC method is always better for the MCS approach. Algorithm for generating Sobol sequence samples can be found in (Bratley, 1988). However, in many programming languages (e.g. Matlab or Python), this algorithm has already been coded and is readily available. The quasi-random sequence are deterministic: for example, the N first samples of the Sobol sequence in d -dimension always gives the same numbers.

2.3 Surrogate modeling approach

As stated in the previous sections, the accuracy of the MCS approach can be quite high but, the computational efficiency is quite low. Although it is possible to reduce the computational cost by using the LHS or, Sobol sequence, still these approaches require a lot of model evaluation to obtain an accurate result. To overcome this issue, the surrogate modeling approaches (Ghanem and Spanos, 1991; Xiu and Karniadakis, 2002; Wan and Karniadakis, 2005) were developed by the researchers. Surrogate model is also known as meta-model. In surrogate modeling, the stochastic response quantity is approximated by a suitable function such that a trade-off can be maintained between the accuracy and the efficiency. According to the mathematical form of the function, different surrogate models have been developed in the past two decades. However, surrogate modeling approach can be broadly classified into two different categories namely intrusive approach (Le Matre et al., 2001; Xiu and Karniadakis, 2002; Gerritsma et al., 2010) and non-intrusive approach (Sudret, 2008; Blatman and Sudret, 2010b; Luchtenburg et al., 2014). The general outline of formulating both the approaches are discussed in the next sub-sections.

2.3.1 General outline of intrusive surrogate model

Although the mathematical formulation for all the surrogate models are different, the general outline of formulating an intrusive surrogate model is described below:

- First of all, the problem to be solved is mathematically formulated by some governing differential equations or by any discretization approach such as FE model, finite difference model.
- In the second step, the QoI is replaced by a mathematical function of a suitable surrogate model.
- Then, the problem is solved by a suitable approach (e.g. Galerkin projection) to get the stochastic response quantity. For a dynamical system, a system must be solved at each time-step during the time-integration procedure. Therefore, the intrusive approach requires the mathematical formulation of a physical system to compute a stochastic QoI.

2.3.2 General outline of non-intrusive surrogate model

For the non-intrusive approach, the formulation is different than the intrusive approach. The non-intrusive surrogate model is formulated generally in the following way:

- First of all, the QoI is required at some predefined samples. The samples can be obtained from a field measurement or from some experimental design point approach (sampling approach). Then, the QoI is evaluated at the predefined sample points. The physical system is solved numerically by a deterministic model (e.g. FE model) for the number of predefined sample points which is often considered as the computationally expensive step.
- Then, a suitable mathematical model is identified based on the available physical informations to obtain the surrogate model.
- The accuracy of the surrogate model needs to be checked, which can be made using an independent set of sample points. The responses predicted from the new set of samples must be compared with the ‘exact’ QoI, i.e. obtained either from measurements or from the initial model. However, cross-validation (Blatman and Sudret, 2011) can also be used without any new sample to measure the accuracy of the surrogate model.
- The surrogate model in the previous step can be used to predict the QoI at a large set of samples (N_{MCS}) with a negligible computational cost as compared to the MCS of the initial model. Furthermore, the statistical quantities (e.g. mean, standard deviation) of the uncertain QoI can be computed easily from the predicted QoI.

Based on the mathematical form of the surrogate model, several surrogate models have been developed in the past two decades. The most popular surrogate models are polynomial chaos expansion (PCE) (Xiu and Karniadakis, 2002; Jacquelin et al., 2015a; Mai and Sudret, 2017; Bhattacharyya, 2018), Kriging (Santner et al., 2003; Kaymaz, 2005), support vector machine (SVM) (Collobert and Bengio, 2001; Bourinet et al., 2011), radial basis function (RBF) (Deng, 2006; Li et al., 2018; Wu et al., 2019), artificial neural network (Hosni Elhewy et al., 2006; Tripathy and Bilonis, 2018) and moving least square method (Lancaster and Salkauskas, 1981). Out of all the surrogate models, PCE and Kriging have been used extensively for the development of a proper surrogate model for mechanical systems. Therefore, PCE and Kriging models are described in the next sections in an elaborated way. Along with this, SVM and RBF are also described briefly.

2.4 Polynomial chaos expansion for dynamical systems

2.4.1 Formulation of polynomial chaos expansion

Polynomial Chaos Expansion (PCE) is one of the most widely used surrogate models for the propagation and quantification of uncertainty. This method was first implemented in structural mechanics for the finite element (FE) approach by Ghanem and Spanos (1991) which is also known as spectral approach. However, this approach was introduced by Wiener (1938) for solving stochastic partial differential equation having Gaussian input random variable. Further, it was modified by Xiu and Karniadakis (2002) to account the other types of statistical distributions (e.g. uniform, gamma). The already available PCE was coupled with the Askey scheme (Koekoek and Swarttouw, 1996) to propose generalized PCE and this was proved to be applicable for most of the random variables. The PCE has been used a lot in different areas for almost two decades. The PCE model is discussed in this section considering the time-dependent uncertain QoI.

Consider $(\Omega, \mathcal{F}, \mathcal{P})$ be the complete probability space, in which Ω is the sample space consisting of all events \mathcal{F} and $\mathcal{P}: \mathcal{F} \rightarrow [0, 1]$ is the probability measure. The uncertain quantities can be described with random variables $\xi = \{\xi_1, \xi_2, \dots, \xi_d\}$: in the following, all the random variables are assumed to be independent. ‘ d ’ is a non-zero integer and is the number of uncertain parameters. According to the PCE (Xiu and Karniadakis, 2002), the uncertain QoI of a dynamical system is expressed as:

$$y(\xi, t) = \sum_{i=1}^{\infty} a_i(t) \phi_i(\xi) \quad (2.1)$$

where $y(\xi, t)$ is the time-dependent uncertain QoI. $\phi_i(\xi)$ are the multivariate orthogonal polynomial basis functions and $a_i(t)$ are the time-dependent PCE coefficients. For the multivariate polynomials, if $i > j$ then the degree of $\phi_i \geq$ the degree of ϕ_j , and the degree of $\phi_1 = 0$. The multivariate orthogonal polynomials are constructed from the tensor product of the univariate orthogonal polynomials due to the independent random variables:

$$\phi_i(\xi) = \prod_{j=1}^d \varphi_{i,j}(\xi_j) \quad (2.2)$$

where $\varphi_{i,j}(\xi_j)$ is the i -th univariate orthogonal polynomial basis function for the j -th random variable. These orthogonal polynomials must satisfy the following condition with respect to the joint PDF:

$$\langle \varphi_{i_1} \varphi_{i_2} \rangle = \int_{\mathbb{R}_\xi} \varphi_{i_1}(\xi) \varphi_{i_2}(\xi) f_\xi(\xi) d\xi = h^2 \delta_{i_1 i_2} \quad (2.3)$$

where $\delta_{i_1 i_2}$ is the Kronecker delta which is 1 when $i_1 = i_2$ and zero for the other cases. h is a constant: it is 1 for the orthonormal polynomial basis functions; $\langle \bullet \rangle$ represents the expectation operator on the orthogonal polynomials. The family of the univariate orthogonal polynomial basis functions for a random variable is chosen as per the Askey scheme and the orthogonal polynomials for different types of input random variables are given in Table 2.1.

For the practical implementation of the PCE model, the expression in Equation 2.1 is truncated, which involves a finite number of terms in the polynomial basis. Hence, the truncated PCE model is represented by:

$$y(\xi, t) \approx \sum_{i=1}^n a_i(t) \phi_i(\xi) \quad (2.4)$$

Table 2.1: Type of orthogonal polynomials for different types of input random variables in PCE (Xiu and Karniadakis, 2002)

| Variable type | Random variable | Type of orthogonal polynomial | Support |
|---------------|-------------------|-------------------------------|----------------------|
| Continuous | Gaussian | Hermite | $[-\infty, \infty]$ |
| | Gamma | Laguerre | $[0, \infty]$ |
| | Beta | Jacobi | $[a, b]$ |
| | Uniform | Legendre | $[a, b]$ |
| Discrete | Poisson | Charlier | $\{0, 1, \dots\}$ |
| | Binomial | Krawtchouk | $\{0, 1, \dots, N\}$ |
| | Negative binomial | Meixner | $\{0, 1, \dots\}$ |
| | Hypergeometric | Hahn | $\{0, 1, \dots, N\}$ |

where n is the finite number of terms in the expansion. The total number of terms is calculated as:

$$n = \binom{d+p}{p} = \frac{(d+p)!}{d!p!} \quad (2.5)$$

where p is the maximum degree of the polynomials. The main difficulty in the PCE model is the computation of the PCE coefficients. The PCE coefficients can be computed by several ways. For the intrusive approach, the PCE coefficients are usually computed by the Galerkin projection approach (Gerritsma et al., 2010; Jacquelin et al., 2015b). On the contrary, for the non-intrusive approach, the PCE coefficients can be computed through different procedure such as stochastic collocation approach (Gerstner and Griebel, 1998; Zhang et al., 2014; Ozen and Bal, 2017b), regression approach (Blatman and Sudret, 2010b,a; Bhattacharyya, 2018). Out of all, the Galerkin projection approach and the regression approach are discussed below.

2.4.2 Computation of PCE coefficients by Galerkin projection

The usual approach for computing the PCE coefficients in an intrusive approach is the Galerkin projection. To illustrate this, consider a dynamical system having an uncertain QoI y and the random variables are denoted by ξ :

$$\mathcal{L}(\xi, t; y) = g(\xi, t) \quad (2.6)$$

where, \mathcal{L} is a differential operator and $g(\xi, t)$ is a function with the random variables. Now, the QoI y can be expressed by the PCE in Equation 2.4. Therefore, after substituting the response in terms of PCE, Equation 2.6 can be written as:

$$\mathcal{L}\left(\xi, t; \sum_{i=1}^n a_i(t) \phi_i(\xi)\right) = g(\xi, t) \quad (2.7)$$

Now, it is required to project both sides of Equation 2.7 on each of the polynomial basis functions to get the n differential equations which means tensorial multiplication is performed with the both sides of the equation:

$$\forall j = 1, 2, \dots, n \quad \left\langle \mathcal{L}\left(\xi, t; \sum_{i=1}^n a_i(t) \phi_i(\xi)\right), \phi_j \right\rangle = \langle g(\xi, t), \phi_j \rangle \quad (2.8)$$

The unknown coefficients a_i are then determined by solving the n deterministic differential equations. As it can be seen from Equation 2.8 the system is time-dependent, the system must be solved inside the time integration procedure. The time integration of the dynamical system can be performed by the Runge-Kutta method, the Crank-Nicolson scheme (Crank and Nicolson, 1996) or the Newmark's time integration method (Newmark, 1959).

2.4.3 Computation of PCE coefficients by a regression approach

Regression approach is utilized to compute the PCE coefficients in a non-intrusive PCE model formulation. Ordinary least square (OLS) approach is one of the appropriate solutions for computing the unknown PCE coefficients. It is a non-intrusive approach and it requires the QoI at some predefined sample points. Hence, N number of realizations of the random variables is given by a matrix $\Xi = \{\xi_1, \xi_2, \dots, \xi_d\} \in \mathbb{R}^{N \times d}$: $\xi_i \in \mathbb{R}^{N \times 1}$ is the vector having all the N realizations for the i -th random variable whereas Ξ_i represents the i -th row of the matrix Ξ (i.e. i -th realization for all the random variables), and Ξ_{ij} represents the i, j -the element of the matrix Ξ . The QoI is then evaluated at the N sample points utilizing a deterministic code (e.g. FE model), which gives the matrix $Y = \{Y_1, Y_2, \dots, Y_N\}^T \in \mathbb{R}^{N \times n_t}$: n_t is the total number of time-steps for the time integration of the dynamical system. Having these quantities, the PCE model is approximated by Equation 2.4:

$$Y(\Xi, t) \approx \sum_{i=1}^n \Phi^{(i)}(\Xi) a_i(t) \quad (2.9)$$

where $\Phi(\Xi) \in \mathbb{R}^{N \times n}$ is the polynomial basis matrix having all the polynomial basis functions evaluated at the N sample points and $\Phi^{(i)}(\Xi) \in \mathbb{R}^{N \times 1}$ is the vector having all the N realizations of the i -th PC. $a_i(t)$ are the time-dependent PCE coefficients, which are computed using the OLS approach. In the OLS approach, the coefficients are computed by minimizing the mean square error:

$$\forall t_k, k \in \{1, \dots, n_t\} \quad a(t_k) = \arg \min_{a(t_k)} \frac{1}{N} \sum_{i=1}^N \left[Y(\Xi_i, t_k) - \sum_{j=1}^n \Phi^{(j)}(\Xi_i) a_j(t_k) \right]^2 \quad (2.10)$$

The solution of the above-mentioned equation is explicitly given by:

$$\forall t_k, k \in \{1, \dots, n_t\} \quad a(t_k) = \left[\Phi^T(\Xi) \Phi(\Xi) \right]^{-1} \Phi^T(\Xi) Y(\Xi, t_k) \quad (2.11)$$

The main difficulty with the Galerkin and the OLS approaches for a dynamical system is that the coefficient vector is computed at each time-step and the number of time step n_t is quite high for a dynamical system, which may lead to a high computational cost.

2.4.4 Post-processing of PCE results

The statistical response quantities (e.g. mean and standard deviation) are the important quantities for UQ of a system. PCE has the ability to compute the statistical moments using almost no computational cost. Indeed, the multivariate polynomials are orthonormal with respect to the marginal PDF of the input random variables which means:

$$\forall i > 1 \quad \langle \phi_i(\xi) \rangle = 0 \quad (2.12)$$

$$\langle \phi_i(\xi) \phi_j(\xi) \rangle = \delta_{ij} \quad (2.13)$$

The predicted mean and standard deviation are given by:

$$\hat{\mu}(y(\xi, t)) = a_1(t) \quad (2.14)$$

$$\hat{\sigma}(y(\xi, t)) = \sqrt{\sum_{i=2}^n a_i^2(t)} \quad (2.15)$$

Another important result for UQ is the PDF of the predicted response at a given time. Usually the PDF can be estimated from the response with a large number of sample points. Once the PCE coefficients are computed, the response quantity can be easily predicted by Equation 2.9. Only the orthogonal polynomials are evaluated for a large number of samples N_{pred} . The PDF of the predicted response can be computed using the kernel density estimator (Bowman and Azzalini, 1997):

$$\hat{f}_{\hat{h}}(Y_{\text{pred}}(t)) = \frac{1}{N_{\text{pred}} \hat{h}} \sum_{i=1}^{N_{\text{pred}}} K\left(\frac{Y_{\text{pred}}(t) - Y_{\text{pred},i}(t)}{\hat{h}}\right) \quad (2.16)$$

where $K(\bullet)$ is a kernel smoothing function (e.g. uniform, normal) and \hat{h} is the bandwidth. The above-mentioned procedure is incorporated in the Matlab software as *ksdensity* function which is used in this thesis with the default settings.

2.5 PCE models applied to dynamical systems: available approaches

An extensive review is conducted here to get an outlook of the available approaches using the PCE model for the dynamical systems. The present discussion is based on the two different categories of surrogate modeling approach as discussed in section 2.3. Firstly, the intrusive approaches are discussed: they require the differential equation of a dynamical system. Afterwards, the non-intrusive approaches will be discussed.

2.5.1 Intrusive approaches

As discussed in the Galerkin projection approach (subsection 2.4.2), the intrusive approach requires the governing differential equation of the system to propagate uncertainties through the system. Hence, the stochastic QoI is directly computed by solving the governing differential equation of a dynamical system. The PCE model was used in the context of the nonlinear dynamical systems by Ghanem and Spanos (1993). The time-dependent QoI was approximated by the PCE model while the PCE coefficients were computed using the Galerkin approach as described previously in this chapter.

Further, an adaptive PCE model has been developed by Li and Ghanem (1998) to capture the nonlinear behavior of a dynamical systems with higher order terms in the PCE basis. Firstly, the PCE terms are separated in three categories: one linear contribution for K -dimension (out of d -dimension), another linear contribution for the $(d - K)$ -dimension and

one nonlinear contribution for K -dimension only. Then, a Galerkin projection is performed to compute the coefficients in each iteration only using the linear terms, and the L_2 norm of all the PCE coefficients is computed up to the available time series. The nonlinear term is then added for a dimension (out of K -dimension) which produces large L_2 norm. In this way, the nonlinear terms are added with the existing linear PCE model. A duffing oscillator excited with a random process acceleration has been investigated using this approach and it was useful to capture the high order nonlinearity of the duffing oscillator.

The Galerkin projection approach has been also used by Le Matre et al. (2001) to solve the stochastic incompressible Navier-Stokes equation. Until this investigation, the PCE model was only applied the Gaussian input random variables. In 2002, Xiu and Karniadakis (2002) proposed the generalized PCE model, which accounts the Gaussian and also the other types of random variables as given in Table 2.1. The generalized PCE model is termed as PCE model throughout this thesis. The PCE model was then applied to random oscillators by Lucor et al. (2004) having different types of input random variables. Further, the adaptive PCE model developed by Li and Ghanem (1998) was applied to a duffing oscillator (Lucor and Karniadakis, 2004) subjected to random process excitation having the other types of random variables. Although with the adaptive PCE, it was possible to reduce the error with time as compared to the PCE model, the error in the prediction of the second order moment was overestimated in the later time. Therefore, Lucor and Karniadakis (2004) observed that the increase of the number of interaction terms between the random variables is improving the accuracy in the later time.

A different kind of adaptive PCE model was proposed (Wan and Karniadakis, 2005) by decomposing the random space in several segments which is called multi-element PCE (ME-PCE) model. The idea behind the formulation of the ME-PCE was to decompose the random space into the total number of random variables and, further, these sub-domains are divided into two local random variables. The PCE model is then applied on the decomposed domains with only two random variables which is much simpler as compared to the initial problem with a large set of random variables. The ME-PCE model was applied to the Kraichnan-Orszag three mode problem (Orszag and Bissonnette, 1967) and a stochastic advection-diffusion problem. It was possible to propagate the uncertainties through the nonlinear dynamical systems using low degree polynomials by the ME-PCE model with low computational cost as it requires much less terms in the PCE basis and hence, the number of PCE coefficients is much smaller in this case. Further, this ME-PCE model was applied to a stochastic flow problem (Wan and Karniadakis, 2006) to investigate the uncertainty in the drag and lift coefficients when a noisy flow is passing through a stationary circular cylinder.

To improve the accuracy of the Galerkin projection based PCE, a different kind of polynomial basis function has been used by Le Maître et al. (2007) to propagate uncertain parameters through chemical systems. The polynomial basis functions have been constructed using a multi wavelet basis, which is almost similar to the ME-PCE model (Wan and Karniadakis, 2005). The polynomial basis is not dependent on the dimensionality of the dynamical system instead, it depends on the number of sub domains. Although this strategy has increased the prediction accuracy, it is not so efficient as compared to the PCE model. The PCE model was investigated by Le Maître et al. (2004) using Haar polynomial basis function (Burrus et al., 1998) instead of the polynomial basis function proposed by Xiu and Karniadakis (2002). The Haar polynomial basis function was found to be robust as compared to the Legendre polynomial. A basis enrichment scheme was proposed by Ghosh and Ghanem (2008) for a non-smooth random eigenvalue problem. It was seen that the enrichment was suitable to

make a statistical characterization of the eigenvalues and the eigenvectors. However, the enrichment is highly dependent on the knowledge about a physical system, hence, a general framework for all the problems was not possible to propose. Further, two approaches have been used by Ghosh and Ghanem (2008) to compute the PCE coefficients namely Galerkin projection and Newton-Raphson iteration based approach, and both the approaches were successfully applied in accordance with the basis enrichment scheme.

A quite interesting intrusive approach was proposed by Gerritsma et al. (2010), which is called time-dependent generalized PCE (TDgPCE) model. This method utilized a different kind of modification criterion for the basis function. The main problem with the PCE is that the polynomial basis is not optimal with the increase of time for the long time integration problems. Therefore, the main idea behind the TDgPCE is that the optimal polynomial basis (i.e. with few terms and a low polynomial degree, but with a good accuracy) changes with the time. A new polynomial basis is chosen at different times t . The new random functions are constructed in a way such that they satisfy the condition of an ideal random function (Doi and Imamura, 1969) i.e. the new random functions must satisfy the orthogonality condition (Equation 2.3) to formulate a PCE model. The polynomials must change with the time so that the PCE can capture the PDF of a QoI by an optimum set of polynomials. Same phenomenon has been utilized by Gerritsma et al. (2010) to construct new orthogonal polynomial functions. In the time integration procedure, the response in the previous time step is considered as the new random variable in the current time step. Therefore, instead of constructing new basis function from the orthogonal family as given in Table 2.1, the new orthogonal polynomial basis functions are constructed using the Gram-Schmidt orthogonalization procedure in terms of the predicted QoI of previous time steps and, at time $t = t_i$ the solution is considered to be the new random variable for $t = t_{i+1}$. Although the TDgPCE approach was useful for propagating uncertainties through the Kraichnan-Orszag problem (Gerritsma et al., 2010), it suffers to predict the time-dependent statistical moments for a single degree of freedom (SDOF) dynamical system as investigated in Appendix A. The SDOF dynamical system has been investigated for different natural frequencies in Appendix A and it was found that TDgPCE approach was able to predict the stochastic response when the natural frequency is close to the excitation frequency, however, it was unable to predict the stochastic response quantity in the later time when the natural frequency is quite high as compared to the excitation frequency. Another drawback of TDgPCE is that the new polynomial basis function was constructed at each time-step for the Kraichnan-Orszag problem which is a quite computationally expensive.

A different kind of dynamical PCE model was proposed by Ozen and Bal (2016, 2017a) to handle the stochastic partial differential equation driven by Brownian motion. The dynamical PCE (Ozen and Bal, 2017a) was applied to the stochastic Burgers equation and Navier-Stokes equation driven by white noise force. A combination of TDgPCE and ME-PCE has been proposed by Heuveline and Schick (2014) for the long time integration of dynamical systems. The three mode Kraichnan-Orszag problem and a stochastic time-dependent chemical problem were investigated using the combined approach which improved the prediction accuracy significantly. A different kind of PCE for the dynamical systems was proposed by Maitre et al. (2010) based on time scale transformation. The time domain was rescaled to a smaller time domain based on the idea taken from (Witteveen and Bijl, 2008a,b). Therefore, the PCE was applied in the rescaled time domain to propagate the uncertain response quantity. This approach was applied for UQ of a chemical process having two random variables and a good accuracy was achieved for the long time integration. During the computation of the PCE

coefficients by Galerkin projection, the right side of the spectral functions are rational and it often requires high degree polynomial to assess a stochastic system properly. To enhance the efficiency with low degree polynomial, a Krylov subspace projection approach (Nair and Keane, 2002) has been used in conjunction with the PCE model by Kundu and Adhikari (2013, 2014). Krylov subspace helps to predict the response quantity in the reduced domain using low degree polynomial which subsequently reduced the computational cost.

The intrusive approach for the dynamical system has also been adopted in the frequency domain (Jacquelin et al., 2015a,c, 2017). The first two moments of the steady-state response for the linear dynamical systems was obtained in (Jacquelin et al., 2015c) by the PCE model. However, the required polynomial degree was much high. For accelerating the approximation, Aitken's criterion (Brezinski, 1996) has been used in (Jacquelin et al., 2015a), which accelerates the convergence of the first two statistical moments. To accurately compute the PDF and the statistical moments an extended Padé approximation (Matos, 1996) based PCE has been developed in (Jacquelin et al., 2017): it was useful in predicting an accurate results using low degree polynomial. Some other application of the Galerkin projection based PCE model can be found in (Kundu and Adhikari, 2015; Pryse et al., 2018).

2.5.2 Non-intrusive approaches

The above discussion was solely based on the intrusive approach in which the governing differential equations of the system are required. However, for a practical problem (e.g. FE large scale problem), the governing differential equation is often not available or it is much difficult to solve a system considering the mathematical form of a surrogate model. In that case, it is necessary to apply the non-intrusive approaches for propagating the input random variables through a dynamical system.

Initially, the non-intrusive approach was applied on the spectral projection based approach. Unlike the Galerkin projection approach, the PCE model as given in Equation 2.4 is projected on the polynomial basis functions and the coefficients are further computed using the statistical simulation. This approach was utilized by Ghosh and Iaccarino (2007) to compute the PCE coefficients. Along with this, a different type of polynomial basis function (a composition of *sine* and *cosine* function) has been used by Ghosh and Iaccarino (2007) to propagate the uncertainties through a carbon monoxide surface oxidation model. Although the results were sufficiently good, this basis function is dependent on the specific problem. A different kind of non-intrusive approach was proposed by Pettit and Beran (2006) in which the the Haar polynomial basis function (Burrus et al., 1998) has been used for constructing the PCE model. Pettit and Beran (2006) have found that the coefficients corresponding to the Haar polynomial bases can be computed more efficiently and accurately using the Mallat's pyramid algorithm (Strang and Nguyen, 1996; Burrus et al., 1998). This method was applied for UQ of a sinusoidal function and a 2-DOF nonlinear dynamical system.

The OLS approach as discussed in section 2.4.3 was applied by Sudret (2008) for global sensitivity analysis. It was adopted in the UQ domain for structural engineering problems by Blatman and Sudret (2008). Along with this, the important polynomial bases were selected using a forward-backward approach which ultimately improved the accuracy and the efficiency of the predicted results. However, all these approaches were developed in the context of static systems. Later, a sparse PCE model (Blatman and Sudret, 2011) has been combined with the principal component analysis (PCA) (Jolliffe, 2002) approach for UQ of a one-dimensional diffusion problem by Blatman and Sudret (2013). The important polynomials

were identified by the least angle regression (LARS) (Efron et al., 2004) to formulate the sparse PCE model (Blatman and Sudret, 2011). The uncertain parameters were propagated by Blatman and Sudret (2013) using the sparse PCE model (Blatman and Sudret, 2011) and the time-dependent behavior of the response quantity was addressed using the dominant principal components by the PCA approach. The PCE coefficients have been computed by using an alternating least square (ALS) approach (Beylkin and Mohlenkamp, 2002, 2005) by Doostan and Iaccarino (2009); Doostan et al. (2013) to substantially reduce the computational cost. The ALS approach helps in solving a high-dimensional problem with low rank and the computational cost increases linearly with respect to the dimensionality of the problem. However, this method has not been investigated in the context of dynamical systems.

A different type of non-intrusive approach was proposed by Luchtenburg et al. (2014), which is almost similar to the TDgPCE approach. In this method, the orthogonal polynomial basis has been modified with time using a flow map composition technique. A long-time integration of a stochastic differential equation uses a short-time flow map of the orthogonal polynomial basis function. More specifically, at the new time-step, new basis functions are generated and the previous basis function is also used. As it uses flow maps of all the previous time-steps, it is important to specify that the degree of the polynomial should be kept small i.e. the response should be represented by low-degree orthogonal polynomial. Let us consider a simple ordinary differential equation (ODE):

$$\frac{dy(t, \xi)}{dt} = g(t, y; \xi) \quad (2.17)$$

Now, consider $\psi_{t_0}^{t_f}$ be the flow map such that $\psi_{t_0}^{t_f}(\xi)$ is the solution of Equation 2.17. Therefore, Equation 2.17 becomes:

$$\frac{d\psi_{t_0}^t(\xi)}{dt} = g(t, y_0; \xi) \quad (2.18)$$

where y_0 is the initial condition at $t = 0$. For any time t_i , the long-time flow map is defined by:

$$\psi_{t_0}^{t_i} = \psi_{t_{i-1}}^{t_i} \circ \psi_{t_{i-2}}^{t_{i-1}} \circ \dots \circ \psi_{t_1}^{t_2} \circ \psi_{t_0}^{t_1} \quad (2.19)$$

This equation defines the flow map for long-time integration problem whereas each of the small part defines the short-time flow map. Consequently, any short time flow map (for time-step Δt) is defined by the PCE expansion as:

$$\psi_{t_0}^{t_0+\Delta t} = \sum_{j=0}^Q \sum_{i=1}^n \hat{a}_{t_0, ij}^{t_0+\Delta t} \phi_i(\xi) \Theta_j(y) \quad (2.20)$$

where $\Theta_j(y)$ is the basis function of the response quantity which is calculated in a similar way to Equation 2.2. Q is the degree of the basis function $\Theta_j(y)$, which can be different from p . The flow map for any time-step Δt can be found by solving Equation 2.17. Equation 2.20 has been solved by Luchtenburg et al. (2014) in a non-intrusive way by a stochastic collocation method. UQ of a nonlinear double gyre flow has been carried out using this method (Luchtenburg et al., 2014) and it outperforms the PCE model with low degree polynomial. However, this method struggles in computational efficiency for highly nonlinear and high-dimensional problem. It is clearly stated by Luchtenburg et al. (2014) that the computational cost is very high even for low-dimensional problem with low degree polynomial. The reason is that

the degree of the resulting polynomial increases exponentially with the number of time-steps and a very small time-step is required for a highly nonlinear problem. As the PCE model was solved by the stochastic collocation approach (Luchtenburg et al., 2014), it also has a drawback: the number of collocation points increases exponentially (Palar et al., 2016) with the increase of the dimensionality of a system.

A different non-intrusive approach has been proposed by Spiridonakos and Chatzi (2015). The time dependent nonlinear behavior and the randomness have been decoupled by the Nonlinear Auto-Regressive with eXogenous input (NARX) model and the PCE model, respectively: the resulting surrogate model is called PCE-NARX model. The nonlinear time dependent behavior has been modeled using a polynomial NARX model (Chen and Billings, 1989) and the NARX model was formulated in a similar way to the PCE model as given in Equation 2.4. In addition, the important NARX polynomial bases for a specific problem were selected using genetic algorithm. The coefficients corresponding to the important polynomials were uncertain and, then, were approximated by a sparse PCE model. The sparse PCE model was constructed using a least square optimization procedure. Time-dependent stochastic quantities of a nonlinear dynamic oscillator were predicted using the PCE-NARX model: a good accuracy and efficiency have been achieved using the PCE-NARX surrogate model. A similar kind of sparse PCE-NARX model was investigated by Mai et al. (2016) for nonlinear dynamical systems, which used the sparse PCE model proposed in (Blatman and Sudret, 2011). The polynomial NARX model was also used by Mai et al. (2016) and the important terms in the NARX polynomial basis were selected using the LARS approach (Efron et al., 2004). The PCE coefficients were obtained by the OLS approach (Mai et al., 2016). The sparse PCE-NARX model has been applied to a Duffing oscillator and Bouc-Wen oscillator for UQ in the time domain and very good results were obtained with much less number of model evaluations as compared to MCS. A different kind of non-intrusive approach was proposed by the same researchers (Mai and Sudret, 2017) which is called time warping PCE. A time warping PCE model was constructed in a similar way to the approach proposed by Maitre et al. (2010) by rescaling the time domain. Then the PCA based PCE (Blatman and Sudret, 2013) was applied on the rescaled time-dependent response quantities for UQ of the dynamical systems. Recently, a mixed sparse grid collocation approach has been used in conjunction with the PCE model by Bhusal and Subbarao (2019) to propagate uncertainties through linear and nonlinear dynamical systems. The mixed sparse grid points were obtained for a multi-dimensional problem based on the PDF of the input random variables, hence, the PCE polynomial basis functions are much more representative for a dynamical system.

2.6 Kriging surrogate model

Out of all the surrogate models, Kriging (Krige, 1951; Sacks et al., 1989; Kaymaz, 2005), also known as Gaussian process regression, has also emerged rapidly in the last two decades. The name Kriging came after a South African engineer Krige (Krige, 1951) investigated this approach for the statistical characterization of the mining engineering resources. Kriging was applied on geo-statistics by Matheron (Matheron, 1963). Further, it was used to analyze the data taken from a computational experiment (e.g. FE simulation) (Sacks et al., 1989; Santner et al., 2003). Kriging has been used extensively for the reliability analysis problems (Kaymaz, 2005; Echard et al., 2011; Gaspar et al., 2014; Lu et al., 2018a; Lelièvre et al., 2018), for UQ problems having static QoI (Kersaudy et al., 2015; Mukhopadhyay et al., 2016;

Bhattacharyya, 2018) and for the optimization problems (Dubourg et al., 2011; Durantin et al., 2016; Moustapha et al., 2016).

2.6.1 Construction of the model

Recall the realizations of the d dimensional random variables $\Xi = \{\boldsymbol{\xi}_1, \boldsymbol{\xi}_2, \dots, \boldsymbol{\xi}_d\}$ and the corresponding responses are given by $Y = \{Y(\Xi_1), Y(\Xi_2), \dots, Y(\Xi_N)\}^T \in \mathbb{R}^{N \times 1}$. The superscript T represents the transpose of the corresponding matrix or vector. The responses are computed by a computational model \mathcal{M} , therefore, $Y(\Xi) = \mathcal{M}(\Xi)$. Note that the response quantity is independent of time here, which is given by the Kriging model as:

$$\mathcal{M}(\Xi) = \boldsymbol{\psi}(\Xi) \boldsymbol{\beta} + Z(\Xi) \quad (2.21)$$

In Equation 2.21, the first part of the expression $\boldsymbol{\psi}(\Xi) \boldsymbol{\beta}$ represents the regression part (also known as ‘trend’) of the model which can also be written as:

$$\boldsymbol{\psi}(\Xi) \boldsymbol{\beta} = \sum_{i=1}^{n_\beta} \beta_i \psi_i(\Xi) \quad (2.22)$$

where $\psi_i(\Xi)$ are the polynomial basis functions and β_i are the corresponding coefficients of the basis functions. n_β represents the total number of terms in the basis function which depends on the degree of the polynomial. According to the form of the polynomial, the Kriging model has several variants in the literature (Mukhopadhyay et al., 2016). Ordinary Kriging considers only the constant term in the polynomial basis function. In contrast, the regression function for universal Kriging model is given in Equation 2.22. The second part of Equation 2.21 defines the Gaussian process with mean zero and the process covariance is:

$$\text{cov}[Z(\Xi_i), Z(\Xi_j)] = \sigma_Z^2 \mathcal{R}(\Xi_i, \Xi_j); \quad i, j = 1, 2, \dots, N \quad (2.23)$$

where, Ξ_i and Ξ_j are two different sample points, σ_Z^2 is the process variance and $\mathcal{R}(\Xi_i, \Xi_j)$ is the auto-correlation function between two sample points. This auto-correlation function maintains the smoothness of the fitted model. A variety of function has been adopted by the researchers Kaymaz (2005); Rasmussen and Williams (2006); Bhattacharyya (2018); Sacks et al. (1989) such as linear, exponential, Gaussian and Matérn auto-correlation functions. The type of auto-correlation function should be chosen having proper knowledge of the response function, but in reality the response is not known beforehand. However, previous researches have shown Kaymaz (2005); Bhattacharyya (2018) that the Gaussian function is efficient in fitting the Kriging model for most of the engineering problems. For that reason, the Gaussian function is used for fitting the Kriging model in the present research work. The Gaussian auto-correlation function is given by:

$$\mathcal{R}(\Xi_i, \Xi_j) = \prod_{k=1}^d \exp \left[-\theta_k (\boldsymbol{\xi}_{i,k} - \boldsymbol{\xi}_{j,k})^2 \right] \quad (2.24)$$

The auto-correlation function is dependent on the hyper-parameter $\boldsymbol{\theta} = \{\theta_1, \theta_2, \dots, \theta_d\}$ which is determined by the maximum likelihood estimation (MLE) Sacks et al. (1989). Thus, the parameter $\boldsymbol{\theta}$ is estimated by maximizing the log-likelihood function

$$\ell = -\frac{1}{2} \left(N \ln \sigma_Z^2 + \ln |\mathcal{R}| \right) \quad (2.25)$$

In Equation 2.25, \mathcal{R} is the correlation matrix of dimension $N \times N$ and $|\mathcal{R}|$ is the determinant of the correlation matrix. The correlation matrix for N sample points is given by:

$$\mathcal{R} = \begin{bmatrix} \mathcal{R}(\Xi_1, \Xi_1) & \cdots & \mathcal{R}(\Xi_1, \Xi_N) \\ \vdots & \ddots & \vdots \\ \mathcal{R}(\Xi_N, \Xi_1) & \cdots & \mathcal{R}(\Xi_N, \Xi_N) \end{bmatrix} \quad (2.26)$$

2.6.2 Prediction

For the prediction using the Kriging model, the unknown parameters of the Kriging model need to be computed first. The unknown parameters $\hat{\beta}$ and $\hat{\sigma}_Z^2$ are calculated as:

$$\hat{\beta} = \left(\boldsymbol{\psi}^T \mathcal{R}^{-1} \boldsymbol{\psi} \right)^{-1} \boldsymbol{\psi}^T \mathcal{R}^{-1} Y \quad (2.27)$$

$$\hat{\sigma}_Z^2 = \frac{1}{N} \left(Y - \boldsymbol{\psi} \hat{\beta} \right)^T \mathcal{R}^{-1} \left(Y - \boldsymbol{\psi} \hat{\beta} \right) \quad (2.28)$$

Now consider any untried sample point for the prediction $\Xi_0 \in \mathbb{R}^d$. The function value at the new sample Ξ_0 is predicted by the best linear unbiased predictor (BLUP):

$$\hat{\mathcal{M}}(\Xi_0) = w^T(\Xi_0) Y \quad (2.29)$$

where, $w^T(\Xi_0)$ is the unknown weighted coefficient. The BLUP can be found by minimizing the mean square error (MSE) which is given by

$$\text{MSE} \left[\hat{\mathcal{M}}(\Xi_0) \right] = \mathbb{E} \left[\left(w^T(\Xi_0) Y - \mathcal{M}(\Xi_0) \right)^2 \right] \quad (2.30)$$

where, $\mathbb{E}[\bullet]$ is the expectation operator. The minimization problem of MSE is solved subject to the unbiased constraint

$$\mathbb{E} \left[w^T(\Xi_0) Y \right] = \mathbb{E} \left[\mathcal{M}(\Xi_0) \right] \quad (2.31)$$

By solving the minimization problem, the BLUP and the variance are predicted as:

$$\hat{\mathcal{M}}(\Xi_0) = \hat{\beta}^T \boldsymbol{\psi}(\Xi_0) + r^T(\Xi_0) \mathcal{R}^{-1} \left(Y - \hat{\beta}^T \boldsymbol{\psi} \right) \quad (2.32)$$

$$\sigma_{\hat{M}}^2(\Xi_0) = \hat{\sigma}_Z^2 \left(1 - \begin{bmatrix} \boldsymbol{\psi}^T(\Xi_0) & r^T(\Xi_0) \end{bmatrix} \begin{bmatrix} 0 & \boldsymbol{\psi}^T \\ \boldsymbol{\psi} & \mathcal{R} \end{bmatrix}^{-1} \begin{bmatrix} \boldsymbol{\psi}(\Xi_0) \\ r(\Xi_0) \end{bmatrix} \right) \quad (2.33)$$

where, $r(\Xi_0) = \{ \mathcal{R}(\Xi_0, \Xi_1), \mathcal{R}(\Xi_0, \Xi_2), \dots, \mathcal{R}(\Xi_0, \Xi_N) \}$ is the correlation matrix between the new untried sample point and the initial samples. Therefore, once the unknown parameters using the Kriging model are estimated, the prediction of the response at the untried point can be made easily by utilizing Equation 2.32.

2.7 Radial basis function surrogate model

Radial basis function (RBF) is another surrogate model, which has been used a lot for the reliability analysis (Deng, 2006; Dai et al., 2011; Li et al., 2018) and sensitivity analysis (Wu et al., 2016; Yun et al., 2018; Wu et al., 2019). RBF was proposed by Hardy (1971) to figure out irregular topographic contour of geographical data. RBF is generally used as a non-intrusive surrogate model. Therefore, it requires the response quantity evaluated at some predefined sample points. For the formulation of the RBF model, the same notations as defined in section 2.6.1 are used. The response quantity is predicted by the RBF model as follows:

$$\hat{\mathcal{M}}(\Xi_0) = \sum_{i=1}^N \gamma_i \kappa(\|\Xi_0 - \Xi_i\|) \quad (2.34)$$

where $\hat{\mathcal{M}}(\Xi_0)$ is the predicted response quantity at any untried sample Ξ_0 . $\kappa(\bullet)$ is the basis function for the RBF model and γ_i are the coefficients of the RBF model. $\|\Xi_0 - \Xi_i\|$ is the Euclidean distance between the predicted sample Ξ_0 and the i -th sample point Ξ_i which can be represented as:

$$\|\Xi_0 - \Xi_i\| = \sqrt{(\Xi_0 - \Xi_i)^T (\Xi_0 - \Xi_i)} \quad (2.35)$$

The unknown coefficients γ_i can be found by minimizing the mean square error as given in Equation 2.10. Another important issue with the RBF model is the choice of a suitable basis function κ . Several kernel functions are available for the RBF surrogate model (Tripathy, 2010) to construct the basis function. Note that, the prediction quantity in Equation 2.34 does not depend on time. Therefore, for a dynamical system, the RBF model must be evaluated at each time step which is drawback similar to the previous surrogate models in this chapter.

A RBF model based artificial neural network (ANN) has been used by Zakian (2017) for the stochastic dynamic analysis of soil media in the frequency domain considering random field shear modulus of the soil mass and the seismic excitation as the random process. RBF based ANN model has also been used by Elanayar and Shin (1994) for the approximation of a nonlinear state space model. RBF model has been used for the system identification problem (Li and Zhao, 2006).

2.8 Support vector machine surrogate model

Support vector machine (SVM) (Cortes and Vapnik, 1995) is a tool for the statistical learning. SVM is classified in two different categories namely SVM for classification and for regression. The later is used as a surrogate model for the prediction of an uncertain response quantity.

SVM for regression is also used as a non-intrusive surrogate model, therefore, the same sample matrix $\Xi \in \mathbb{R}^{N \times d}$ and the corresponding response vector $Y \in \mathbb{R}^{N \times 1}$ are used here for the construction of the SVM surrogate model. The SVM model is given by:

$$\mathcal{M}(\Xi) = \Xi \mathbf{c} + \mathcal{C} \quad (2.36)$$

where $\mathbf{c} = \{c_1, c_2, \dots, c_d\}^T \in \mathbb{R}^{d \times 1}$ and \mathcal{C} are the unknown parameters of the SVM model. The SVM model parameters can be estimated in several ways according to the formulation. One of the possible ways is the estimation of parameters such that the predicted results at the

training samples are less than an error ε_{SVM} . The following optimization problem is solved to get the parameters of the SVM model:

$$\min \frac{1}{2} \|\mathbf{c}\|^2 + m \sum_{i=1}^N (\eta_i + \eta_i^*) \quad (2.37)$$

$$\begin{aligned} \text{s.t. } Y_i - \Xi_i \mathbf{c} - \mathcal{C} &\leq (\varepsilon_{\text{SVM}} + \eta_i); \eta_i \geq 0 \\ \Xi_i \mathbf{c} + \mathcal{C} - Y_i &\leq (\varepsilon_{\text{SVM}} + \eta_i^*); \eta_i^* \geq 0 \end{aligned} \quad (2.38)$$

where the second part of Equation 2.37 defines the risk part (Al-Anazi and Gates, 2010). η_i and η_i^* are the slack variables (Cheng et al., 2017), which focus on the symmetry boundary by a loss function. The loss function is given by:

$$\begin{aligned} |Y - \mathcal{M}(\Xi)| &= 0; & |Y - \mathcal{M}(\Xi)| &\leq \varepsilon_{\text{SVM}} \\ &= |Y - \mathcal{M}(\Xi)| - \varepsilon_{\text{SVM}}; & \text{otherwise} \end{aligned} \quad (2.39)$$

The optimization problem in Equation 2.37 is solved using the Lagrangian multiplier approach. m and ε_{SVM} are chosen by the cross-validation (CV) approach. The SVM model in Equation 2.36 ultimately expressed in terms of a kernel function after solving the optimization problem in Equation 2.37. Several kernel functions are available in the literature (Cheng et al., 2017) e.g. linear, polynomial, Gaussian.

The SVM surrogate model has been used for the reliability analysis (Bourinet et al., 2011; Bourinet, 2016) and for the sensitivity analysis (Cheng and Lu, 2018a; Steiner et al., 2019). The use of SVM for a dynamical system in time domain is a numerically intensive procedure as the SVM model parameters must be obtained at each time step.

2.9 UQ of stochastic impact problems: Literature review

UQ of uncertain impact oscillator is one of the main objectives of this research. The vibro-impact (VI) oscillator (Feng et al., 2009; Sampaio and Soize, 2007; Liao et al., 2018) is a class of impact oscillator. The most important aspect of a VI oscillator is the non-smooth behavior of the response quantities due to impact. The response behavior of a VI oscillator is very complex. The response between two consecutive impacts of a VI oscillator usually behaves like a continuous dynamical system and a different behavior is generally observed during an impact (Zhu, 2015). Several random VI oscillators have been investigated in the literature (Jing and Young, 1990; Namachchivaya and Park, 2005; Feng et al., 2009; Zhu, 2015). For obtaining the stochastic behavior of the response quantity, the stochastic averaging method has been used a lot in the literature (Namachchivaya and Park, 2005; Feng et al., 2008, 2009; Zhao et al., 2016). The stochastic averaging method formulates a dynamical system as a low dimension problem without changing the essential behavior of the system (Chai et al., 2018). Further, the low dimensional governing differential equation is formulated using the Fokker-Planck (FP) equation (Namachchivaya and Park, 2005; Zhu, 2014a,b) and the stationary PDF is computed by solving the FP equation of the dynamical system. The stationary PDF of a Duffing oscillator has been obtained by Zhu (2014a) using the FP equation under a Gaussian white noise excitation. The stochastic averaging method has also been used to analyze a VI system under Gaussian white noise excitation by Gu and Zhu (2014). A review of random impact

vibration has been performed by Dimentberg and Iourtchenko (2004). A stochastic Duffing-Van der Pol VI system has been analyzed by the stochastic averaging method (Feng et al., 2009) under additive and multiplicative stochastic excitation. A friction problem has been investigated (Qiao and Ibrahim, 1999) by the stochastic averaging technique. The friction was considered by Qiao and Ibrahim (1999) when a rotating disc comes in contact with a rigid pin. The FP equation was obtained for a vibro-impact Duffing-Van der Pol oscillator by Kumar et al. (2016) after performing a non-smooth co-ordinate transformation such that the non-smooth behavior of the system was described by a continuous dynamical system.

A different approach called exponential-polynomial closure (EPC) was used to solve the FP equation by Zhu (2014a). The EPC approach has also been used in conjunction with the FP equation in several researches (Zhu, 2014b, 2015). On the other hand, Iourtchenko and Song (2006) rely on the MCS approach for obtaining the PDF of a VI system under inelastic impact conditions.

The application of a surrogate modeling approach is very limited in the literature for an impact dynamical system. Recently, a PCE model was used for a friction problem which can be appraised as a contact problem (Nechak et al., 2011, 2013). The ME-PCE model has also been used by Nechak et al. (2012) for uncertain dry friction system. The ME-PCE approach has been used by Sarrouy et al. (2013) for uncertainty propagation through a brake sequel linear system. The UQ was performed considering the eigenvectors as the QoI, and the friction coefficient and the contact force between a disc and a pad were considered as the uncertain parameters. A friction induced vibration problem as been investigated by Nechak and Sinou (2017) using the PCE model. The Chebyshev polynomials were used in conjunction with the PCE model to account the interval parameter uncertainties. The stability of an uncertain break sequel problem has been investigated by Nechak et al. (2018) using the PCE model with the Wiener-Haar expansion (Pettit and Beran, 2006). Further, to deal with a similar problem investigated by Nechak and Sinou (2017), the hybrid PCE-Kriging surrogate model has been used by Denimal et al. (2018) which increased the accuracy and the efficiency as compared to the PCE model. All the above-mentioned investigations are mainly focused on the contact problem and not exactly the impact problem which is the main focus of this thesis.

A car crash FE model has been investigated under impact condition by Moustapha et al. (2016) for reliability based design optimization (RBDO). Mainly, a subsystem of a car was investigated for the optimization under two uncertain parameters namely the initial speed and the barrier position. The uncertain parameters were propagated using an adaptive Kriging surrogate model to get the constraints for the solution of the optimization problem. Furthermore, the same problem was investigated for UQ using Kriging and SVM approach by Moustapha et al. (2018) and the contact force, the side-member compression, the left and the right side-member force were considered as the QoI. For this problem, SVM was found better as compared to Kriging surrogate model. Although the crash problem has been investigated (Moustapha et al., 2016, 2018), the time-dependent uncertainty propagation through the system was not investigated in their research. Therefore, the present research presented in this thesis is tried to fill up the void in the research by addressing the uncertainty propagation through impacted dynamical system (e.g. a crash problem).

2.10 Need of the research

From all the available researches on the UQ of dynamical systems and UQ of impacted dynamical systems, several researches need arise. All the needs are listed below:

- Most of the surrogate modeling approaches for dynamical systems were developed based on the PCE model. Therefore, other surrogate modeling approaches (e.g. Kriging, SVM) need to be investigated for UQ of nonlinear dynamical systems. This point will be partially addressed in the present thesis.
- The surrogate modeling approaches investigated till now are either based on improvement of the polynomial basis function or based on the dynamical behavior of a response quantity (e.g. PCE-NARX model). These approaches are not always applicable for real world engineering applications because these models have been developed focusing some specific dynamical systems. In particular, the PCE-NARX model has not been applied to impacted systems. This part will be investigated in the present research work.
- The main constraint of the PCE model for a dynamical system in time domain is that the PCE coefficients need to be computed at each time-step which is often computationally expensive. Consequently, it is necessary to investigate an approach for reducing the number of PCE coefficients, which will be investigated in the present research work.
- UQ of stochastic impacted dynamical system is very limited in the literature. In most of the cases, the stationary PDF was obtained for the VI oscillators. Very few research works have been conducted on UQ of impact dynamical system by the surrogate modeling approach. Indeed, the surrogate modeling approaches have not been utilized for UQ of impact oscillators (only used for friction problem). Hence, the surrogate modeling approach needs to be investigated in the context of impacted oscillators. This part will be addressed in the current research work.
- The non-intrusive surrogate models are constructed using the responses at some pre-defined experimental design points. For a dynamical system, the required number of sample points is not known beforehand. Therefore, a methodology is needed to obtain the optimum number of samples for a dynamical system to minimize the computational cost. This part is addressed in the present research work.

Chapter 3

Kriging-NARX model for dynamical systems

3.1 Introduction

Most of the surrogate models for the dynamical systems have been developed based on PCE. Out of all the surrogate approaches, the PCE-NARX model (Spiridonakos and Chatzi, 2015; Mai et al., 2016) was found to be useful as it decouples the time dependent nonlinear behavior and the randomness. The main idea behind the PCE-NARX model is that the time-dependent nonlinear behavior is modeled by the NARX model and the uncertain parameters of the dynamical system are propagated using the PCE surrogate model. The Auto-Regressive with eXogenous input (ARX) model has been used along with PCE by several researchers (Kopsaftopoulos and Fassois, 2013; Kumar and Budman, 2014; Sakellariou and Fassois, 2016). Although it was possible to propagate the uncertainties through the nonlinear dynamical systems properly by the PCE-NARX model, the other surrogate models should be explored in the context of dynamical systems to reduce the computational cost by reducing the polynomial degree of the surrogate model and the number of model evaluations.

Besides PCE, several other surrogate models have been developed in the literature as mentioned in section 2.3. Out of all the other approaches, Kriging (Krige, 1951; Sacks et al., 1989; Kaymaz, 2005) has emerged rapidly in the last two decades. The use of Kriging models is limited in the literature for the dynamical systems. A Kriging model has been used by McFarland et al. (2008) for the calibration and for the UQ of multivariate outputs (e.g. time-dependent outputs). Further, the high-dimensional outputs were represented by PCA by Higdon et al. (2008) and the Kriging model was applied on the reduced space. A similar research work has been conducted by Guo and Hesthaven (2019) for the time-dependent problems. The Kriging approach has been used in conjunction with the spectral approach for the prediction of frequency response function (FRF) by Kundu et al. (2014).

The Kriging surrogate model deals with the global approximation and the local approximation. The global approximation is performed by the polynomial basis functions in a similar way to the PCE model. Additionally, the local error is minimized using a Gaussian process. To use the advantages of the Kriging surrogate model, a surrogate modeling approach is developed in this chapter by combining the NARX model with the Kriging model. NARX model is used to capture the nonlinear time-dependent behavior of the response characteristics while the uncertain parameters are propagated by the Kriging surrogate model. The developed

methodology and the results of this chapter have been published in (Bhattacharyya et al., 2019, 2020).

3.2 NARX model

3.2.1 Overview of NARX model

Nonlinear Auto-Regressive with eXogenous input (NARX) model is mainly used for the system identification of the time-dependent response quantities. An extensive research has been performed in the past for developing different types of NARX models (Leontaritis and Billings, 1985; Chen and Billings, 1989; Billings and Wei, 2005, 2008). The auto-regressive (AR) models are broadly categorized in two distinct category namely linear and nonlinear AR model. The development and implementation procedure for most of the AR models are described by Billings (2013). A brief overview of only the NARX model is presented in the present research work.

NARX model was developed as a system identification tool for the nonlinear dynamical systems (Chen and Billings, 1989; Wei and Billings, 2009; Billings, 2013). More specifically, the time-dependent response characteristics of a dynamical system at the current time can be predicted by the responses of some previous times and the excitation of some previous and current times through a suitable NARX model. If we consider a dynamical system having time-dependent excitation, then according to the NARX model, the dynamical system can be expressed as:

$$y(t) = \mathcal{F}[z(t)] + \varepsilon(t) \quad (3.1)$$

where, $z(t) = \{x(t), x(t - \Delta t), x(t - 2\Delta t), \dots, x(t - n_{x_m}\Delta t), y(t - \Delta t), y(t - 2\Delta t), \dots, y(t - n_{y_m}\Delta t)\}^T$ is the vector having all the lagged system excitation and response components which forms the time-dependent auto-regressive response model $\mathcal{F}[\bullet]$. $\varepsilon(t)$ is the residual of the NARX model which is supposed to be a normally independent distributed (NID) process with zero mean and Δt is the time-step chosen for the NARX model. n_{x_m} and n_{y_m} are the maximum time lags for the excitation and the response quantity, respectively. It is obvious that the underlying form of the function $\mathcal{F}[\bullet]$ must be nonlinear to capture the strong non-linearity of a dynamical system. Consequently, different types of functions have been used by the researchers such as polynomial (Cantelmo and Piroddi, 2010), wavelet (Billings and Wei, 2005), sigmoid function (Sjöberg et al., 1995), radial basis function (Kang Li et al., 2005) and neural network (Tsunghan Lin et al., 1996). Out of these, the effectiveness of polynomial function has already been shown in the literature (Leontaritis and Billings, 1985; Cantelmo and Piroddi, 2010; Cheng et al., 2011). Therefore, a linear-in-parameter form of polynomial can be used, it is represented by:

$$\mathcal{F}[z(t)] = \sum_{i=1}^M a_i f_i[z(t)] \quad (3.2)$$

where M is the total number of terms in the NARX polynomial basis function, $f_i[z(t)]$ are the polynomial basis functions and a_i are the corresponding coefficients of the NARX model. The polynomial basis for the NARX model is dependent on the time varying excitation and response. Consequently, the polynomial basis vector (at a particular time t_i) and the coefficient matrix for a particular sample point k are represented by:

$$\mathbf{f}_k(t_i, \Xi_k) = \{f_1[z_k(t_i, \Xi_k)], f_2[z_k(t_i, \Xi_k)], \dots, f_M[z_k(t_i, \Xi_k)]\}^T; \quad \mathbf{f}_k \in \mathbb{R}^{M \times 1} \quad (3.3)$$

$$\mathbf{a}^k = \{a_1, a_2, \dots, a_M\}; \quad \mathbf{a}^k \in \mathbb{R}^{1 \times M} \quad (3.4)$$

Now, if we discretize the total time T in n_t number of times i.e. $t \in \{t_1, t_2, \dots, t_{n_t}\}$, the polynomial basis matrix can be given by $\mathbf{f}_k \in \mathbb{R}^{M \times n_t}$.

The main issues with the NARX model are the formulation of a suitable basis to capture the nonlinear behavior of a response for a nonlinear dynamical system and the estimation of the coefficients for the NARX model.

3.2.2 Model formulation and parameter estimation of the NARX model

The polynomial basis function for the NARX model can be formulated by two variables, i.e. excitation and response of the dynamical system, either as an independent variable basis function (Spiridonakos and Chatzi, 2015) or as a composition of both variables (Mai et al., 2016) with certain maximum degree of the polynomial basis. The linear-in-parameter NARX model as given in Equation 3.2 is almost similar to the form of the PCE model (Xiu and Karniadakis, 2002). It is useful to impose similar type of polynomial basis function for the NARX model. Consequently, a similar type of polynomial basis function for the NARX model has been used by Mai et al. (2016) which has been very accurate in capturing the non-linearity of a dynamical system. Therefore, a similar form of polynomial basis has been adopted here. Another important issue with the polynomial basis is the selection of the maximum time lags n_{x_m} and n_{y_m} for the excitation and the response, respectively. The maximum time lags are selected according to the number of DOF of a dynamical system which are considered as twice the number of DOF of the system (Spiridonakos and Chatzi, 2015; Mai et al., 2016).

On the other hand, the computation of the NARX coefficients is one of the challenging tasks in the construction of the NARX model. The coefficients of the NARX model can be computed easily by the OLS approach due to the linear-in-parameter model like PCE (Xiu and Karniadakis, 2002). However, it has often been found in the literature (Blatman and Sudret, 2011; Spiridonakos and Chatzi, 2015) that all the terms in the polynomial basis do not get involved in predicting the response characteristics of a system. Thus, it is important to capture the important terms in the polynomial basis function which are solely responsible for the response behavior of a system. Recently, important NARX basis terms were identified using genetic algorithm by Spiridonakos and Chatzi (2015).

3.2.3 Sparse NARX model

Due to the form of the NARX model (Equation 3.2), the important terms can be identified with popularly used methods: least angle regression (LARS) (Efron et al., 2004) or least absolute shrinkage and selection operator (LASSO) (Tibshirani, 1996). LASSO has been used by Cantelmo and Piroddi (2010) to select the important terms in the NARX polynomial basis. LARS has been used recently for the system identification problem (Zhang and Li, 2015) and for the identification of linear-in-parameter model (Zhao et al., 2017). LARS has also been used for adaptive PCE (Blatman and Sudret, 2011) to reduce the number of terms in the polynomial basis which enhanced the efficiency of the model. LARS is used here to select the important terms of the NARX model polynomial basis function which would ultimately reduce the total number of terms of the model.

As the NARX model is deterministic, one needs to fit a NARX model for each of the initial sample points in case of a stochastic dynamical system: it can be computationally

expensive. For that reason, it is important to obtain a single NARX model which can represent the responses for all the sample points. The idea of formulating a single NARX model is that the NARX model should be identified from the samples which have a highly nonlinear behavior as compared to the other samples. For that reason, it is first required to select the samples exhibiting high non-linearity. The responses having a highly nonlinear behavior can be selected by the measurement of the non-linearity of the response (Spiridonakos and Chatzi, 2015) or by specifying some threshold value for the response series (Mai et al., 2016). A combination of both the mentioned methods (Spiridonakos and Chatzi, 2015; Mai et al., 2016) has been utilized here to capture the highly nonlinear response series. Firstly, the response versus the restoring force is plotted arbitrarily without performing any simulations (keeping other parameters constant at their mean values). The intensity of the response is increased up to a certain limit till the nonlinear behavior is noticed in the force-displacement relationship. From the restoring force curve, the threshold value for a response series can be selected easily by observing the starting point of the non-linearity of the response series. Imposing the threshold value would reduce the number of samples to $N_1 < N$. Now, for each of the N_1 samples, a sparse NARX model is formulated using the LARS algorithm. Consequently, N_1 full NARX models are formulated at the initial step. If we consider the k -th experiment out of N_1 experiments the for full NARX model, the response for the k -th sample is given by:

$$Y(t, \Xi_k) \approx \mathbf{a}^k \mathbf{f}_k(\Xi_k) \quad (3.5)$$

where, \mathbf{f}_k is the matrix having all the M terms of the NARX model polynomial basis for all the time-steps with dimension $M \times n_t$ which is formulated recursively by the current and the previous excitations, and the previous responses.

Remark 3.1. *One should discretize the total time T with a suitable time-step Δt (small enough to capture the dynamics correctly). Besides, the time-step plays a vital role in case of a NARX model. The same time-step for the time integration and for the construction of the NARX model is used in this chapter.*

The response series for the k -th sample point is known beforehand which is denoted by $Y(t, \Xi_k)$. Thus, the coefficients of the NARX model can be obtained by the minimization of the residual error:

$$\varepsilon(t, \Xi_k) = Y(t, \Xi_k) - \mathbf{a}^k \mathbf{f}_k(t, \Xi_k) \quad (3.6)$$

The sum square error of the predicted response series is given by:

$$\sum_{i=1}^{n_t} [\varepsilon(t_i, \Xi_k)]^2 = \sum_{i=1}^{n_t} [Y(t_i, \Xi_k) - \mathbf{a}^k \mathbf{f}_k(t_i, \Xi_k)]^2 \quad (3.7)$$

The minimization of the sum square error can be solved to get the coefficients (\mathbf{a}^k) of the NARX model. Before computing the NARX coefficients, the important terms of the NARX polynomial basis are selected by LARS algorithm in this step for N_1 number of NARX model.

Among the N_1 NARX models, some models are identical. The unique NARX models are selected from the N_1 number of NARX models, such that all the models in the set of the unique NARX models are different. Therefore, the number of NARX models is reduced to $N_2 \leq N_1$. It is obvious that the number of terms in all the unique NARX models must be $M_1 \leq M$. Now, the response series of the dynamical system are predicted for the N samples by utilizing the coefficients of each of the unique NARX models. For that reason, it is important to know

the coefficients for all the N sample points beforehand. These coefficients are computed here by the OLS approach using only the retained M_1 terms in the polynomial basis matrix for the corresponding unique sparse NARX model.

$$\mathbf{a}(\Xi_k) = \underset{\mathbf{a}}{\operatorname{argmin}} \left[\varepsilon^T(\Xi_k) \varepsilon(\Xi_k) \right] = Y(\Xi_k) \left[\mathbf{f}_k^T(\Xi_k) \mathbf{f}_k(\Xi_k) \right]^{-1} \mathbf{f}_k^T(\Xi_k) \quad (3.8)$$

$$k = 1, 2, \dots, N$$

Further, the responses for the dynamical system are reconstructed using the coefficients obtained from Equation 3.8 at N sample points. To check the adequacy of a particular sparse NARX model, the mean error (Mai et al., 2016) for each of the sample points is computed as:

$$\epsilon_k = \frac{\sum_{i=1}^{n_t} \left[Y(t_i, \Xi_k) - \hat{Y}(t_i, \Xi_k) \right]^2}{\sum_{i=1}^{n_t} \left[Y(t_i, \Xi_k) - \bar{Y}(\Xi_k) \right]^2} \quad (3.9)$$

where, $\bar{Y}(\Xi_k)$ is the time average of the k -th response series which is given by:

$$\bar{Y}(\Xi_k) = \frac{1}{n_t} \sum_{i=1}^{n_t} Y(t_i, \Xi_k) \quad (3.10)$$

The mean predicted error for all the sample points by a particular sparse NARX model out of N_2 sparse NARX models is given by:

$$\bar{\epsilon} = \frac{1}{N} \sum_{i=1}^N \epsilon_i \quad (3.11)$$

The finally selected sparse NARX model is the one having the predicted mean error for the N sample points lower than a threshold value. The threshold value of the mean error is imposed as 1×10^{-3} in the present research work, which is proposed by Mai et al. (2016).

Remark 3.2. *It is important to mention that if the predicted mean errors for two different NARX model are found identical (or lower than the threshold value) then the sparse NARX model having less number of terms in the polynomial basis is selected as the final sparse NARX model.*

3.3 Kriging-NARX model

The Kriging-NARX (KNARX) model is formulated here in a similar way to the sparse PCE-NARX model (Mai et al., 2016). As mentioned in section 2.10, the PCE models have been investigated mostly for stochastic dynamical systems. Therefore, to investigate the other surrogate models, a step is taken here to construct the surrogate model using the NARX model and the Kriging model. More specifically, the uncertain parameters are propagated by the Kriging surrogate model for the KNARX model while the PCE model was used for the sparse PCE-NARX model.

Consider a dynamical system having the uncertain parameters $\Xi = \{\xi_1, \xi_2, \dots, \xi_d\}$, then the time dependent response for the k -th sample of the system can be represented by a NARX model as:

$$y(t, \Xi_k) = \sum_{i=1}^M a_i(\Xi_k) f_i[z_k(t)]; \quad k = 1, 2, \dots, N \quad (3.12)$$

It is observed from Equation 3.12 that the coefficients of the NARX model are dependent on the sample points, which does not make the model stochastic in nature. To get the independent coefficients of the NARX model, the NARX coefficients are represented by the Kriging surrogate model as given in Equation 2.21:

$$\mathbf{a}_i(\Xi) = \boldsymbol{\psi}(\Xi) \beta_i + Z_i(\Xi); \quad i = 1, 2, \dots, M \quad (3.13)$$

where $\mathbf{a}_i \in \mathbb{R}^{N \times 1}$ is the coefficient vector for the i -th term in the NARX model.

Remark 3.3. *Each of the coefficients of the NARX model must be identified: therefore, the Kriging model should be calibrated M times (M is the total number of terms for a full NARX model). Each of the coefficients acts as the single response quantity for the Kriging model.*

Further, the model is constructed by the Kriging surrogate model as discussed in section 2.6.1. Therefore, for all the sample points, the Kriging-NARX (KNARX) model is expressed as:

$$y(t, \Xi) = \sum_{i=1}^M (\boldsymbol{\psi}(\Xi) \beta_i + Z_i(\Xi)) f_i[z(t)] \quad (3.14)$$

The coefficient of the regression part β and the Gaussian process part $Z(\Xi)$ are dependent on the number of terms in the NARX model, whereas the polynomial basis function of the Kriging model for all the NARX coefficients remain the same as the basis is purely dependent on the uncertain parameters.

The response quantity of a dynamical system at some untried sample points Ξ_0 can be predicted by a BLUP as mentioned in Equation 2.32 in accordance with the full NARX model in an auto-regressive manner.

$$\hat{y}(t, \Xi_0) \approx \sum_{i=1}^M \left[\hat{\beta}_i^T \boldsymbol{\psi}(\Xi_0) + r^T(\Xi_0) \mathcal{R}^{-1} \left(\hat{\beta}_i^T \boldsymbol{\psi}(\Xi_0) \right) \right] \psi_i[z(t)] \quad (3.15)$$

Equation 3.15 predicts the time-dependent response characteristics of a dynamical system having d uncertain parameters. It is evident from Remark 3.3 that the computational cost increases with the increase of the number of terms in the NARX polynomial basis. For that reason, the sparse NARX model as discussed in section 3.2.3 is used here in accordance with the Kriging surrogate model. Consequently, the number of terms for the NARX model is decreased to $M_1 < M$ which ultimately reduces the number of Kriging model calibration (M_1) and the computational cost. The algorithm for constructing the sparse KNARX model is provided in Table 3.1.

3.4 Numerical application to nonlinear dynamical systems

The sparse KNARX model as described in the previous section has been utilized for UQ of three nonlinear stochastic dynamical systems. For each of the examples, the accuracy of the sparse KNARX model is measured using the predicted mean error as given in Equation 3.11 (taking MCS as the reference), and the value of the coefficient of correlation R^2 between the MCS results and the results predicted by a surrogate model. UQ for all the problems is made by predicting the time dependent mean and standard deviation of the responses. Further, the PDFs of the responses are also predicted at some times. The computational efficiency is

Table 3.1: Algorithm for the sparse KNARX model

-
1. Declare the d number of uncertain variables with the type of distribution.
 2. Generate N sample points for the uncertain variables.
 3. Draw the restoring force versus response curve to decide the threshold value for capturing the nonlinear response series.
 4. Get the response of the dynamical system up to time T for each of the N samples.
 5. Select the samples and the response series having high order non-linearity using some threshold (according to step 3) on the response series. This step selects N_1 samples ($N_1 < N$).
 6. Decide the maximum time lags n_{x_m} and n_{y_m} for the excitation and the response quantity, respectively. Decide the type of NARX polynomial basis function along with the maximum degrees also.
 7. For each of the N_1 samples, build the NARX model (see Equation 3.1 and Equation 3.2) which has M number of terms.
 8. Select the most important terms for each of the N_1 NARX models using LARS (Efron et al., 2004).
 9. Select the N_2 different sparse NARX models having similar terms in the NARX polynomial basis ($N_2 \leq N_1$).
 10. Perform OLS on N samples for the N_2 sparse NARX models to get the NARX coefficients of all the response series.
 11. Reconstruct the N response series using the coefficients computed in step 10 by all the N_2 sparse NARX models.
 12. Predict the mean error $\bar{\epsilon}$ for all the N_2 number of sparse NARX models using Equation 3.11.
 13. Select the most appropriate sparse NARX model having $\bar{\epsilon}$ lower than some threshold value (1×10^{-3} for the present case) and less terms (M_1) in the NARX polynomial (according to Remark 3.2).
 14. Calibrate $M_1 < M$ number of Kriging models using the NARX coefficients as the response parameter and the sample points generated in step 2 as the uncertain input quantities.
 15. Generate a large number of new untried samples for the prediction.
 16. Predict the NARX coefficients for the untried samples using Kriging models generated in step 14.
 17. Predict the response series, in a auto-regressive way (see Equation 3.15), at the untried samples generated in step 15 using the coefficients of step 16 and the M_1 number of NARX polynomial bases selected in step 13.
-

Table 3.2: Uncertain parameters for the Duffing oscillator

| Variable | Distribution type | Mean | Standard deviation | Unit |
|---------------|-------------------|--------|--------------------------|---------------------|
| ω | Uniform | 2π | $\frac{\pi}{\sqrt{3}}$ | rad s^{-1} |
| ζ | Uniform | 0.03 | $\frac{0.015}{\sqrt{3}}$ | — |
| ε | Uniform | 100 | $\frac{10}{\sqrt{3}}$ | — |
| A | Normal | 0.6 | 0.06 | N |
| ω_x | Normal | 1 | 0.1 | rad s^{-1} |

measured through the computational cost (CPU time), the number of the surrogate model used for the calibration and the number of initial sample points N . The first two problems are also solved by the Kriging model to measure the efficiency and the accuracy of the sparse KNARX model over the Kriging. For the first three examples, the results predicted with sparse KNARX are also compared with the recently proposed sparse PCE-NARX surrogate model (Mai et al., 2016).

According to step 2 of Table 3.1, a suitable sample point generation strategy is required for the generation of the initial samples. Consequently, one of the most widely used sampling strategies, LHS as used by Mai et al. (2016); Chatterjee and Chowdhury (2017), has been utilized for the generation of the initial number of sample points, N .

3.4.1 Duffing oscillator

A non-linear Duffing oscillator is considered for the illustration of the proposed model. The governing differential equations of the Duffing oscillator are given by:

$$\ddot{y}(t) + 2\zeta\omega\dot{y}(t) + \omega^2 [y(t) + \varepsilon y^3(t)] = x(t) \quad (3.16)$$

$$x(t) = A \sin(\omega_x t) \quad (3.17)$$

In Equation 3.16, ω represents the natural frequency considering the undamped linear structure ($\varepsilon = 0, \zeta = 0$), ζ is the damping ratio and ε controls the non-linearity of the system. $x(t)$ denotes the excitation part of the dynamical system which was considered in this case (see Equation 3.17). The initial conditions are $y(0) = 0$ and $\dot{y}(0) = 0$. The numerical integration has been performed for $T = 30$ s with a time-step of $\Delta t = 0.01$ s through Matlab solver *ode45*. All the parameters of the Duffing oscillator were considered uncertain (i.e. $\xi = \{\omega, \zeta, \varepsilon, A, \omega_x\}$). The distribution types along with the parameters of the distribution are listed in Table 3.2.

The time dependent stochastic displacement of the Duffing oscillator was predicted by the MCS, Kriging, sparse PCE-NARX (Mai et al., 2016) and sparse KNARX models. MCS has been performed with 3×10^4 sample points and $N = 50$ samples have been generated by LHS for the prediction of the stochastic response behavior using Kriging. The Kriging model has been calibrated for each time-step (i.e. 3001 times). The step by step procedure of constructing the sparse KNARX model (according to Table 3.1) is described below:

1. For the Duffing oscillator, $d = 5$ (see Table 3.2).
2. The sparse KNARX model was constructed using $N = 25$ LHS points.

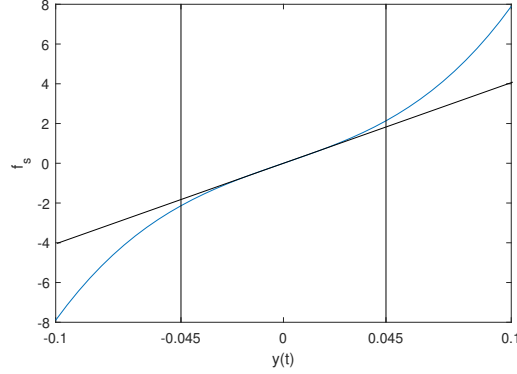


Figure 3.1: Displacement versus restoring force plot (blue curve) for the Duffing oscillator

3. For the construction of the sparse KNARX and the sparse PCE-NARX model, it is important to specify the threshold value for capturing the nonlinear response series according to step 3 of Table 3.1. Full NARX models are to be constructed on those samples which satisfy the criterion of threshold value. For that reason, the displacement $y(t)$ versus restoring force $f_s = \omega^2 [y(t) + \varepsilon y^3(t)]$ has been plotted in Figure 3.1 (keeping other parameters constant at their mean values). From Figure 3.1, it is clear that the displacement behaves almost linearly for $y(t) \in [-0.045 \text{ m}, 0.045 \text{ m}]$ and beyond this region, the displacement is highly nonlinear. Consequently, to capture the highly nonlinear response series, the threshold value for the nonlinear displacement was set as $\max(|y(t)|) > 0.045 \text{ m}$. Thus, only those samples will be picked for the construction of NARX model which falls beyond the region $y(t) \in [-0.045 \text{ m}, 0.045 \text{ m}]$.
4. The displacement series were then obtained with $N = 25$ samples. Out of all the response series, the displacement versus the restoring force for two different samples (13-th and 25-th sample point) are plotted in Figure 3.2. It is clearly seen that the 13-th sample point exhibits higher order non-linearity than the 25-th sample point. It should be noted that the region of displacement value is almost restricted in $[-0.02 \text{ m}, 0.02 \text{ m}]$ for the 25-th sample point which is far less than the specified threshold value. On the other hand, the displacement is far beyond the threshold value and behaves nonlinearly for the 13-th sample point.
5. After imposing the above-specified threshold criterion, only $N_1 = 2$ samples were selected as the highly nonlinear response series. Thus, only 2 full NARX models are required for the Duffing oscillator using the sparse KNARX model ($N = 25$). The following NARX basis function was chosen to construct the full NARX model:

$$f_i [z(t)] = x^{l_i} (t - n_{x_i} \Delta t) y^{m_i} (t - n_{y_i} \Delta t) \quad (3.18)$$

where, x and y are the excitation and the response of the Duffing oscillator, respectively.

6. The maximum time lags were chosen as twice the number of DOF (Spiridonakos and Chatzi, 2015; Mai et al., 2016) of the Duffing oscillator i.e. 2 with $n_x \in \{0, 1, 2\}$ and $n_y \in \{1, 2\}$. $l_i \in \{0, 1\}$ and $m_i = \{0, 1, 2, 3\}$ were chosen with a maximum degree of the polynomial i.e. $l_i + m_i \leq 3$ due to the cubic non-linearity of the problem. 22 terms

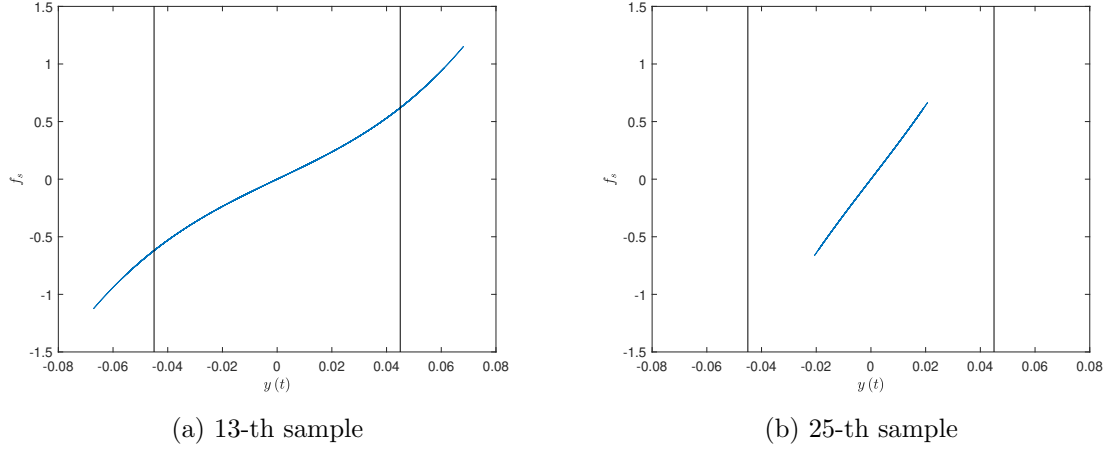


Figure 3.2: Displacement versus restoring force plots (blue curves) of two different realizations for the Duffing oscillator

Table 3.3: The polynomials selected by the LARS algorithm for the Duffing oscillator

| Model 1 ($M_1 = 9$) | Model 2 ($M_1 = 8$) |
|--------------------------------------|--------------------------------------|
| $x(t)$ | $x(t)$ |
| $x(t - 2\Delta t)$ | $x(t - 2\Delta t)$ |
| $y(t - \Delta t)$ | $y(t - \Delta t)$ |
| $y(t - 2\Delta t)$ | $y(t - 2\Delta t)$ |
| $y^2(t - \Delta t)$ | $y^2(t - \Delta t)$ |
| $y^3(t - \Delta t)$ | $y^3(t - \Delta t)$ |
| $y^3(t - 2\Delta t)$ | $y^3(t - 2\Delta t)$ |
| $x(t - 2\Delta t)y^2(t - 2\Delta t)$ | $x(t - 2\Delta t)y^2(t - 2\Delta t)$ |
| $x(t - 2\Delta t)y(t - 2\Delta t)$ | |

were found in the polynomial basis for the full NARX model utilizing all the possible combinations including the constant term i.e. $i = 1, 2, \dots, 22$ in Equation 3.18.

7. Therefore, 2 full NARX models were constructed using the basis function as given in Equation 3.18, and they have 22 terms in the NARX polynomial basis matrix.
8. The sparse NARX models were then constructed using the LARS algorithm by selecting the most important terms in the bases for both full NARX models.
9. The sparse NARX models were then retained; both sparse NARX models were found unique, i.e. with a different set of terms in the polynomial basis. The polynomials selected by the LARS algorithm for both NARX models are listed in Table 3.3.
10. The coefficients for all the 25 samples were obtained by the OLS approach for both sparse NARX models. For this step, $N \times N_2$ OLS problems were solved.
11. Then, the response series were reconstructed again in a recursive manner using the coefficients and the polynomial bases.

12. $\bar{\epsilon}$ was then computed for both sparse NARX models for the N samples.
13. $\bar{\epsilon}$ by both sparse NARX models was found below the threshold value. Hence, Model 2 of Table 3.3 was chosen as the best sparse NARX model (according to Remark 3.2) and the predicted mean error for the $N = 25$ samples was found as $\bar{\epsilon} = 1.68 \times 10^{-7}$.
14. The coefficient vector $\mathbf{a}_i(\Xi) \in \mathbb{R}^{N \times 1}; i = 1, \dots, 8$ corresponding to each of the polynomials is uncertain. These 8 coefficient vectors were considered as the uncertain response quantities for the Kriging model. Hence, the unknown parameters of the Kriging model $\hat{\beta}, \hat{\sigma}_Z^2$ were computed by the MLE for all the 8 NARX coefficients separately. Consequently, 8 Kriging models were identified.
15. The 3×10^4 MCS samples were used here for the prediction by the surrogate model.
16. The 8 NARX coefficient vectors for the 3×10^4 samples were then predicted using the 8 calibrated Kriging models by BLUP.
17. Further, the predicted coefficients and the selected polynomials were used to predict the response series auto-regressively for the 3×10^4 MCS samples.

The 25 LHS samples were also utilized to derive the sparse PCE-NARX (Mai et al., 2016) model. The sparse PCE model was constructed using the UQLab module (Marelli and Sudret, 2014). For the PCE model, the polynomial degree was varied between 1 and 20. However, the predicted response has not converged using the sparse PCE-NARX model with the same number of samples. For that reason, the number of samples for the sparse PCE-NARX model was increased to $N = 35$ and the time dependent responses were predicted with the sparse PCE-NARX model. Here, the final sparse NARX model was found having $M_1 = 9$ terms in the NARX polynomial basis which are $\{y(t - \Delta t), y(t - 2\Delta t), y^2(t - \Delta t), y^3(t - \Delta t), y^3(t - 2\Delta t), x(t), x(t - 2\Delta t), x(t)y(t - \Delta t), x(t - 2\Delta t)y^2(t - 2\Delta t)\}$.

To reduce further the computational cost, another study has been performed using less number of initial samples with $N = 21$ (for sparse KNARX). In this case, 3 samples were retained initially based on the criterion of threshold value of the response series and the 3 full NARX models were formulated using the basis function as mentioned in Equation 3.18. The finally selected sparse NARX model was Model 1 of Table 3.3 and the predicted mean error of the selected sparse NARX model was found as $\bar{\epsilon} = 1.80 \times 10^{-7}$ for the 21 samples. Further, the coefficients corresponding to the sparse NARX polynomial bases were modeled using the Kriging surrogate model.

The time varying stochastic response characteristics were predicted by the time dependent mean and standard deviation which are plotted in Figure 3.3. The figure clearly depicts the efficiency (initial number of sample points N) and the accuracy of the sparse KNARX model over the Kriging model. The sparse KNARX has predicted better results with fewer number of model evaluations ($N = 21$). To illustrate the accuracy of the sparse KNARX, the instantaneous response characteristics are also plotted. The scatter diagrams and the PDFs of the predicted response are plotted in Figure 3.4 at three different times (10 s, 20 s and 30 s). The accuracy metrics of the instantaneous response characteristics are listed in Table 3.4. They clearly suggest that the sparse KNARX and sparse PCE-NARX give much more accurate results than Kriging. The accuracy of the sparse KNARX model is also comparatively higher using less model evaluations than the sparse PCE-NARX model.

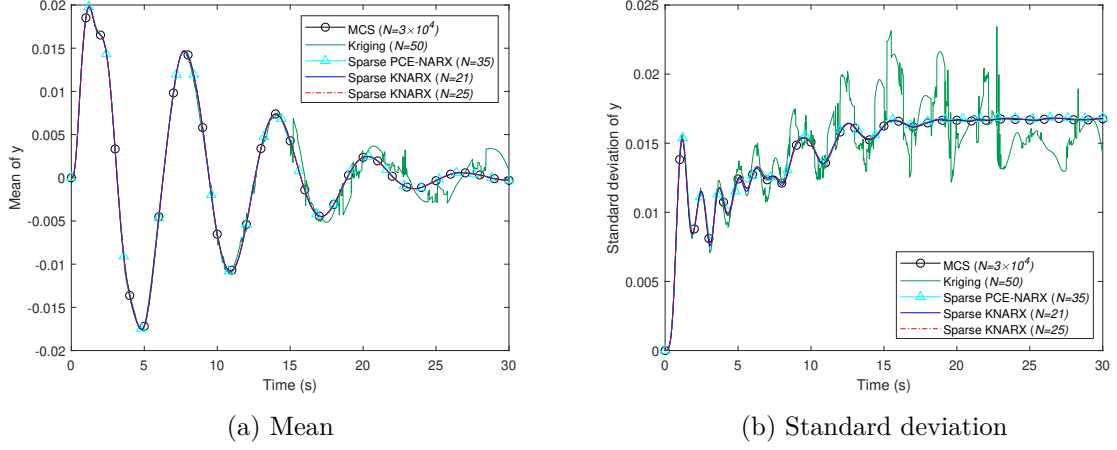
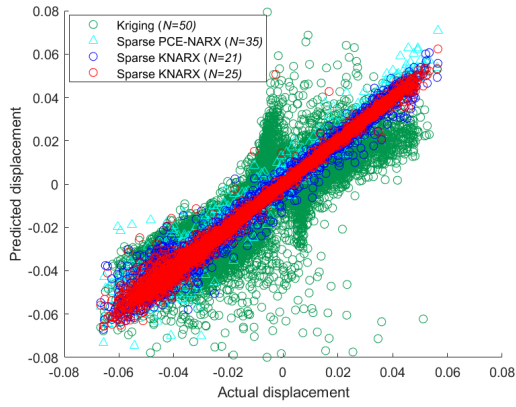


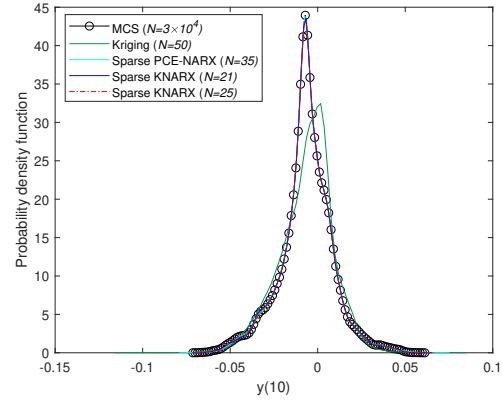
Figure 3.3: Statistical response characteristics of the Duffing oscillator

Table 3.4: Accuracy of the surrogate models in predicting instantaneous response characteristics for the Duffing oscillator

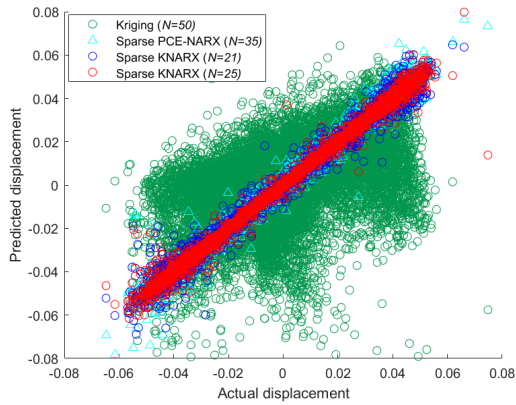
| Method | N | Time instance | $\epsilon_y(t)$ | R^2 |
|-----------------|-----|---------------|-------------------------|--------|
| Kriging | 50 | $t = 10$ s | 337.8×10^{-3} | 0.6622 |
| Sparse PCE-NARX | 35 | | 9.6×10^{-3} | 0.9904 |
| Sparse KNARX | 21 | | 8.8×10^{-3} | 0.9912 |
| Sparse KNARX | 25 | | 4.6×10^{-3} | 0.9954 |
| Kriging | 50 | $t = 20$ s | 926.9×10^{-3} | 0.0731 |
| Sparse PCE-NARX | 35 | | 4.4×10^{-3} | 0.9956 |
| Sparse KNARX | 21 | | 5.4×10^{-3} | 0.9946 |
| Sparse KNARX | 25 | | 3.1×10^{-3} | 0.9969 |
| Kriging | 50 | $t = 30$ s | 1701.1×10^{-3} | — |
| Sparse PCE-NARX | 35 | | 2.3×10^{-3} | 0.9977 |
| Sparse KNARX | 21 | | 3.0×10^{-3} | 0.9970 |
| Sparse KNARX | 25 | | 2.0×10^{-3} | 0.9980 |



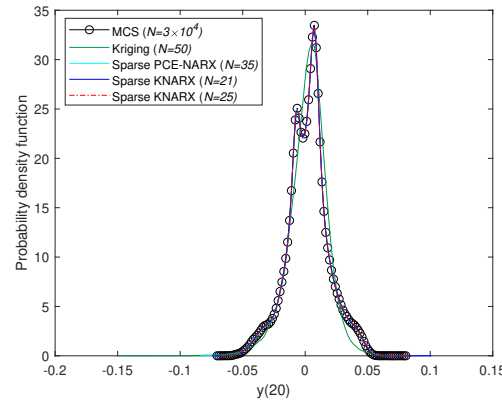
(a) Scatter plot at $t = 10$ s



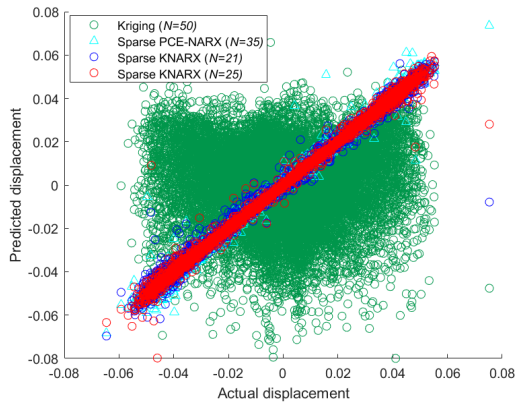
(b) PDF at $t = 10$ s



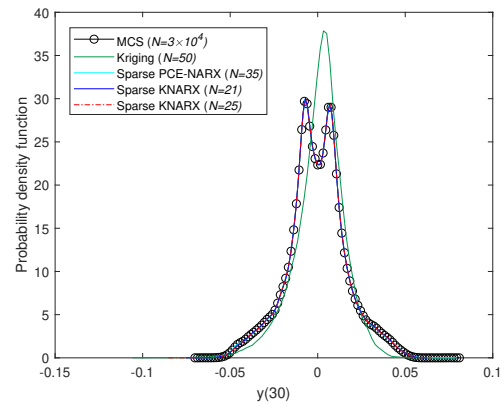
(c) Scatter plot at $t = 20$ s



(d) PDF at $t = 20$ s



(e) Scatter plot at $t = 30$ s



(f) PDF at $t = 30$ s

Figure 3.4: Comparison of instantaneous response characteristics for the Duffing oscillator at different time instances

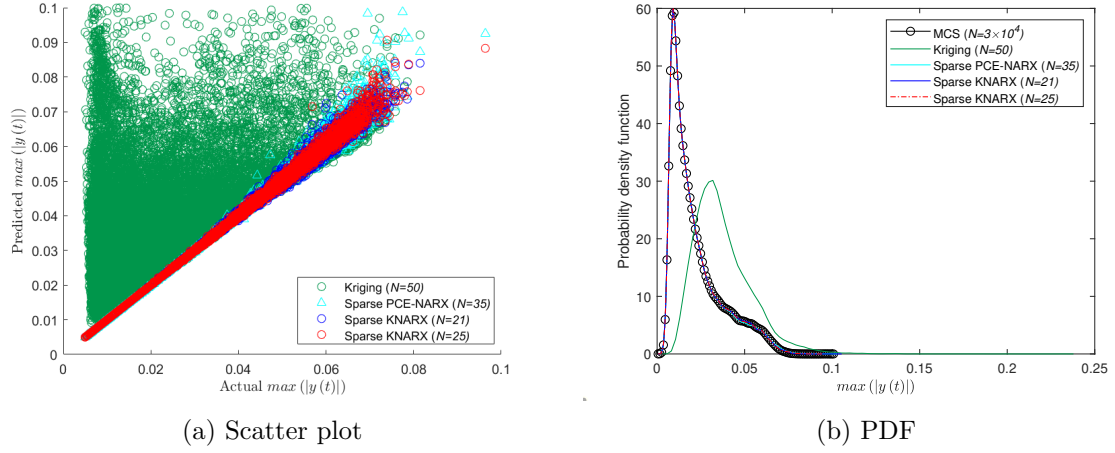
Figure 3.5: Comparison of predicted $\max(|y(t)|)$ for the Duffing oscillator

Table 3.5: Comparison of accuracy and efficiency of the surrogate models for the Duffing oscillator

| Method | N | $\bar{\epsilon}$ | Accuracy | | Efficiency | |
|-----------------|-----------------|----------------------|---------------------------|----------------------|------------|--------------|
| | | | $\epsilon_{\max(y(t))}$ | $R^2_{\max(y(t))}$ | n_K | CPU time (s) |
| Kriging | 50 | 1.5 | 2100.7×10^{-3} | — | 3001 | 530.95 |
| Sparse PCE-NARX | 35 | 1.1×10^{-3} | 2.9×10^{-3} | 0.9971 | 9 | 30.55 |
| Sparse KNARX | 21 | 1.2×10^{-3} | 1.4×10^{-3} | 0.9986 | 9 | 26.13 |
| Sparse KNARX | 25 | 5.9×10^{-4} | 1.0×10^{-3} | 0.9990 | 8 | 24.63 |
| MCS | 3×10^4 | — | — | — | — | 705.43 |

The stochastic absolute maximum displacement $\max(|y(t)|)$, plotted in Figure 3.5, ultimately measures the safety corridor for the dynamical system. It is seen clearly that the sparse KNARX outperforms the Kriging and the sparse PCE-NARX with fewer samples in predicting the PDF of $\max(|y(t)|)$, and the accuracy of the sparse KNARX given by the R^2 value in Table 3.5 is very close to 1.0 with $N = 25$.

Further, the accuracy of the overall model was computed by the mean error (Equation 3.11) for the predicted responses and the error for the predicted $\max(|y(t)|)$. The efficiency of the sparse KNARX has already been shown by the initial number of sample points. An accurate result was predicted by the sparse KNARX even with less model evaluations ($N = 21$) as compared to the other methods. The efficiency of the sparse KNARX was also measured by the number of surrogate model calibrations (n_K) for a method and by the CPU time. All the accuracy and the efficiency measurement metrics are reported in Table 3.5. Table 3.5 suggests that the sparse KNARX model outperforms the Kriging and the sparse PCE-NARX model in accuracy and efficiency. The CPU time is noticeably lower with higher value of N for the sparse KNARX model due to fewer Kriging model calibration.

Table 3.6: Uncertain parameters for the Bouc-Wen oscillator

| Variable | Distribution type | Mean | Standard deviation | Unit |
|------------|-------------------|--------|--------------------|---------------------|
| ζ | Uniform | 0.02 | 0.002 | — |
| ω | Uniform | 2π | 0.2π | rad s^{-1} |
| α | Uniform | 50 | 5 | — |
| A | Uniform | 1 | 0.1 | N |
| ω_x | Uniform | π | 0.1π | rad s^{-1} |

3.4.2 Bouc-Wen oscillator

A non-linear Bouc-Wen oscillator (Bouc, 1967; Wen, 1976) was investigated in this example. The governing differential equation for the Bouc-Wen oscillator is given by:

$$\begin{aligned}
 \ddot{y}(t) + 2\zeta\omega\dot{y}(t) + \omega^2[\rho y(t) + (1-\rho)w(t)] &= -x(t) \\
 \dot{w}(t) = \gamma\dot{y}(t) - \alpha|\dot{y}(t)||w(t)|^{n-1}w(t) - \beta\dot{y}(t)|w(t)|^n & \\
 x(t) = A\sin(\omega_x t) &
 \end{aligned} \tag{3.19}$$

where, ζ and ω are the damping ratio and the natural frequency of the oscillator respectively. $\rho = 0$, $\gamma = 1$, $\beta = 0$ and $n = 1$ were considered for this problem. $x(t)$ is the excitation and $w(t)$ is the hysteretic displacement as given by Wen (1976). The initial conditions at rest are $y(0) = 0$, $\dot{y}(0) = 0$ and $w(0) = 0$. In a similar way to Mai and Sudret (2017), 5 uncertain parameters were considered for the oscillator, which are $\xi = \{\zeta, \omega, \alpha, A, \omega_x\}$. The statistical distributions for all the uncertain parameters are given in Table 3.6.

The stochastic response was computed for the oscillator in the time domain $t \in [0\text{s}, 30\text{s}]$ with a time-step of $\Delta t = 0.005\text{s}$. As it has already been illustrated through the previous example in section 3.4.1, Kriging is unable to predict the stochastic response behavior for the non-linear dynamical systems even with more samples than the sparse KNARX. Therefore, Kriging has not been utilized from now onward. In a similar way to the previous example, the sparse KNARX model has been constructed with two different sizes of sample points $N = 40$ and $N = 10$. A different type of basis function has been considered for the Bouc-Wen oscillator according to Mai et al. (2016), which is given by:

$$f_i[z(t)] = \left\{ x^{l_i}(t - n_{x_i}\Delta t) |\dot{y}(t - \Delta t)|^{m_i}, \dot{y}^{l_i}(t - n_{y_i}\Delta t) |\dot{y}(t - \Delta t)|^{m_i} \right\} \tag{3.20}$$

In Equation 3.20, the basis function relies on the excitation and the velocity of the oscillator. Thus, the velocity was computed by the sparse KNARX model and further, the displacement of the system was obtained through numerical integration by utilizing the Matlab solver *ode45*. $l_i \in \{0, 1\}$ and $m_i \in \{0, 1\}$ were considered for the oscillator as Equation 3.19 is linear with respect to the excitation and the velocity. $n_{x_m} = n_{y_m} = 4$ was considered as the problem can be appraised as a 2-DOF system due to the extra hysteretic displacement i.e. $n_x \in \{0, \dots, 4\}$ and $n_y \in \{1, \dots, 4\}$. 21 terms were found in the full NARX polynomial basis matrix by utilizing Equation 3.20 and imposing all the mentioned conditions.

A threshold similar to the previous example was employed to detect the highly non-linear samples. The threshold value for the response of the Bouc-Wen oscillator was chosen as $\max(|\dot{y}(t)|) > 0.3\text{ m s}^{-1}$. The threshold value reduced the number of samples from $N = 40$ to $N_1 = 3$ which means only 3 full NARX models were formulated utilizing the basis functions

of Equation 3.20, and furthermore, the LARS algorithm has been employed to make the full NARX models sparse. All the three sparse NARX models were found unique in this step. Therefore, the coefficients for all the 40 initial samples were computed by the OLS for the 3 sparse NARX models and the mean errors (Equation 3.11) were predicted by computing the time series in a recursive manner. The finally selected sparse NARX model produced a mean error of $\bar{\epsilon} = 1.10 \times 10^{-5}$ for the 40 samples and contains 8 terms in the polynomial basis matrix which are $\{ |\dot{y}(t - \Delta t)|, x(t), x(t - 4\Delta t), x(t - 4\Delta t) |\dot{y}(t - \Delta t)|, \dot{y}(t - \Delta t), \dot{y}(t - 4\Delta t), \dot{y}(t - \Delta t) |\dot{y}(t - \Delta t)|, \dot{y}(t - 4\Delta t) |\dot{y}(t - \Delta t)| \}$.

A similar procedure was adopted by substantially reducing the initial number of sample points to $N = 10$. 4 samples were found mostly non-linear based on the previous threshold value. Out of the 4 full NARX models, 2 were found as unique sparse NARX models after applying the LARS for the detection of the most important terms. Therefore, one sparse NARX model was selected based on the predicted mean error from both sparse NARX models. The final sparse NARX model was found to have the same terms in the polynomial basis as the previous one with $N = 40$.

The stochastic responses were also predicted here by the sparse PCE-NARX model (Mai et al., 2016). However, the sparse PCE-NARX model was unable to predict the stochastic response behavior with $N = 40$ model evaluations for the Bouc-Wen oscillator. For that reason, the number of model evaluations was increased to $N = 50$ and the stochastic responses were predicted with the same $M_1 = 8$ terms in the sparse NARX model as in the sparse KNARX model with $N = 40$.

The uncertain response characteristics predicted were the displacement and the velocity of the Bouc-Wen oscillator. The time dependent mean and the standard deviation of $y(t)$ and $\dot{y}(t)$ are shown in Figure 3.6 and Figure 3.7, respectively. The figures show that both the statistical moments predicted by the sparse KNARX are following the MCS results with utmost accuracy. However, the accuracies of the statistical moments are deteriorating from the initial time-steps using the sparse PCE-NARX model even with more samples. The scatter diagrams and the PDFs at three different times (10 s, 20 s and 30 s) are also plotted in Figure 3.8 and Figure 3.9 for the displacement and the velocity, respectively. It is seen from all the figures that the sparse KNARX performs well in all instances with very few samples. The error metrics for all the instantaneous displacements and velocities are given in Table 3.7. An excellent accuracy in terms of error ϵ and R^2 value is noticed for all the time instances for the sparse KNARX model.

For the prediction of the safety corridor under uncertainty, the scatter plots and the PDFs of the maximum absolute displacement and velocity are plotted in Figure 3.10 and Figure 3.11, respectively. The worst prediction is noticed for the PDFs by the sparse PCE-NARX model, whereas an excellent accuracy is observed in both cases for the predicted maximum responses by the sparse KNARX model. These plots, which represent the uncertain maximum response behavior, can be utilized to measure the safety margin of the system.

In a similar way to the previous example, the accuracy and the efficiency measurement metrics are given in Table 3.8. The table shows that the sparse KNARX has predicted results with higher accuracy and lower computational cost. The efficiency of the proposed sparse KNARX method is also observed over the recently proposed time warping PCE method (Mai and Sudret, 2017) which required $N = 100$ ($\gg N = 10$) samples to predict the stochastic response behavior for the same example.

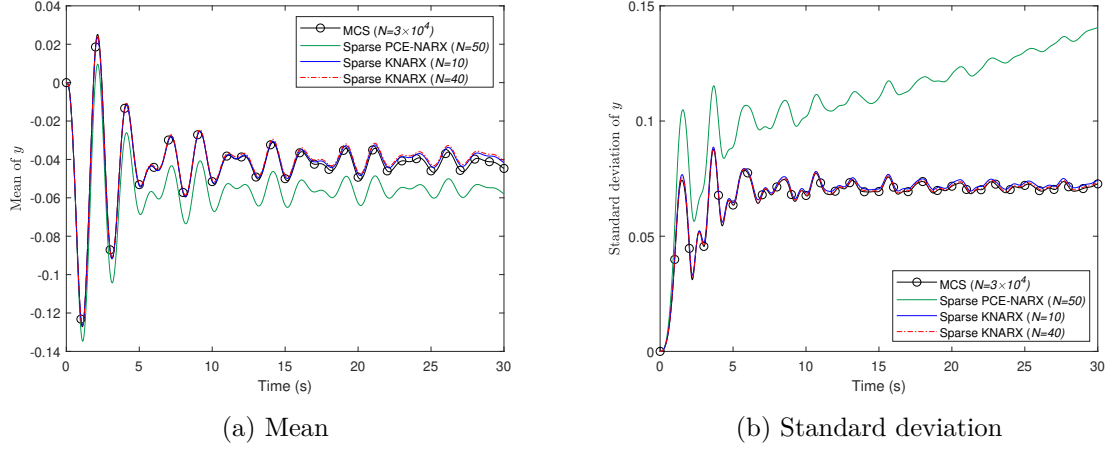


Figure 3.6: Statistical response characteristics for the displacement of the Bouc-Wen oscillator

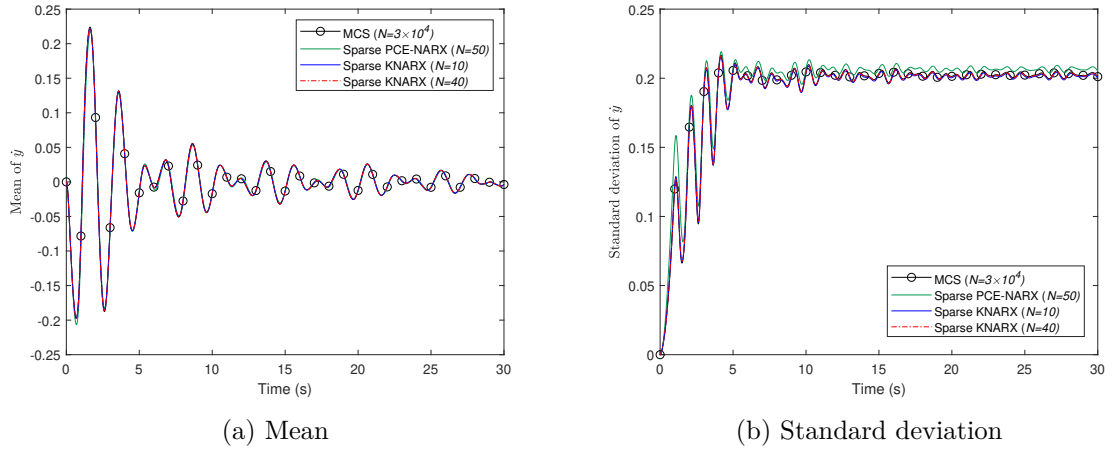


Figure 3.7: Statistical response characteristics for the velocity of the Bouc-Wen oscillator

Table 3.7: Accuracy of the surrogate models in predicting the instantaneous response characteristics for the Bouc-Wen oscillator

| Method | N | Time instance | Displacement | | Velocity | |
|-----------------|-----|---------------|-------------------------|--------|-----------------------|--------|
| | | | ϵ | R^2 | ϵ | R^2 |
| Sparse PCE-NARX | 50 | $t = 10$ s | 660.0×10^{-3} | 0.3370 | 44.0×10^{-3} | 0.9557 |
| Sparse KNARX | 10 | | 6.8×10^{-3} | 0.9932 | 0.9×10^{-3} | 0.9991 |
| Sparse KNARX | 40 | | 3.8×10^{-3} | 0.9962 | 0.5×10^{-3} | 0.9995 |
| Sparse PCE-NARX | 50 | $t = 20$ s | 880.0×10^{-3} | 0.1224 | 48.0×10^{-3} | 0.9519 |
| Sparse KNARX | 10 | | 8.6×10^{-3} | 0.9914 | 1.0×10^{-3} | 0.9990 |
| Sparse KNARX | 40 | | 5.6×10^{-3} | 0.9944 | 0.5×10^{-3} | 0.9995 |
| Sparse PCE-NARX | 50 | $t = 30$ s | 1140.0×10^{-3} | — | 50.0×10^{-3} | 0.9503 |
| Sparse KNARX | 10 | | 10.8×10^{-3} | 0.9892 | 1.1×10^{-3} | 0.9989 |
| Sparse KNARX | 40 | | 7.8×10^{-3} | 0.9922 | 0.5×10^{-3} | 0.9995 |

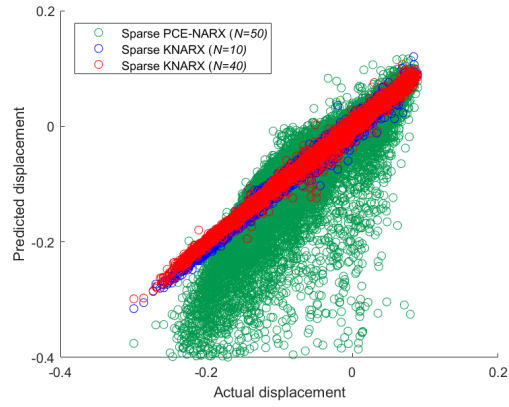
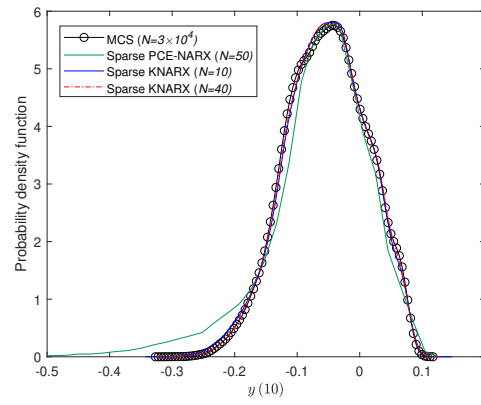
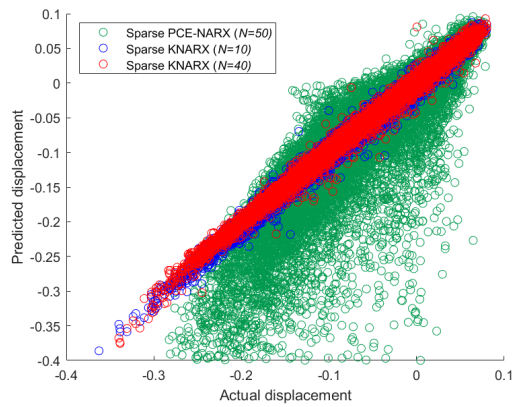
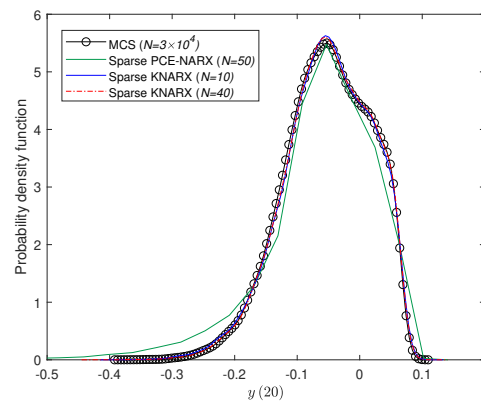
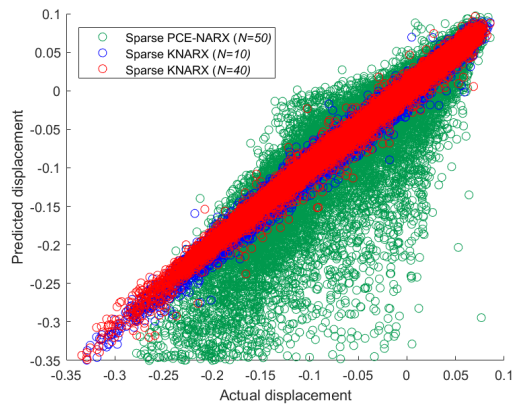
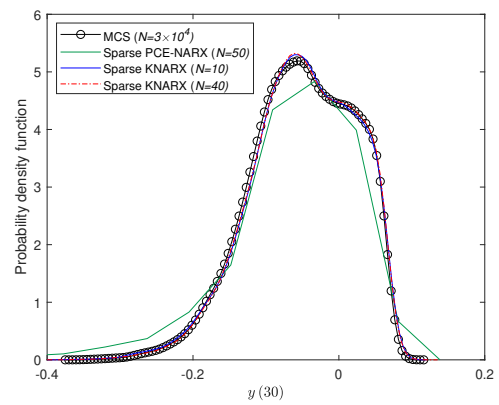
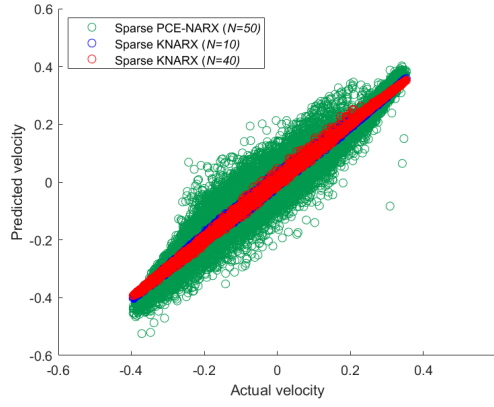
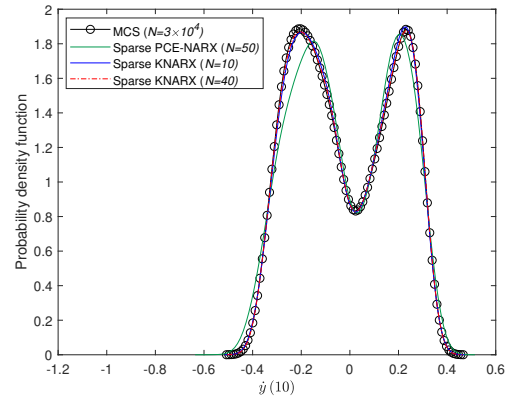
(a) Scatter plot at $t = 10$ s(b) PDF at $t = 10$ s(c) Scatter plot at $t = 20$ s(d) PDF at $t = 20$ s(e) Scatter plot at $t = 30$ s(f) PDF at $t = 30$ s

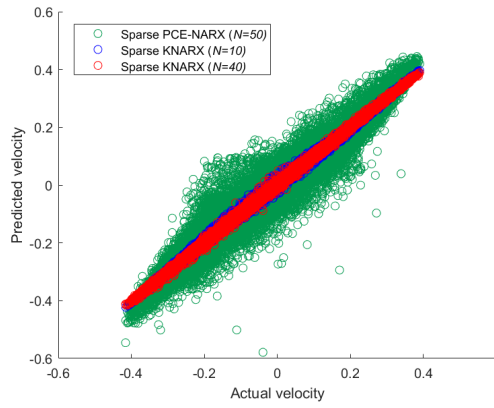
Figure 3.8: Prediction of instantaneous displacement characteristics for the Bouc-Wen oscillator at different times



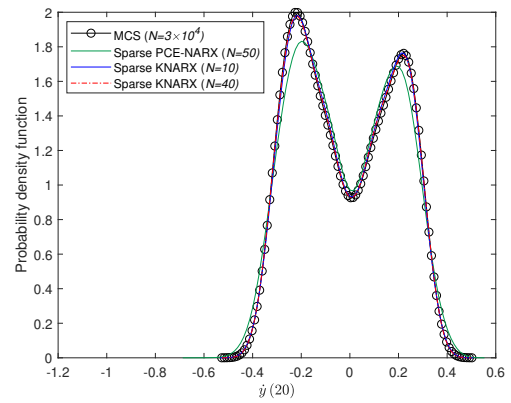
(a) Scatter plot at $t = 10$ s



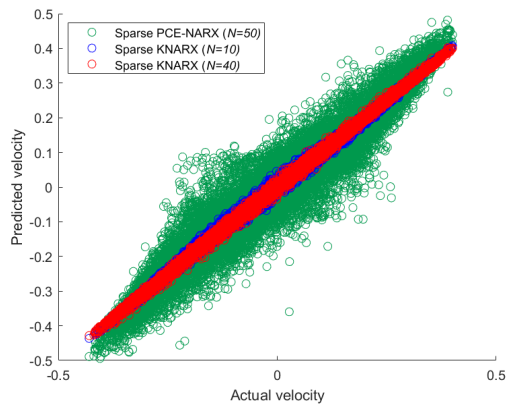
(b) PDF at $t = 10$ s



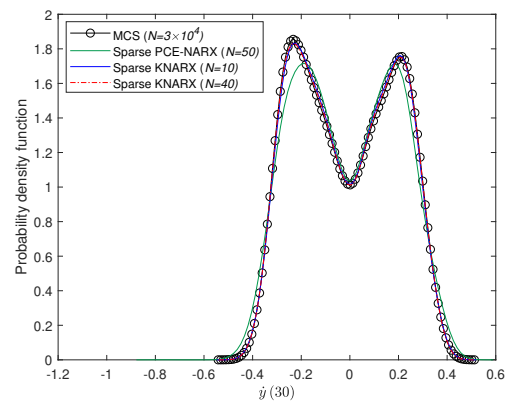
(c) Scatter plot at $t = 20$ s



(d) PDF at $t = 20$ s

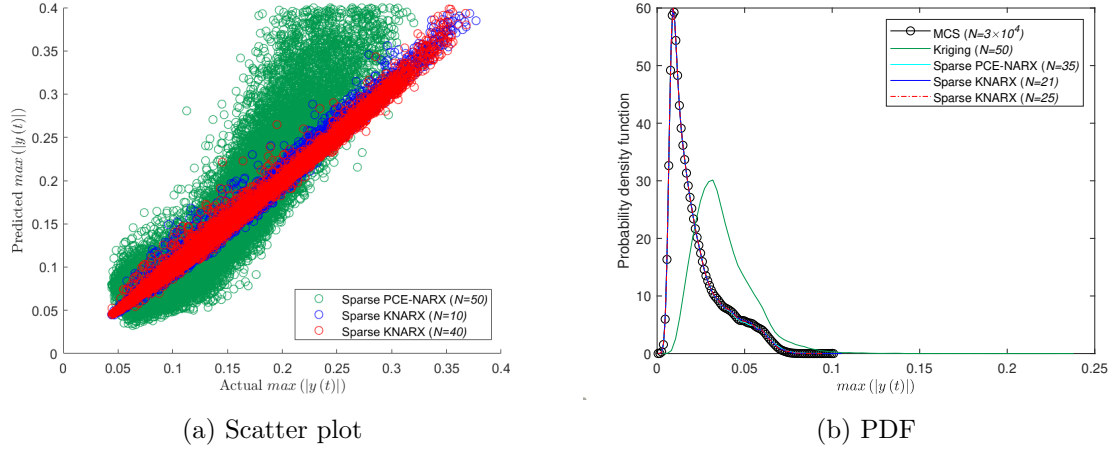
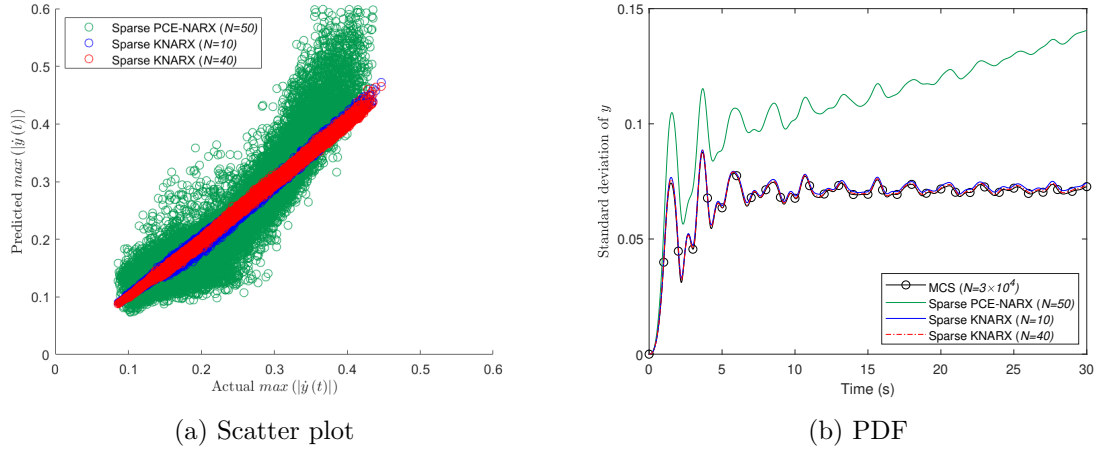


(e) Scatter plot at $t = 30$ s



(f) PDF at $t = 30$ s

Figure 3.9: Prediction of instantaneous velocity characteristics for the Bouc-Wen oscillator at different times

Figure 3.10: Comparison of predicted $\max(|y(t)|)$ for the Bouc-Wen oscillatorFigure 3.11: Comparison of predicted $\max(|\dot{y}(t)|)$ for Bouc-Wen oscillatorTable 3.8: Accuracy and efficiency of the surrogate models in computing $\dot{y}(t)$ for the Bouc-Wen oscillator

| Method | N | $\bar{\epsilon}$ | Accuracy | | Efficiency | |
|-----------------|-----------------|----------------------|---------------------------|----------------------|------------|--------------|
| | | | $\epsilon_{\max(y(t))}$ | $R^2_{\max(y(t))}$ | n_K | CPU time (s) |
| Sparse PCE-NARX | 50 | 9.3×10^{-2} | 2.6×10^{-1} | 0.7414 | 8 | 27.40 |
| Sparse KNARX | 10 | 1.9×10^{-3} | 4.6×10^{-3} | 0.9954 | 8 | 19.12 |
| Sparse KNARX | 40 | 8.0×10^{-4} | 1.9×10^{-3} | 0.9981 | 8 | 21.72 |
| MCS | 3×10^4 | — | — | — | — | 1223.17 |

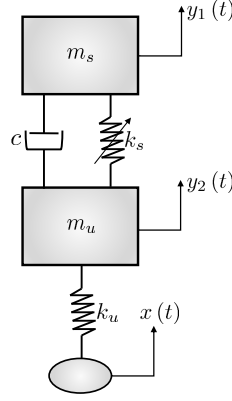


Figure 3.12: A 2-DOF dynamical system

Table 3.9: Uncertain parameters for the 2-DOF dynamical system

| Variable | Distribution type | Mean | Standard deviation | Unit |
|------------|-------------------|--------|---------------------------|---------------------|
| k_s | Normal | 2000 | 200 | N m^{-3} |
| k_u | Normal | 2000 | 200 | N m^{-1} |
| m_s | Normal | 20 | 2 | kg |
| m_u | Normal | 40 | 4 | kg |
| c | Normal | 600 | 60 | N s m^{-1} |
| A | Uniform | 0.1 | $\frac{0.01}{\sqrt{3}}$ | m |
| ω_x | Uniform | 2π | $\frac{0.2\pi}{\sqrt{3}}$ | rad s^{-1} |

3.4.3 A 2-DOF dynamical system

Finally, a 2-DOF dynamical system (Mai et al., 2016) has been considered for the applicability of the proposed sparse KNARX model. The dynamical system is shown in Figure 3.12 and the governing differential equation of the problem is:

$$\begin{aligned}
 m_s \ddot{y}_1(t) &= -k_s [y_1(t) - y_2(t)]^3 - c [\dot{y}_1(t) - \dot{y}_2(t)] \\
 m_u \ddot{y}_2(t) &= k_s [y_1(t) - y_2(t)]^3 + c [\dot{y}_1(t) - \dot{y}_2(t)] + k_u [x(t) - y_2(t)] \\
 x(t) &= A \sin(\omega_x t)
 \end{aligned} \tag{3.21}$$

where m_s is the mass which is connected with the mass m_u by a non-linear spring with stiffness k_s and a damper with damping coefficient c . k_u is a linear spring attached to the ground having a sinusoidal displacement function $x(t)$.

In a similar way to Mai et al. (2016), all the parameters of the system are considered uncertain i.e. $\xi = \{k_s, k_u, m_s, m_u, c, A, \omega_x\}$. The mean and the standard deviation of all the uncertain parameters are given in Table 3.9.

The main aim of this example is to predict the uncertain response $y_1(t)$ of mass m_s which is attached with the non-linear spring. This system has been solved by the sparse KNARX model with two different number of sample points ($N = 50$ and $N = 20$). As it has been seen from the previous two examples that the sparse PCE-NARX model is unable to predict the stochastic response behavior of the dynamical systems using the same number of samples,

the sparse PCE-NARX model is not utilized for this problem. However, one can refer to Mai et al. (2016) for the results with the sparse PCE-NARX model of this example. The problem has been solved in the time domain $t \in [0 \text{ s}, 30 \text{ s}]$ with a time-step of $\Delta t = 0.01 \text{ s}$ by *ode45*. The initial conditions for the system at rest ($t = 0 \text{ s}$) are given by:

$$\begin{aligned} y_1(0) &= 0 \\ \dot{y}_1(0) &= 0 \\ y_2(0) &= 0 \\ \dot{y}_2(0) &= 0 \end{aligned} \tag{3.22}$$

For the construction of the NARX model, the NARX basis function was chosen similar to the Duffing oscillator. The NARX basis function for this problem is given by:

$$f_i[z(t)] = x^{l_i}(t - n_{x_i}\Delta t) y_1^{m_i}(t - n_{y_i}\Delta t) \tag{3.23}$$

In Equation 3.23, $l_i \in \{0, 1\}$ and $m_i \in \{0, 1, 2, 3\}$ with $l_i + m_i \leq 3$ were chosen due to the cubic non-linearity of the system. $n_x \in \{0, 1, \dots, 4\}$, $n_y \in \{1, \dots, 4\}$ were chosen because the system has 2-DOF. The full NARX model was constructed with this NARX basis which has $M = 58$ terms. Initially, after investigating the response versus the restoring force, a threshold criterion of the responses has been decided as $\max(|y_1(t)|) > 1.2 \text{ m}$ which reduced the number of samples to $N_1 = 10$. Consequently, only 10 full NARX models were constructed by using the function mentioned in Equation 3.23. The sparsity was introduced at this step by using the LARS algorithm on the 10 full NARX models to get the unique sparse NARX models which further reduced the number of unique sparse NARX models to $N_2 = 5$. Thus, 5 unique sparse models were used to get the coefficients of the sparse NARX models by OLS for $N = 50$ samples. The mean error for each of the sparse NARX models was computed using Equation 3.11 and the finally selected sparse NARX model has a mean error of $\bar{\epsilon} = 2.95 \times 10^{-4}$ with 5 terms in the NARX polynomial out of 58 which are $\{y_1(t - \Delta t), y_1(t - 4\Delta t), y_1^3(t - \Delta t), x(t - 4\Delta t), x(t - 4\Delta t) y_1^2(t - 4\Delta t)\}$.

The same example has also been solved by reducing the initial number of sample points to $N = 20$. For this case, initially, 3 samples were selected from the measure of non-linearity and 3 full NARX models were constructed using the basis function as mentioned in Equation 3.23. Further, all the 3 NARX models were found unique sparse NARX model utilizing the LARS. The predicted mean error for the 20 samples using the finally selected sparse NARX model was $\bar{\epsilon} = 1.85 \times 10^{-6}$ with 5 terms in the polynomial. Here, the 5 terms are $\{y_1(t - \Delta t), y_1(t - 4\Delta t), x(t), x(t - 4\Delta t), x(t - 4\Delta t) y_1^2(t - 4\Delta t)\}$. The same number of Kriging models were calibrated as the previous case to make the sparse NARX model stochastic.

The time dependent mean and standard deviation of the displacement (y_1) and velocity (\dot{y}_1) were predicted. The time dependent statistical characteristics of displacement and velocity are plotted in Figure 3.13 and Figure 3.14, respectively. Both figures suggest good agreement between the sparse KNARX and the MCS even with very few sample points.

In a similar way to the previous examples, the instantaneous predicted displacements by the sparse KNARX are compared with the MCS results at three different times. The instantaneous scatterplots and the PDFs are plotted in Figure 3.15. The errors of the predicted responses at three different times along with the R^2 values are given in Table 3.10. The results show a high accuracy of the sparse KNARX in predicting the instantaneous response characteristics. The accuracy and the efficiency are also noticed for the sparse KNARX at

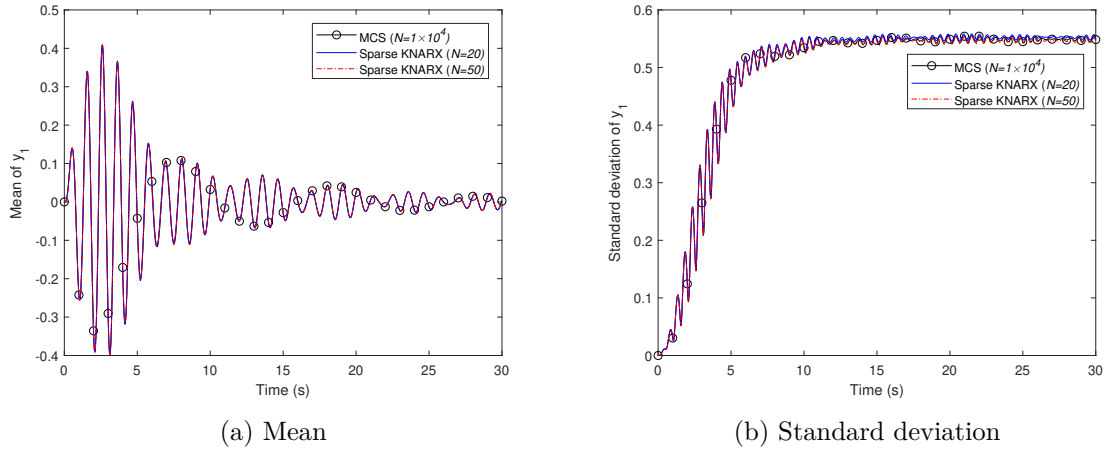


Figure 3.13: Statistical response characteristics for displacement ($y_1(t)$) of the 2-DOF dynamical system

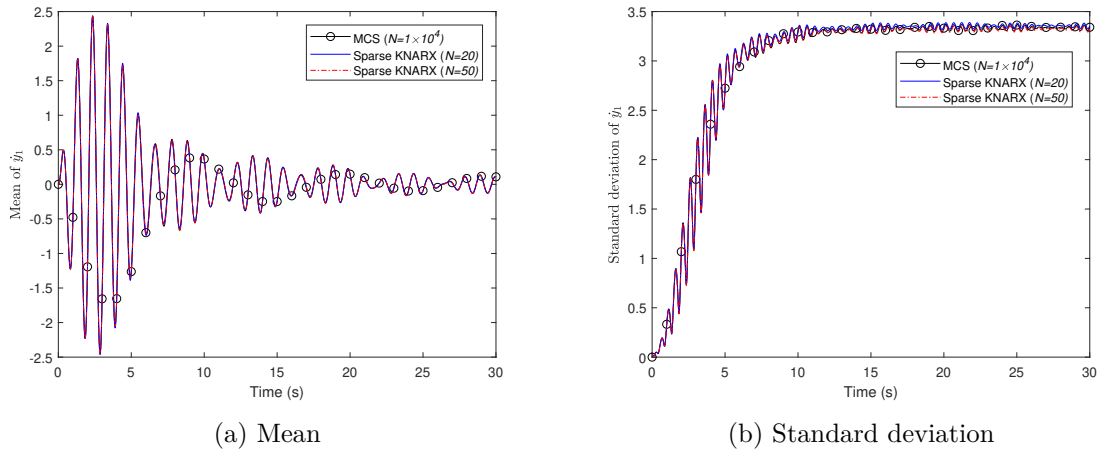


Figure 3.14: Statistical response characteristics for velocity ($\dot{y}_1(t)$) of the 2-DOF dynamical system

Table 3.10: Accuracy of sparse KNARX in predicting instantaneous response characteristics for the 2-DOF dynamical system

| N | Time instance | $\epsilon_{y_1(t)}$ | R^2 |
|-----|---------------|-----------------------|--------|
| 20 | $t = 10$ s | 11.6×10^{-3} | 0.9884 |
| 50 | | 1.1×10^{-3} | 0.9989 |
| 20 | $t = 20$ s | 16.2×10^{-3} | 0.9838 |
| 50 | | 1.9×10^{-3} | 0.9981 |
| 20 | $t = 30$ s | 16.2×10^{-3} | 0.9838 |
| 50 | | 2.3×10^{-3} | 0.9977 |

Table 3.11: Accuracy and efficiency of sparse KNARX in computing $y_1(t)$ for the 2-DOF dynamical system

| Method | N | Accuracy | | | Efficiency | |
|--------------|-----------------|----------------------|-----------------------------|------------------------|------------|--------------|
| | | $\bar{\epsilon}$ | $\epsilon_{\max(y_1(t))}$ | $R^2_{\max(y_1(t))}$ | n_K | CPU time (s) |
| Sparse KNARX | 20 | 8.9×10^{-3} | 15.4×10^{-3} | 0.9846 | 5 | 7.76 |
| Sparse KNARX | 50 | 1.2×10^{-3} | 1.7×10^{-3} | 0.9983 | 5 | 22.62 |
| MCS | 3×10^4 | — | — | — | — | 466.34 |

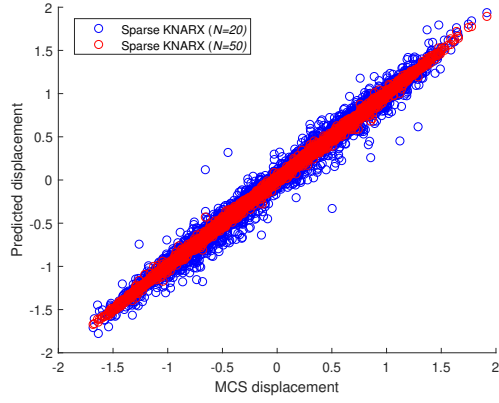
30 s ($N = 50$, $\epsilon_{y_1(t)} = 2.3 \times 10^{-3}$) as compared to the recently proposed sparse PCE-NARX model ($N = 100$, $\epsilon_{y_1(t)} = 4.21 \times 10^{-3}$) (Mai et al., 2016). The accuracy of the stochastic response behavior has also been checked by plotting the absolute maximum displacement and the velocity in Figure 3.16 and Figure 3.17 respectively, which show good agreement with MCS.

The global mean error of the predicted time series is measured by using Equation 3.11. Along with this, the accuracy in predicting the maximum absolute displacement using different sample points were calculated using Equation 3.9 and R^2 value. All these results along with the efficiency measurement metrics of the proposed sparse KNARX are listed in Table 3.11. Here, the CPU time of the sparse KNARX model has not been emphasized by the number of surrogate model calibration (n_K), instead it is greatly affected by the initial number of model evaluations (N). All the results show that the sparse KNARX performs very well at all instances.

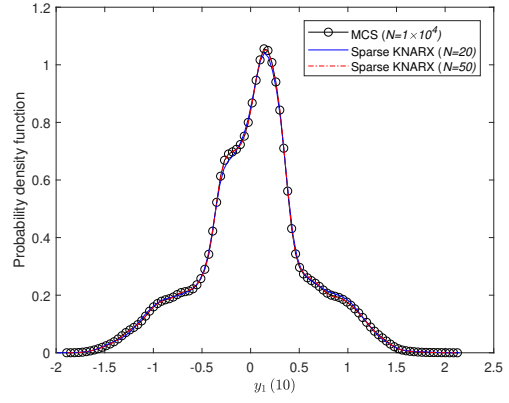
3.5 Failure of the auto-regressive model for an impact oscillator

The examples presented in this chapter have shown that the NARX model can capture the nonlinear behavior of a dynamical system very well. For that reason, it was possible to propagate the uncertain parameters through the nonlinear dynamical systems properly using a low number of sample points. In this section, an impacted dynamical system is investigated using several auto-regressive (AR) models to check the capability in capturing the nonlinear behavior of an impacted oscillator. The main difference with the previous examples is that the impact oscillators are non-smooth in nature. Before propagating the uncertain parameters, first it is important to identify an oscillator using a suitable AR model. The NARX model

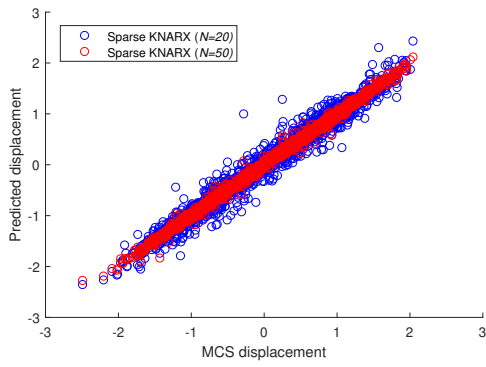
3.5. FAILURE OF THE AUTO-REGRESSIVE MODEL FOR AN IMPACT OSCILLATOR 47



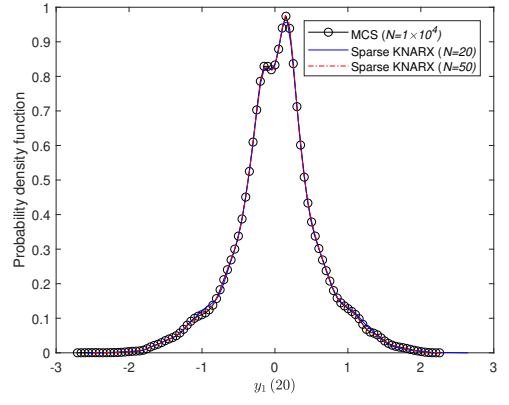
(a) Scatter plot at $t = 10$ s



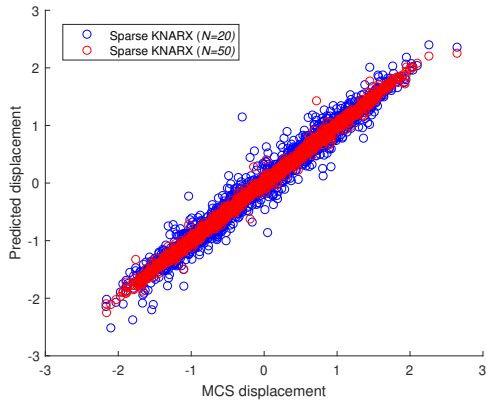
(b) PDF at $t = 10$ s



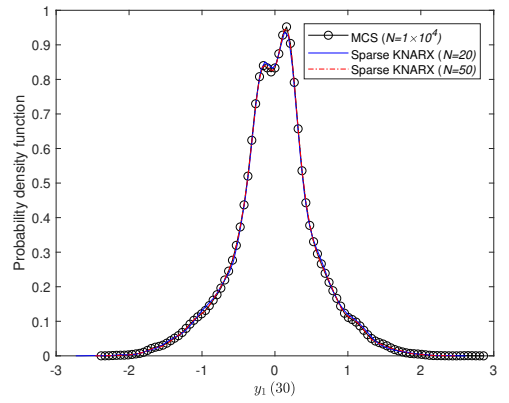
(c) Scatter plot at $t = 20$ s



(d) PDF at $t = 20$ s



(e) Scatter plot at $t = 30$ s



(f) PDF at $t = 30$ s

Figure 3.15: Prediction of instantaneous displacement characteristics for 2-DOF dynamical system at different time instances

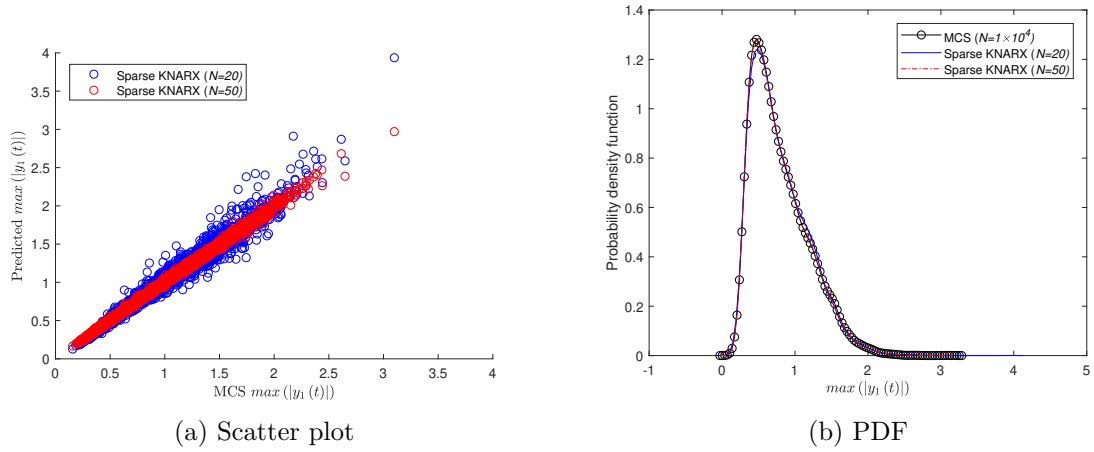


Figure 3.16: Comparison of predicted $\max(|y_1(t)|)$ for the 2-DOF dynamical system

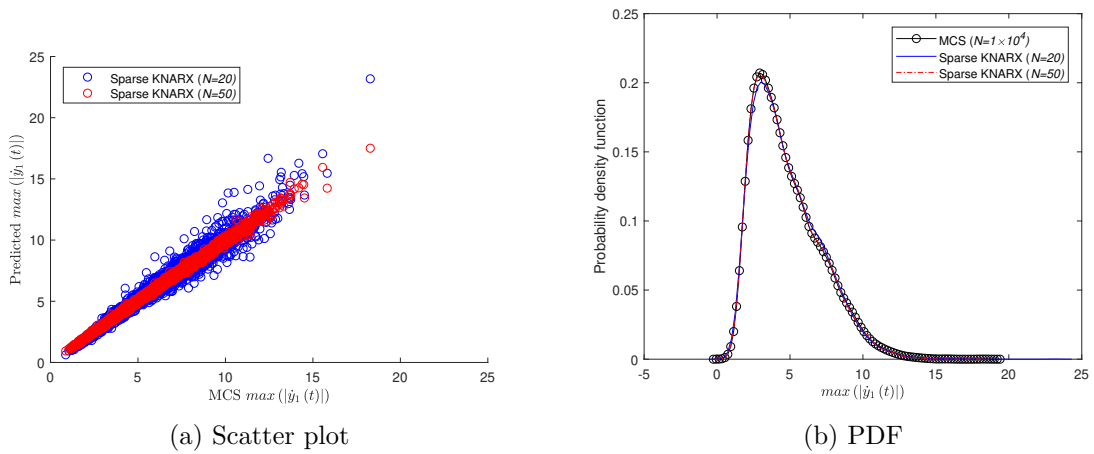


Figure 3.17: Comparison of predicted $\max(|\dot{y}_1(t)|)$ for the 2-DOF dynamical system

can be used for the identification of an impact oscillator when it is excited with an external force (forced vibration problem). However, the oscillator investigated here is a free vibration problem excited with the initial conditions. Therefore, the identification of a deterministic impact dynamical system is investigated in this section using several AR models without the exogenous input part. A brief description of several AR models used in this section is given below.

3.5.1 Linear auto-regressive model

Let us consider a time dependent response quantity $y(t) = \{y(t_1), y(t_2), \dots, y(t_{n_t})\}$. Here t represents the discretized time vector and t_i is an element of vector t . The main objective of an AR model is to re-construct a specified time series. The linear AR model (Wold, 1938; Box et al., 1994) is given by:

$$y(t) + a_1 y(t - \Delta t) + a_2 y(t - 2\Delta t) + \dots + a_{n_y} y(t - n_y \Delta t) = \varepsilon(t) \quad (3.24)$$

where the a_i are the coefficients of the linear AR model. n_y is the maximum time lag of the response and $\varepsilon(t)$ is the residual of the fitted AR model which is supposed to be a Gaussian white noise. The AR model specified here does not consider the excitation part. The responses at any time-step is computed from the responses at the previous time-steps along with the corresponding coefficients. Therefore, the identification of this linear AR model requires finding out the coefficients in Equation 3.24. In the present work, the Matlab system identification toolbox was used: the AR model was obtained by *ar* Matlab function. Several strategies are available to find out the AR coefficients. A forward-backward approach (Marple, S. L., 1987) is used to find out the AR model coefficients, which utilizes the minimization of the sum of square of the residual error to identify the AR coefficients.

3.5.2 Nonlinear AR model

The nonlinear AR model is an extension of the linear AR model and is almost similar to the NARX model. A similar form to the NARX model is used here for the nonlinear AR (NAR) model. The NAR model is defined as:

$$y(t) = \mathcal{F}[z(t)] + \varepsilon(t) \quad (3.25)$$

where $z(t_i) = \{y(t - \Delta t), y(t - 2\Delta t), \dots, y(t - n_y \Delta t)\}^T$ is the vector having all the lagged system response and $\mathcal{F}[\bullet]$ is a nonlinear model with the lagged response terms. n_y is the maximum time lag of the response. Therefore, the most important aspect of the NAR model is the type of nonlinear model. In a similar way to the NARX model, the NAR model is given by:

$$\mathcal{F}[z(t)] = \sum_{j=1}^M a_j f_j[z(t)] \quad (3.26)$$

The parameters of the above-mentioned equation have been defined in Equation 3.2. The computation of the NAR coefficients is one of the main issues in this model. Due to the similar form to the NARX model, the NAR coefficients can also be computed by the OLS approach. Therefore, the coefficients were computed by minimizing the residual error using the OLS approach for the impacted dynamical systems.

3.5.3 Nonlinear wavelet AR model

In the previous section, the polynomials were used in the AR model. A different form can also be used for the underlying function $\mathcal{F}[z(t)]$. A wavelet family (Qinghua Zhang, 1997) has been used here for the nonlinear model of the NAR model to identify the response of an impacted dynamical system. More specifically, a wavelet network (Qinghua Zhang, 1997) is utilized in the present AR model to capture the non-linearity in the response quantity. The wavelet based nonlinear AR model is readily available in the Matlab system identification toolbox as *wavenet* function, this function was used in the present work.

3.5.4 Identification of an impact oscillator by AR models

Problem definition

A 2-DOF nonlinear impact oscillator was considered for the present investigation. The impact oscillator is shown in Figure 3.18. The mass of the structure is m_{st} and the mass of the projectile is m_p . The governing differential equation of the 2-DOF impact oscillator is given by:

$$\begin{aligned} m_{st}\ddot{y}_{st} + c_{st}\dot{y}_{st} + k_{st}y_{st} + f_c &= 0 \\ m_p\ddot{y}_p - f_c &= 0 \end{aligned} \quad (3.27)$$

where the structure mass m_{st} is attached to the ground by a linear spring having stiffness k_{st} and by a damper with viscous damping c_{st} . y_{st} and y_p are the displacements of the structure and the projectile, respectively. f_c is the contact force due to the contact between the projectile with the nonlinear spring having stiffness k_c and the contact was modeled by the Hertz law (Johnson, 1985; Buezas et al., 2013). The contact force is defined as:

$$\begin{aligned} f_c &= k_c(y_{st} - y_p)^{\frac{3}{2}}; \quad y_{st} \geq y_p \\ &= 0 \quad ; \quad y_{st} < y_p \end{aligned} \quad (3.28)$$

The values of all the parameters (except k_{st}) for the impact oscillator are given in Table 3.12. The system was solved in the time domain $t \in [0\text{ s}, 10^{-3}\text{ s}]$ with a time-step of $\Delta t = 10^{-6}\text{ s}$. The main objective of this study is the system identification of the projectile responses (i.e. displacement and velocity). The responses are computed here under the initial condition which are given by:

$$\begin{aligned} y_{st}(0) &= 0 \\ \dot{y}_{st}(0) &= 0 \\ y_p(0) &= 0 \\ \dot{y}_p(0) &= -v_0 \end{aligned} \quad (3.29)$$

where the initial velocity of the projectile is equal to $v_0 = 10\text{ m s}^{-1}$.

The impact oscillator was solved for two different conditions, namely a single impact condition and a multi-impact condition by tuning the linear stiffness k_{st} . For the single impact and for the multi-impact conditions, $k_{st} = 2.4 \times 10^2\text{ MN m}^{-3/2}$ and $k_{st} = 2.4\text{ MN m}^{-3/2}$ were considered, respectively.

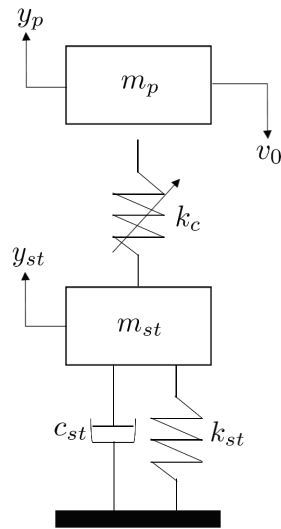


Figure 3.18: 2-DOF nonlinear impact oscillator

Table 3.12: Parameters of the impact oscillator

| Parameter | Value | Unit |
|--------------|------------------|----------------------|
| m_{st} | 60 | g |
| m_p | 330 | g |
| k_c | 16×10^3 | $\text{MN m}^{-3/2}$ |
| ζ_{st} | 0.5% | — |

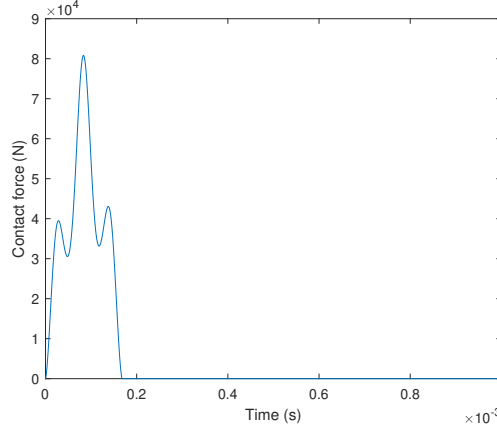


Figure 3.19: Deterministic contact force for the single impact oscillator

System identification of a single impact oscillator in time domain $[0\text{ s}, 10^{-3}\text{ s}]$

A first attempt was taken to identify the above-described impact oscillator using the AR models. For the linear AR model and the wavelet AR model, the only input is the maximum time lag (n_y) for the response quantity. On the other hand, the NAR model requires the time lag and the maximum degree (m) of the nonlinear polynomial. In a similar way to the NARX model, the time lag was chosen twice the DOF number of the system i.e. $n_y = 4$ for the linear AR model and the maximum degree for the NAR model was chosen as $m = 3$. For the wavelet AR model, the time lag was chosen as $n_y = 1$. The actual result was computed by performing the time integration using the Matlab function *ode45*. The contact force between the structure and the projectile is plotted in Figure 3.19 and it is seen that a single impact occurs in the whole time span. The displacement and the velocity predicted by all the methods are shown in Figure 3.20. It is seen from Figure 3.20a that the projectile displacements predicted by all the methods are not following the actual result. It is seen that the NAR model predicted displacement has diverged from the initial time-step. For the projectile velocity (Figure 3.20b), the NAR model was also unable to predict the response from the initial time. On the contrary, an excellent accuracy is observed for the wavelet AR model whereas the linear AR model was unable to predict the velocity from the initial time step.

System identification of the single impact oscillator in time domain $[0\text{ s}, 1.9 \times 10^{-4}\text{ s}]$

The system identification of the nonlinear impacted dynamical system is then much more difficult than the smooth dynamical system with the conventional AR model for a long time. Therefore, to reduce the complexity of the problem, a system identification is investigated in this section for a shorter time span. More specifically, the system identification was performed up to a small time beyond the impact duration. Therefore, the time domain was here $t \in [0\text{ s}, 1.9 \times 10^{-4}\text{ s}]$ with a time step of $\Delta t = 10^{-6}\text{ s}$. All the other parameters of the system were unchanged. The predicted displacement and the predicted velocity are plotted in Figure 3.21. It is noticeable that the time lags are different for each of the AR models. The time lags were chosen from several trials. The linear AR model has predicted better result for the projectile displacement whereas the wavelet AR model has predicted better result for the projectile

3.5. FAILURE OF THE AUTO-REGRESSIVE MODEL FOR AN IMPACT OSCILLATOR53

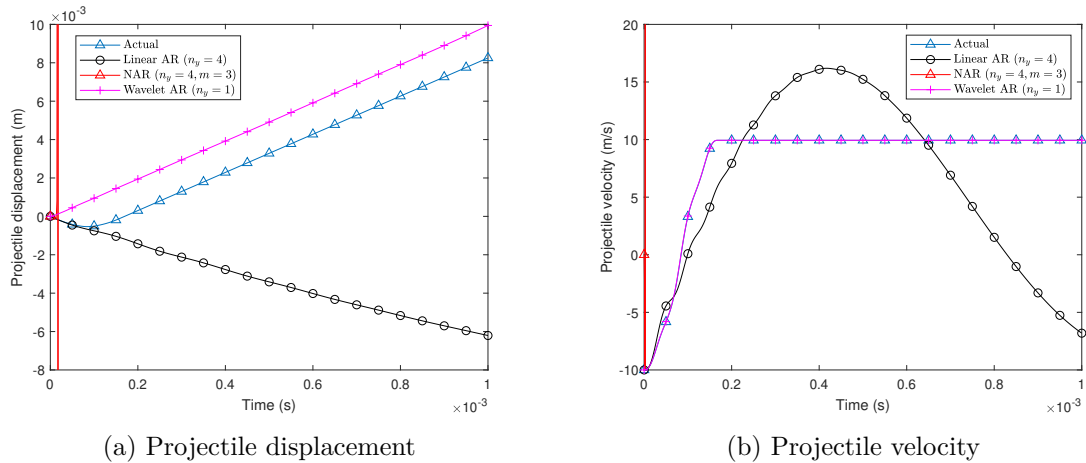


Figure 3.20: Identification of the response quantities for the single impact oscillator in time domain $[0 \text{ s}, 10^{-3} \text{ s}]$

velocity. All the other AR models are incapable to predict the responses properly.

System identification of multi-impact oscillator

A multi-impact nonlinear dynamical system is now investigated. For the formulation of the system as multi-impact dynamical system, the linear stiffness was decreased to $k_{st} = 2.4 \text{ MN m}^{-1}$. The time domain was decided slightly beyond the impact region $t \in [0 \text{ s}, 1.8 \times 10^{-3} \text{ s}]$. For the time integration, the time-step was chosen the same as for the single impact oscillator. The contact force is plotted with respect to the time in Figure 3.22. It is seen from the figure that the contact between the structure and the projectile has happened for five times here. The system identification was performed for the projectile displacement and for the projectile velocity. The predicted displacement and velocity by the AR models are shown in Figure 3.23. Figure 3.23a shows that the results predicted by all the AR models for the projectile displacement are not satisfactory. On the other hand, the projectile velocity is predicted quite well up to the first impact with the wavelet AR model (Figure 3.23b), however the divergence is noticed after the first impact. All the other AR models were not capable to predict the projectile velocity.

In conclusion, it has been observed from the above study that all the AR models have failed to identify the response quantities of the deterministic impact oscillator properly. For the single impact oscillator, the projectile displacement was predicted only within a short time range which was also due to the fact that the response behaves like a half sinusoidal curve. Although the projectile velocity for the single impact oscillator was predicted quite well by the wavelet AR model, it has been observed that, in the case of the multi-impact oscillator, the wavelet AR model can predict the velocity during the first impact only. Erroneous results were also observed for the projectile displacement of the multi-impact oscillator. Therefore, the identification of an impact oscillator is much more difficult than the one for a nonlinear dynamical system due to its non-smooth nature.

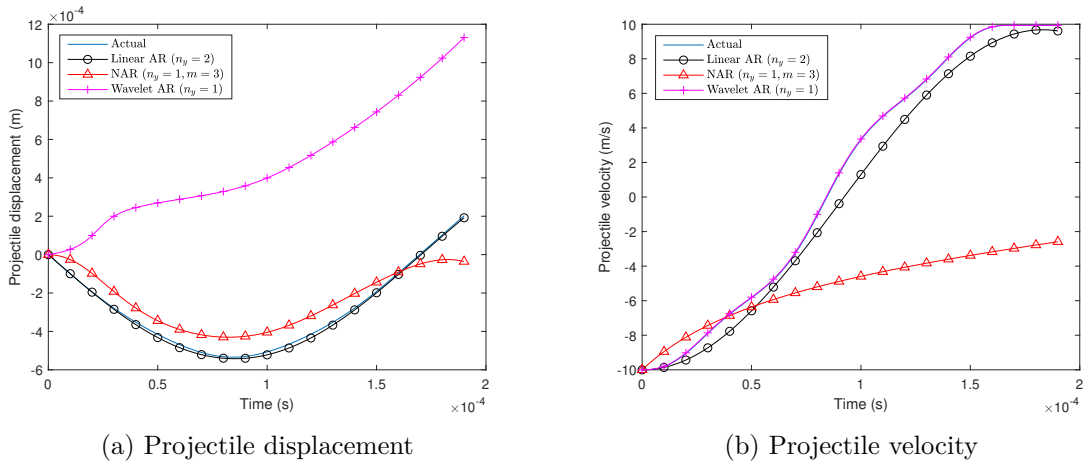


Figure 3.21: Identification of the response quantities for the single impact oscillator in time domain $[0\text{s}, 1.9 \times 10^{-4}\text{s}]$

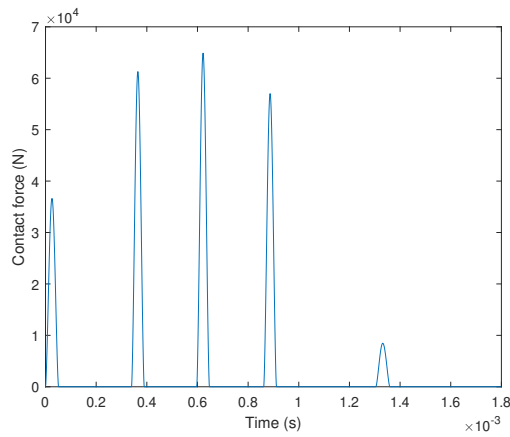


Figure 3.22: Deterministic contact force for the multi-impact oscillator

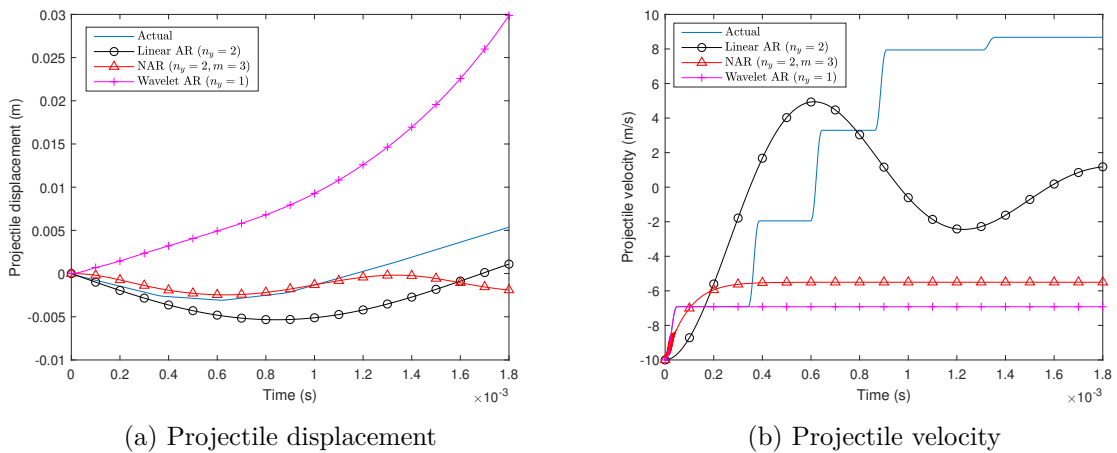


Figure 3.23: Identification of the response quantities for the multi-impact oscillator

3.6 Concluding remarks

A surrogate model has been developed in this chapter by combining the NARX model and the Kriging model, which is almost similar to the sparse PCE-NARX model (Mai et al., 2016). The proposed model is known as the sparse KNARX model. The time-dependent nonlinear behavior and the randomness have been decoupled using the NARX model and the Kriging model, respectively. Several nonlinear dynamical systems have been investigated using the sparse KNARX model and the results have been compared with the MCS and sparse PCE-NARX model results. It has been found that the sparse KNARX has predicted the time-dependent statistical moments accurately for all the examples using less model evaluations than the sparse PCE-NARX model. Along with this, the time-dependent PDF was also predicted quite well by the sparse KNARX model.

Although it was possible to identify properly the nonlinear dynamical system by the NARX model, the main challenge of this thesis is the propagation of uncertainty through an impact dynamical system. It is clear from the results presented in section 3.5 that the non-smooth behavior of the response has not been identified properly by the AR models. Hence, the sparse KNARX model can not be used for the stochastic impact oscillators and a suitable approach for propagating uncertain parameters through a random impact oscillator is investigated in chapter 4. Furthermore, this chapter has highlighted the interest of sparsity. The LARS algorithm is currently used. However, it seems interesting to investigate other alternatives. This will be done in chapter 5.

Chapter 4

Proper orthogonal decomposition based PCE model

4.1 Introduction

From the study of the previous chapter, it is clear that the NARX model or any other AR models are fully dependent on the behavior of the response quantity and finding a suitable AR model for the impacted dynamical system is very difficult due to the non-smooth behavior of the response quantities. Although the AR models failed to identify the impacted dynamical system in the previous chapter, it was learned from the previous study that decoupling the time domain and the randomness can improve the efficiency of a surrogate model substantially.

The time domain and the randomness can also be decoupled using model order reduction (MOR) techniques (Chinesta et al., 2011; Chatterjee, 2000; Kunisch and Volkwein, 1999; Schmid, 2010). MOR techniques include proper generalized decomposition (Chinesta et al., 2011; Giner et al., 2013; Leon et al., 2018; Tsiolakis et al., 2019), proper orthogonal decomposition (POD) (Chatterjee, 2000; Christensen et al., 1999; Peng and Mohseni, 2016; Holmes et al., 2012), dynamic mode decomposition (Schmid, 2010; Abdo et al., 2019; De Vuyst and Villon, 2019). POD has been used in dimensionality reduction of ordinary differential equation (Moore, 1979) and partial differential equation (Kunisch and Volkwein, 1999, 2002). POD has been used by Higdon et al. (2008) for the dimensionality reduction of high-dimensional outputs. POD has been used extensively for the fluid dynamics problems (Zimmermann and Görtz, 2010; Mohebujjaman et al., 2017; Christensen et al., 1999; Gunzburger et al., 2017). Mostly, the coherent structure of a fluid flow has been studied by the POD approach (Sirovich, 1987; Christensen et al., 1999; Holmes et al., 2012; Kostova-Vassilevska and Oxberry, 2018). POD has the capability to decompose the spatio-temporal response of a system, by projecting the response on a basis that depends on the space domain. PCA (also known as POD) based PCE has been used by Blatman and Sudret (2013) for reducing the dimensionality of the stochastic diffusion problem. The POD based PCE model was also used by Raisee et al. (2015) for the stochastic heat diffusion problem. Recently, the Kriging model has been combined with the POD approach (Guo and Hesthaven, 2019; Mohammadi and Raisee, 2019). The ‘trend’ of the Kriging surrogate model was approximated with the PCE approach by Mohammadi and Raisee (2019). Furthermore, the number of terms in the PCE model was reduced using the POD approach. A time dependent problem has been investigated in (Guo and Hesthaven, 2019) using the POD and Gaussian process regression approaches.

The POD approach has been utilized in this chapter along with the PCE model to propose a new approach called POD-PCE approach. If we consider the PCE model, the PCE coefficients must be computed at each time-step for a dynamical system. Therefore, to reduce the computations of the PCE coefficients, the time-dependent stochastic response is projected on the POD modes, which depend on the time: therefore, the coefficients depend only on the random variables. The methodology developed in this chapter has been published by Jacquelin et al. (2019). The present research work is very close to the method developed by Guo and Hesthaven (2019), but was developed independently: the proposed methodology was obtained before being aware of their work.

4.2 Proper orthogonal decomposition

Proper orthogonal decomposition is mainly used for the identification of low order bases for a given set of snapshots (Sirovich, 1987). The orthogonal bases are selected corresponding to the dominating singular values of the snapshots. In our case, the time-dependent stochastic response quantities behave almost similarly. Recall the responses of a dynamical system for N initial samples $Y(\Xi, t) \in \mathbb{R}^{N \times n_t}$: each column of matrix Y contains the stochastic response at each time-step. Hence, a kind of correlation matrix for the stochastic response quantity (Berkooz et al., 1993) can be defined as:

$$C = Y(\Xi, t)^T Y(\Xi, t) \quad (4.1)$$

The above-mentioned correlation matrix C is often divided either by N (Feeny and Kappagantu, 1998; Feeny, 2002) or by $(N - 1)$ (Blatman and Sudret, 2013). However, dividing by a constant has no real influence on the use of the POD approach in this study. The orthogonal vectors are found from the eigenvalue decomposition of the correlation matrix C which should satisfy the following condition:

$$CV_i = \lambda_i V_i; \quad i = 1, \dots, n_t \quad (4.2)$$

where the V_i form an orthogonal basis and are called proper orthogonal modes (POM). The λ_i are the eigenvalues of the decomposition and represent a kind of energy (Chatterjee, 2000) related to the corresponding POM. The POM can also be obtained from the singular value decomposition (SVD) (Chatterjee, 2000) in the following way:

$$Y = V\Sigma U \quad (4.3)$$

where V is the matrix having all the POM and Σ is a diagonal matrix. Each column of matrix V is given by a POM. The diagonal terms of Σ represent the kind of energy involved in the corresponding POM. For the present work, the SVD as given in Equation 4.3 has been utilized.

The POM are sorted according to the decreasing magnitude of the corresponding eigenvalues λ_i . The POM are normalized here as follows:

$$\mathbf{V}_i = \frac{V_i}{\|V_i\|} \quad (4.4)$$

where $\|\bullet\|$ is the L2-norm of the corresponding vector.

Having the orthonormal POM, the uncertain response series can be represented by:

$$y(\xi, t) = \sum_{i=1}^{n_t} b_i(\xi) \mathbf{V}_i^T(t) \quad (4.5)$$

where the $b_i(\xi)$ are the random coefficients corresponding to the POM and need to be evaluated.

It should be noted from Equation 4.5 that the responses are projected on n_t orthonormal POM. However, in the present case $N < n_t$. Hence, the total energy is recovered only in the first N eigenvalues and the responses should be projected using only the first N POM, as only the N first eigenvalues are different from zero. Furthermore, it has been seen in the literature (Sirovich, 1987; Azeez and Vakakis, 2001) that only $n_b < N$ POM are usually required to keep a given value (E_{POD}) of the total POD energy. Therefore, using the reduced number of orthonormal POM, the random responses can be represented by:

$$y(\xi, t) \approx \sum_{i=1}^{n_b} b_i(\xi) \mathbf{V}_i^T(t) \quad (4.6)$$

and the energy criterion is given by:

$$\frac{\sum_{i=1}^{n_b} \lambda_i}{\sum_{i=1}^N \lambda_i} = E_{\text{POD}} \quad (4.7)$$

In the literature, E_{POD} is usually between 99% and 99.99% (Sirovich, 1987; Ma et al., 2000; Azeez and Vakakis, 2001).

4.3 POD-PCE model

It is noticeable from Equation 4.6 that the time-dependent uncertain response quantity is represented by the POM and the corresponding coefficients, decoupling the time-dependent behavior and the randomness. Indeed the POM are not dependent on the random variables while the coefficients $b_i(\xi)$ are only dependent on the random variables. Therefore, the coefficients in Equation 4.6 are random and can be estimated using the PCE model. The random coefficients can be expressed using the truncated PCE model (refer to Equation 2.4) as:

$$b_i(\xi) \approx \sum_{j=1}^n a_{j,i} \phi_j(\xi) \quad (4.8)$$

In the above-mentioned equation, $b_i(\xi)$ is considered as the response quantity for the PCE model, which needs to be computed. Considering the N initial samples for the response quantity $Y(\Xi, t)$, the time-dependent response in Equation 4.6 is represented by:

$$Y(\Xi, t) = \sum_{i=1}^{n_b} b_i(\Xi) \mathbf{V}_i^T(t) \quad (4.9)$$

where $b_i(\Xi) \in \mathbb{R}^{N \times 1}$ is the i -th POD coefficient vector and $\mathbf{V}_i(t) \in \mathbb{R}^{n_t \times 1}$ is the corresponding POM. Each coefficient $b_i(\Xi)$ is known and is computed by projecting the random response matrix $Y(\Xi, t)$ on the corresponding orthonormal POM:

$$b_i(\Xi) = Y(\Xi, t) \mathbf{V}_i(t); \quad i = 1, \dots, n_b \quad (4.10)$$

Having the random POD coefficients, the PCE coefficient vector $\mathbf{a}_i \in \mathbb{R}^{n \times 1}$ for the i -th POM can be computed using the OLS approach as described in section 2.4.3. The PCE coefficients are computed as:

$$\forall i = 1, \dots, n_b \quad \mathbf{a}_i = \left[\Phi^T(\Xi) \Phi^T(\Xi) \right]^{-1} \Phi^T(\Xi) b_i(\Xi) \quad (4.11)$$

Once the truncated PCE coefficients are computed, the combined POD-PCE model is given by:

$$y(\xi, t) \approx \sum_{i=1}^{n_b} \sum_{j=1}^n a_{j,i} \phi_j(\xi) \mathbf{V}_i(t) \quad (4.12)$$

The step by step procedure to construct a POD-PCE model is given in Algorithm 4.1.

Algorithm 4.1 Algorithm for the construction of POD-PCE model

- 1: **procedure** POD-PCE(N, d, p)
 - 2: Obtain N samples for the uncertain parameters by LHS
 - 3: **for** $i = 1 : N$ **do**
 - 4: $Y(\Xi_i, t) = \mathcal{M}(\Xi_i, t)$
 - 5: $\Phi_i = \Phi(\Xi_i)$ ▷ Refer to Equation 2.2 and Equation 2.9
 - 6: **end for**
 - 7: $(V, \lambda) = \text{eig}(C)$ or obtained with the SVD of Y ▷ Refer to Equation 4.2 or to Equation 4.3
 - 8: Obtain n_b by energy criterion ▷ Refer to Equation 4.7
 - 9: Obtain \mathbf{V}_i ▷ Refer to Equation 4.4
 - 10: **for** $i = 1 : n_b$ **do**
 - 11: Obtain POD coefficient $b_i(\Xi)$ ▷ Refer to Equation 4.10
 - 12: Obtain PCE coefficient vector \mathbf{a}_i ▷ Refer to Equation 4.11
 - 13: **end for**
 - 14: **end procedure**
-

4.4 Post-processing of POD-PCE results

In a similar way to the statical system (refer to section 2.4.4), the time-dependent statistical moments can be computed by post-processing the results obtained from the POD-PCE model. The time-dependent mean is given by:

$$\begin{aligned} \hat{\mu}(y(\xi, t)) &= \mathbb{E} \left[\sum_{i=1}^{n_b} b_i(\xi) \mathbf{V}_i(t) \right] \\ &= \sum_{i=1}^{n_b} \mathbb{E} \left[\sum_{j=1}^n a_{j,i} \phi_j(\xi) \right] \mathbf{V}_i(t) \\ &= \sum_{i=1}^{n_b} a_{1,i} \mathbf{V}_i(t) \end{aligned} \quad (4.13)$$

where $a_{1,i}$ is the PCE coefficient corresponding to the constant polynomial basis function for the i -th POM. Therefore, the time-dependent mean can be computed only with the PCE

Table 4.1: Parameters of the uniformly distributed random variables for the impact oscillator

| Random variable | Lower bound | Upper bound | Unit |
|-----------------|---------------------------------|---------------------------------|----------------------|
| m_p | $330 - 33\sqrt{3}$ | $330 + 33\sqrt{3}$ | g |
| k_c | $16 \times 10^3 - 1600\sqrt{3}$ | $16 \times 10^3 + 1600\sqrt{3}$ | MN m ^{-3/2} |
| v_0 | $-10 + \sqrt{3}$ | $-10 - \sqrt{3}$ | m s ⁻¹ |

coefficients and the POM. In a similar way, the time-dependent standard deviation can be computed as:

$$\begin{aligned}
\hat{\sigma}(y(\xi, t)) &= \sqrt{\text{var} \left[\sum_{i=1}^{n_b} b_i(\xi) \mathbf{V}_i(t) \right]} \\
&= \sqrt{\sum_{i=1}^{n_b} \text{var} [b_i(\xi)] \mathbf{V}_i^2(t) + 2 \sum_{1 \leq i_1 < i_2 \leq n_b} \text{cov} [b_{i_1}(\xi) b_{i_2}(\xi)] \mathbf{V}_{i_1}(t) \mathbf{V}_{i_2}(t)} \\
&= \sqrt{\sum_{i=1}^{n_b} \left[\sum_{j=2}^n a_{j,i}^2 \right] \mathbf{V}_i^2 + 2 \sum_{1 \leq i_1 < i_2 \leq n_b} \left[\sum_{j=2}^n a_{j,i_1} a_{j,i_2} \right] \mathbf{V}_{i_1}(t) \mathbf{V}_{i_2}(t)} \quad (4.14)
\end{aligned}$$

where $\text{var}[\bullet]$ and $\text{cov}[\bullet]$ represent the variance and covariance of the corresponding component. It is seen clearly from Equation 4.13 and Equation 4.14 that both the time-dependent statistical moments are computed from the POD-PCE model without any additional computational cost.

4.5 Application to an impact oscillator

In this section, UQ of the impact oscillator defined in section 3.5.4 has been investigated. UQ has been performed for projectile displacement y_p , projectile velocity \dot{y}_p and contact force f_c separately. The reference solution was computed by the MCS approach using LHS points. For the PCE and POD-PCE models, the initial responses were computed on the LHS points. The accuracy of the predicted result was measured using the mean relative error as given in Equation 3.11. The MCS samples N_{MCS} have been used for the prediction, therefore, the number of samples in Equation 3.11 must be replaced by N_{MCS} for the present case.

For the present investigation, m_p , k_c and v_0 were considered uniformly distributed independent random variables with a coefficient of variation equal to 0.1. The parameters of the distribution for all the random variables are given in Table 4.1. The structure mass $m_{st} = 60$ g and the damping ratio $\zeta_{st} = 0.5\%$ were considered constants for this oscillator.

The number of contacts is tuned by varying k_{st} , as done in the previous chapter. In the present study, two cases have been investigated: (i) single impact ($k_{st} = 240$ MN m⁻¹), (ii) multiple impact ($k_{st} = 2.4$ MN m⁻¹).

4.5.1 Case 1: Single impact oscillator

The impact oscillator is tuned here such that the contact between the structure and the projectile occurs only once in the total time period. A value of $k_{st} = 240$ MN m⁻¹ was

considered. The time domain for this system was $t \in [0 \text{ ms}, 1 \text{ ms}]$. The time integration was performed using the Matlab function *ode45* at a time-step of $\Delta t = 1 \text{ } \mu\text{s}$. As a result, $n_t = 1001$ time-steps can be found in the full time domain.

For the reference solution, the stochastic responses were computed by MCS using $N_{\text{MCS}} = 10^4$ model evaluations. On the other hand, the POD-PCE and the PCE models were constructed using much less model evaluations (N). Legendre polynomials were used for the PCE models with degree $p = 2$ and $p = 3$. $n = 10$ and $n = 20$ terms were found in the truncated PCE model for $p = 2$ and $p = 3$, respectively.

Influence of the number of model evaluations

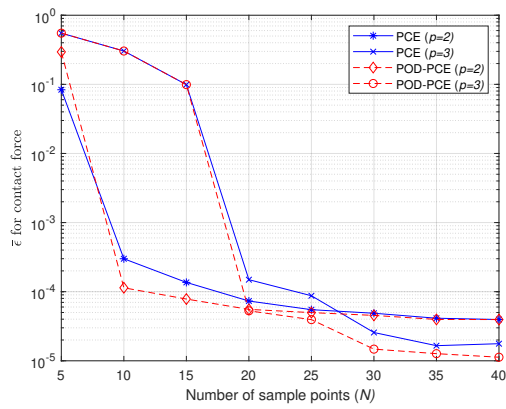
First of all, the influence of N on the accuracy was studied for both surrogate models. The evaluation of the mean relative errors for all the response quantities is shown in Figure 4.1. It is seen clearly that with the increase of N the mean relative error reduces for all the response quantities. It is noticeable that for a particular polynomial degree and a given N , $\bar{\epsilon}$ calculated with the PCE and with the POD-PCE models are almost the same. However, a slightly higher accuracy is noticed for the POD-PCE model for the contact force with $p = 3$ and the accuracy of PCE models for the projectile velocity is greater than the one for the POD-PCE models. These results suggest that the POD-PCE model and the PCE model give comparable results. An accurate identification of a model with n coefficients is generally possible only if $N \geq n$ (a rule of thumb is that N should be twice or three times the number of unknowns (n)). Accordingly, the responses with $p = 2$ are in good agreement with the MCS responses with $N \geq 10$ because $n = 10$ terms were found in the PCE polynomials, whereas $p = 3$ requires at least $N = 20$ model evaluation to compute the PCE coefficients accurately ($n = 20$). With $N = 20$ and $p = 3$, the surrogate model has almost the same accuracy as that with $p = 2$ and $N = 20$. Moreover, the increment of the accuracy beyond $N = 20$ samples is much less for all the response quantities. Therefore, a good accuracy is achieved using $N = 20$ for all responses. For that reason, all the stochastic responses for the single impact oscillator presented in the following are using $N = 20$.

Contact force

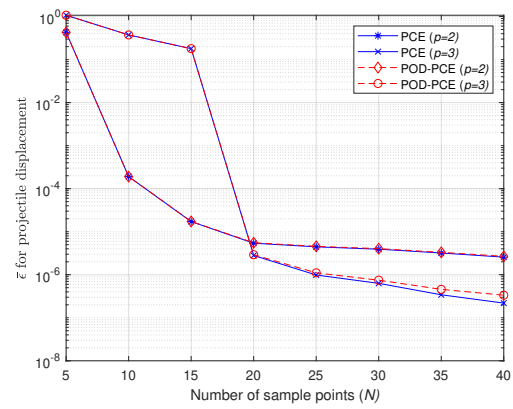
The time-dependent mean ($\hat{\mu}$) and standard deviation ($\hat{\sigma}$) of the contact force are plotted in Figure 4.2a and Figure 4.2b, respectively. It is seen that the contact between the structure and the projectile occurs only once during the total time period. The mean and the standard deviation are predicted quite well by both surrogates using $N = 20$. However, the PCE coefficient vector was computed at each time-step for the PCE model (refer Equation 2.10). Conversely, the time-dependent stochastic contact force was obtained with only $n_b = 5$ POM by the POD-PCE model. Hence, the PCE coefficient vector was computed only 5 times for the POD-PCE model which is much less than 1001. The total number of computed coefficients ($n_{\text{tot}} = n \times n_t$ for PCE and $n_{\text{tot}} = n \times n_b$ for POD-PCE) is shown in Table 4.2 for both surrogates, which is 200 times more for the PCE model as compared to the POD-PCE model. The time-dependent errors for the statistical moments were computed using the following expression:

$$\epsilon(t) = \frac{|\text{Mom}(Y_{\text{MCS}}) - \text{Mom}(Y_{\text{pred}})|}{\max |\text{Mom}(Y_{\text{MCS}})|} \quad (4.15)$$

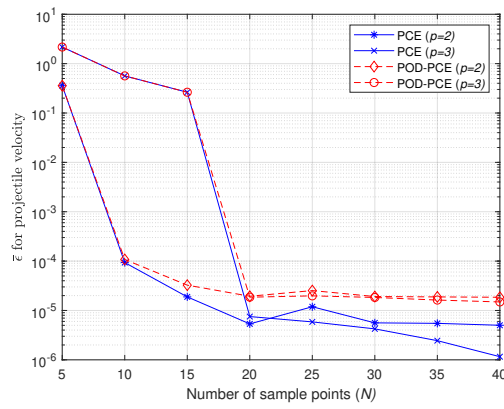
where $\text{Mom}(\bullet)$ is any statistical moment ($\hat{\mu}$ or $\hat{\sigma}$) of the corresponding response quantity.



(a) $\bar{\epsilon}$ for contact force



(b) $\bar{\epsilon}$ for projectile displacement



(c) $\bar{\epsilon}$ for projectile velocity

Figure 4.1: Evaluation of the mean relative errors of all the stochastic response quantities for the single impact oscillator

As the time-dependent contact force is zero beyond the contact end, the zoomed view of the time-dependent errors for $\hat{\mu}_{f_c}$ and $\hat{\sigma}_{f_c}$ of the contact force are shown in Figure 4.3a and Figure 4.3b, respectively. It is seen clearly that the magnitude of error in the prediction of $\hat{\sigma}_{f_c}$ is higher than that in the prediction of $\hat{\mu}_{f_c}$. It can also be seen that the time-dependent errors are sometimes almost zero by both surrogate models. It is noticeable that the time-dependent accuracy of $\hat{\sigma}$ is lower with $p = 2$ than with $p = 3$ in most of the times. The main reason is that the number of sample points is $2n$ with $p = 2$ and it is n with $p = 3$. As discussed above, the PCE coefficients can be computed much accurately if $N \geq 2n$. The overall accuracies of all the models were computed using Equation 3.11 and are listed in Table 4.2. It is noticeable that the errors predicted by the POD-PCE models are slightly less than the PCE models. Moreover, a good accuracy has been achieved by both surrogate models using few model evaluations, but the POD-PCE model requires only 5 POM to achieve a good accuracy.

Projectile displacement

The time-dependent statistical moments of projectile displacement y_p are shown in Figure 4.2c and Figure 4.2d using $N = 20$. Good agreement of the surrogate predicted results with the MCS results is noticed for both cases. The projectile displacement is linearly increasing with time beyond the contact region as the velocity is constant during that period (Figure 4.2e). As the PCE coefficients are time-dependent, the PCE coefficient vector was computed 1001 times. However, 99.99% of the energy was recovered using only 2 POM for the POD-PCE model. Hence, the PCE coefficients vector was computed only twice instead of 1001 times which ultimately led to compute only 0.2% coefficients for the POD-PCE models with respect to the PCE models. The time-dependent errors for both statistical moments were computed using Equation 4.15 and are plotted in Figure 4.3c and Figure 4.3d. Although the errors are very low, lower errors were predicted using $p = 3$ for both surrogates in predicting $\hat{\mu}$. Noticeably, the lower errors were obtained with $p = 2$ for $\hat{\sigma}$ as compared to $p = 3$ which suggest that, in the later case, the number of model evaluations should be increased to get better results. The overall accuracy of both surrogates is measured using the mean relative error which is listed in Table 4.2. It is noticeable from the table that almost the same accuracies have been achieved using both surrogates: the POD-PCE model requires only 2 POM to achieve such a high level of accuracy.

Projectile velocity

In a similar way to the previous two responses, the stochastic projectile velocity was also computed using the surrogate models. All the surrogate model parameters remain the same for the projectile velocity. Time-dependent mean and standard deviation of \dot{y}_p are shown in Figure 4.2e and Figure 4.2f, respectively. The prediction accuracies of all the surrogates are very high and are very close to each other. For the POD-PCE model, the 99.99% energy level is achieved using only $n_b = 3$ POM: only 3 PCE coefficient vectors were computed for the POD-PCE model instead of 1001 PCE coefficient vectors for the PCE model.

The time-dependent errors were also computed for the predicted stochastic velocity \dot{y}_p and are shown in Figure 4.3e and Figure 4.3f. As the projectile velocity beyond the contact period is constant, the time-dependent error is also constant in the region. Here the error for $\hat{\sigma}_{\dot{y}_p}$ by the POD-PCE model with $p = 3$ is much less as compared to the PCE model. As the rule of thumb, the required number of model evaluations for the PCE model might be greater

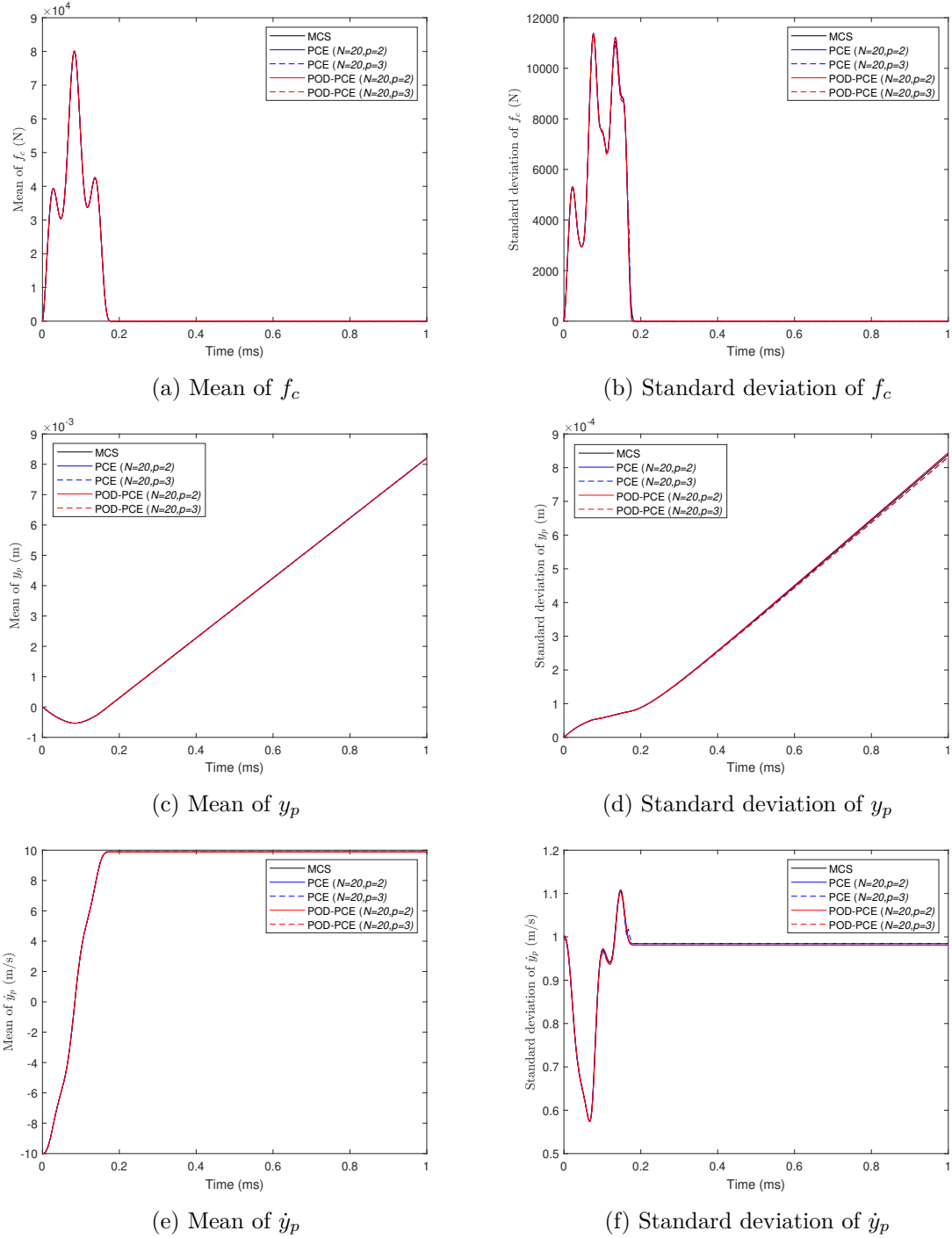
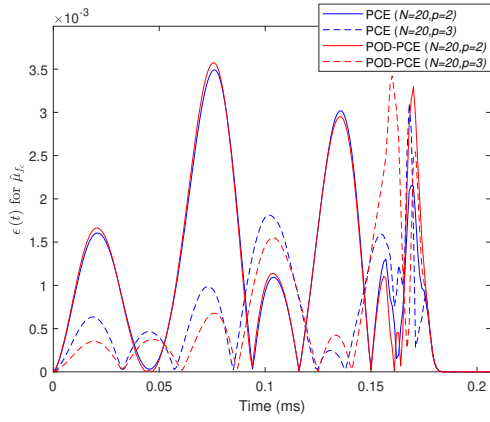
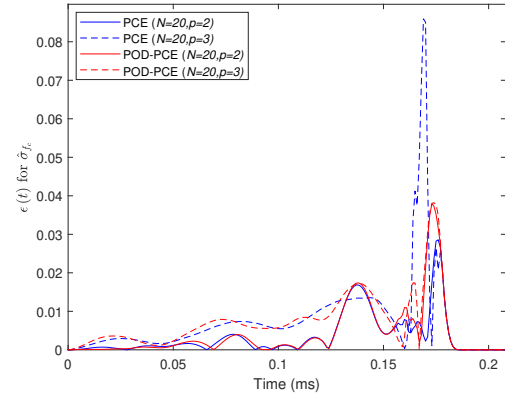


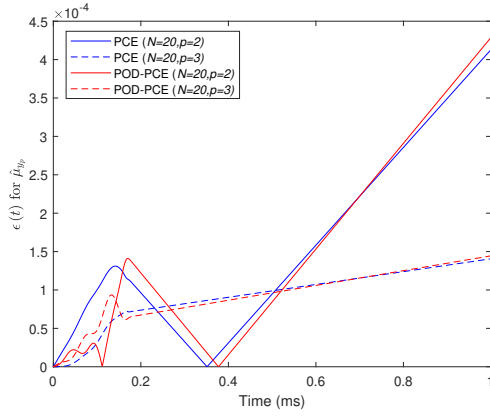
Figure 4.2: Time-dependent statistical moments of the stochastic response quantities for the single impact oscillator: MCS was performed using $N_{\text{MCS}} = 10^4$ model evaluations



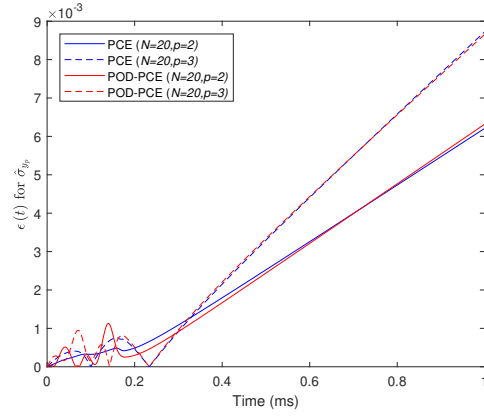
(a) Error for $\hat{\mu}$ of f_c (zoom view over the impact duration)



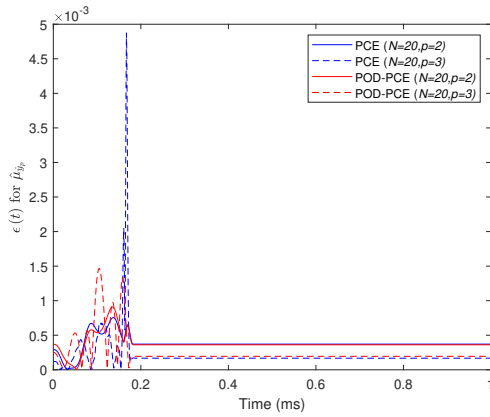
(b) Error for $\hat{\sigma}$ of f_c (zoom view over the impact duration)



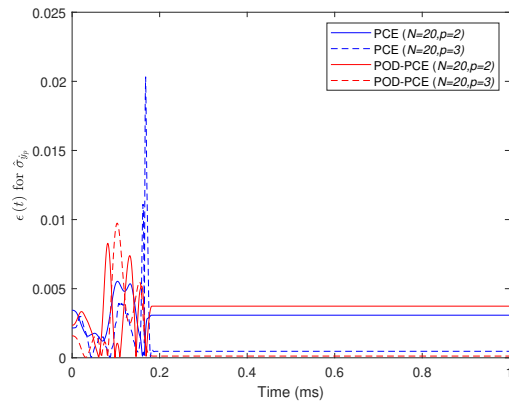
(c) Error for $\hat{\mu}$ of y_p



(d) Error for $\hat{\sigma}$ of y_p



(e) Error for $\hat{\mu}$ of \dot{y}_p



(f) Error for $\hat{\sigma}$ of \dot{y}_p

Figure 4.3: Time-dependent errors for the statistical moments of the stochastic responses of single impact oscillator

Table 4.2: Accuracy of different surrogate models in assessing the stochastic response quantities for the single impact oscillator by $N = 20$

| Method | p | Contact force | | | Projectile displacement | | | Projectile velocity | | |
|---------|-----|---------------|-----------|------------------------|-------------------------|-----------|-----------------------|---------------------|-----------|------------------------|
| | | n_b | n_{tot} | $\bar{\epsilon}$ | n_b | n_{tot} | $\bar{\epsilon}$ | n_b | n_{tot} | $\bar{\epsilon}$ |
| PCE | 2 | - | 10010 | 6.21×10^{-5} | - | 10010 | 5.41×10^{-6} | - | 10010 | 5.34×10^{-6} |
| PCE | 3 | - | 20020 | 14.90×10^{-5} | - | 20020 | 2.80×10^{-6} | - | 20020 | 7.52×10^{-6} |
| POD-PCE | 2 | 5 | 50 | 5.54×10^{-5} | 2 | 20 | 5.53×10^{-6} | 3 | 30 | 19.40×10^{-6} |
| POD-PCE | 3 | 5 | 100 | 5.28×10^{-5} | 2 | 40 | 2.92×10^{-6} | 3 | 60 | 18.50×10^{-6} |

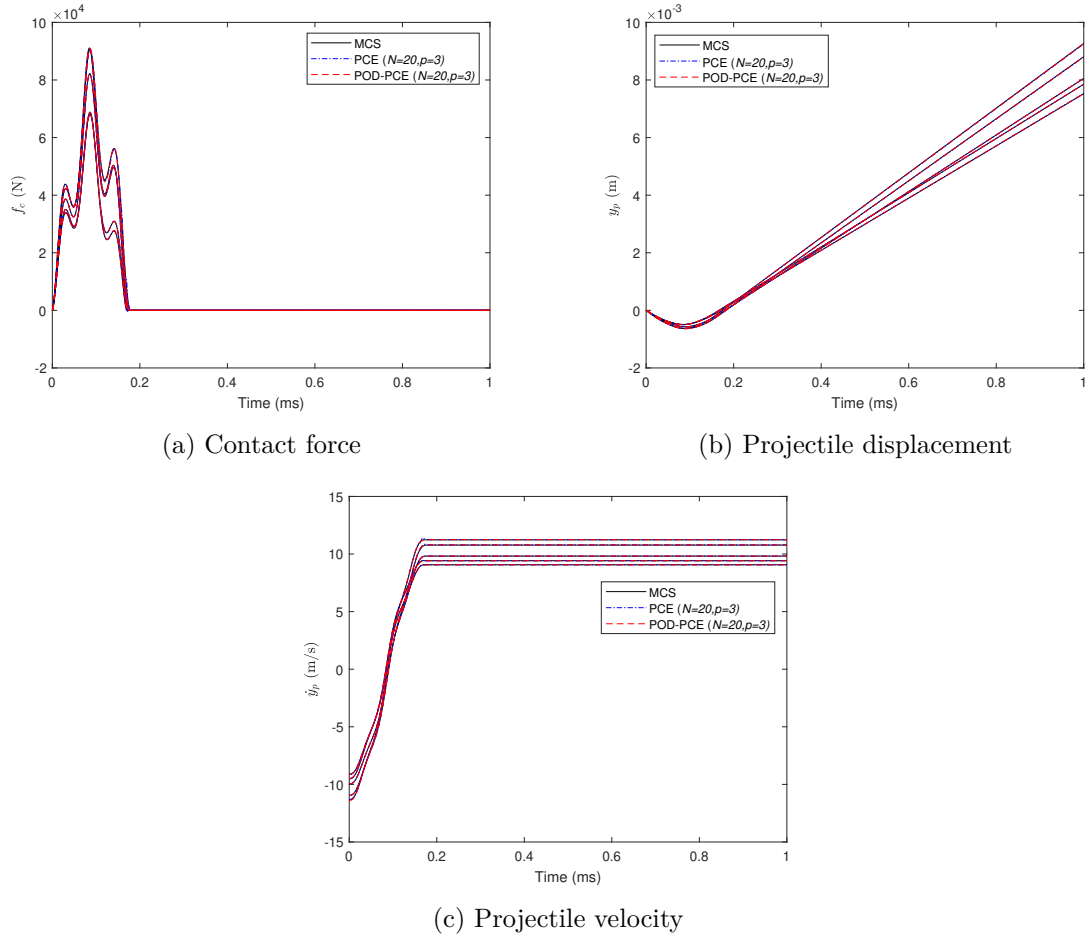


Figure 4.4: Comparison of responses for single impact oscillator at 5 samples: $m_p \in \{342.71, 292.84, 365.62, 310.35, 373.82\}g$, $k_c \in \{13.97, 13.87, 14.61, 14.23, 13.63\} \times 10^3 \text{MN m}^{-3/2}$, $v_0 \in \{-11.32, 9.51, 9.96, 9.11, 10.95\} \text{m s}^{-1}$

than the number of terms in the PCE basis for some time-steps. For that reason, the time-dependent error is higher with the PCE model at some time-steps. The overall accuracies of all the surrogates are listed in Table 4.2. The mean relative errors by all the surrogates are close to each other.

Comparison of predicted responses

To compare closely the surrogate models predicted results, the results obtained for 5 particular samples randomly drawn are plotted in Figure 4.4, as well as the results calculated from the identified surrogate models. It is seen that all the responses are predicted quite well by both surrogate models for all the 5 samples.

4.5.2 Case 2: Multiple impact oscillator

The same oscillator as defined in section 3.5.4 is considered here with $k_{st} = 2.4 \text{MN m}^{-1}$ such that multiple contacts occur between the structure and the projectile. The time domain

considered here is $t \in [0 \text{ ms}, 3 \text{ ms}]$ and the time integration was performed at a time-step of $\Delta t = 1 \mu\text{s}$. Consequently, $n_t = 3001$ number of time-steps can be found in the total time period.

Stochastic responses were computed considering the three input random variables as mentioned in Table 4.1. For the multiple impact oscillator, MCS was performed using 10^4 model evaluations on LHS points for all the stochastic response quantities.

Influence of the number of model evaluations

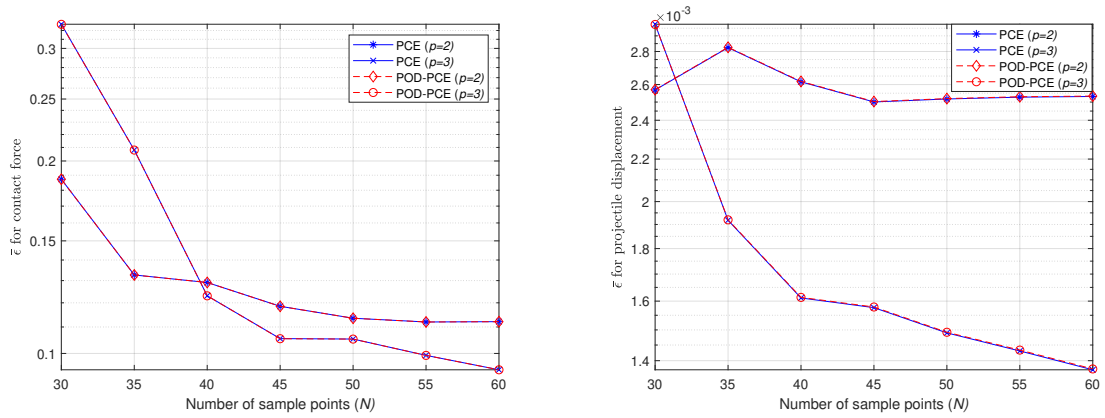
In a similar way to the single impact oscillator, the influence of the number of model evaluations was investigated for the surrogate models. The initial number of samples for the surrogate model was decided as $N = 30$. The relative error with respect to N for all the responses is shown in Figure 4.5. It is noticeable that the accuracy is increased with the increase of N for all the response quantities. The magnitude of error for the contact force is quite higher as compared to the other response quantities because the jumps during the contacts are quite high for the contact force and therefore, the non-smooth behavior is also quite high. Moreover, a quite good accuracy was achieved using $N = 50$ samples for all the response quantities. Hence, all the results presented in the following discussion used $N = 50$ samples.

Contact force

The first two statistical moments of the contact force are plotted in Figure 4.6a and Figure 4.6b. The surrogate models were constructed using $N = 50$ LHS points and predicted at $N_{\text{MCS}} = 10^4$ samples. It is seen clearly from the mean force that five contacts occur during the whole time period and the maximum contact force occurs during the second contact. Despite multiple impacts, the mean force was predicted quite well by both surrogates. However, tiny discrepancies are noticed in the standard deviation of f_c . The time-dependent errors were also computed for both surrogates. The time-dependent errors are shown in Figure 4.7a and Figure 4.7b for the impact duration only, as the force is always null after the impact. It is noticeable that the time-dependent errors are quite low during the first two contacts for both statistical moments. Furthermore, the errors started to increase more and more with time. Indeed, it is difficult to predict such non-smooth uncertain behavior with smooth functions (i.e. PCE). Both surrogates have predicted a lower error with $p = 3$ as compared to $p = 2$ for $\hat{\sigma}$. The level of overall accuracies is listed in Table 4.3. It is noticeable that a large number of POM ($n_b = 31$) was required to keep 99.99% of the POD energy with the retained POM: the PCE coefficient vector was therefore computed 31 times. However, it is much less than the computation of the coefficient vector for the PCE model, which is 3001 for the PCE model. Indeed n_{tot} for the POD-PCE model is approximately 1% of the time-dependent PCE model.

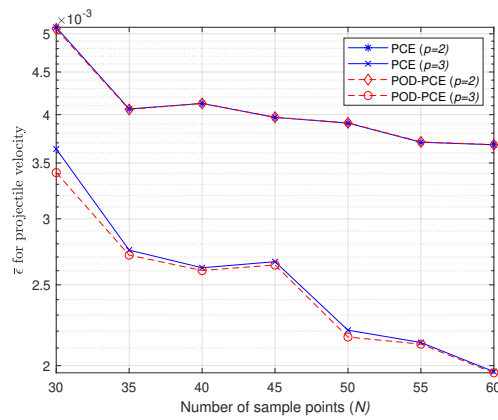
Projectile displacement

The stochastic projectile displacement y_p was computed by both surrogates using 50 LHS points. Time-dependent moments of y_p are shown in Figure 4.6c and Figure 4.6d. Both moments are predicted quite well using both surrogates. It is noticeable for the multiple impact oscillator also that the projectile velocity is constant beyond the contact region. As a result, the projectile displacement is linearly increasing with time. The time-dependent errors were computed for the moments of y_p and are plotted in Figure 4.7c and Figure 4.7d.



(a) $\bar{\epsilon}$ for contact force

(b) $\bar{\epsilon}$ for projectile displacement



(c) $\bar{\epsilon}$ for projectile velocity

Figure 4.5: Evaluation of mean relative error for all the stochastic response quantities of the multiple impact oscillator

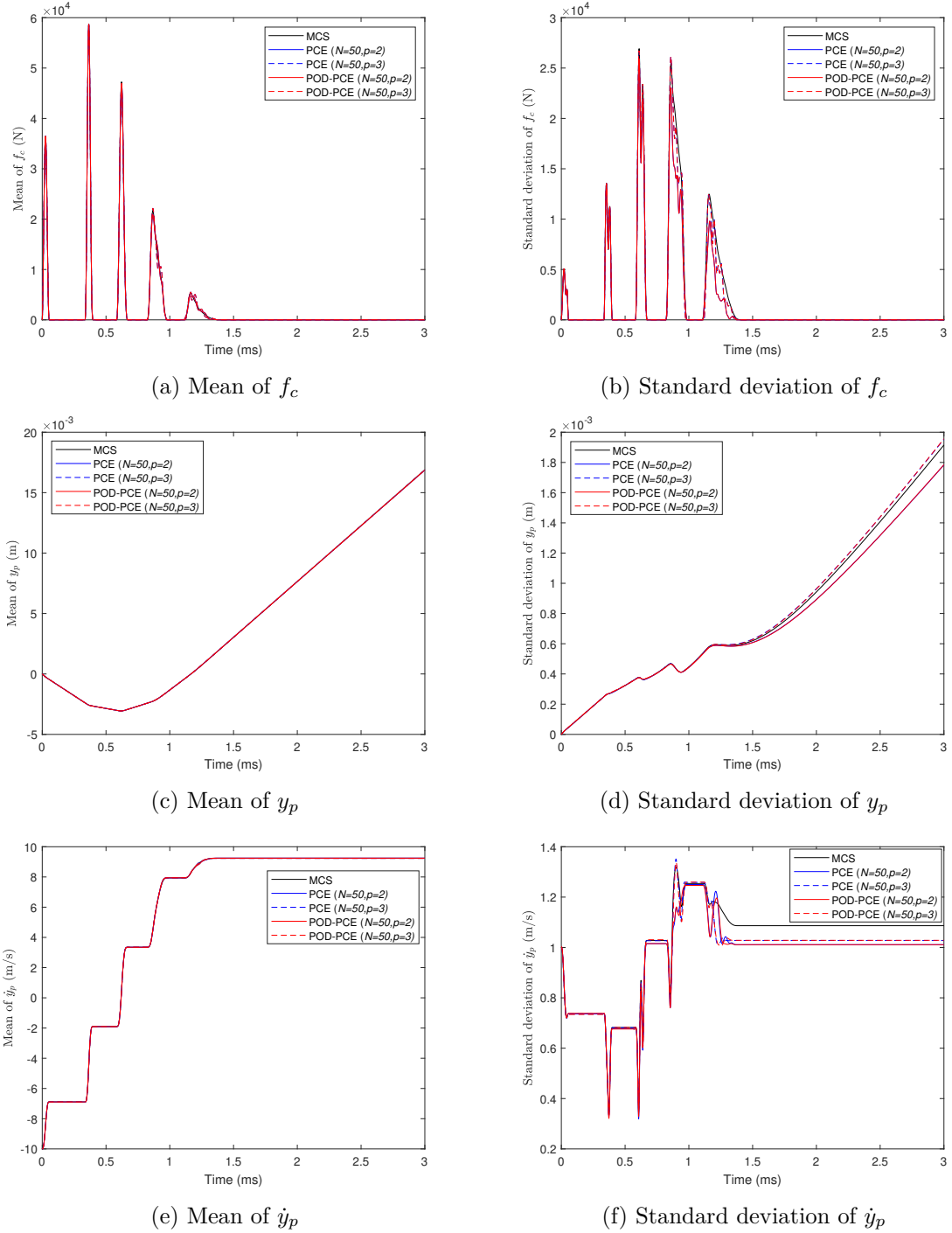
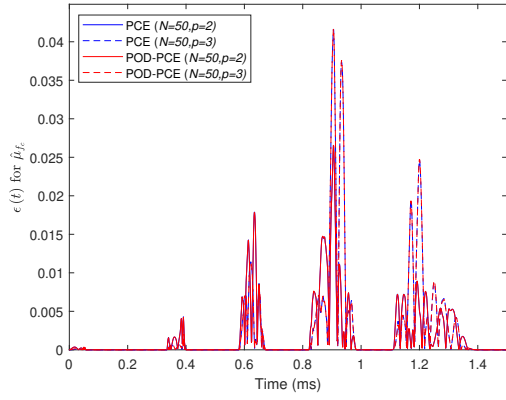
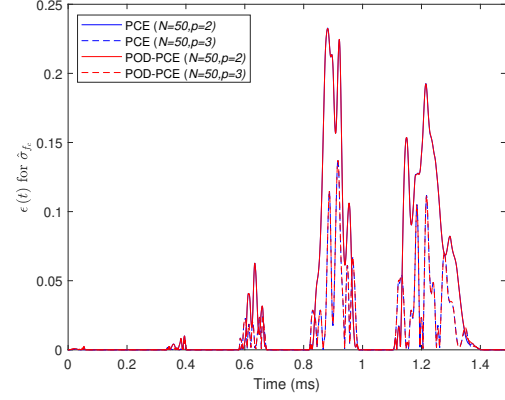


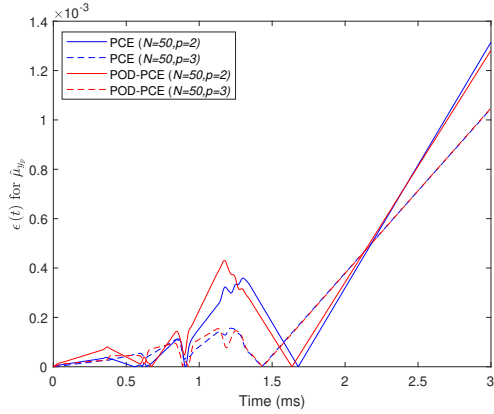
Figure 4.6: Time-dependent statistical moments of the stochastic responses for the multiple impact oscillator: MCS was performed using $N_{\text{MCS}} = 10^4$ model evaluations



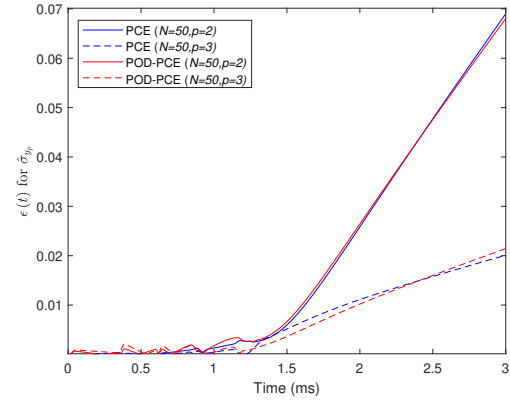
(a) Error for $\hat{\mu}$ of f_c (zoom view over the impact duration)



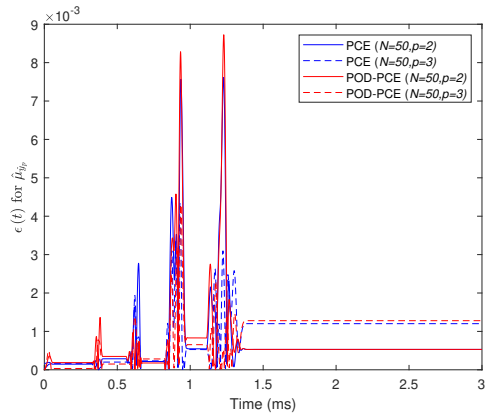
(b) Error for $\hat{\sigma}$ of f_c (zoom view over the impact duration)



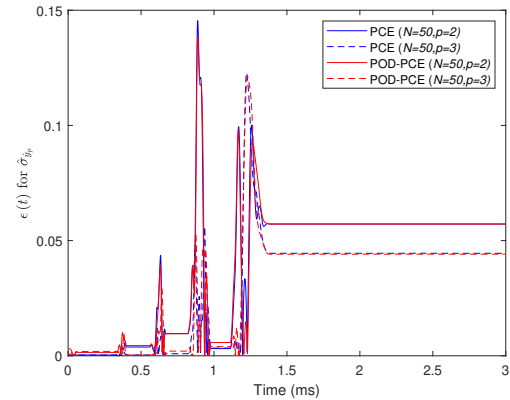
(c) Error for $\hat{\mu}$ of y_p



(d) Error for $\hat{\sigma}$ of y_p



(e) Error for $\hat{\mu}$ of \dot{y}_p



(f) Error for $\hat{\sigma}$ of \dot{y}_p

Figure 4.7: Time-dependent errors for the statistical moments of the responses of multiple impact oscillator

Table 4.3: Accuracy of different surrogate models in assessing the stochastic responses for the multiple impact oscillator using $N = 50$

| Method | p | Contact force | | | Projectile displacement | | | Projectile velocity | | |
|---------|-----|---------------|-----------|-----------------------|-------------------------|-----------|-----------------------|---------------------|-----------|-----------------------|
| | | n_b | n_{tot} | $\bar{\epsilon}$ | n_b | n_{tot} | $\bar{\epsilon}$ | n_b | n_{tot} | $\bar{\epsilon}$ |
| PCE | 2 | - | 30010 | 1.14×10^{-1} | - | 30010 | 2.52×10^{-3} | - | 30010 | 3.91×10^{-3} |
| PCE | 3 | - | 60020 | 1.05×10^{-1} | - | 60020 | 1.49×10^{-3} | - | 60020 | 2.21×10^{-3} |
| POD-PCE | 2 | 31 | 310 | 1.13×10^{-1} | 3 | 30 | 2.52×10^{-3} | 9 | 90 | 3.91×10^{-3} |
| POD-PCE | 3 | 31 | 620 | 1.05×10^{-1} | 3 | 60 | 1.49×10^{-3} | 9 | 180 | 2.16×10^{-3} |

In a similar way to the behavior of the responses, the errors are also linearly increasing with time. Slightly lower errors were predicted by both surrogate models with $p = 3$ because the number of model evaluations is greater than $2n$ for the present case. Here the time-dependent errors with a particular polynomial degree p by both surrogates are following almost the same path. Along with this, the overall accuracies of all the surrogates are listed in Table 4.3. It seems that both approaches have predicted exactly the same mean relative errors, however, the PCE coefficient vector was computed 3 times instead of 3001 for the POD-PCE model: it is the main advantage of the POD-PCE model.

Projectile velocity

UQ was also performed on the projectile velocity. The stochastic response behavior in time domain is shown in Figure 4.6e and Figure 4.6f. Jumps are noticed in the stochastic behavior of \dot{y}_p . However, the moments were predicted quite well by both surrogates using much less model evaluations as compared to MCS. The time-dependent errors for both statistical moments are plotted in Figure 4.7e and Figure 4.7f. Lower errors are noticed using $p = 3$ for both surrogate models during the contacts. The errors beyond the contact region are constant with time as both statistical moments are constant beyond the contact period. The overall accuracies are given in Table 4.3. It is noticeable that almost the same overall accuracies have been achieved by both surrogates. However, for the POD-PCE model, the PCE coefficient vector was computed only 9 times: it is 3001 for the PCE model.

Comparison of predicted responses

In a similar way to the single impact oscillator, the predicted stochastic responses by the surrogates were plotted and compared with the MCS results at the same 5 samples. The comparison is shown in Figure 4.8. It seems that the contact force is predicted quite well during the first two contacts, whereas it is very difficult to predict the contact forces towards the end of the contacts. $\bar{\epsilon}$ for these 5 samples was found to be the same as the $\bar{\epsilon}$ for the 10^4 samples. It is noticeable that for both methods some negative forces are predicted towards the end of the contacts, which is not physically correct. On the other hand, the projectile displacement and the projectile velocity are predicted quite well at the 5 samples using both approaches compared to the contact force.

Influence of the number of model evaluations for the contact force

To mitigate the issue of the non-physical forces, the contact force was predicted by both surrogates increasing the sample points. The predicted contact force along with the MCS results with $p = 3$ is shown in Figure 4.9 using different samples. Although the number of model evaluations was increased up to $N = 300$, it is seen from the figures that some negative forces are always present. One of the possible reasons for the failure is that the polynomial degree for the PCE model was sufficient. For that reason, the same study was performed by increasing the polynomial degree to $p = 5$. The contact force was predicted by the surrogates using $p = 5$ which is shown in Figure 4.10. It is seen from the figures that the negative forces are always predicted even with $N = 1000$ and $p = 5$.

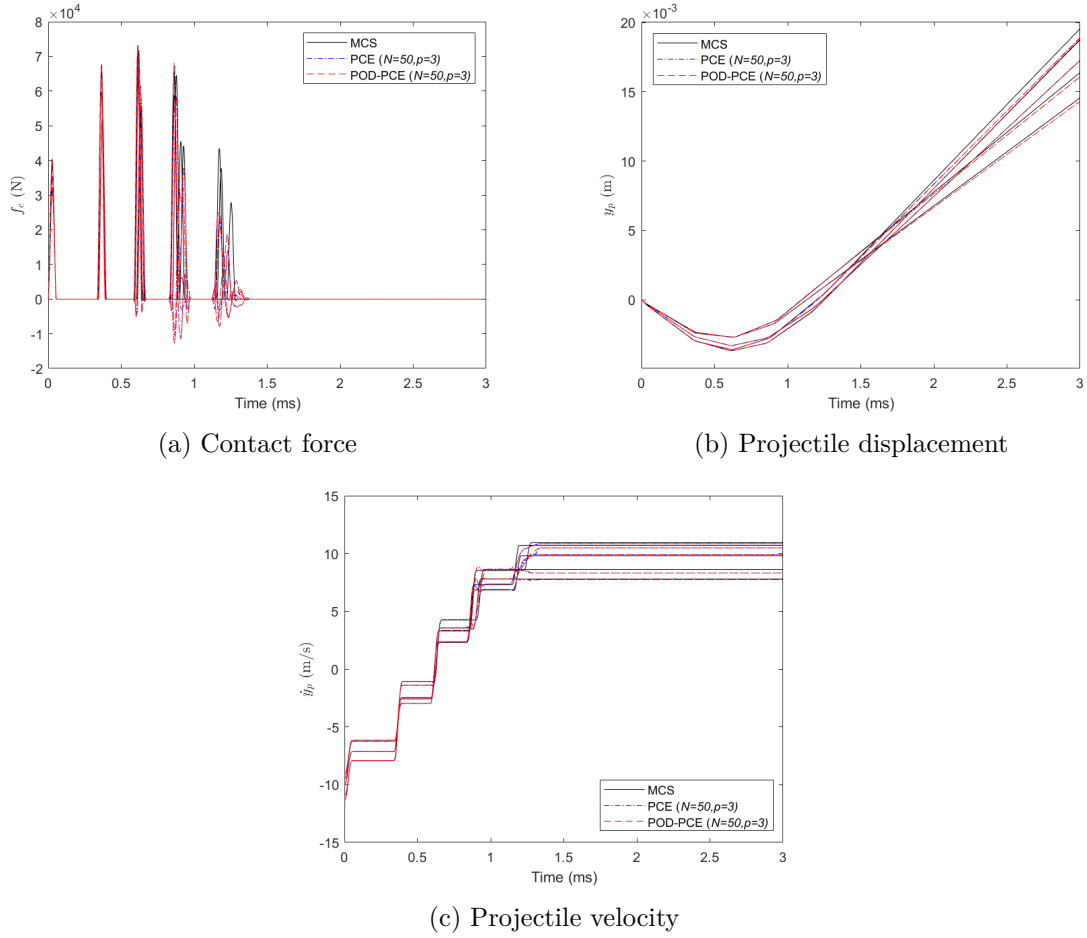


Figure 4.8: Comparison of responses for the multiple impact oscillator at 5 samples: $m_p \in \{342.71, 292.84, 365.62, 310.35, 373.82\}g$, $k_c \in \{13.97, 13.87, 14.61, 14.23, 13.63\} \times 10^3 \text{MN m}^{-3/2}$, $v_0 \in -\{11.32, 9.51, 9.96, 9.11, 10.95\} \text{m s}^{-1}$

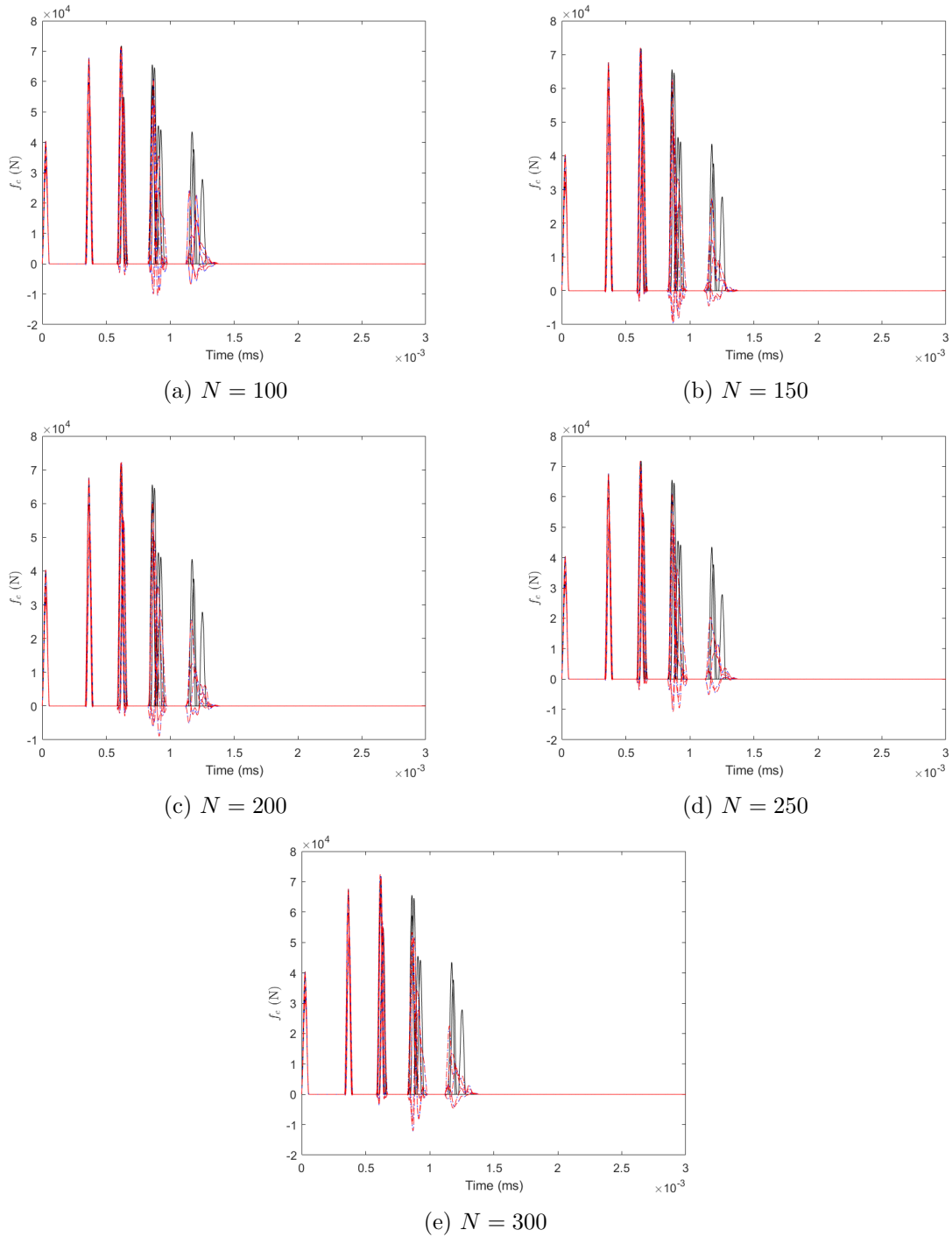


Figure 4.9: Prediction of contact force at 5 samples with $p = 3$: —MCS, - - -PCE, - - -POD-PCE

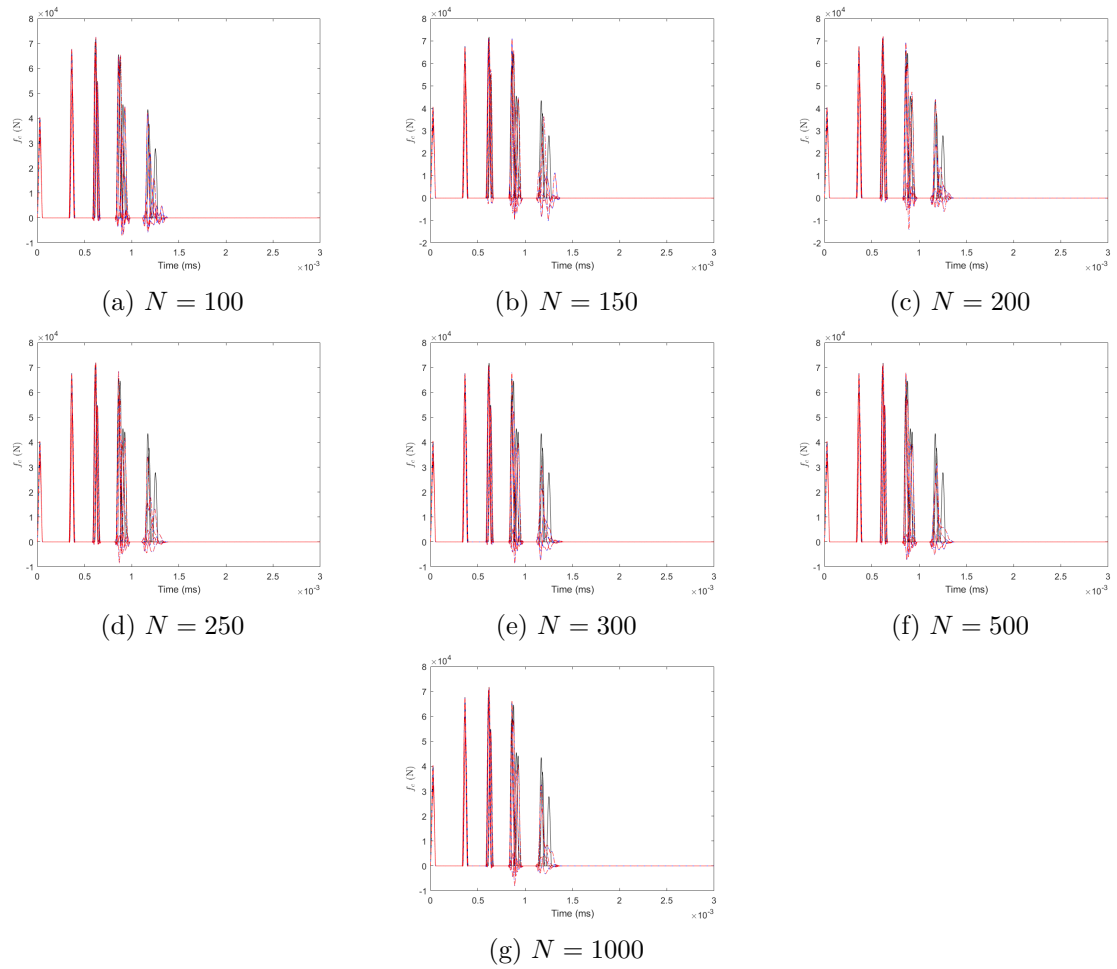


Figure 4.10: Prediction of contact force at 5 samples with $p = 5$: —MCS, - - -PCE, - - -POD-PCE

Influence of the polynomial degree for contact force

For further investigation, the surrogate models were constructed using $N = 1000$ samples with increasing the polynomial degree p . The polynomial degree was varying from $p = 6$ to $p = 15$ and all the predicted results are shown in Figure 4.11. It is seen that with such high number of model evaluations and large polynomial degree ($p = 10$), the non-physical negative force is eliminated for the third contact. However, the non-physical force is always predicted for the fourth and for the fifth contact period. Increasing the polynomial degree to $p = 14$ and $p = 15$, it is seen that a worst contact force is predicted by both surrogate models. Moreover, the issue of the non-physical negative force was minimized to some extent by increasing the PCE polynomial degree and the number of model evaluations. It should be noted from the figures (Figure 4.9, Figure 4.10 and Figure 4.11) that the non-physical negative forces predicted by both surrogate models are following almost the same paths: it implies the non-physical negative force was not governed by the POD approach instead, it was predicted due to the PCE model. Indeed, the behavior of the contact force is almost like Gibbs phenomenon (Gibbs, 1898, 1899) or the Runge phenomenon, and predicting the non-smooth behavior using a smooth function (PCE model) is always very challenging.

4.6 Concluding remarks

A non-intrusive surrogate model has been presented in this chapter for the impact dynamical systems, which is called POD-PCE model. The time-dependent non-smooth behavior and the randomness have been decoupled using the POD approach and the uncertain parameters have been propagated by the PCE model. The time-dependent UQ can be performed using the conventional PCE surrogate model, but in that case the PCE coefficient vector has to be computed at each time-step. For that reason, time-dependent uncertain response quantity was projected on the reduced POM such that a low number of PCE coefficients is required.

A nonlinear impact oscillator has been investigated for UQ with both different conditions, for which the sparse KNARX model has failed: a single contact between the structure and the projectile was considered first, and then multiple contacts between the structure and the projectile were considered. UQ was performed for the projectile displacement, the projectile velocity and the contact force. The stochastic responses were computed very well by the PCE and the POD-PCE models. For the POD-PCE model, the highest number of PCE coefficients identification was about 1% (for contact force of the multiple impact oscillator) with respect to the PCE model which is very less and at the same time, the predicted accuracies by the POD-PCE model were almost similar to the PCE results. Obviously, the time to compute the POM must be taken into account. However, as the number of model evaluations is low, the required number of POM is low as well. Therefore, the numerical cost to compute the POM is low, and the total numerical cost to obtain the POD-PCE model is much lower than the one to obtain the PCE model at each time step.

Although both surrogate models predicted good results, some non-physical contact forces were predicted for the multiple impact oscillator by both surrogate models at some sample points. To eliminate such error, the number of model evaluations and the PCE polynomial degree were increased. The non-physical contact force could be reduced to some extent with these modifications, however, it was not possible to eliminate fully the non-physical contact force prediction by both surrogate models. The non-physical forces may also be a consequence of over-fitting, and may be minimized using a sparse PCE model by selecting the important

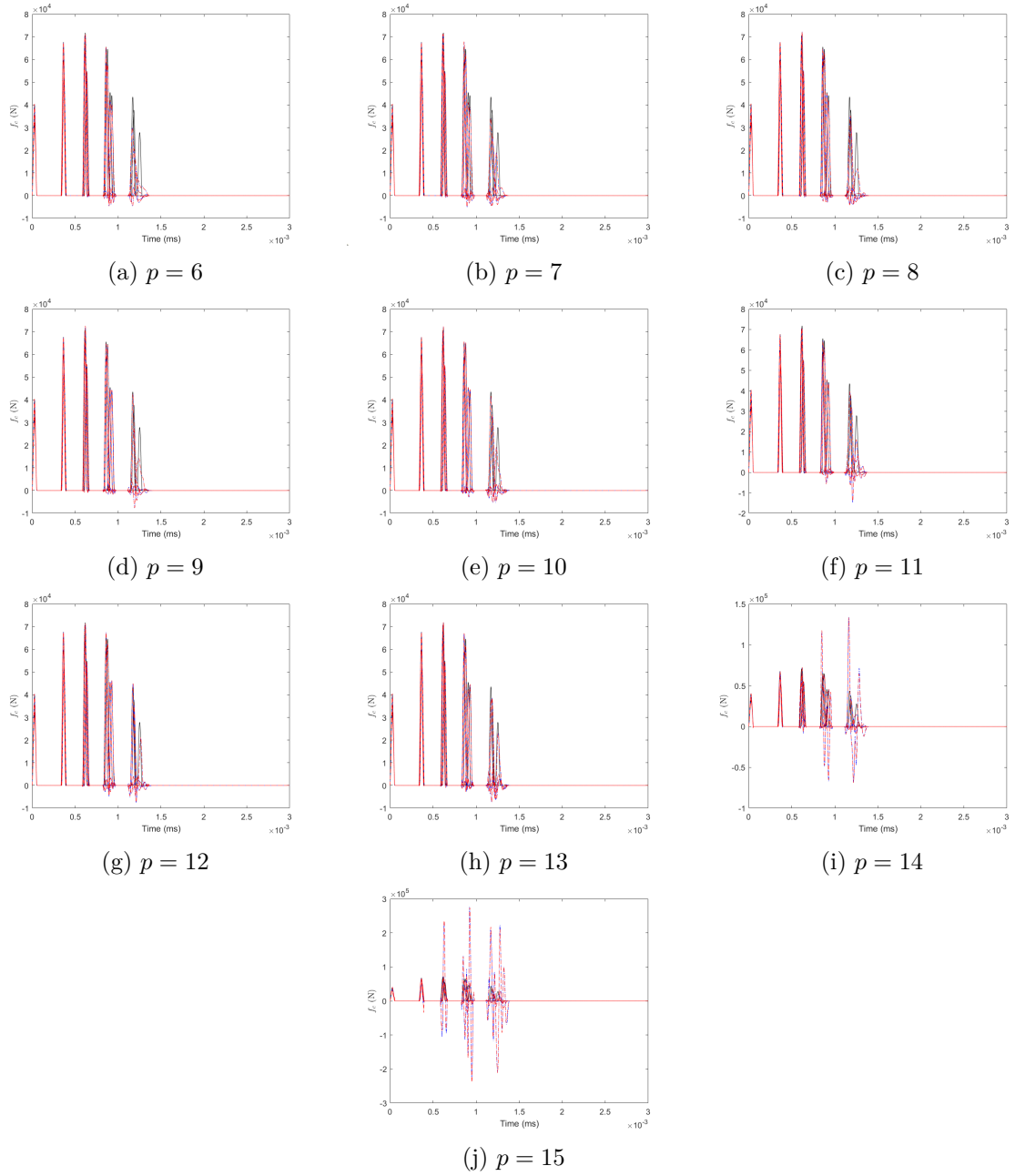


Figure 4.11: Prediction of contact force at 5 samples with $N = 1000$ for different polynomial degrees: —MCS, - · - · -PCE, - - -POD-PCE

terms in the PCE polynomial basis. Consequently, a sparse PCE approach is investigated in the next chapter.

Chapter 5

Variational Bayesian inference based sparse PCE model

5.1 Introduction

The POD-PCE model as introduced in chapter 4 is effective in propagating the uncertain parameters through an impact oscillator. Although the number of PCE coefficient estimation was much less for the POD-PCE model as compared to the PCE model, the number of coefficients would be high if a high polynomial degree is used. It has been often found in the literature that all the polynomials in the PCE model do not contribute to the response (Blatman and Sudret, 2008, 2011; Jakeman et al., 2015; Guo et al., 2018). Along with this, the use of all the polynomials may not be optimal for a response. Therefore, selecting the most appropriate terms in the PCE basis and computing the corresponding coefficients are the main challenges for formulating a sparse PCE model. Indeed, choosing the important terms in the PCE basis reduces the chances of overfitting and increases the accuracy of the PCE model. For that reason, a sparse PCE model is investigated in this chapter.

Several sparse PCE model have already been investigated in the past two decades (Blatman and Sudret, 2011; Jakeman et al., 2015; Cheng and Lu, 2018a; Shao et al., 2017; Abraham et al., 2018; Cheng et al., 2019). LARS (Efron et al., 2004) based sparse PCE model has been investigated by Blatman and Sudret (2011) which is available in the UQLab (Marelli and Sudret, 2014) open source software. A weighted regression approach was utilized by Jakeman et al. (2015) to introduce the sparsity in the PCE model. A weighted ℓ_1 minimization approach was used by Peng et al. (2014) and a gradient enhanced ℓ_1 minimization approach has been used by Peng et al. (2016) for the formulation of sparse PCE model. Some other ℓ_1 minimization approach for constructing a sparse PCE model can be found in the literature (Huan et al., 2018; Guo et al., 2018; Salehi et al., 2018). A homotopy algorithm D-MORPH (Li and Rabitz, 2010) based sparse PCE has been developed by Cheng and Lu (2018b) and a SVM based PCE model has been proposed by Cheng and Lu (2018a) for global sensitivity analysis. Although several approaches have been investigated by the researchers to obtain a sparse PCE model, less attention has been paid towards the investigation of a sparse PCE model by Bayesian approach. A Bayesian inference based on Kashyap information criterion has been utilized by Shao et al. (2017) for formulating a sparse PCE model and a different type of Bayesian inference based sparse PCE model has been investigated by Zhou et al. (2019b) allocating the priors for the important polynomials.

A Bayesian inference based PCE is formulated in this chapter. Firstly, the PCE coefficients are obtained with a variational Bayesian inference. Then, the important terms in the PCE basis are identified using the automatic relevance determination approach.

5.2 Bayesian inference in PCE model

Bayesian inference has already been proved efficient and accurate in assessing model parameters for dynamical systems (Green, 2015) and pattern recognition (Bishop and Tipping, 2000; Karagiannis and Lin, 2014). For that reason, the coefficients of the PCE are estimated here using a variational Bayesian (VB) inference (Drugowitsch, 2013; Fox and Roberts, 2012; Ghahramani and Beal, 2001; Attias, 1999). The generalized framework for the Bayesian inference and the VB inference in the context of PCE are described in the next sub-sections.

5.2.1 Generalized Bayesian inference in PCE

Recall the notations for the formulation of a PCE model. The uncertain parameters are given by ξ and the corresponding realizations are given by the experimental design matrix $\Xi \in \mathbb{R}^{N \times d}$. The PCE model is formulated in this chapter considering the time-independent QoI. The uncertain QoI is given by y and the QoI at the initial N realizations is given by a vector $Y \in \mathbb{R}^{N \times 1}$. Therefore, the truncated PCE model defined in Equation 2.4 can be represented as:

$$Y(\Xi) = \Phi(\Xi) a + \varepsilon_p \quad (5.1)$$

where ε_p is the residual due to the truncation and is supposed to be a zero mean Gaussian white noise with variance ς^{-1} . The coefficients vector $a \in \mathbb{R}^{n \times 1}$ is the only unknown in Equation 5.1. The coefficient are computed here through the Bayesian estimation using the available data i.e. $Y(\Xi)$ and $\Phi(\Xi)$. Therefore, having the observed responses $Y = \{Y_1, Y_2, \dots, Y_N\}^T$, the posterior distribution of the Bayesian model parameter is represented by Bayes' rule as:

$$p(\Theta|Y) = \frac{p(Y|\Phi, \Theta)p(\Theta)}{p(Y)} \quad (5.2)$$

where Θ is the Bayesian model parameter, which includes a : Θ will be defined below. In Equation 5.2, $p(Y|\Phi, \Theta)$ is the likelihood function which is computed based on the distribution of the parameters and $p(\Theta)$ is the prior distribution of the model parameters before noticing the available responses. $p(Y)$ is the marginal likelihood which is given by:

$$p(Y) = \int p(Y|\Phi, \Theta)p(\Theta) d\Theta \quad (5.3)$$

The main objective of the Bayesian framework is to assess the posterior distribution having a proper knowledge of the prior and the likelihood functions. The distribution of the likelihood function and the prior are formulated in Appendix B. Knowing that the Y_i are assumed to be normally distributed with mean $\Phi_i a$ and variance ς^{-1} in which Φ_i is the i -th row of the multivariate polynomial basis matrix. As indicated in Appendix B, the priors (a, ς) are supposed to have a normal-gamma distribution, then the prior is further parameterized by a hyper-prior α . According to the formulation, the Bayesian model parameter is given by $\Theta \in \{a, \varsigma, \alpha\}$. The dependency between all the Bayesian model parameters is shown

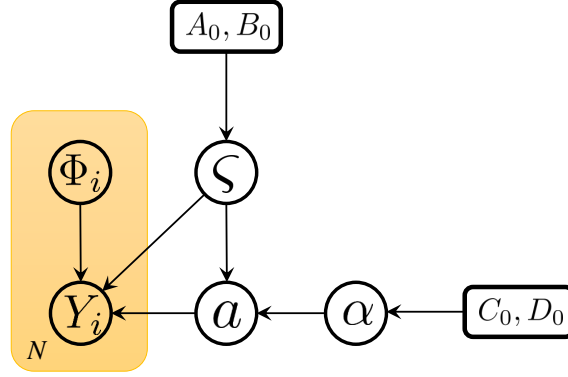


Figure 5.1: Graphical model representing the dependencies between the Bayesian model parameters

in Figure 5.1. A_0, B_0 are the distribution parameters for ς and C_0, D_0 are the distribution parameters for α .

Therefore, considering all the Bayesian model parameters, the joint distribution in Equation 5.2 can be represented by:

$$p(a, \varsigma, \alpha | Y) = \frac{p(Y | \Phi, a, \varsigma) p(a | \varsigma, \alpha) p(\varsigma) p(\alpha)}{p(Y)} \quad (5.4)$$

The parameters of the Bayesian model $\Theta \in \{a, \varsigma, \alpha\}$ can be computed having the proper knowledge of the priors and the hyper priors. In practice, we don't have proper knowledge about the priors. For that reason, several methods are available in the literature to assess the posterior approximately based on random sampling (Gilks et al., 1996; Sun, 2013), which require a large computational cost. To avoid the computational burden of the sampling based approaches, a VB inference has been utilized here to infer the posterior.

5.2.2 Variational Bayesian inference

The VB inference is utilized here to estimate the posterior of the Bayesian inference model parameter by a simple optimization process (Ghahramani and Beal, 2001). Indeed the objective is to find a distribution $q(\Theta)$ which is also known as variational distribution (Bishop, 2006) and a variational lower bound (VLB), which is constructed as:

$$\mathcal{L}[q(\Theta)] = \int_{\Theta} q(\Theta) \ln \frac{p(Y|\Theta)p(\Theta)}{q(\Theta)} d\Theta = \int_{\Theta} q(\Theta) \ln \frac{p(\Theta|Y)p(Y)}{q(\Theta)} d\Theta \quad (5.5)$$

$$= \int_{\Theta} q(\Theta) \ln \frac{p(\Theta|Y)}{q(\Theta)} d\Theta + \int_{\Theta} q(\Theta) \ln p(Y) d\Theta \quad (5.6)$$

It should be noted that according to the definition of a probability distribution, the integral of the variational distribution is $\int_{\Theta} q(\Theta) d\Theta = 1$. Therefore, Equation 5.6 is rearranged as:

$$\mathcal{L}[q(\Theta)] = \int_{\Theta} q(\Theta) \ln \frac{p(\Theta|Y)}{q(\Theta)} d\Theta + \ln p(Y) \quad (5.7)$$

and the log-marginal likelihood is given by:

$$\ln p(Y) = \mathcal{L}[q(\Theta)] + \text{KL}(q(\Theta) \parallel p(\Theta|Y)) \quad (5.8)$$

where $\text{KL}(\bullet)$ is the Kullback-Leibler (KL) divergence from q to p which has the form of:

$$\text{KL}(q(\Theta) \parallel p(\Theta|Y)) = - \int_{\Theta} q(\Theta) \ln \frac{p(\Theta|Y)}{q(\Theta)} d\Theta \quad (5.9)$$

The best estimate of $p(\Theta|Y)$ is reached for the variational distribution that minimizes the KL divergence (Bishop, 2006; Franck and Koutsourelakis, 2016). Accordingly, Equation 5.8 shows that the best estimate is found by maximizing the VLB \mathcal{L} with respect to $q(\Theta)$. For assessing the variational distribution, a flexible choice has been utilized using the mean field theory of physics (Parisi, 1988; Peierls, 1938), called factorized distribution. The factorized distribution is described in the next section in a detailed way.

5.2.3 Factorized distribution

The factorized distribution of $q(\Theta)$ is in the form of a product of the corresponding distribution (Bishop, 2006):

$$q(\Theta) = \prod_{i=1}^{N_e} q(\Theta_i) \quad (5.10)$$

where N_e is the number of subsets in the Bayesian model parameter Θ . Here, we have three parameters a, ς, α . However, due to the joint probability distribution, $q(\Theta)$ is subdivided in two components. Hence, Equation 5.10 can be represented by

$$q(\Theta) = q(a, \varsigma) q(\alpha) \quad (5.11)$$

This equation defines $N_e = 2$ for the present Bayesian formulation. For the forthcoming derivations, the notation given in Equation 5.10 will be used instead of Equation 5.11.

For the optimization, the lower bound \mathcal{L} is maximized with respect to each element of the distribution independently, while the other elements are kept fixed. Therefore, utilizing the factorized distribution (see Equation 5.10) in Equation 5.5, and considering that all the parameters are fixed except Θ_j , the VLB is represented as (Jacobs et al., 2018):

$$\mathcal{L}[q(\Theta)] = \int \prod_{i=1}^{N_e} q(\Theta_i) \left(\ln p(Y, \Theta) - \sum_{i=1}^{N_e} \ln q(\Theta_i) \right) d\Theta \quad (5.12)$$

$$\begin{aligned} &= \int q(\Theta_j) \left(\int \ln p(Y, \Theta) \prod_{i \neq j} q(\Theta_i) d\Theta_i \right) d\Theta_j \\ &\quad - \int q(\Theta_j) \ln q(\Theta_j) d\Theta_j + \text{const} \end{aligned} \quad (5.13)$$

$$= \int q(\Theta_j) \ln \tilde{p}(Y, \Theta_j) d\Theta_j - \int q(\Theta_j) \ln q(\Theta_j) d\Theta_j + \text{const} \quad (5.14)$$

where const denotes a constant term. In Equation 5.13, the terms $\sum_{i \neq j} \int q(\Theta_i) \ln q(\Theta_i) d\Theta_i$ are incorporated in the constant term. A new distribution term is defined in Equation 5.14 as $\tilde{p}(y, \Theta_j)$ (Bishop, 2006) which is given by:

$$\ln \tilde{p}(Y, \Theta_j) = \int \ln p(Y, \Theta) \prod_{i \neq j} q(\Theta_i) d\Theta_i = \mathbb{E}_{i \neq j} [\ln p(Y, \Theta)] \quad (5.15)$$

where $\mathbb{E}_{i \neq j} [\bullet]$ defines the expectation with respect to all the distribution $q(\Theta_i)$ for $i \neq j$.

The maximum of the VLB for the j -th distribution $q(\Theta_j)$, keeping others fixed at $q(\Theta_{i \neq j})$, is reached when $q(\Theta_j) = \tilde{p}(Y, \Theta_j)$ (Jacobs et al., 2018), which gives:

$$\ln q(\Theta_j) = \mathbb{E}_{i \neq j} [\ln p(Y, \Theta)] \quad (5.16)$$

Therefore, the optimal solution of the variational distribution is obtained utilizing Equation 5.16. The convergence of the lower bound is guaranteed (Boyd and Vandenberghe, 2004) because the VLB is convex with respect to each of its components $q(\Theta_i)$. The convergence of the VLB is described through the following equation, derived from Equation 5.5:

$$\mathcal{L}[q(\Theta)] = \int_{\Theta} q(\Theta) \ln p(Y, \Theta) d\Theta - \int_{\Theta} q(\Theta) \ln q(\Theta) d\Theta \quad (5.17)$$

$$= \mathbb{E}_{\Theta} [\ln p(Y, \Theta)] - \mathbb{E}_{\Theta} [\ln q(\Theta)] \quad (5.18)$$

5.3 Variational Bayesian inference based PCE

As already discussed in the previous section, the variational distribution is assessed by partitioning the Bayesian model parameters into two variational distributions. The two components of the variational distribution are maximized separately while the other one is fixed. Therefore, the variational posterior $q(a, \varsigma)$ is given by Equation 5.16, while keeping the other one $q(\alpha)$ fixed:

$$\ln q_k(a, \varsigma) = \ln p(Y|\Phi, a, \varsigma) + \mathbb{E}_{\alpha} [\ln p(a, \varsigma|\alpha)] \quad (5.19)$$

where $\ln p(Y|\Phi, a, \varsigma)$ and $\ln p(a, \varsigma|\alpha)$ are given by Equation B.3 and Equation B.6, respectively. In the following, k in the subscript represents the updated parameter for a particular iteration in the optimization process. Therefore, substituting those expressions and absorbing all the terms independent of a and ς in the constant, Equation 5.19 becomes:

$$\begin{aligned} \ln q_k(a, \varsigma) &= \left(\frac{n}{2} + A_0 - 1 + \frac{N}{2} \right) \ln \varsigma \\ &\quad - \frac{\varsigma}{2} \left(a^T \left(\mathbb{E}_{\alpha} [\Lambda] + \sum_{i=1}^N \Phi_i^T \Phi_i \right) a + \sum_{i=1}^N Y_i^2 - 2 \sum_{i=1}^N Y_i \Phi_i a + 2B_0 \right) \\ &\quad + \text{const} \end{aligned} \quad (5.20)$$

In a similar way to the Bayesian formulation, the VB inference for the $q(a, \varsigma)$ is also inferred by the conjugate normal-gamma distribution:

$$q_k(a, \varsigma) = \mathcal{N}(a|a_k, \varsigma^{-1}V_k) \text{Gam}(\varsigma|A_k, B_k) \quad (5.21)$$

Equation 5.21 is similar to Equation B.5. Therefore, by equating the coefficient of $-\frac{\varsigma}{2}a^T a$ between Equation 5.21 and Equation 5.20, the parameter V_k is computed as (Jacobs et al., 2018):

$$V_k^{-1} = \sum_{i=1}^N \Phi_i^T \Phi_i + \mathbb{E}_{\alpha} [\Lambda] \quad (5.22)$$

The expectation on α is calculated via the moment of the corresponding distribution (Bishop, 2006). Therefore, the second term in Equation 5.22 is computed by:

$$\mathbb{E}_{\alpha} [\Lambda] = \Lambda_k \quad (5.23)$$

Similarly, the updated coefficients of the PCE model are found by equating the coefficients of a between Equation 5.21 and Equation 5.20:

$$a_k = V_k \sum_{i=1}^N \Phi_i^T Y_i \quad (5.24)$$

The coefficients of the PCE model are thus updated at each iteration of the optimization process using Equation 5.24. However, to update the whole variational distribution $q(a, \varsigma)$, the parameters of the gamma distribution must be updated. Expanding the gamma distribution, Equation 5.21 can be represented as:

$$\begin{aligned} \ln q_k(a, \varsigma) &= \ln \mathcal{N}(a|a_k, \varsigma^{-1}V_k) - \frac{\varsigma}{2} \left(\sum_{i=1}^N Y_i^2 + 2B_0 - a_k^T V_k^{-1} a_k \right) \\ &+ \left(A_0 - 1 + \frac{N}{2} \right) \ln \varsigma \end{aligned} \quad (5.25)$$

Equating the coefficient of ' ς ' in Equation 5.25 and the PDF of a gamma distribution, the updated parameter of the gamma distribution B_k is determined by:

$$B_k = B_0 + \frac{1}{2} \left(\sum_{i=1}^N Y_i^2 - a_k^T V_k^{-1} a_k \right) \quad (5.26)$$

Similarly, equating the coefficients of ' $\ln \varsigma$ ', the other parameter of the gamma distribution A_k is calculated as:

$$A_k = A_0 + \frac{N}{2} \quad (5.27)$$

Therefore, the updated variational distribution of $q(a, \varsigma)$ is inferred by updating Equation 5.22, 5.24, 5.26 and 5.27 in each iteration of the optimization process.

In a similar way, the other part of the factorized distribution in Equation 5.11, $q(\alpha)$, is also maximized considering $q(a, \varsigma)$ is fixed. Consequently, according to Equation 5.16, the variational posterior for α is given by:

$$\ln q_k(\alpha) = \ln p(\alpha) + \mathbb{E}_{a, \varsigma} [\ln p(a, \varsigma|\alpha)] \quad (5.28)$$

$$= \sum_{j=1}^n (C_0 - 1) \ln \alpha_j - D_0 \alpha_j + \frac{1}{2} \ln \alpha_j - \frac{\alpha_j}{2} \mathbb{E}_{a, \varsigma} [\varsigma a_j^2] + \text{const} \quad (5.29)$$

In Equation 5.29, $p(\alpha)$ and $p(a, \varsigma|\alpha)$ are given by Equation B.8 and Equation B.6, respectively. All the terms independent of α are absorbed in the constant. For the conjugacy in the variational distribution, $q(\alpha)$ is inferred by the gamma distribution:

$$\ln q_k(\alpha) = \sum_{j=1}^n \ln \text{Gam}(\alpha_j | C_k, D_{k_j}) \quad (5.30)$$

By comparing the coefficients of $\ln \alpha_j$ and α_j between Equation 5.29 and 5.30, C_k and D_{k_j} are given by:

$$C_k = C_0 + \frac{1}{2} \quad (5.31)$$

$$D_{k_j} = D_0 + \frac{1}{2} \mathbb{E}_{a, \varsigma} [\varsigma a_j^2] \quad (5.32)$$

The expectation over the parameters (Bishop, 2006) is given by:

$$\mathbb{E}_{a,\varsigma} [\varsigma a_j^2] = a_{k_j}^2 \frac{A_k}{B_k} + V_{k_{jj}} \quad (5.33)$$

where k_{jj} in the subscript denotes the diagonal elements of the updated V_k matrix and k_j denotes the j -th coefficient in the updated PCE coefficient vector. The expectation on each of the element of the diagonal matrix Λ is given by:

$$\mathbb{E}_\alpha [\alpha_j] = \frac{C_k}{D_{k_j}} \quad (5.34)$$

Therefore, $\mathbb{E}_\alpha [\Lambda]$ is the matrix having all the diagonal elements computed by Equation 5.34:

$$\mathbb{E}_\alpha [\Lambda] = \text{diag} (\mathbb{E}_\alpha [\alpha]) \quad (5.35)$$

A_k and C_k are the constants which are not updated in the optimization procedure. In contrast, B_k and D_k are updated in each iteration. Consequently, B_k and D_k are initialized at their initial values B_0 and D_0 , respectively. Along with this, a_k and V_k are also initialized for the optimization problem:

$$a|_{k=0} = (\Phi^T \Phi)^{-1} \Phi^T y \quad (5.36)$$

$$V|_{k=0} = \Phi^T \Phi \quad (5.37)$$

The updated coefficient vector of the PCE model is computed by the updated coefficient according to Equation 5.24 at the end of the maximization of the variational distribution $q(\Theta)$. According to the above discussion, this maximization is performed in two segments through the factorized distribution. The numerical computation procedure of VLB using factorized distribution is described in Appendix C. The convergence of the maximization is noticed through computing the VLB. As a consequence, at step k , the relative evaluation of the VLB with respect to the previous step (in percent) is compared to a predefined threshold $T_{\mathcal{L}}$:

$$\frac{\mathcal{L}[q(\Theta)]_k - \mathcal{L}[q(\Theta)]_{k-1}}{\mathcal{L}[q(\Theta)]_{k-1}} \times 100 \leq T_{\mathcal{L}} \quad (5.38)$$

A pseudo-code of VB based PCE is given in Algorithm 5.1.

5.4 Sparse VB-PCE model by automatic relevance determination

The sparsity in the polynomial basis is introduced here using the Automatic Relevance Determination (ARD) (Burden et al., 2000; Li et al., 2002). It is noticed from Figure 5.1 that ‘ a ’ depends on the parameter ‘ α ’ in the Bayesian model. The hyper-priors are computed for each element of the polynomial basis and measure the effectiveness of each of the polynomials. Therefore, the hyper-priors are utilized here to select the important terms in the polynomial basis.

The ARD value (Wipf and Nagarajan, 2008; Jacobs et al., 2018) is defined by α_j^{-1} for the corresponding coefficient a_j in the PCE model. After performing the VB inference on the PCE

Algorithm 5.1 Pseudo-code for VB inference based PCE formulation

```

1: procedure VBPCe( $\Phi, Y, T_{\mathcal{L}}, A_0, B_0, C_0, D_0$ )
2:    $k = 0$ 
3:   Compute  $A_k$  and  $C_k$  ▷ Refer to Equation 5.27 and Equation 5.31
4:    $B_k = B_0$ 
5:    $D_k = D_0$ 
6:   for  $j = 1 : n$  do
7:     Compute  $\mathbb{E}_{\alpha} [\alpha_j]$  ▷ Refer to Equation 5.34
8:   end for
9:   Obtain matrix  $\mathbb{E}_{\alpha} [\Lambda]$  ▷ Refer to Equation 5.35
10:  while  $\frac{\mathcal{L}[q(\Theta)]_k - \mathcal{L}[q(\Theta)]_{k-1}}{\mathcal{L}[q(\Theta)]_{k-1}} \times 100 > T_{\mathcal{L}}$  do
11:     $k = k + 1$ 
12:    Compute  $V_k^{-1}$  ▷ Refer to Equation 5.22
13:    Update  $a_k$  ▷ Refer to Equation 5.24
14:    Update  $B_k$  ▷ Refer to Equation 5.26
15:    for  $j = 1 : n$  do
16:      Update  $\mathbb{E}_{a, \varsigma} [\varsigma a_j^2]$  ▷ Refer to Equation 5.33
17:      Update  $D_{k_j}$  ▷ Refer to Equation 5.32
18:      Update  $\mathbb{E}_{\alpha} [\alpha_j]_k$  ▷ Refer to Equation 5.34
19:    end for
20:    Obtain updated matrix  $\mathbb{E}_{\alpha} [\Lambda]_k = \text{diag} (\mathbb{E}_{\alpha} [\alpha])$  ▷ Refer to Equation 5.35
21:    Update VLB  $\mathcal{L} [q (\Theta)]_k$  ▷ Refer to Equation C.8
22:  end while
23:  return  $a, \mathcal{L} [q (\Theta)], \mathbb{E}_{\alpha} [\Lambda]$ 
24: end procedure

```

model, the maximized VLB along with all the model parameters are available. Therefore, the expectation of the hyper-prior as computed in Equation 5.34 is used to compute the ARD value for the model which has n terms in the polynomial basis matrix. Therefore, the ARD values for all the elements in the orthonormal polynomial basis are defined as:

$$\mathbf{A}^s = \text{diag} \left(\mathbb{E}_\alpha [\Lambda]^{-1} \right) \quad (5.39)$$

where $\text{diag} \left(\mathbb{E}_\alpha [\Lambda]^{-1} \right)$ is the vector of the diagonal terms of the inverse sparse matrix containing the hyper-priors for all the terms in the polynomial basis. The superscript s represents the number of iteration for the ARD value. Hence, after the convergence of the VB inference (using Algorithm 5.1), the ARD value is calculated and some terms from the orthonormal polynomial basis are discarded at this step based on the threshold value of ARD. The threshold value for ARD is evaluated as:

$$\ln T_A^s = \min (\ln A^s) + \frac{\max (\ln A^s) - \min (\ln A^s)}{e} \quad (5.40)$$

where the resolution of the threshold e can be tuned to increase or decrease the threshold value. If the ARD value for an orthonormal polynomial falls below the threshold value (i.e. $\ln A_i^s < \ln T_{A,i}^s; i = 1, 2, \dots, n$) then the orthonormal polynomial is discarded in the next iteration. Therefore, the number of terms in the orthonormal polynomial Φ^{s+1} is reduced in the next iteration ($n^{s+1} < n^s$).

Remark 5.1. *The ARD values for some terms, which are highly relevant for the PCE model, may be very high. Consequently, the threshold value is also high. Therefore, a less relevant term (but relevant for the PCE model) with low ARD value may be discarded which results in a less accurate PCE model. For that reason, the threshold value is obtained here using the natural logarithm of the ARD value to discriminate between the less sensitive terms.*

The final sparse PCE model is selected by calling the VB framework iteratively. Therefore, the number of terms in the polynomial is reduced in each iteration and the iteration process continues until one term remains in the orthonormal polynomial ($n = 1$). The final selection is made by utilizing the VLB value associated with a particular sparse PCE model. The chosen final sparse PCE model is the one which has the highest value of VLB $\mathcal{L}(\Theta)^s$:

$$\Phi^* = \Phi^{s^*} \quad (5.41)$$

where s^* is the index having the maximum value of the VLB. The accuracy of the VB model is fully dependent on the VLB. Therefore, choosing the sparse PCE model based on the VLB value selects the most important terms in the orthonormal polynomial basis. The proposed model is called sparse VB inference based PCE (SVB-PCE) model. A pseudo-code for the SVB-PCE model is given in Algorithm 5.2.

5.5 Proposed UQ framework by SVB-PCE model

The proposed framework utilizes Algorithm 5.1 and Algorithm 5.2 for UQ. The important terms in the orthonormal polynomial basis are selected using the VB algorithm based on ARD. The PCE coefficients are also computed within the SVB framework, which is an advantage of the method. The first two statistical moments (i.e. mean and standard deviation) can be

Algorithm 5.2 Pseudo-code for the SVB-PCE model

```

1: procedure SVB-PCE( $\Phi, Y, e$ )
2:    $s = 0$ 
3:    $\Phi^0 = \Phi$ 
4:   while  $n > 1$  do                                      $\triangleright$  Perform iteration until 1 term remains
5:      $s = s + 1$ 
6:      $(a^s, \mathcal{L}[q(\Theta)]^s, \mathbb{E}_\alpha[\Lambda]^s) = \text{VBPCe}(\Phi^{s-1}, Y, T_{\mathcal{L}}, A_0, B_0, C_0, D_0)$     $\triangleright$  Refer to
       Algorithm 5.1
7:     Compute  $A^s$                                           $\triangleright$  Refer to Equation 5.39
8:     Calculate  $\ln T_{\Lambda}^s$                               $\triangleright$  Refer to Equation 5.40
9:      $\Phi^- = \emptyset$ 
10:    for  $j = 1 : n$  do
11:      if  $\ln A^s \leq \ln T_{\Lambda}^s$  then
12:         $\Phi^- = \Phi^- \cup \Phi_j$ 
13:      end if
14:    end for
15:     $\Phi^s = \Phi^{s-1} \setminus \Phi^-$ 
16:     $n = \text{card}(\Phi^s)$ 
17:  end while
18:   $s^* = \text{ind}(\max \mathcal{L}(\Theta)^s)$ 
19:   $\Phi^* = \Phi^{s^*}$ 
20:   $\mathbf{a}^* = a^{s^*}$ 
21:   $\text{ind}^* = \text{ind}(\text{card}(\Phi^*))$                               $\triangleright$  Get the index of final set
22:  return  $\mathbf{a}^*, \Phi^*, \text{ind}^*$ 
23: end procedure

```

computed efficiently by post-processing the PCE coefficients as given in Equation 2.14 and Equation 2.15.

The procedure of UQ using the SVB-PCE model is shown in Figure 5.2 which requires the responses and the orthonormal polynomial bases at some initial sample points. LHS is used here for the generation of the initial samples.

For the implementation of the SVB framework within PCE, some initial parameters of the Bayesian model are required. The parameters of the hyper-prior are chosen, as proposed by Jacobs et al. (2018), as $A_0 = C_0 = 1 \times 10^{-2}$ and $B_0 = D_0 = 1 \times 10^{-4}$. A threshold value for the VLB \mathcal{L} must be initialized in Algorithm 5.1. The threshold $T_{\mathcal{L}}$ for the change in the VLB with respect to the previous iteration is decided as 0.001%. The resolution for computing the threshold of ARD value is chosen as $e = 1000$ which was proposed by Jacobs et al. (2018).

5.6 UQ of test functions by SVB-PCE model

In this section, the SVB-PCE model has been utilized for UQ of two mathematical functions. UQ is made by estimating the first two statistical moments and the PDF of the stochastic response. Both examples are also solved by the sparse PCE model based on the LARS method (Blatman and Sudret, 2011): it is called LARS-PCE and was obtained with the UQLab software (Marelli and Sudret, 2014).

The accuracy of the results obtained by the surrogate models has been measured with respect to the MCS results and it has been computed using a percentage error (PE):

$$PE = \sqrt{\frac{\sum_{N_{\text{MCS}}} (Y - \hat{Y})^2}{\sum_{N_{\text{MCS}}} Y^2}} \times 100 \quad (5.42)$$

where Y is the MCS solution and \hat{Y} is the solution predicted either by SVB-PCE or by LARS-PCE. N_{MCS} is the number of prediction samples.

The computational cost is affected by the total number of terms in the PCE orthonormal polynomial basis. For that reason, a sparsity index (SI) has been computed. The SI is given by the ratio of the number of terms detected by the sparse algorithms, to the number of terms for the full PCE model: a low percentage of SI indicates a low computational cost. A low SI reduces the chances of over-fitting using a limited number of model evaluations which ultimately increases the accuracy of the PCE model. The computational cost is also affected by the number of model evaluations. An accurate result with a low number of model evaluations indicates a computationally efficient surrogate model.

5.6.1 Ishigami function

The Ishigami function is a benchmark mathematical functions which has been used many times in the literature (Blatman and Sudret, 2010b; Cheng and Lu, 2018b): it is given by:

$$y = \sin \xi_1 + 7 \sin^2 \xi_2 + 0.1 \xi_3^4 \sin \xi_1 \quad (5.43)$$

where ξ_1 , ξ_2 and ξ_3 are statistically independent random variables uniformly distributed in $[-\pi, \pi]$. It is noticed from Equation 5.43 that the function is nonlinear. The MCS was performed on $N_{\text{MCS}} = 10^5$ samples to get the reference solution.

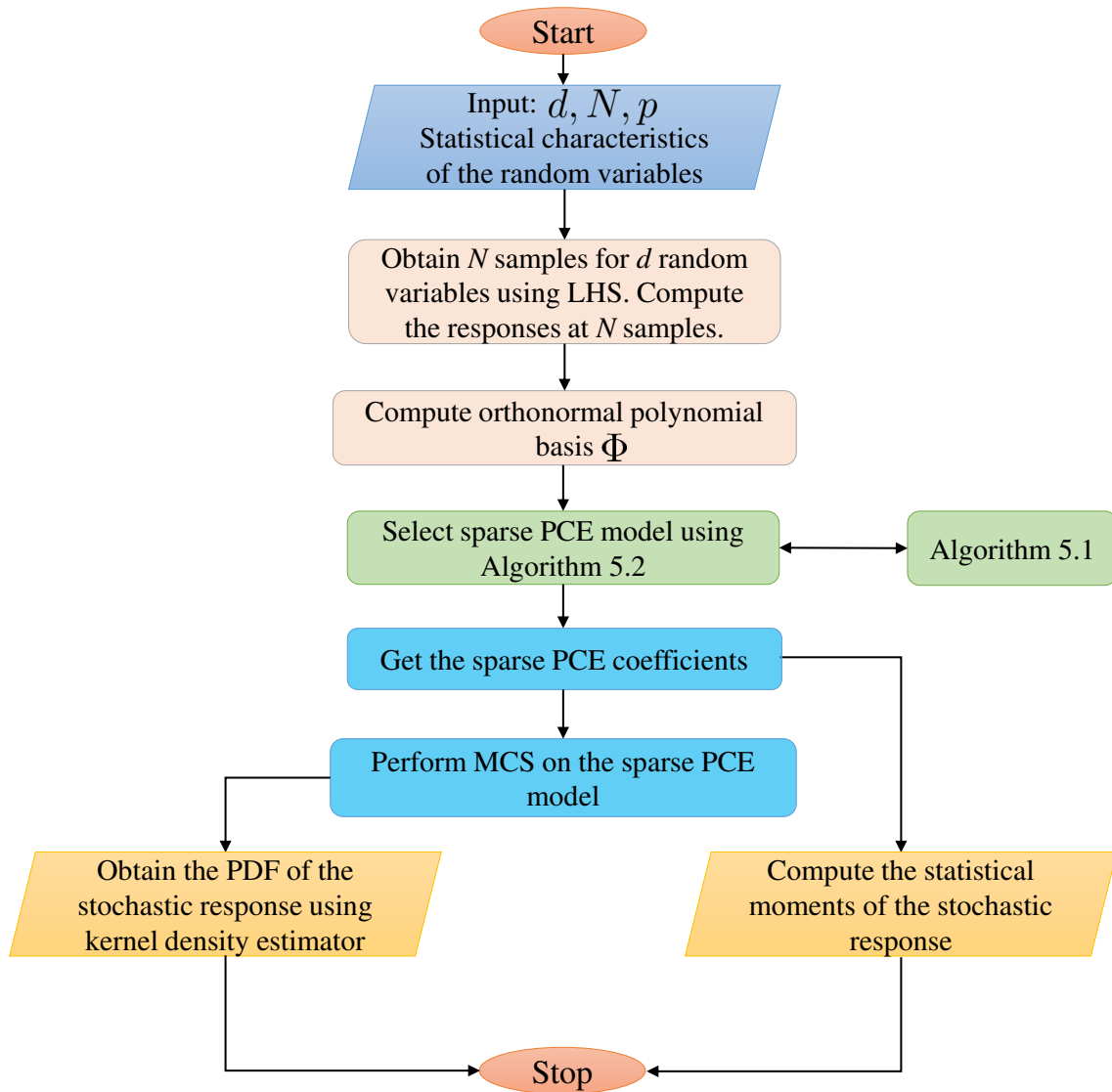


Figure 5.2: Flowchart of the SVB-PCE for UQ

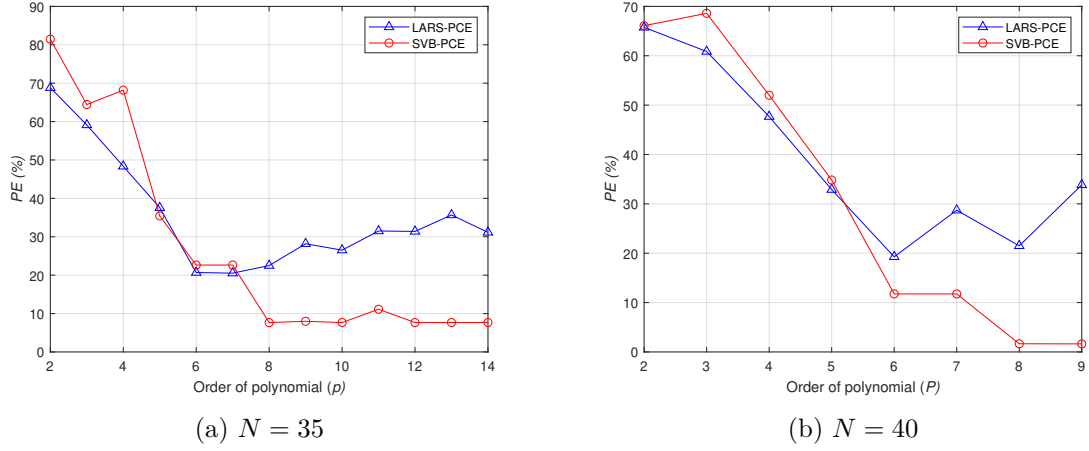


Figure 5.3: Evaluation of PE for different polynomial degrees by the SVB-PCE and the LARS-PCE models

Table 5.1: Statistical moments of the response for the Ishigami function using $N = 40$ and $p = 8$

| Method | $\hat{\mu}_y$ | PE(%) | $\hat{\sigma}_y$ | PE(%) |
|----------|---------------|-------|------------------|-------|
| MCS | 3.4917 | - | 3.7206 | - |
| LARS-PCE | 3.4312 | 1.73 | 3.2768 | 11.93 |
| SVB-PCE | 3.4908 | 0.03 | 3.7198 | 0.02 |

For the surrogate models, the SVB-PCE and the LARS-PCE models were identified with different polynomial degrees p . Legendre polynomials were used for all the random variables. The percentage error (PE) for different polynomials degrees is plotted in Figure 5.3 using $N = 35$ and $N = 40$ LHS points separately. It is seen that with the increase of the polynomial degree, PE for the SVB-PCE reduces rapidly as compared to the LARS-PCE model. For both $N = 35$ and $N = 40$ samples, the SVB-PCE model predicted good results using polynomial degree $p = 8$. On the other hand, PE of the LARS-PCE model is higher for most of the polynomial degrees.

As the PE computed with $p = 8$ was quite low, it was used for the further study of the Ishigami function. Therefore, the PE was computed by increasing the sample points starting from $N = 20$ with the increase of 5 samples fixing $p = 8$: this process continued until PE less than 2% was obtained. The evaluation of PE for both surrogates with N is plotted in Figure 5.4. It is noticeable that $PE \leq 2\%$ was obtained by the SVB-PCE model using only $N = 40$ samples, whereas, the LARS-PCE model requires $N = 70$ samples.

The PDF was obtained using $N = 40$ and $p = 8$ for both surrogates. The PDF plots using all the approaches are shown in Figure 5.5. It is seen clearly that the PDF obtained by the SVB-PCE model is closer to the MCS result as compared to the LARS-PCE result.

The mean ($\hat{\mu}_y$) and the standard deviation ($\hat{\sigma}_y$) were obtained by post-processing the PCE coefficients and are presented in Table 5.1. The PE for the surrogate predicted moments were computed using Equation 5.42 and are also reported in Table 5.1. It is seen from the table that the most accurate results were obtained by the SVB-PCE model.

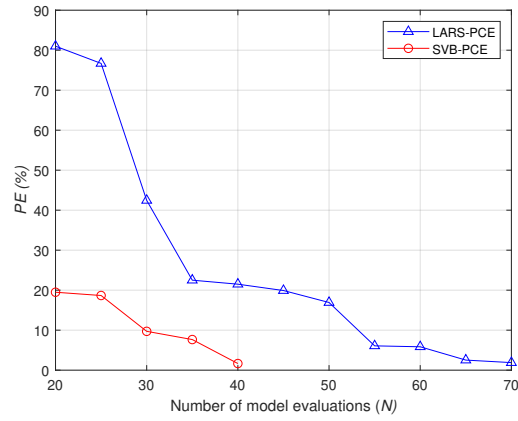


Figure 5.4: Evaluation of PE with the increase of sample points for the Ishigami function with $p = 8$

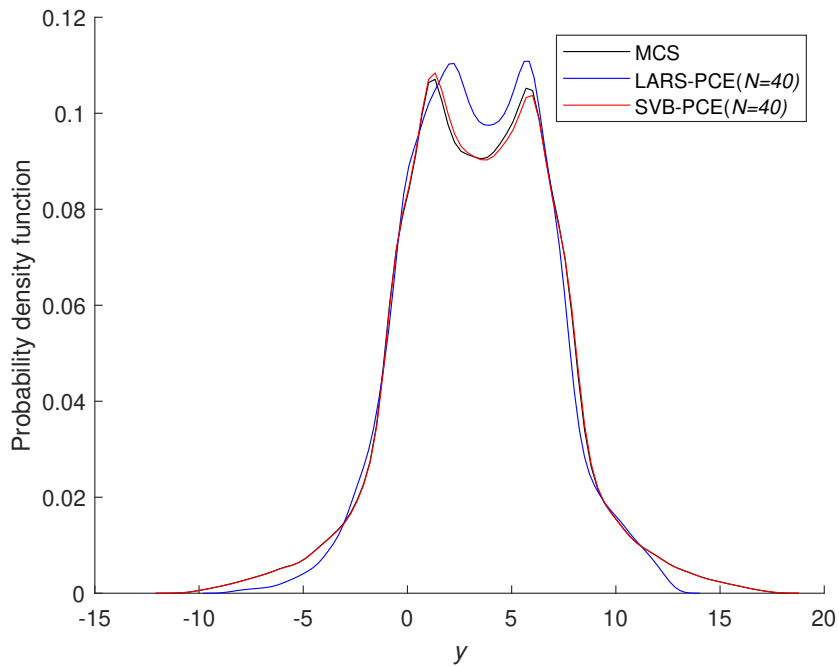


Figure 5.5: PDF of the Ishigami function by MCS, LARS-PCE and SVB-PCE models

Table 5.2: Percentage error (PE) and sparsity index (SI) for the Ishigami function using $N = 40$ and $p = 8$

| Method | PE (%) | SI |
|----------|--------|-------------------------|
| LARS-PCE | 21.50 | 22/165 \approx 13.33% |
| SVB-PCE | 1.65 | 13/165 \approx 7.88% |

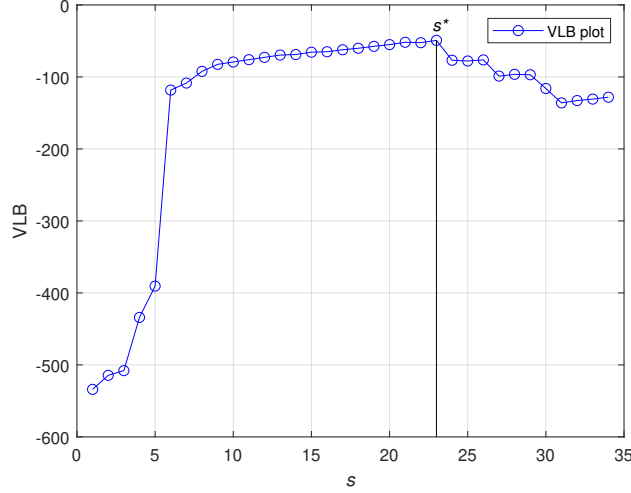


Figure 5.6: Evaluation of variational lower bound (VLB) for the Ishigami function using $N = 40$ and $p = 8$

The accuracy metric and the sparsity index (SI) are given in Table 5.2 for $N = 40$ and $p = 8$. The accuracy is much higher for the SVB-PCE model using $N = 40$ samples. The evaluation of the VLB for the SVB-PCE model with $N = 40$ and $p = 8$ is shown in Figure 5.6. It is seen that the VLB value was increased up to a certain iteration then it was decreased, and the s^* is the index having the highest VLB value which selects the final sparse PCE model for the Ishigami function. The SVB-PCE model requires few terms (only 13 out of 165 possible terms) from the orthonormal basis to achieve a high accuracy.

5.6.2 High-dimensional function

The second mathematical function considered here is the high-dimensional function (Marelli and Sudret, 2014):

$$y = 3 - \frac{5}{d} \sum_{i=1}^d i \xi_i + \frac{1}{d} \sum_{i=1}^d i \xi_i^3 + \ln \left[\frac{1}{3d} \sum_{i=1}^d i (\xi_i^2 + \xi_i^4) \right] \quad (5.44)$$

where $d = 20$ is the number of random variables. All the random variables ($\xi_i; i = 1, \dots, 20$) are uniformly distributed in $[1, 2]$. As a result, Legendre polynomials were used for computing the PCE basis. For the reference solution, MCS was performed on $N_{\text{MCS}} = 10^5$ samples. For the SVB-PCE and the LARS-PCE models, the maximum degree of polynomial was considered as $p = 2$. As a consequence, a total $n = 231$ terms were found in the polynomial basis of the full PCE model.

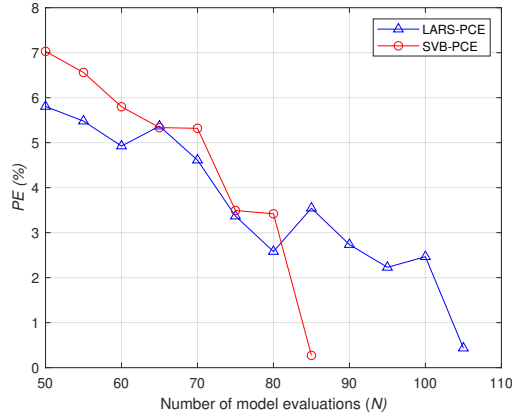


Figure 5.7: Evaluation of percentage error (PE) with the increase of sample points for the high-dimensional function

Table 5.3: Statistical moments of the response for the high-dimensional function using $N = 85$ and $p = 2$

| Method | $\hat{\mu}_y$ | PE (%) | $\hat{\sigma}_y$ | PE (%) |
|----------|---------------|--------|------------------|--------|
| MCS | -32.9941 | - | 1.8729 | - |
| LARS-PCE | -33.1630 | 0.51 | 1.4811 | 20.92 |
| SVB-PCE | -32.9951 | 0.00 | 1.8742 | 0.07 |

For this example, a convergence study was performed to check the evolution of PE with the increase of the model evaluation number. The initial number of samples was set as $N = 50$ LHS points and it was increased by 5 LHS points at each step until PE is less than 2%. The evaluation of PE with the samples are shown in Figure 5.7. It is seen that this level of accuracy is achieved by the SVB-PCE model using $N = 85$ LHS points, whereas it requires $N = 105$ LHS points for the LARS-PCE model.

In a similar way to the previous example, the PDF of the response is plotted using $N = 85$ samples by both approaches along with the MCS result in Figure 5.8. It is seen clearly that the SVB-PCE model has predicted a much accurate PDF which is almost following the PDF computed by the MCS.

The first two statistical moments of the stochastic response were also computed by both surrogate models and are listed in Table 5.3. Along with this, the PE was computed with respect to the MCS results, which is listed in Table 5.3. $\hat{\mu}_y$ and $\hat{\sigma}_y$ were obtained more accurately by the SVB-PCE model as compared to the LARS-PCE model using the same sample points.

The PE and the SI for the high-dimensional function are given in Table 5.4. The evaluation of the VLB with the iteration number (s) is plotted in Figure 5.9. The highest VLB was achieved at $s = 77$ which is denoted by s^* on the figure. The trend of the evaluation is almost similar as for the Ishigami function. The number of important terms in the polynomial basis is a little higher for the SVB-PCE model, however, the PE is much lower for the SVB-PCE model using $N = 85$ samples. These results are suggesting that the ability to detect the most important terms is higher by the SVB-PCE as compared to the LARS-PCE model with 85

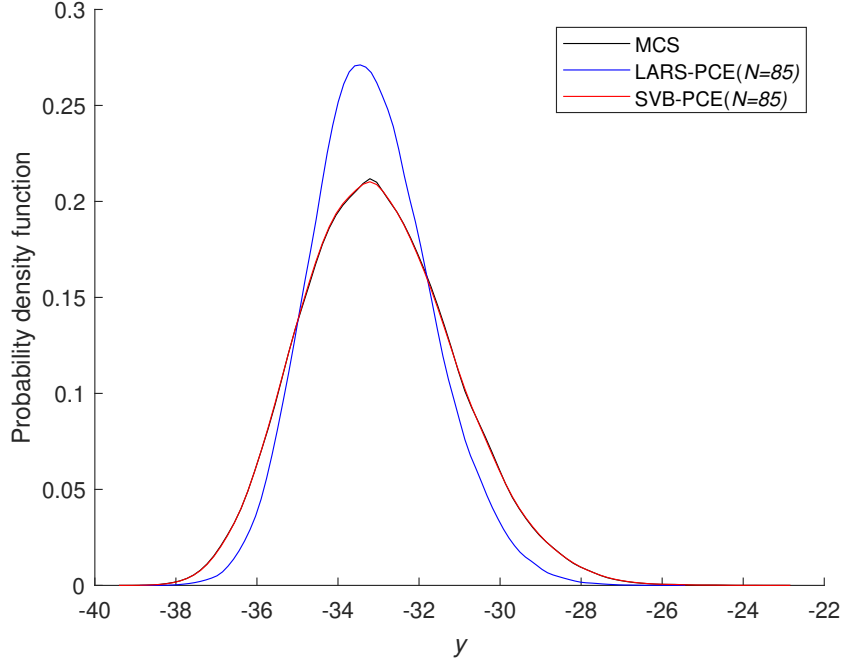


Figure 5.8: PDF of the high-dimensional function by MCS, LARS-PCE and SVB-PCE using $N = 85$ and $p = 2$

Table 5.4: Percentage error (PE) and sparsity index (SI) for the high-dimensional function using $N = 85$ and $p = 2$

| Method | PE (%) | SI |
|----------|--------|-------------------------|
| LARS-PCE | 3.54 | 30/231 \approx 12.99% |
| SVB-PCE | 0.27 | 39/231 \approx 16.88% |

model evaluations.

5.6.3 Observations

The results presented above clearly suggest that the introduction of the sparsity in the PCE model has improved the accuracy significantly using a limited number of model evaluations. To identify a PCE model, the number of model evaluations must be at least equal to the number of terms in the PCE model otherwise, the model is probably inaccurate. Using the sparse approach significantly reduces the number of terms in the PCE mode which ultimately reduces the required number of model evaluations. For both presented test functions, the SVB-PCE predicted results outperform the LARS-PCE predicted results. The Ishigami function was predicted quite well by both surrogate models however, the LARS-PCE took almost the double sample points as compared to the SVB-PCE model to achieve a PE lower than 2%. For the high-dimensional function, the number of model evaluations was also greater by the LARS-PCE model than the SVB-PCE model. The main advantage of the Bayesian formulation is that it takes care about the residual error ε_p of the PCE model. Another advantage of the

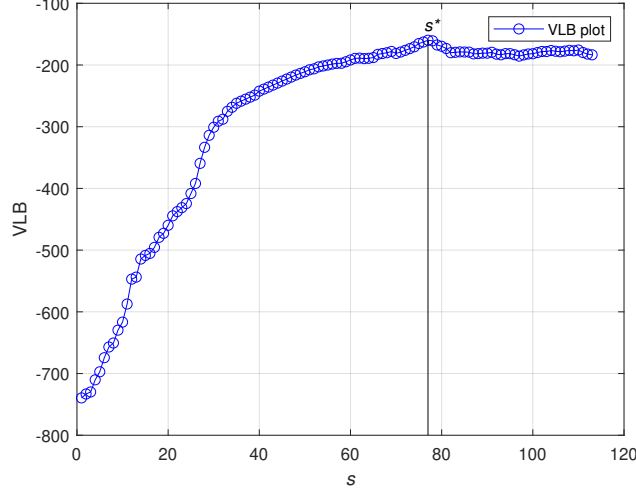


Figure 5.9: Evaluation of variational lower bound (VLB) for the high-dimensional function using $N = 85$ and $p = 2$

SVB approach over the LARS approach is that the number of terms is selected through an optimization approach whereas for the LARS approach, one needs to specify an error criterion. Furthermore, the PCE coefficients are computed within the Bayesian framework which does not require additional OLS to compute the coefficients. Another advantage of the present formulation is that the VB formulation is fully connected to the ARD. Therefore, obtaining a sparse PCE model corresponding to the maximum VLB always selects the best PCE model.

5.7 POD-SVB-PCE model

The SVB-PCE model can be utilized for the impact oscillator, however, the SVB-PCE model must be fitted at each time-step and it is the main drawback. For that reason, it was seen in chapter 4 that the POD-PCE model was useful for propagating uncertainty through an impact oscillator. To reduce further the number of terms or the number of coefficients in the PCE model, the SVB-PCE model is used here instead of the PCE model. Therefore, after obtaining the coefficient vector corresponding to each POM using Equation 4.10, the POD coefficient vectors are represented by the SVB-PCE model as follows:

$$\forall i = 1, \dots, n_b \quad b_i(\Xi) \approx \Phi^* \mathbf{a}^* \quad (5.45)$$

The POD coefficient vectors are then predicted at the new samples using Equation 5.45 and finally, the time-dependent stochastic response can be predicted using Equation 4.9. The pseudo-code for the construction of the POD-SVB-PCE model is given in Algorithm 5.3.

5.8 Application of POD-SVB-PCE model to impact oscillator

It has been noticed from the study in chapter 4 that the stochastic modeling of the multiple impact oscillator is much difficult as compared to the single impact oscillator. For that reason, the multiple impact oscillator is considered here for the application of the POD-SVB-PCE

Algorithm 5.3 Algorithm for the construction of POD-SVB-PCE model

```

1: procedure POD-SVB-PCE( $N, d, p, e$ )
2:   Obtain  $N$  samples for the uncertain parameters by LHS
3:   for  $i = 1 : N$  do
4:      $Y(\Xi_i, t) = \mathcal{M}(\Xi_i, t)$ 
5:      $\Phi_i = \Phi(\Xi_i)$  ▷ Refer to Equation 2.2 and Equation 2.9
6:   end for
7:    $(V, \lambda) = \text{eig}(C)$  ▷ Refer to Equation 4.2
8:   Obtain  $n_b$  by energy criterion ▷ Refer to Equation 4.7
9:   Obtain  $\mathbf{V}_i$  ▷ Refer to Equation 4.4
10:  for  $i = 1 : n_b$  do
11:    Obtain POD coefficient  $b_i(\Xi)$  ▷ Refer to Equation 4.10
12:     $(\mathbf{a}_i^*, \Phi^*, \text{ind}^*) = \text{SVB-PCE}(\Phi, b_i(\Xi), e)$  ▷ Refer to Algorithm 5.2
13:  end for
14: end procedure

```

model. The impact oscillator has been defined in section 3.5.4 and the stochastic modeling of the multiple impact oscillator has been performed in section 4.5.2 by the POD-PCE model. All the uncertain parameters were given in Table 4.1. In a similar way to chapter 4, the time integration was performed in time domain $t \in [0 \text{ ms}, 3 \text{ ms}]$ with a time step of $\Delta t = 1 \mu\text{s}$. The reference solution was computed by MCS with $N_{\text{MCS}} = 10^4$ LHS points.

5.8.1 Contact force

As a good result was obtained in section 4.5.2 with the POD-PCE model using $N = 50$, the evaluation of the mean relative error (Equation 3.11) was computed by increasing the polynomial degree p with $N = 50$ for both surrogate models. The evaluation of the mean relative error is shown in Figure 5.10a. It is seen that $\bar{\epsilon}$ is progressively decreasing with the increase of p for the POD-SVB-PCE model whereas an opposite behavior is noticed for the POD-PCE model. The main reason is that the number of terms in the PCE model increases with the increase of polynomial degree. For instance, $n = 286$ terms are found in the PCE model with polynomial degree $p = 10$. As a result, it is required to solve an under determined problem ($N < n$), whose solution is inaccurate. To investigate this phenomenon more accurately, the maximum number of selected terms by the SVB-PCE model is plotted Figure 5.10c along with the number of terms for the PCE model. The maximum number of selected terms for the POD-SVB-PCE model is given by $n_{\text{max}} = \max(\text{card}(\mathbf{a}_i^*)); i = 1, \dots, n_b$ whereas $n_{\text{max}} = n$ for the POD-PCE model. It is seen that n_{max} is always much less than the number of model evaluations for the POD-SVB-PCE model whereas n_{max} is greater than N beyond $p = 4$. For that reason, the error by the POD-PCE model increases with the increase of p . At the same time, the total number of coefficients (n_{tot}) for both surrogate models is shown in Figure 5.10b with the increase of the polynomial degree. For the POD-PCE model, $n_{\text{tot}} = n_b n$ and $n_{\text{tot}} = \sum_{i=1}^{n_b} \text{card}(\mathbf{a}_i^*)$ for the POD-SVB-PCE model. It is seen that the total number of coefficients increases rapidly with the increase of p for the POD-PCE model. On the contrary, only $n_{\text{tot}} = 107$ coefficients were used to predict the contact force by the POD-SVB-PCE model which has $n_b = 31$ POM. Therefore, the usefulness of the SVB-PCE model is that the POD-SVB-PCE model still predicts the stochastic response with a good

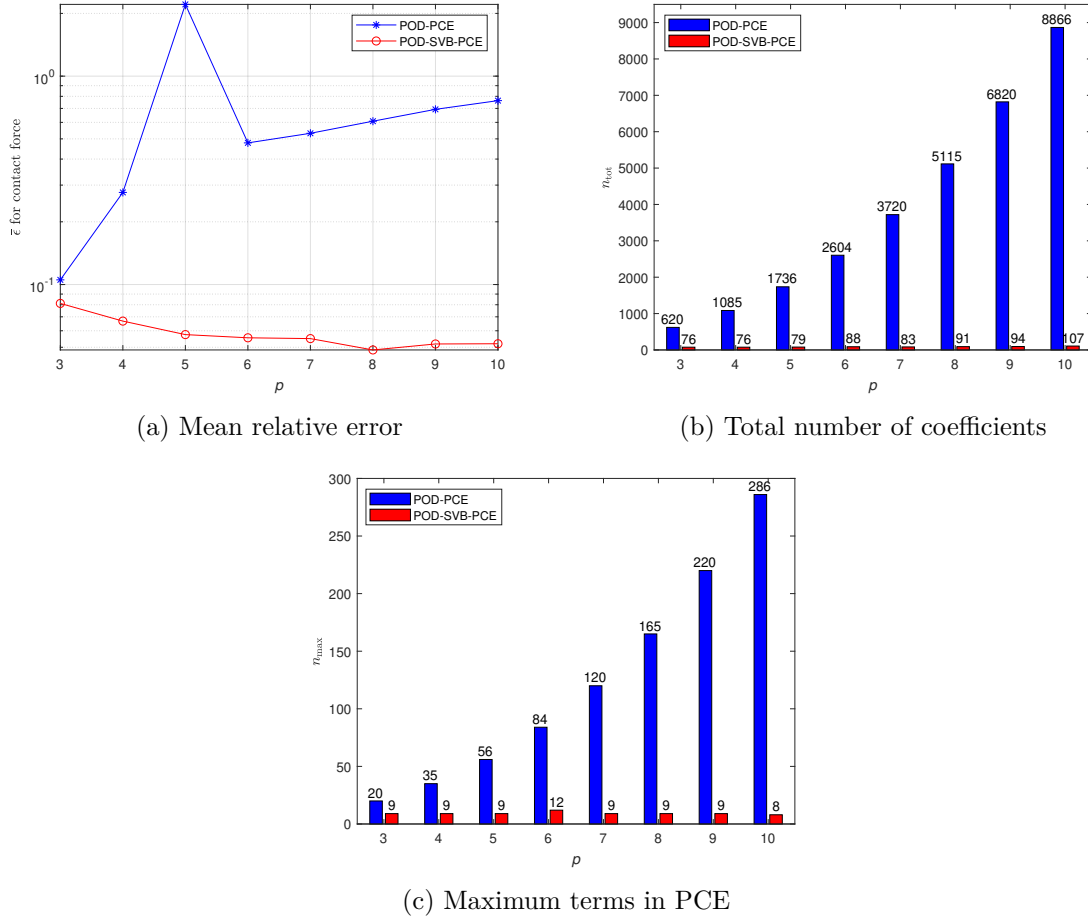


Figure 5.10: Evolution of the mean relative error and the PCE coefficients with the increase of polynomial degree p for the predicted contact force by the POD-PCE and the POD-SVB-PCE models with $N = 50$

accuracy using a low number of model evaluations due to the much smaller number of terms in the PCE model.

Further, the mean relative error was computed with the increase of the number of model evaluations N with $p = 10$, which is shown in Figure 5.11a. The number of samples started with $N = 30$ and is increased up to $N = 60$ at a step of 5 samples. For this case, the mean error progressively decreased with the increase of N using both surrogate models. However, the POD-PCE model was unable to predict a good accuracy because it required at least $N = 286$ sample points to compute the PCE coefficients. A more clear picture is shown in Figure 5.11c and it is seen that for all the cases, n_{\max} is quite smaller compared to N for the POD-SVB-PCE model. The total number of coefficients (n_{tot}) is also shown in Figure 5.11b. For all the sample points, n_{tot} of the POD-SVB-PCE model is approximately 100 times lower compared to the POD-PCE model.

From Figure 5.10a and Figure 5.11a it is clear that the prediction accuracy has been improved by using the SVB-PCE model along with the POD model instead of the PCE model. For this multiple impact oscillator, the predicted mean and standard deviation has

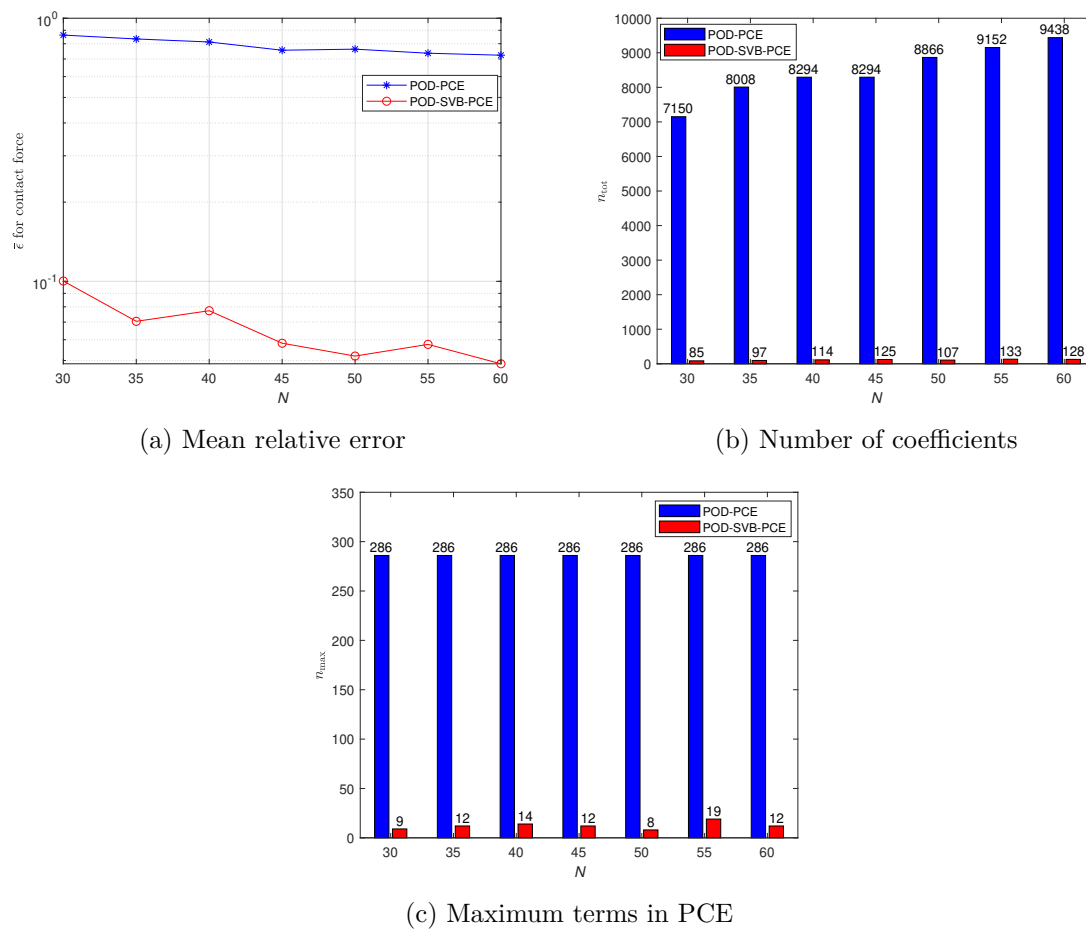


Figure 5.11: Evaluation of the mean relative error with the increase of sample point N for the predicted contact force by the POD-PCE and the POD-SVB-PCE model with $p = 10$

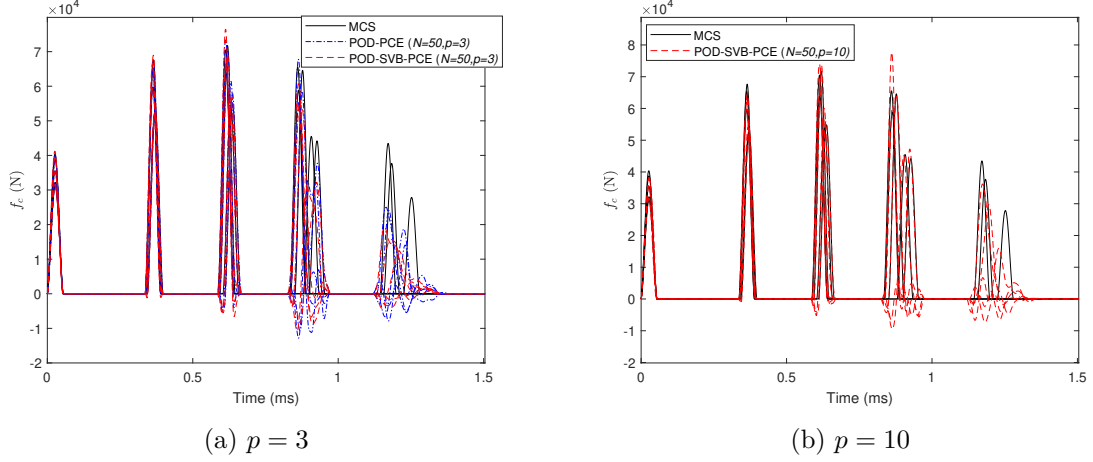


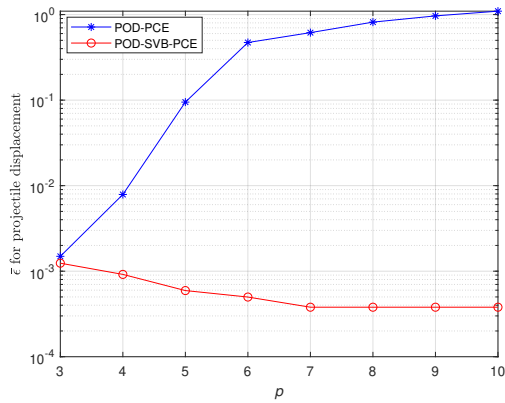
Figure 5.12: Comparison of contact force at 5 samples predicted by the POD-PCE and the POD-SVB-PCE models with $N = 50$ (zoom view over the impact duration)

already been discussed in section 4.5.2. As the predicted accuracy is quite good by the POD-SVB-PCE model, the predicted statistical moments are not discussed here. Instead, only the predicted responses for five samples are plotted in Figure 5.12. It is seen that the non-physical negative forces are minimized with the POD-SVB-PCE model ($p = 3$) for the last two contact forces (Figure 5.12a). The mean relative error for these five samples was found as 10.53×10^{-2} and 8.10×10^{-2} for the POD-PCE and the POD-SVB-PCE models, respectively. Furthermore, with increasing the polynomial degree to $p = 10$, the non-physical forces are also minimized as the mean predicted relative error was found as 5.20×10^{-2} . Although, the non-physical negative forces are minimized to some extent, it was not possible to fully mitigate this problem even with the SVB-PCE model. The main reason is that the contact force is non-smooth in nature and predicting such non-smooth behavior with smooth functions (i.e. SVB-PCE model) is very difficult.

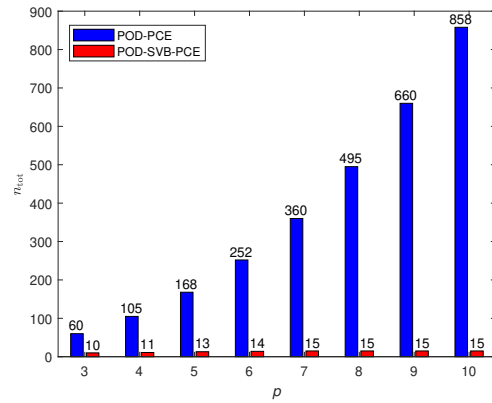
5.8.2 Projectile displacement

For the projectile displacement, a study has also been conducted to see the evolution of the mean error with the increase of the polynomial degree p and it is shown in Figure 5.13a. It is seen that almost the same error is predicted by both surrogate models with $p = 3$ and furthermore, the predicted mean error deteriorates with the increase of polynomial degree for the POD-PCE model as expected, when $N < n$. In contrast, the accuracy of the POD-SVB-PCE model increases with the increase of the polynomial degree using $N = 50$. The relative error for the POD-SVB-PCE model is almost constant after $p = 7$ which indicates that the optimal SVB-PCE model was obtained with $p = 7$. It is seen from Figure 5.13c that the n_{\max} is quite low for the POD-SVB-PCE model even with $p = 10$. The total number of coefficients required for both surrogate models is shown in Figure 5.13b. The POD-SVB-PCE model requires only 15 coefficients (for $n_b = 3$ POM) to achieve a good accuracy for the projectile displacement with $p = 10$ whereas the POD-PCE model requires $n_{\text{tot}} = 858$ coefficients to predict the stochastic response.

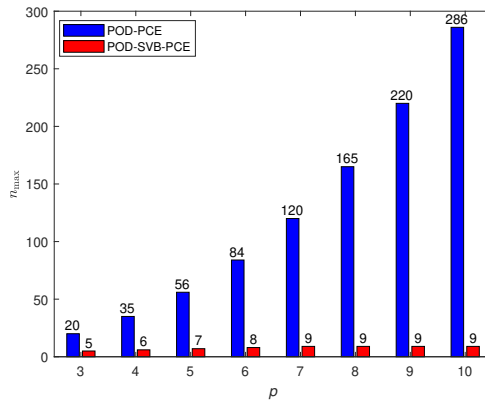
In a similar way to the contact force, the mean relative error was computed with the increase of sample points using $p = 10$: the evolution of $\bar{\epsilon}$ is shown in Figure 5.14a, the



(a) Mean relative error



(b) Number of coefficients



(c) Maximum terms in PCE

Figure 5.13: Evolution of the mean relative error and the PCE coefficients with the increase of polynomial degree p for the predicted projectile displacement by the POD-PCE and the POD-SVB-PCE models with $N = 50$

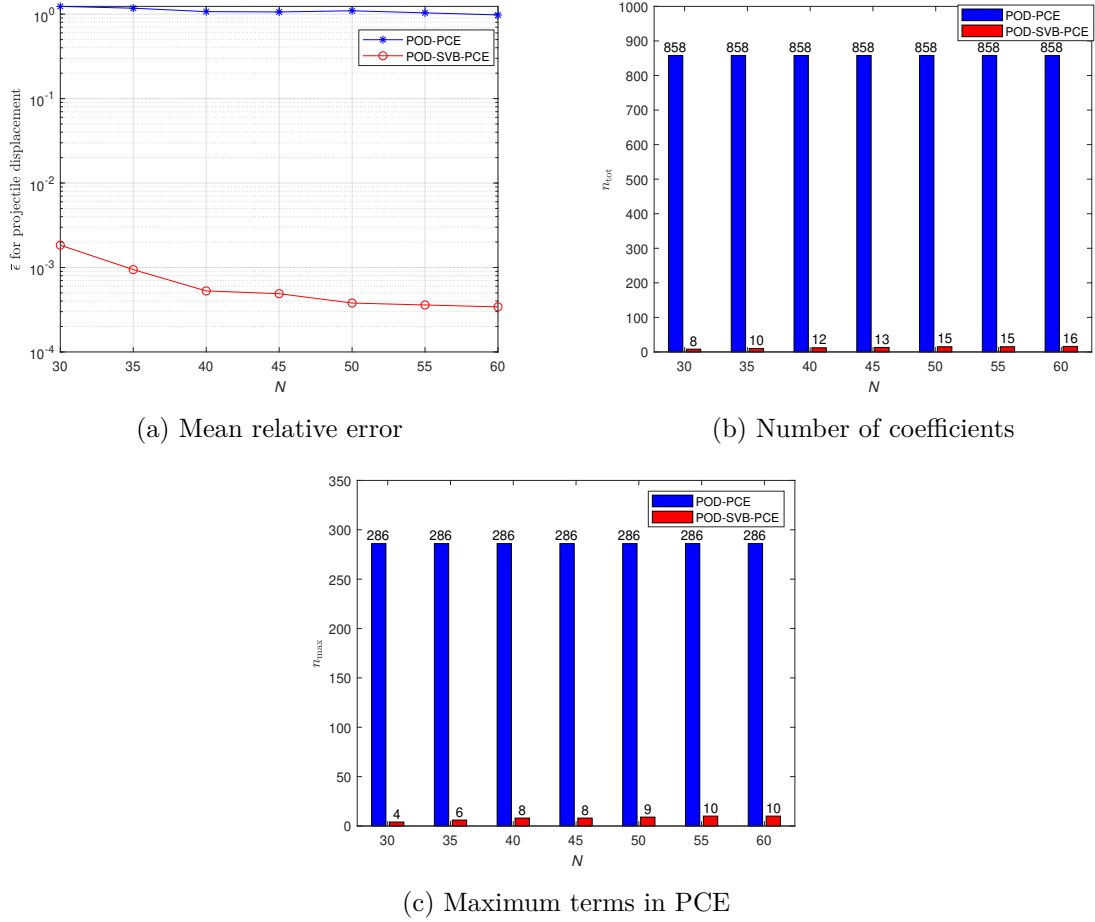


Figure 5.14: Evaluation of the mean relative error with the increase of sample point N for the predicted projectile displacement by the POD-PCE and the POD-SVB-PCE models with $p = 10$

corresponding total number of coefficients is shown in Figure 5.14b and the maximum number of PCE terms is shown in Figure 5.14c. It is seen that the POD-SVB-PCE model has predicted an error lower than 10^{-2} using $N = 30$ samples with only $n_{tot} = 8$ PCE coefficients and with $n_{max} = 4$, which is accurate and efficient. For the POD-PCE model, the number of terms in the basis is $n = 286$, which is higher than the number of model evaluations whereas the maximum PCE terms in case of the POD-SVB-PCE model for all the samples are very low. Therefore, using the SVB-PCE model not only reduces the number of PCE coefficients but also reduces the number of model evaluations to achieve a good accuracy.

5.8.3 Projectile velocity

The behavior of the projectile velocity is different than the others. Several jumps have already been noticed in Figure 4.6e. The mean relative error was computed with the increase of PCE polynomial degree using $N = 50$ for both surrogate models: it is shown in Figure 5.15a. A similar trend of the mean error is noticed for \dot{y}_p as it obtained for y_p . The predicted mean errors for both surrogate models are very close to each other with $p = 3$ and thereafter, it

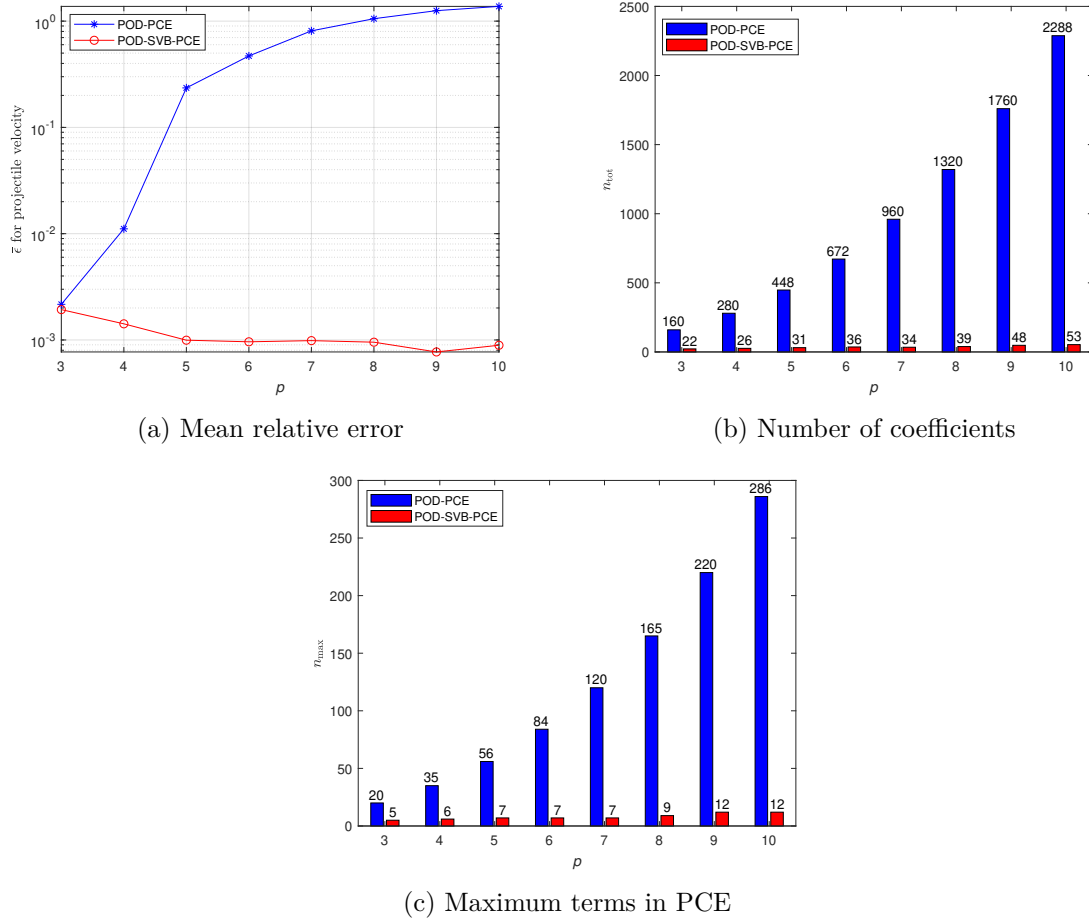


Figure 5.15: Evaluation of the mean relative error with the increase of polynomial degree p for the predicted projectile velocity by the POD-PCE and the POD-SVB-PCE models with $N = 50$

increases for the POD-PCE model due to the insufficient number of model evaluations. The total number of PCE coefficients (n_{tot}) and the maximum terms (n_{max}) in the PCE model are also shown in Figure 5.15b and Figure 5.15c, respectively using different polynomial degrees. It is seen that n_{max} is quite low for all the polynomial degrees by the POD-SVB-PCE model and therefore the number of model evaluations was always greater than n . The total number of coefficients is higher for \dot{y}_p as compared to y_p because the number of POM is $n_b = 8$ for \dot{y}_p . For 8 POM, the POD-SVB-PCE has predicted the responses with a very low number of coefficients without losing the accuracy. Indeed, the number of terms in the POD-SVB-PCE model is approximately 13.75% the number of terms in the POD-PCE model to keep almost the same accuracy with $p = 3$. Furthermore, the required number of terms in the POD-SVB-PCE model was only 2.32% with respect to the POD-PCE model to keep the mean error below 10^{-3} with $p = 10$ and $N = 50$.

To check the influence of N , the mean error was computed increasing N with $p = 10$, which is shown in Figure 5.16a. The number of POM was between 8 and 9 for the projectile velocity. The predicted mean error is always greater than 1 for the POD-PCE model because

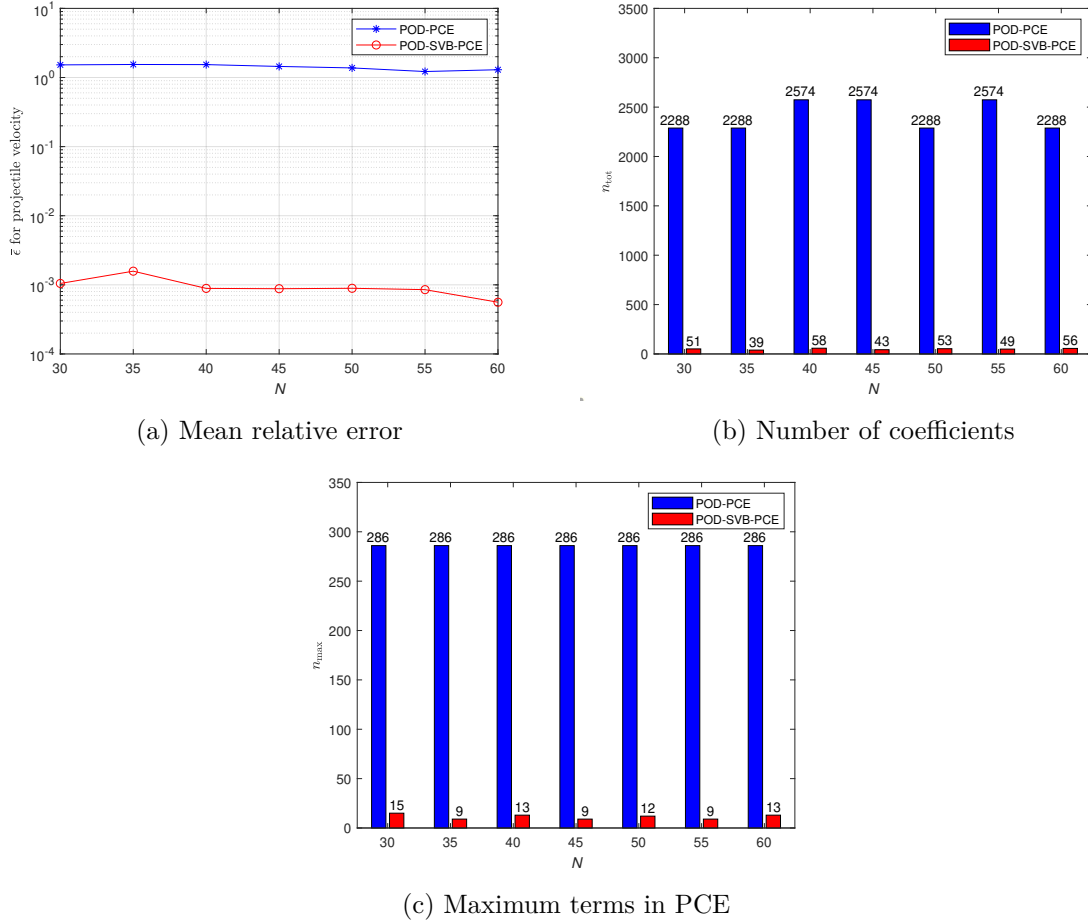


Figure 5.16: Evaluation of the mean relative error with the increase of sample point N for the predicted projectile velocity by the POD-PCE and the POD-SVB-PCE models with $p = 10$

the required number of model evaluations was very low. On the other hand, a good accuracy is maintained by the POD-SVB-PCE model with all the N values because n_{\max} was always much less than N as shown in Figure 5.16c. It is also noticeable from Figure 5.16b that the total number of coefficients was between 39 and 58 which is quite low with respect to the POD-PCE model.

Finally, the predicted projectile velocity at 5 samples is plotted in Figure 5.17 for all approaches. It is seen that the velocity is predicted quite well using both surrogate models using $p = 3$. However, for the POD-SVB-PCE model, only $n_{\text{tot}} = 22$ terms were required as shown in Figure 5.15. For these 5 samples, $\bar{\epsilon}$ was found as 1.90×10^{-3} and 2.23×10^{-3} for the POD-SVB-PCE and the POD-PCE models, respectively with $p = 3$. With $p = 10$, the respective relative errors were 8.91×10^{-4} and 13.76×10^{-1} . Therefore, the POD-SVB-PCE model has predicted better results with $p = 10$ as compared to $p = 3$ for the 5 samples.

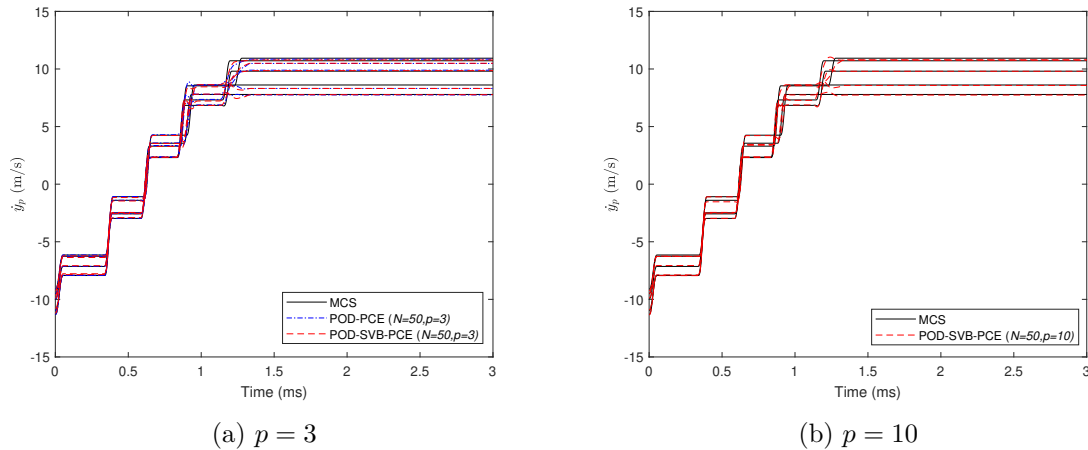


Figure 5.17: Comparison of projectile velocity at 5 samples predicted by the POD-PCE and the POD-SVB-PCE models with $N = 50$

5.9 Concluding remarks

In this chapter, a Bayesian inference based PCE has been formulated. The VB inference (Fox and Roberts, 2012; Ghahramani and Beal, 2001) was used to compute the PCE coefficients. Furthermore, the important terms in the PCE polynomial basis were selected using the ARD approach (Wipf and Nagarajan, 2008; Jacobs et al., 2018). The usefulness of the VB inference is that it considers the residual error of the truncated PCE model while computing the PCE coefficients. The VB inference is fully connected with the ARD, therefore, the important terms were selected using the results from the VB inference.

First of all, the applicability of the SVB-PCE model was tested on two mathematical functions and the results were compared with the MCS and the LARS-PCE model (Blatman and Sudret, 2011). It was found that the SVB-PCE model required a lower number of terms with respect to the LARS-PCE model to achieve the same level of accuracy for both mathematical functions. Furthermore, the SVB-PCE model has been coupled with the POD approach to develop the POD-SVB-PCE model. The multiple impact oscillator investigated in chapter 4 with the POD-PCE model has been investigated here by the POD-SVB-PCE model and the results were compared with the POD-PCE model. The stochastic responses were predicted quite well by the POD-SVB-PCE model with a very low number of PCE coefficients. For the contact force, it was possible to reduce the non-physical negative forces to some extent, however, predicting a non-smooth function by a smooth function (PCE or SVB-PCE) is always a challenging task. The main advantage of the SVB-PCE model is that it was able to predict the stochastic response with a high degree polynomial and with a low number of model evaluations as it selected few terms in the PCE model. On the contrary, the POD-PCE model was unable to predict the stochastic responses properly with the increase of polynomial degree as the number of coefficients was greater than the proposed number of model evaluations. For that reason, a sparse PCE model is always useful when a high degree polynomial basis is required and, at the same time, when the number of model evaluations needs to be minimized.

Chapter 6

Application to crash simulations

6.1 Introduction

The ARD based VB inference as introduced in chapter 5 was useful to select the number of important coefficients for a PCE model. The POD-PCE model was used to reduce the dimensionality of the impact oscillator model in the time domain. Furthermore, it was possible to propagate the uncertain parameters through the impact oscillator using a high degree polynomial and a reduced number of sample points by the the SVB-PCE model.

For a practical problem, the possible number of model evaluations is often limited. Therefore, obtaining a good quality surrogate model with a low number of model evaluations is very challenging. An appropriate surrogate model must be formulated according to the behavior of the response quantity, it is often called an adaptive surrogate model. An adaptive PCE model was formulated by Blatman and Sudret (2011) for the static QoI to select the number of model evaluations and the polynomial degree adaptively. This model was also used by Ni et al. (2017) for a probabilistic power flow problem. A support vector regression based adaptive PCE model was proposed by Cheng and Lu (2018a) to select the polynomial degree for a static QoI properly. Although the available sparse PCE models can be utilized to formulate an adaptive surrogate model for impacted dynamical system in time domain, the main issue is that the surrogate model must be formulated at each time step: it is the main computational issue.

An adaptive surrogate model is formulated in this chapter for impacted dynamical system in time domain. More specifically, the POD-SVB-PCE model introduced in chapter 5 is formulated as an adaptive surrogate model. Firstly, an adaptive SVB-PCE model is formulated for a time-independent QoI and then, the adaptive POD-SVB-PCE model is formulated using the adaptive SVB-PCE model and an error criterion. The adaptive surrogate model is then applied to the UQ of a crash box under impact loading. Additionally, the sensitivity of the uncertain parameters on the response quantity in the time domain is quantified using the developed adaptive POD-SVB-PCE model.

6.2 Adaptive SVB-PCE model

6.2.1 Sequential experimental design

It is often quite difficult to know beforehand the required number of model evaluations for achieving a desired accuracy. Hence, it is important to increase the number of samples in a sequential way such that an optimal number of model evaluations is performed for a specific QoI. Adding extra samples with the existing samples should increase the accuracy of a surrogate model. In this regards, Sobol sequence (Sobol, 1967, 1990) is one of the efficient sampling schemes for generating the samples sequentially as described in section 2.2.2. The convergence rate of the Sobol sequence is higher than the one with the classical Monte Carlo method, which increases the accuracy with a given number of model evaluations. Hence, Sobol sequence is used in this chapter for computing the model evaluations sequentially.

6.2.2 Adaptivity in the polynomial degree

The adaptivity in the polynomial degree is developed based on the leave one out (LOO) error. The LOO error is computed in a similar way to the LOO error by Blatman and Sudret (2011). In LOO error, the PCE model is evaluated using the samples $\Xi \setminus \Xi_i$ which is the set of all the samples without the i -th sample, and the QoI is predicted at the i -th sample. Therefore, the residual error for the i -th sample can be given by:

$$\varepsilon_{res,i} = Y(\Xi_i) - \hat{Y}^{-i}(\Xi_i) \quad (6.1)$$

where $\hat{Y}^{-i}(\Xi_i)$ is the predicted response at the i -th sample point by a PCE model constructed without the i -th sample. This procedure is performed for each of the samples separately and the LOO error is given by:

$$Err_{LOO} = \frac{1}{N} \sum_{i=1}^N \varepsilon_{res,i}^2 \quad (6.2)$$

As indicated by Blatman and Sudret (2011) for a linear regression problem, $\varepsilon_{res,i}$ for the i -th sample can be computed by developing a single PCE model as follows:

$$\varepsilon_{res,i} = \frac{Y(\Xi_i) - \hat{Y}(\Xi_i)}{1 - r_i} \quad (6.3)$$

and therefore, the LOO error can be computed as:

$$Err_{LOO} = \frac{1}{N} \sum_{i=1}^N \left[\frac{Y(\Xi_i) - \hat{Y}(\Xi_i)}{1 - r_i} \right]^2 \quad (6.4)$$

where r_i is the i -th diagonal term of the matrix $\Phi (\Phi^T \Phi)^{-1} \Phi^T$ and Φ is the PCE polynomial basis matrix. The relative LOO error can be defined as:

$$\varepsilon_{LOO} = \frac{Err_{LOO}}{\text{var}(Y)} \quad (6.5)$$

where $\text{var}(Y)$ is the variance of the QoI at the N samples. Furthermore, ε_{LOO} is modified by a multiplying constant as proposed by Chapelle et al. (2002):

$$\varepsilon_{LOO}^* = \varepsilon_{LOO} \Upsilon(p, N) \quad (6.6)$$

where $\Upsilon(p, N)$ is the multiplying constant, which is given by:

$$\Upsilon(p, N) = \frac{N}{N-p} \left[1 + \frac{\text{trace} \left(\frac{1}{N} \Phi^T \Phi \right)^{-1}}{N} \right] \quad (6.7)$$

Therefore, for a SVB-PCE model, the degree of the polynomial p is increased as long as $\varepsilon_{\text{LOO}}^*$ is greater than a threshold value.

6.2.3 Formulation of adaptive SVB-PCE model

The adaptive SVB-PCE model is formulated using the procedures described in sections 6.2.1 and 6.2.2. Therefore, the number of sample points and the polynomial degree are increased adaptively using a Sobol sequence and the LOO error. The procedure of sampling and for adapting the polynomial degree is described below:

1. First, the minimum and the maximum polynomial degrees are specified as p_{\min} and p_{\max} , respectively.
2. During the first iteration, the number of model evaluation and the polynomial degree are fixed at $N_{k_1} = N_{ini}$ and $p_{k_2} = p_{\min}$, respectively. N_{ini} is the initial number of samples, k_1 is the iteration number for the sample point adaptivity and k_2 is the iteration number for the degree adaptivity. Additionally, the maximum number of model evaluations is often restricted according to the budget of the computational cost: it is also initialized here as N_{\max} .
3. Then, the PCE basis matrix is constructed with the polynomial degree $p_{k_2} = p_{\min}$.
4. The sparse basis $\Phi_{k_2}^*$ and the corresponding coefficients $\mathbf{a}_{k_2}^*$ are obtained by the SVB approach (refer to Algorithm 5.2).
5. The modified LOO error $\varepsilon_{\text{LOO},k_2}^*$ is then computed using the sparse basis and the corresponding coefficients.
6. If the obtained $\varepsilon_{\text{LOO},k_2}^*$ is above some threshold value ϑ_{tol} , then the polynomial degree is increased by 1 and the steps 4 and 5 are then performed. This procedure continues until ϑ_{tol} is achieved or, up to p_{\max} .
7. However, the degree adaptivity procedure is terminated if $\varepsilon_{\text{LOO}}^*$ is increased in two consecutive steps due to the over-fitting i.e. if $\varepsilon_{\text{LOO},k_2}^* > \varepsilon_{\text{LOO},k_2-1}^* > \varepsilon_{\text{LOO},k_2-2}^*$. If the same polynomial bases are selected in two consecutive steps, then the iteration is also stopped and the sparse PCE model having the lowest modified LOO error is chosen from this step.
8. At the end of degree adaptivity, the sparse bases, the highest polynomial degree and the modified LOO error are recorded. If the modified LOO error has not reached the threshold value, then the number of sample points is increased in the next step i.e. $N_{k_1} = N_{k_1-1} + N_{incr}$. N_{incr} is the number of samples to be increased in each step. The minimum polynomial degree is set as $p_{\min} = p_{k_2}$ and p_{k_2} is the highest polynomial degree recorded during the degree adaptivity. In this way, the minimum polynomial degree is updated.

9. Now, steps 4 to 7 are carried out again. This procedure continues until the desired accuracy ϑ_{tol} is achieved.
10. The number of model evaluations is increased up to N_{max} and if the LOO error is still higher than the threshold value then the sparse PCE model with the lowest LOO error is chosen. The accuracy can be further increased by increasing N_{max} or by increasing the polynomial degree.

This proposed approach is called adaptive SVB-PCE model. An algorithm for the adaptive SVB-PCE model is given in Algorithm 6.1.

Algorithm 6.1 Pseudo-code for the adaptive SVB-PCE model

```

1: procedure ADAPTIVE SVB-PCE( $N_{\text{ini}}, N_{\text{incr}}, N_{\text{max}}, p_{\text{min}}, p_{\text{max}}, \vartheta_{\text{tol}}$ )
2:    $k_1 = 1$ 
3:    $k_2 = 1$ 
4:    $N_{k_1} = N_{\text{ini}}$ 
5:    $p_{k_2} = p_{\text{min}}$ 
6:   while  $\varepsilon_{\text{LOO},k_1} > \vartheta_{\text{tol}}$  and  $N_{k_1} < N_{\text{max}}$  do  $\triangleright$  Perform iteration until required accuracy
   is achieved
7:     Get the Sobol sequence samples  $\Xi \in \mathbb{R}^{N_{k_1} \times d}$ 
8:     Get the QoI  $Y \in \mathbb{R}^{N_{k_1} \times 1}$ 
9:     while  $\varepsilon_{\text{LOO},k_2} > \vartheta_{\text{tol}}$  and  $p_{k_2} \leq p_{\text{max}}$  do
10:      Obtain  $\Phi_{k_2}$ 
11:      Get  $\mathbf{a}_{k_2}^*, \Phi_{k_2}^*, \text{ind}_{k_2}^*$   $\triangleright$  Refer to Algorithm 5.2
12:      Compute  $\varepsilon_{\text{LOO},k_2}^*$   $\triangleright$  Refer to Equation 6.6
13:       $k_2 = k_2 + 1$ 
14:       $p_{k_2} = p_{k_2-1} + 1$ 
15:      if  $\varepsilon_{\text{LOO},k_2} > \varepsilon_{\text{LOO},k_2-1} > \varepsilon_{\text{LOO},k_2-2}$  then
16:         $k_2 = k_2 - 2$ 
17:        Terminate
18:      else if  $\text{ind}_{k_2} = \text{ind}_{k_2-1} = \text{ind}_{k_2-2}$  then
19:        Terminate
20:      end if
21:    end while
22:     $\varepsilon_{\text{LOO},k_1} = \varepsilon_{\text{LOO},k_2}$ 
23:     $\mathbf{a}_{k_1}^* = \mathbf{a}_{k_2}^*$ 
24:     $\Phi_{k_1}^* = \Phi_{k_2}^*$ 
25:     $\text{ind}_{k_1}^* = \text{ind}_{k_2}^*$ 
26:     $k_1 = k_1 + 1$ 
27:     $N_{k_1} = N_{k_1-1} + N_{\text{incr}}$ 
28:     $p_{\text{min}} = p_{k_2}$ 
29:     $k_2 = 1$ 
30:     $p_{k_2} = p_{\text{min}}$ 
31:  end while
32:  return  $\mathbf{a}_{k_1}^*, \Phi_{k_1}^*, \text{ind}_{k_1}^*, N_{k_1}$ 
33: end procedure

```

6.3 Adaptive POD-SVB-PCE model

The adaptive SVB-PCE model as developed in section 6.2 is useful for propagating and quantifying uncertainty for a statical QoI. However, for a dynamical system, the adaptive SVB-PCE model must be formulated at each time-step. Therefore, an alternate way for the dynamical systems is to use the POD approach along with the adaptive SVB-PCE model. It was already shown in chapter 4, the UQ of an impact oscillator can be performed by a POD-PCE model using a very low number of PCE model formulation. Further, it has been shown in chapter 5 that the use of the SVB-PCE model can drastically reduce the number of terms in the PCE basis. Consequently, using the adaptive SVB-PCE model along with the POD approach would select the optimal number of terms for a PCE model with the optimal number of model evaluations. However, it is evident from Equation 6.4 that the LOO error used for the SVB-PCE model cannot be directly utilized for a time-dependent problem. Therefore, a different kind of error criterion is used to formulate an adaptive POD-SVB-PCE model.

To formulate the adaptive POD-SVB-PCE model, the adaptive SVB-PCE model is used for the prediction of the coefficient vectors of the POM. The mean error defined in Equation 3.11 is used as the LOO error for the formulation of the adaptive POD-SVB-PCE model. The step by step procedure of formulating an adaptive POD-SVB-PCE model is described below:

1. In a similar way to the adaptive SVB-PCE model, the minimum and the maximum polynomial degrees are p_{\min} and p_{\max} . The initial number of model evaluations is defined as $N_{\kappa} = N_{ini}$; κ is the iteration number for the adaptive POD-SVB-PCE model. The number of sample points to be added at each step (N_{incr}) is also specified.
2. In a similar way to the adaptive SVB-PCE model, the maximum number of model evaluations N_{\max} is also initialized: N_{\max} should be specified according to the computational budget.
3. Two threshold values for the LOO errors must be initialized as ϑ_{tol} and ϵ_{tol} for the SVB-PCE model and for the POD-SVB-PCE model, respectively. ϵ_{tol} is used to terminate the adaptive POD-SVB-PCE model for a time-dependent QoI.
4. For the κ -th step, the sample points are obtained with the Sobol sequence and the corresponding model evaluations are also computed.
5. Then, POD is performed to decouple the time-dependent behavior and the randomness which results in obtaining n_b POM. The energy criterion given in Equation 4.7 is used to keep the significant POM.
6. The coefficient vectors b_i ($i = 1, \dots, n_b$) are then obtained using Equation 4.10.
7. The important terms in the PCE basis are selected by using the degree adaptivity part of Algorithm 6.1 for each of the coefficient vectors b_i . At this step, the maximum polynomial degree for each POM is recorded and it will be used in the next iteration as the updated p_{\min} . The LOO error for the POD-SVB-PCE model is then computed in the following way:
 - Firstly, the POD is performed without the j -th sample.

- Then the coefficient vector corresponding to each POM is obtained using Equation 4.10. On obtaining the coefficient vectors, the PCE terms selected in step 7 are used to construct the PCE model. The PCE coefficients are computed here using OLS approach.
- On obtaining the PCE coefficients, the response at the j -th sample is predicted. The relative error at the j -th sample is computed as:

$$\epsilon_{\text{LOO},j} = \frac{\sum_{i=1}^{n_t} \left[Y(t_i, \Xi_j) - \hat{Y}^{-j}(t_i, \Xi_j) \right]^2}{\sum_{i=1}^{n_t} \left[Y(t_i, \Xi_j) - \bar{Y}(\Xi_j) \right]^2} \quad (6.8)$$

where $\hat{Y}^{-j}(t_i, \Xi_j)$ is the predicted response at the j -th sample with the surrogate model constructed using all the samples without the j -th sample point. This error is computed for all the N_κ sample points which lead to compute N_κ POD-SVB-PCE models.

- The mean relative LOO error for the N_κ sample points is computed as:

$$\bar{\epsilon}_{\text{LOO},\kappa} = \frac{1}{N_\kappa} \sum_{i=1}^{N_\kappa} \epsilon_{\text{LOO},i} \quad (6.9)$$

8. If $\bar{\epsilon}_{\text{LOO},\kappa}$ is greater than ϵ_{tol} then the number of model evaluations is increased as $N_\kappa = N_{\kappa-1} + N_{\text{incr}}$. Therefore, the response is evaluated for the extra N_{incr} samples only.
9. After obtaining the response quantity at the extra points, step 5 to step 7 are performed again and $\bar{\epsilon}_{\text{LOO}}$ is computed. The iteration continues until the mean LOO error has reached the specified threshold value ϵ_{tol} or the maximum number of model evaluation (N_{max}) is reached.

An algorithm to obtain the adaptive POD-SVB-PCE is given in Algorithm 6.2.

6.4 Numerical formulation of a crash box

In this section, the numerical formulation of a crash box is discussed. Firstly, the finite element (FE) formulation of a crash box is presented. However, the computational cost of a full crash box is high. For that reason, a symmetrical quarter part of the full crash box is also modeled. A similar kind of study has been conducted by several researchers (Langseth et al., 1999; Zhang et al., 2007; Song et al., 2013; Zhou et al., 2017). To assess the influence of the simplification, a deterministic analysis is carried out for the full crash box and the quarter crash box model.

6.4.1 Finite element model of a crash box

As discussed in section 1.1, a full car model should be investigated to quantify the uncertainty associated with the response quantities for a crash problem. However, a single model evaluation of a car crash model requires almost 24 h (Moustapha et al., 2016) which limits to model a full car crash numerically for UQ. Therefore, a crash box which is one of the main parts during the dissipation of kinetic energy, is investigated here under the impact loading.

Algorithm 6.2 Pseudo-code for the adaptive POD-SVB-PCE model

```

1: procedure ADAPTIVE POD-SVB-PCE( $N_{ini}, N_{incr}, N_{max}, p_{min}, p_{max}, \vartheta_{tol}, \epsilon_{tol}$ )
2:    $\kappa = 1$ 
3:    $k_2 = 1$ 
4:    $N_\kappa = N_{ini}$ 
5:    $p_{k_2} = p_{min}$ 
6:   while  $\bar{\epsilon}_{LOO,\kappa} > \epsilon_{tol}$  and  $N_\kappa \leq N_{max}$  do
7:     Get the Sobol sequence samples  $\Xi \in \mathbb{R}^{N_\kappa \times d}$ 
8:     Get the time-dependent response matrix  $Y(\Xi, t) \in \mathbb{R}^{N_\kappa \times n_t}$ 
9:     Get the POM the SVD of  $Y(\Xi, t)$  ▷ Refer to Equation 4.3
10:    Obtain  $n_b$  POM using energy criterion ▷ Refer to Equation 4.7
11:    for  $i = 1 : n_b$  do
12:      Compute POD coefficient vector  $b_i(\Xi)$  ▷ Refer to Equation 4.10
13:      while  $\epsilon_{LOO,k_2} > \vartheta_{tol}$  and  $p_{k_2} \leq p_{max}$  do ▷ Perform SVB-PCE for  $i$ -th POD
14:        coefficient
15:        Obtain  $\Phi_{k_2}$  ▷ Obtain PCE basis matrix
16:        Get  $\mathbf{a}_{k_2}^*, \Phi_{k_2}^*, \text{ind}_{k_2}^*$  ▷ Refer to Algorithm 5.2
17:        Compute  $\epsilon_{LOO,k_2}^*$  ▷ Refer to Equation 6.6
18:         $k_2 = k_2 + 1$ 
19:         $p_{k_2} = p_{k_2-1} + 1$ 
20:        if  $\epsilon_{LOO,k_2}^* > \epsilon_{LOO,k_2-1}^* > \epsilon_{LOO,k_2-2}^*$  then
21:           $k_2 = k_2 - 2$ 
22:          Terminate
23:        else if  $\text{ind}_{k_2} = \text{ind}_{k_2-1} = \text{ind}_{k_2-2}$  then
24:          Terminate
25:        end if
26:      end while
27:       $\mathbf{a}_{\kappa,i} = \mathbf{a}_{k_2}^*$ 
28:       $\text{ind}_{\kappa,i} = \text{ind}_{k_2}^*$ 
29:       $\Phi_{\kappa,i} = \Phi_{k_2}^*$ 
30:       $p_{min,i} = p_{k_2,i}$ 
31:       $k_2 = 1$ 
32:    end for
33:    for  $j = 1 : N_\kappa$  do ▷ Loop for LOO error
34:      Get  $Y^{-j}$  ▷ The response matrix without the  $j$ -th sample
35:      Perform SVD of  $Y^{-j}$  to get  $n_b$  POM
36:      for  $i = 1 : n_b$  do
37:        Obtain the POD coefficient vectors  $b_i(\Xi \setminus \Xi_j)$ 
38:        Perform OLS to get the coefficient for  $\Phi_{\kappa,i}(\Xi \setminus \Xi_j)$ 
39:      end for
40:      Predict the response at the  $j$ -th sample
41:      Compute mean relative LOO error  $\bar{\epsilon}_{LOO,\kappa}$  ▷ Refer to Equation 6.9
42:    end for
43:  end while
44:  for  $i = 1 : n_b$  do
45:    return  $\mathbf{a}_{\kappa,i}, \Phi_{\kappa,i}, \text{ind}_{\kappa,i}$ 
46:  end for
47:  return POM,  $\bar{\epsilon}_{LOO,\kappa}, N_\kappa$ 
48: end procedure

```

The crash boxes are thin walled structures with a predictable and stable collapse mode (Lu and Yu, 2003). Different types of crash boxes have been investigated under impact loading in the past decades (Alexander, 1960; Abramowicz, 1983; Wierzbicki and Abramowicz, 1983; Abramowicz and Jones, 1984; Dirgantara et al., 2013; Zhou et al., 2017, 2016). The most conventional cross-sections are square, circular and triangular for designing a crash box. Recently, several other types of crash boxes have also been investigated by the researchers such as pentagonal (Song et al., 2013), hexagonal (Zhang and Zhang, 2012; Fan et al., 2013), octagonal (Mamalis et al., 2003; Zhang and Zhang, 2012) and origami crash boxes (Zhou et al., 2016, 2017; Yuan et al., 2019). To improve the efficiency in the energy dissipation, composite material has also been used for crash box (Zarei et al., 2008; Shaik Dawood et al., 2017).

A conventional rectangular shaped crash box with rounded corners was considered for the present study and it is available in <https://www.dynaexamples.com/>. This crash box is called as full crash box in the present study. The numerical modeling of the crash box was performed with the LS-Dyna finite element program. Different FE model views of the crash box are shown in Figure 6.1. All the dimensions are shown in the figure. The crash box is fixed on the left side in Figure 6.1c (i.e. it is fixed at the bottom in the isometric view) and a rigid mass (m_I) strikes from the right side (in negative z direction) with some velocity (v). At the beginning of the simulation, the impacting mass was close to the crash box, but not in contact with it. The mass is known as the impactor for the present work. The contact was modeled with the ‘automatic single surface’ contact option available in the LS-Dyna software because the crash pattern is usually not predefined for a crash box and it can detect the penetration of a shell element from both sides. The full crash box FE model has 1924 nodes and 1876 four-node shell elements (ELEMENT_SHELL keyword was used in LS-Dyna).

The nominal thickness of the crash box is 5 mm. The crash box is made of steel with the modulus of elasticity and the Poisson’s ratio of 200 GPa and 0.3, respectively. The crash box was modeled with an elasto-plastic material behavior (MAT_PIECEWISE_LINEAR_PLASTICITY keyword was used in LS-Dyna). The effective plastic stress-strain curve is shown in Figure 6.2. It is to be noted that the effective plastic strain is plotted in Figure 6.2, which is given by:

$$\gamma_{eff} = \gamma - \frac{\sigma}{E} \quad (6.10)$$

where γ and γ_{eff} are the true strain and the effective strain, respectively. E is the elastic modulus of steel and σ is the applied stress.

6.4.2 Finite element model of a quarter crash box

The quarter part of the crash box as shown in Figure 6.1, was modeled with LS-Dyna software. The quarter crash box is shown in Figure 6.3. In a similar way to the full crash box, the quarter crash box is fixed on the left hand side in Figure 6.3c and the impactor strikes it with velocity v in the negative z direction. Additionally, two free sides have symmetric conditions. The FE model was constructed with 469 four-node shell elements and a total 518 nodes were there in the quarter crash box. The same material properties were used for this quarter crash box as the previous one. As a result, the effective plastic stress-strain diagram shown in Figure 6.2 was used to model the elasto-plastic behavior of the quarter crash box. The thickness of the crash box was also the same i.e. 5 mm.

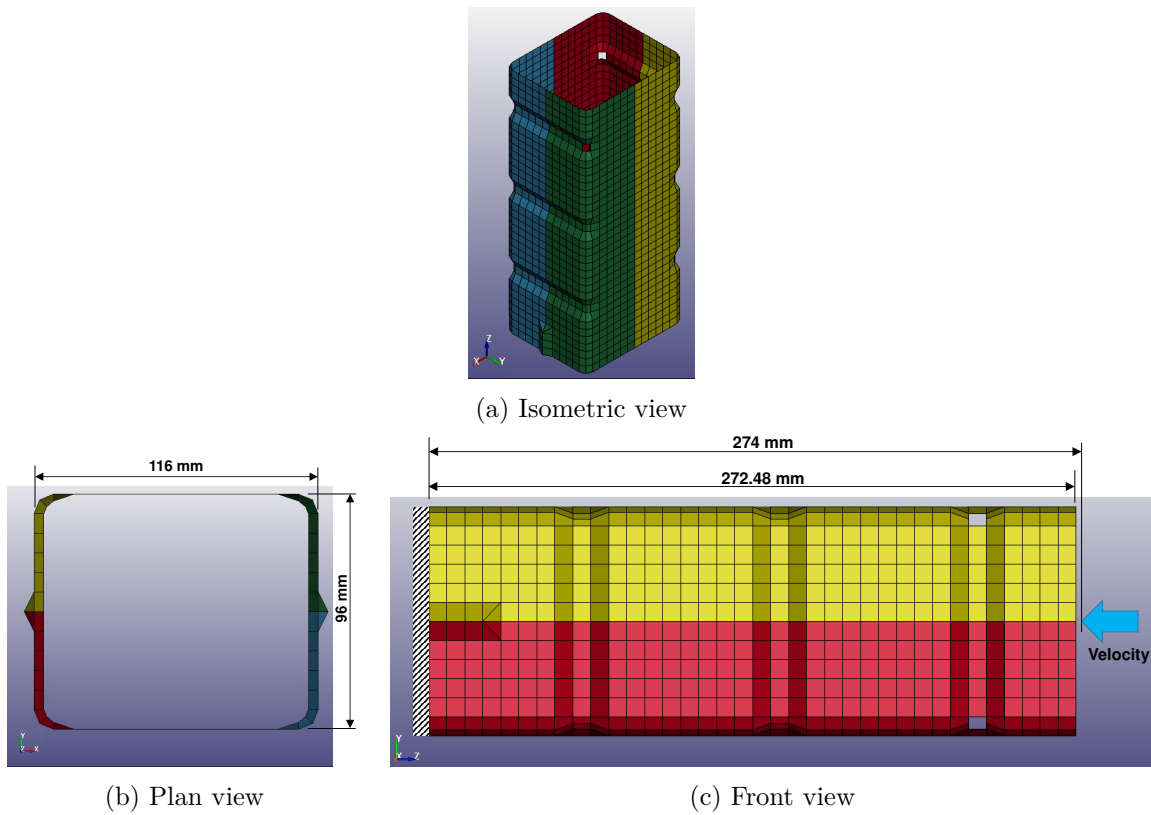


Figure 6.1: Geometrical views of FE model of the full crash box

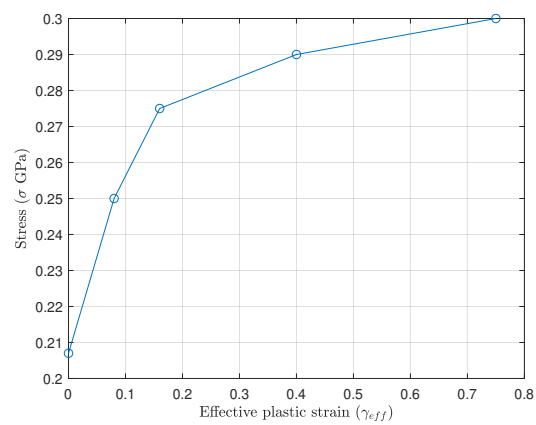


Figure 6.2: Plastic stress-strain diagram

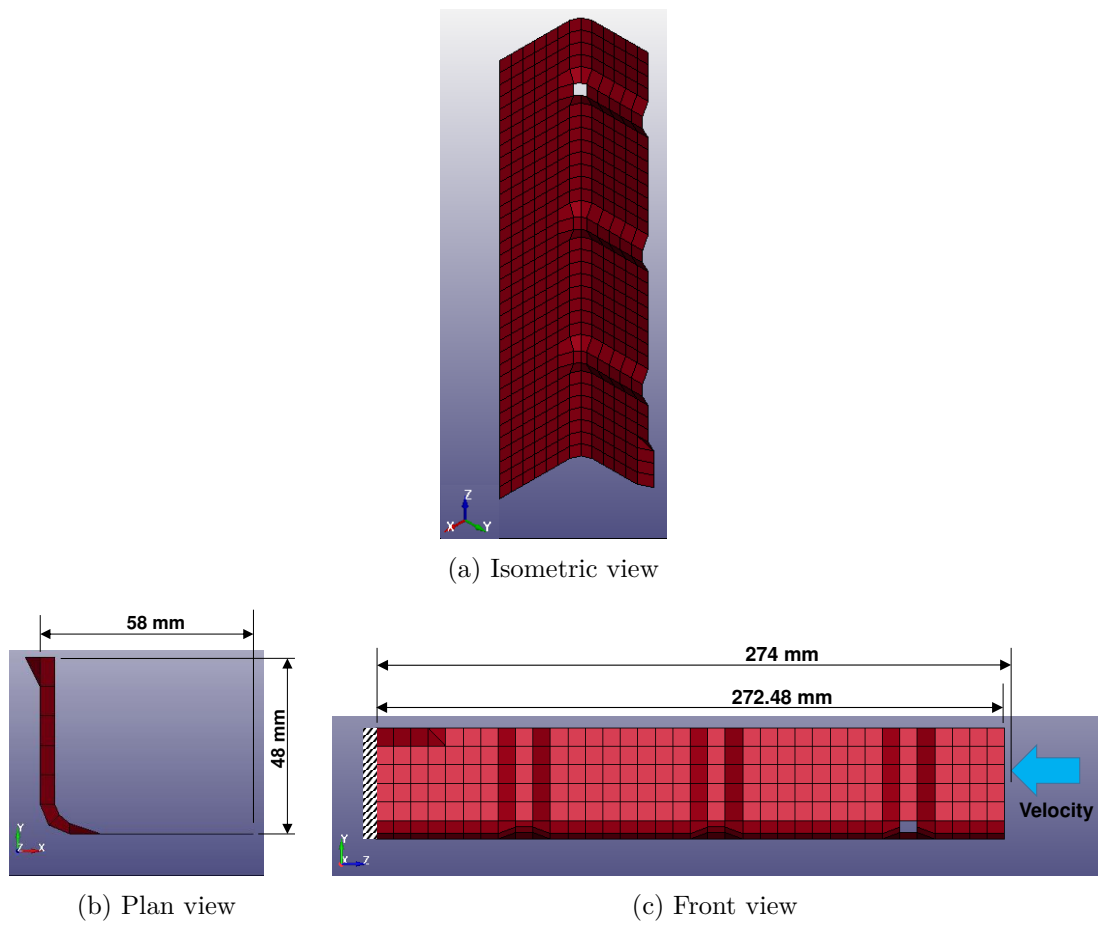


Figure 6.3: Geometrical views of FE model of the quarter crash box

6.4.3 Deterministic analysis of crash boxes

A deterministic analysis of the above-mentioned crash boxes (full and quarter crash boxes) is performed here to compare the response obtained for both crash boxes. The responses are compared to check the adequacy of using the quarter crash box instead of the full crash box. The deterministic analysis was performed using LS-Dyna FE explicit solver. The crash box was crushed by an impactor with a mass of $m_I = 1100$ kg for the full crash box. For the quarter crash box, the impactor mass was divided by 4, i.e. is equal to 275 kg. The impactor initial velocity was considered as $v = 10 \text{ m s}^{-1}$. The crash simulation was performed in the time domain $t \in [0 \text{ ms}, 60 \text{ ms}]$ at a time step of $\Delta t = 0.01 \text{ ms}$. As a result, the explicit contact dynamic problem was solved for $n_t = 601$ time steps.

Firstly, the failure shapes were compared for both crash boxes, and are shown in Figure 6.4 at different times. It is seen from Figure 6.4a that the first fold, the second fold and the third fold during the failure occurred at 5 s, 15 s and 25 s, respectively. The symmetrical quarter crash box also exhibits similar failure modes. Both crash boxes are fully crushed at around $t = 35 \text{ ms}$.

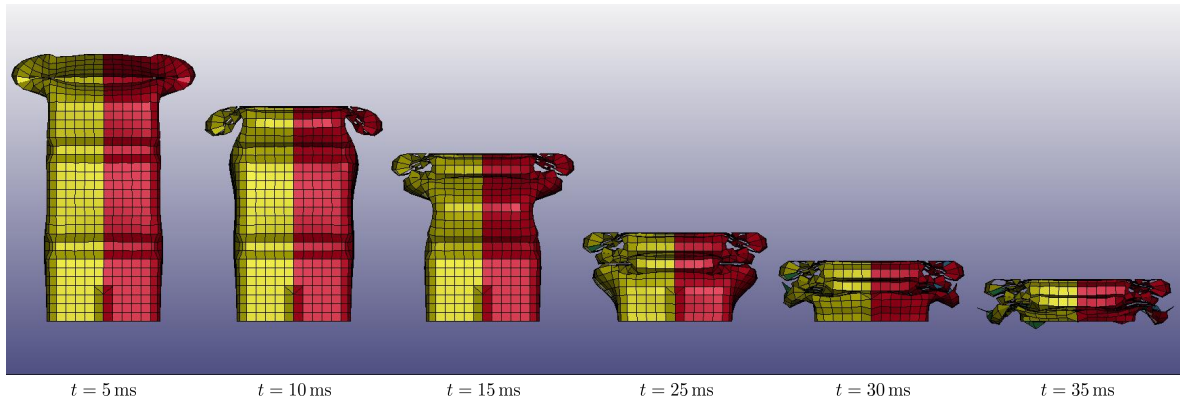
The impactor can be considered as a car and therefore the responses of the impactor is investigated here. From the deterministic analysis, different time-dependent response quantities were obtained for the impactor (displacement, velocity, contact force, kinetic energy, internal energy), which are shown in Figure 6.5. The time-dependent displacement and velocity of the impactor are shown in Figure 6.5a and Figure 6.5b, respectively. The relative error for the corresponding responses were computed using Equation 3.9 and were found as 2.95×10^{-5} and 1.41×10^{-4} , respectively. It is seen from the figures that for the impactor displacement and velocity, the results of both crash boxes are following almost the same line. As the impactor mass was rescaled for the symmetrical quarter crash box, it has predicted almost the same response behavior with time. For the other response quantities (i.e. kinetic energy, internal energy and contact force), the responses by the quarter crash box are almost 1/4-th of the full crash box. It is seen from Figure 6.5 that the scaled kinetic energy and internal energy (with a factor 4) of the quarter crash box are almost identical to those of the full crash box. The relative error for the kinetic energy and for the internal energy was 1.01×10^{-5} and 7.77×10^{-4} , respectively. For the contact force, the scaled contact force for the quarter crash box almost follows the same behavior as the contact force for the full crash box and the relative error for the contact force was 2.22×10^{-2} .

From the above-presented results, it is clear that the results obtained from both crash boxes are almost similar. Indeed the relative errors for all the responses are quite low. Furthermore, the CPU time required for the full and the quarter crash boxes were 83 s and 51 s, respectively. Therefore, using the quarter crash box would save approximately 40% computational cost without losing the accuracy. For that reason, UQ is performed only with the quarter crash box in the next section.

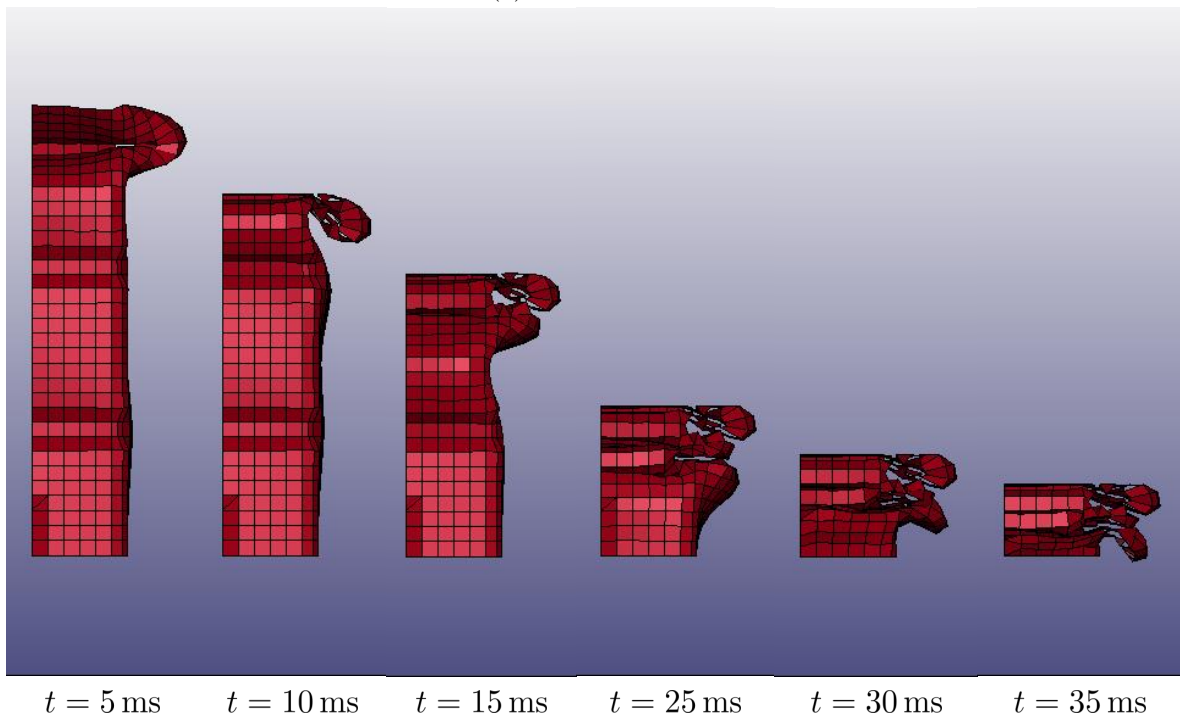
6.5 Uncertainty quantification of quarter crash box

6.5.1 Problem definition

The quarter crash box is investigated here considering some uncertain parameters. UQ of the quarter crash box was performed considering three different end conditions for the non impacted side: (i) the end of the crash box is fixed as shown in Figure 6.3, (ii) the end of the



(a) Full crash box



(b) Quarter crash box

Figure 6.4: Failure shapes at different times for both crash boxes under impact loading

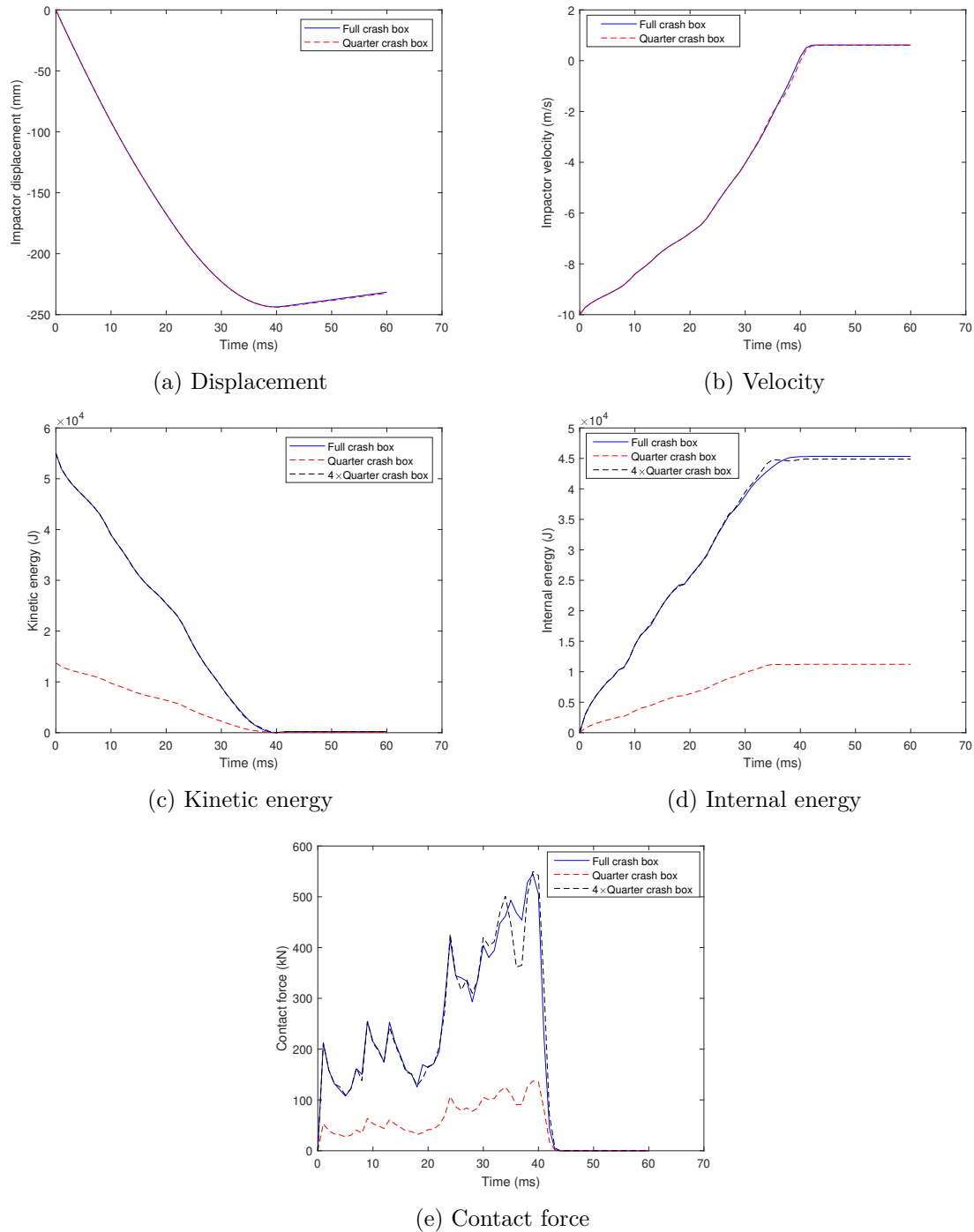


Figure 6.5: Comparison of the response quantities for both crash boxes for deterministic analysis

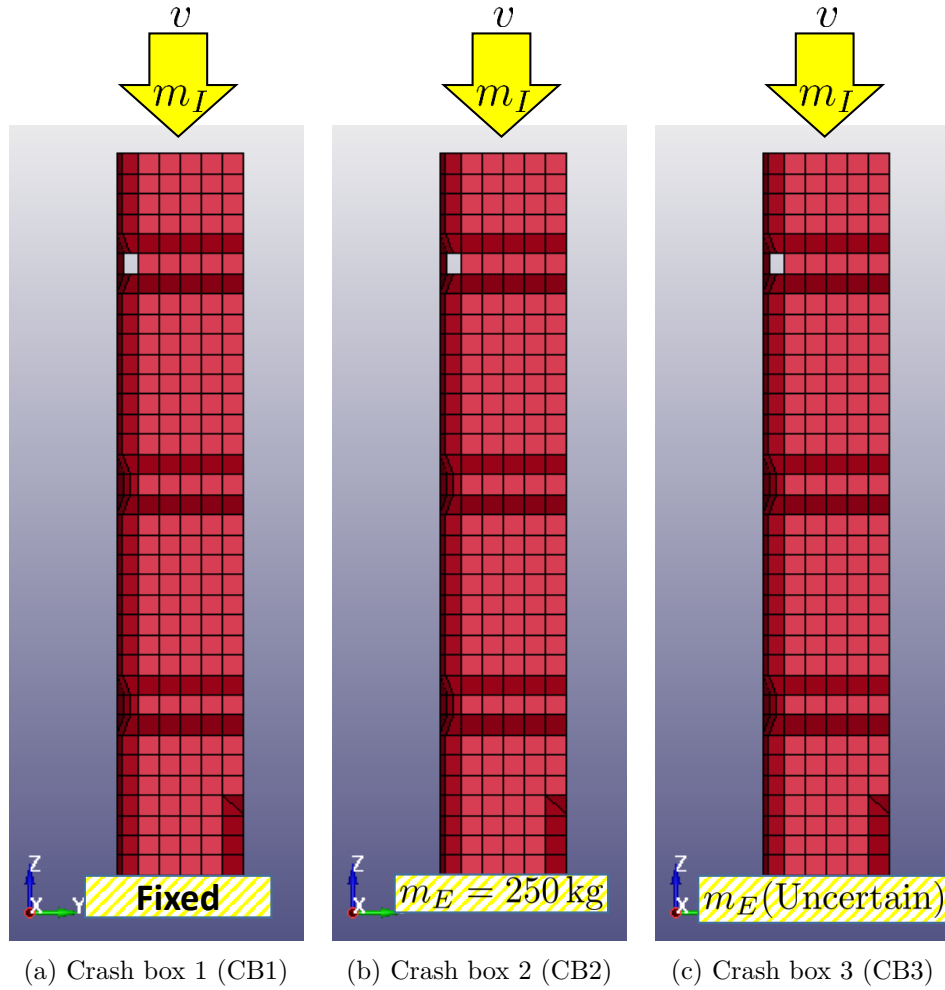


Figure 6.6: The symmetrical quarter crash box with different end conditions

crash box is free but a deterministic mass is attached at the end, (iii) the end is free and an uncertain mass is attached at the end. All the three crash boxes are shown in Figure 6.6 and are designated by crash box 1 (CB1), CB2 and CB3, respectively. The impactor mass and the end mass are designated by m_I and m_E , respectively.

The crash boxes were analyzed considering three uncertain parameters namely the impactor mass (m_I), the thickness (H) of the crash boxes and the material property. The uncertainty was considered in the material property by a multiplicative constant applied to the stress component in the stress-strain curve i.e. the stress axis values in Figure 6.2 were multiplied with a constant (c_σ). For the CB3, an additional uncertain parameter was considered as the end mass. Therefore, the first two crash boxes were modeled using three uncertain parameters and the last one was modeled with four uncertain parameters. All the uncertain parameters were considered uniformly distributed and the distribution parameters are listed in Table 6.1. The impactor velocity was considered constant as $v = 10 \text{ m s}^{-1}$ and the time domain of the crash problem was $t \in [0 \text{ ms}, 60 \text{ ms}]$ at a time-step of $\Delta t = 0.01 \text{ ms}$.

The failure shape for CB1 has already been shown in Figure 6.4b. The failure shape of CB2 is shown in Figure 6.7. It is seen that the first fold happened at 5 ms and the second

Table 6.1: Parameters of the uniformly distributed random variables for the crash boxes

| Variable name | Random variable | Bounds for uncertain parameters | | | Unit |
|---------------------------|-----------------|---------------------------------|-----------|-----------|------|
| | | CB1 | CB2 | CB3 | |
| Impactor mass | m_I | [225,275] | [225,275] | [225,275] | kg |
| Crash box thickness | H | [5,6] | [5,6] | [5,6] | mm |
| Stress multiplying factor | c_σ | [0.8,1.2] | [0.8,1.2] | [0.8,1.2] | – |
| End mass | m_E | – | – | [225,275] | kg |

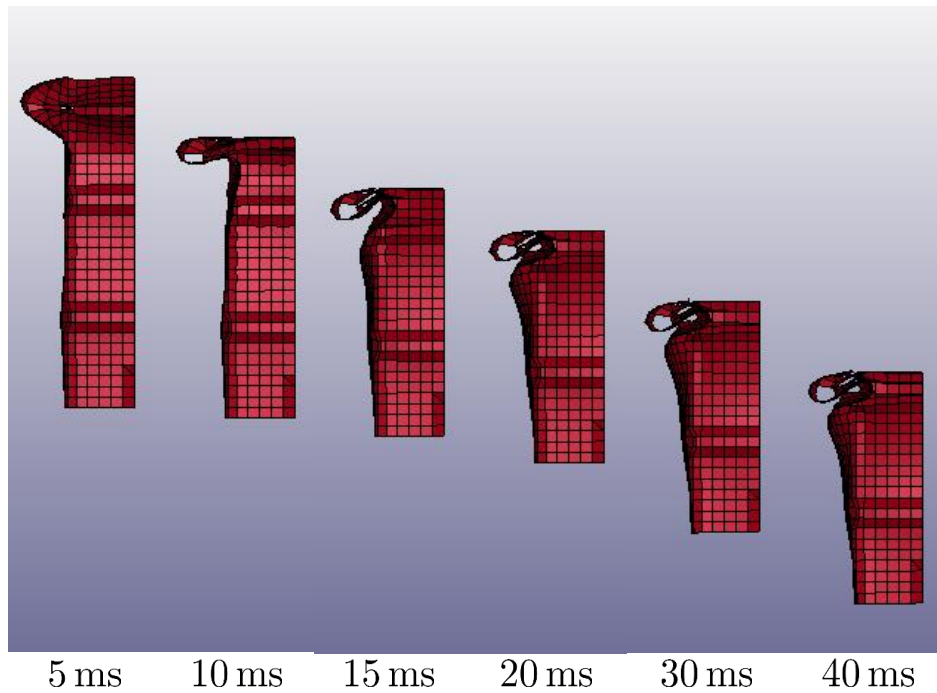


Figure 6.7: Failure shapes of CB2 at different time instances

fold started around 20 ms. After that, CB2 moves freely because the end is free. The same behavior is observed for CB3.

Time-dependent UQ was performed considering the impactor displacement, impactor velocity and the contact force as the QoI. For the safety of a car, the maximum contact force, and the total energy dissipation can be regarded as one of the important QoI. Therefore, UQ was also performed for the maximum contact force and the total energy dissipation.

6.5.2 Uncertainty quantification of crash boxes

UQ was performed by the adaptive POD-SVB-PCE model of the QoI (impactor displacement, impactor velocity, contact force) for CB1, CB2 and CB3. Legendre polynomials were used for the uncertain parameters. Two cases were investigated separately for each QoI considering the domain of the polynomial degree as $p \in \{1, \dots, 5\}$ and $p \in \{1, \dots, 10\}$. For the SVB-PCE model, the threshold value for the LOO error was set to $\vartheta_{\text{tol}} = 1 \times 10^{-3}$. On the contrary, the adaptive POD-SVB-PCE model was constructed considering two different threshold values of

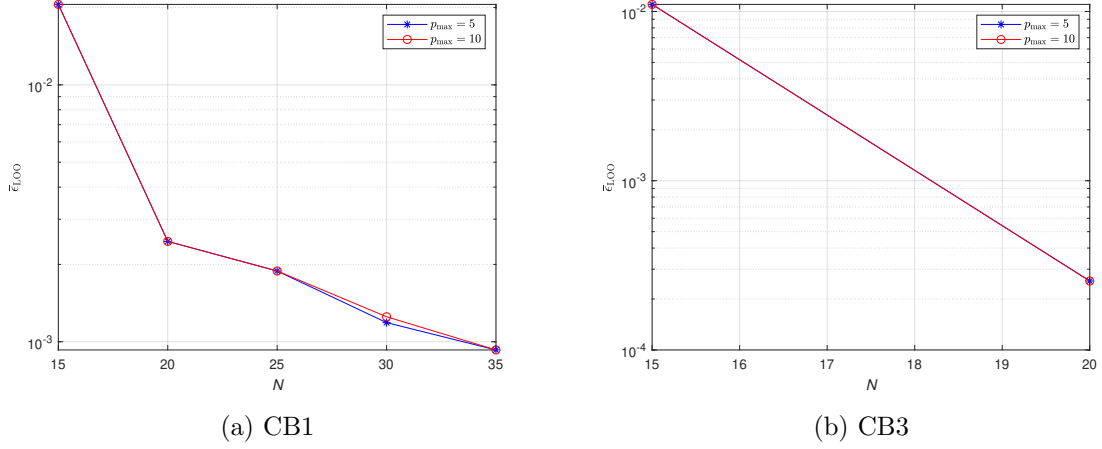


Figure 6.8: Evolution of LOO error for the impactor displacement of crash boxes

$\epsilon_{tol} = 1 \times 10^{-2}$ and $\epsilon_{tol} = 1 \times 10^{-3}$.

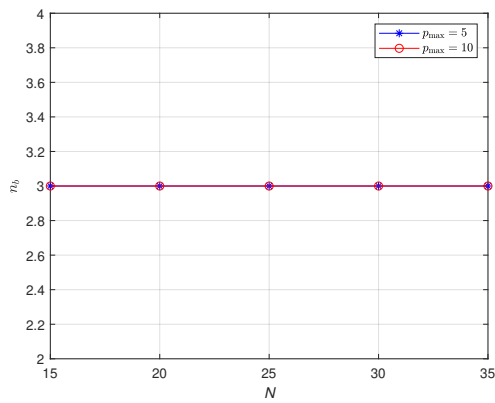
The crash box was simulated with LS-Dyna to get the model evaluations and it was performed by a Python program. A custom Python module enabled to extract the results from LS-Dyna output files. As the cost of the FE formulation for a single model evaluation is little high, it was not possible to get the MCS results for a large number of samples. For the reference result, the MCS was performed at $N_{MCS} = 10^3$ LHS points for all the crash boxes. The required CPU times for CB1, CB2 and CB3 were 18.23 h, 13.38 h and 12.87 h, respectively. For the adaptive POD-SVB-PCE model, Sobol sequence was used to increase the number of model evaluation adaptively. The maximum number of model evaluations was restricted to $N_{max} = 200$.

Impactor displacement

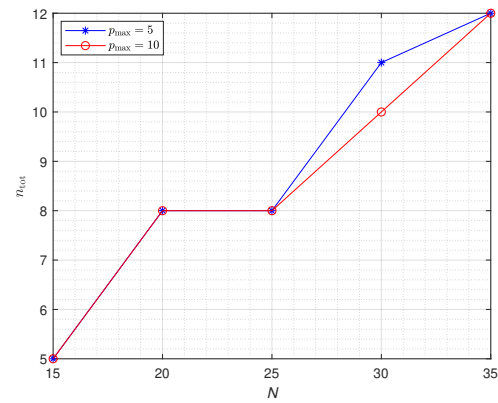
Firstly, the adaptive POD-SVB-PCE model was constructed for the impactor displacement. The initial number of model evaluation was fixed as $N_{ini} = 15$ and the number of samples was increased in step by $N_{incr} = 5$. The evolution of the LOO error for the impactor displacement of CB1 and CB3 is shown in Figure 6.8. For CB2, the required accuracy of 1×10^{-3} was achieved in the first iteration with $N = 15$ only. It is observed from the figure that the desired accuracy of 1×10^{-3} was obtained using $N = 35$ and $N = 20$ samples for CB1 and CB3, respectively. Furthermore, the same results were obtained whatever the maximum polynomial degree. The main reason is that the highest polynomial degree was 5 even using $p_{max} = 10$.

The evolution of the POM number and the total number of PCE coefficients with the sample number are shown in Figure 6.9 for CB1 and CB3. It is seen that the number of POM is constant with the increase of the sample number and the total numbers of PCE coefficients are quite small for all the sample points. Only $n_{tot} = 12$ and $n_{tot} = 14$ coefficients were required to predict 3 POD coefficient vectors for CB1 and CB3, respectively. For CB2, the impactor displacement was also obtained with 3 POM and the required number of coefficients was $n_{tot} = 10$ with a maximum PCE degree equal to 3.

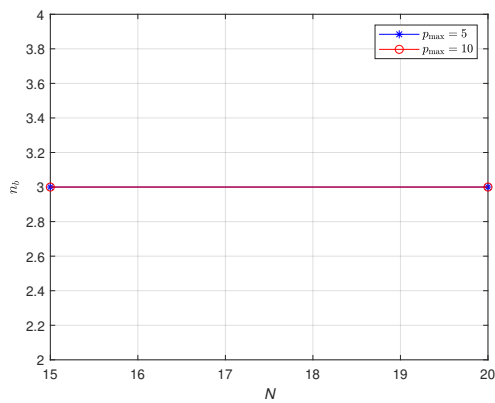
Although the MCS result was not available for a large number of samples, the statistical moments were estimated with $N_{MCS} = 10^3$ sample points and then, the adaptive POD-SVB-PCE model predicted statistical moments were compared with the MCS results, which are



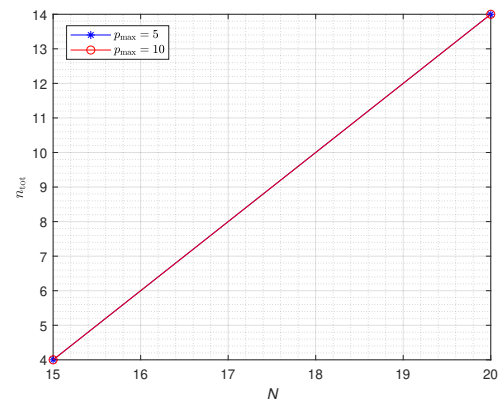
(a) Number of POM for CB1



(b) Total number of PCE coefficients for CB1



(c) Number of POM for CB3



(d) Total number of PCE coefficients for CB3

Figure 6.9: Evolution of the POM number (a)-(c) and the total number of PCE coefficients (b)-(d) with the increase of the sample number for the impactor displacement of crash boxes

Table 6.2: Predicted mean relative error $\bar{\epsilon}$ and number of sample points N for the impactor displacement of the crash boxes with the obtained adaptive POD-SVB-PCE model

| ϵ_{tol} | p_{max} | $\bar{\epsilon}(N)$ | | |
|-------------------------|------------------|---------------------------|---------------------------|---------------------------|
| | | CB1 | CB2 | CB3 |
| 1×10^{-2} | 5 | $2.20 \times 10^{-3}(20)$ | $3.48 \times 10^{-4}(15)$ | $3.41 \times 10^{-4}(20)$ |
| 1×10^{-3} | 5 | $1.26 \times 10^{-3}(35)$ | $3.48 \times 10^{-4}(15)$ | $3.41 \times 10^{-4}(20)$ |

shown in Figure 6.10. An almost similar variation of the statistical moments are observed for CB2 and CB3, which may reveal that the uncertain end mass has probably no influence on the results. For CB1, the most accurate result was predicted when the LOO error achieved 1×10^{-3} and all the surrogate model predicted results are the same for CB2 and CB3.

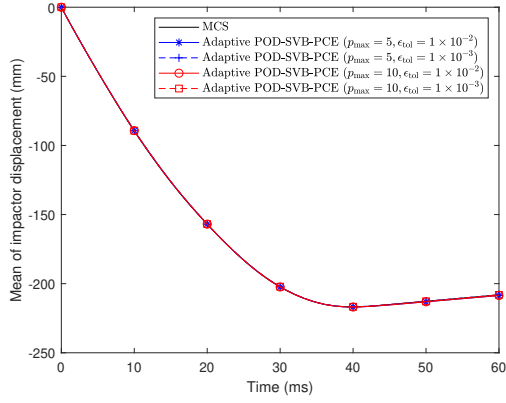
The impactor displacement predicted by the adaptive POD-SVB-PCE model was also compared with the FE computed results at 3 samples which are shown in Figure 6.11 for all the crash boxes with a LOO error of 1×10^{-3} . The samples were selected randomly from the 10^3 samples for all the crash boxes. It is seen that the displacements are predicted quite well for all the crash boxes. Furthermore, the obtained adaptive POD-SVB-PCE models were used to predict the responses at the 10^3 samples for all the crash boxes. The mean predicted errors are listed in Table 6.2. For CB2 and CB3, the mean predicted errors are quite close to each other, however CB2 took less samples than CB3. All the predicted errors are very close to the LOO errors obtained for the corresponding adaptive POD-SVB-PCE models in Figure 6.8. Therefore, the adaptive POD-SVB-PCE models are quite reliable to use for a practical problem.

Impactor velocity

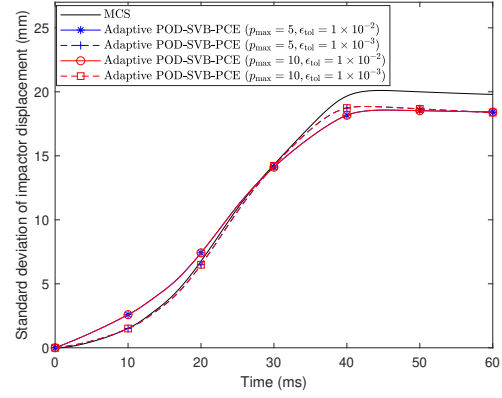
In a similar way to the impactor displacement, the adaptive POD-SVB-PCE model was also obtained for the impactor velocity. The variation of the LOO error with the number of sample points is shown in Figure 6.12. Unlike the impactor displacement, it is observed that the desired accuracy was obtained by the adaptive POD-SVB-PCE model using a higher number of samples: $N = 50$, $N = 35$ and $N = 40$ samples were required for CB1, CB2 and CB3, respectively with $p_{\text{max}} = 10$. The effect of using a high polynomial degree is noticeable in all three crash boxes. For CB1 and CB2, 10 model evaluations were saved with $p_{\text{max}} = 10$ while it saved 15 samples for CB3 with respect to $p_{\text{max}} = 5$. This is the main advantage of an adaptive surrogate model.

The evolution of the number of POM and the required total number of PCE coefficients are shown in Figure 6.13. The number of POM is noticeably higher for the impactor velocity as compared to the impactor displacement. The required number of POM for CB1 is comparatively higher as compared to CB2 and CB3. As a result, the total number of PCE coefficients is also high for CB1. For all the crash boxes, the number of total PCE coefficients is higher with $p_{\text{max}} = 10$ than with $p_{\text{max}} = 5$ which depicts higher degree terms were required with $p_{\text{max}} = 10$ to propagate the uncertain parameters. As a result, it was possible to achieve a good accuracy using a low number of samples with $p_{\text{max}} = 10$. Effectively, the required maximum degrees on achieving the desired accuracy of 1×10^{-3} were 5 (CB1, CB2, CB3) with $p_{\text{max}} = 5$, and 7 (CB1), 10 (CB2) and 6 (CB3) with $p_{\text{max}} = 10$.

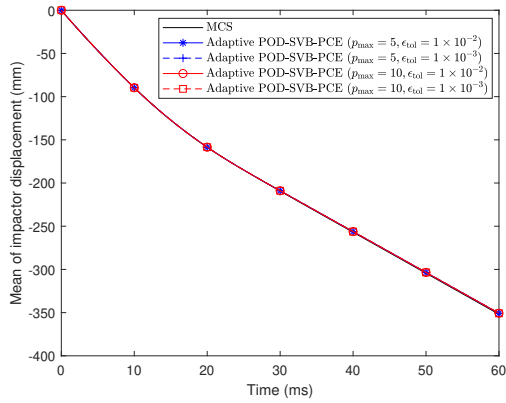
The time-dependent moments were computed for $N_{\text{MCS}} = 10^3$ samples, and are shown



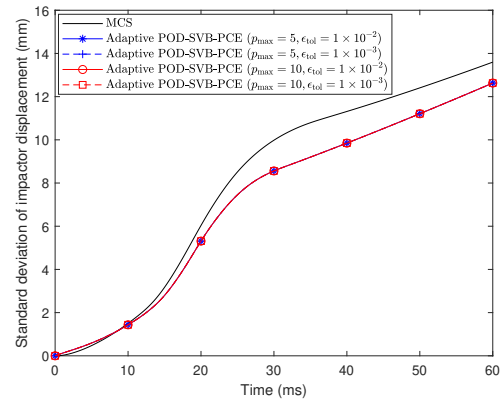
(a) Mean for CB1



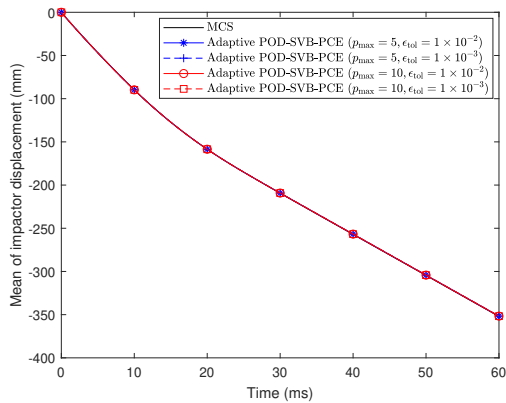
(b) Standard deviation for CB1



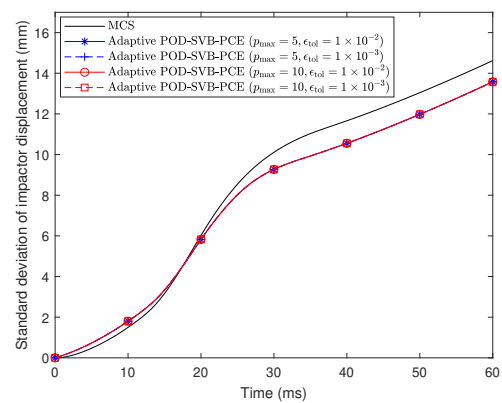
(c) Mean for CB2



(d) Standard deviation for CB2



(e) Mean for CB3



(f) Standard deviation for CB3

Figure 6.10: Comparison of statistical moments for the impactor displacement of crash boxes by different methods

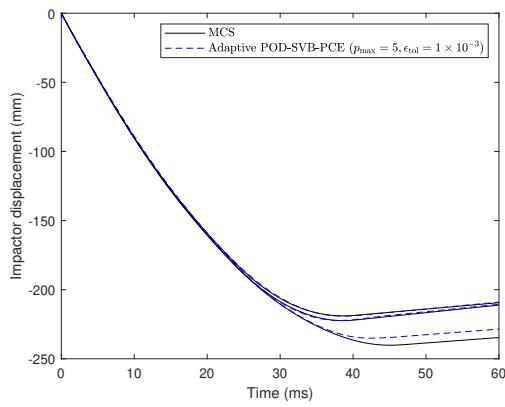
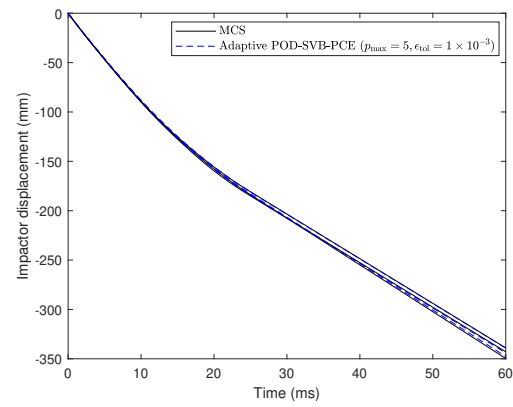
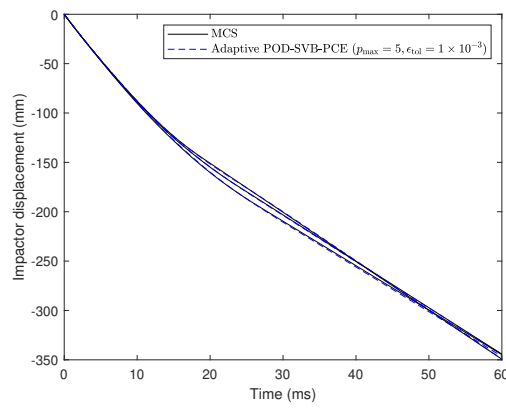
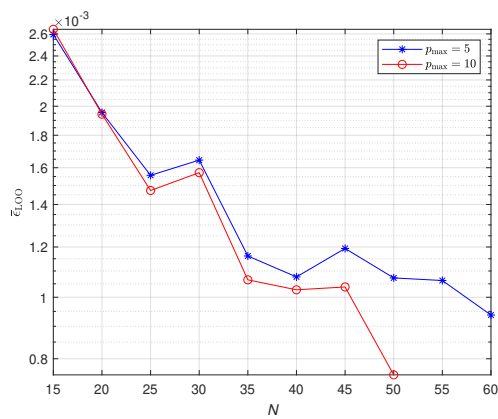
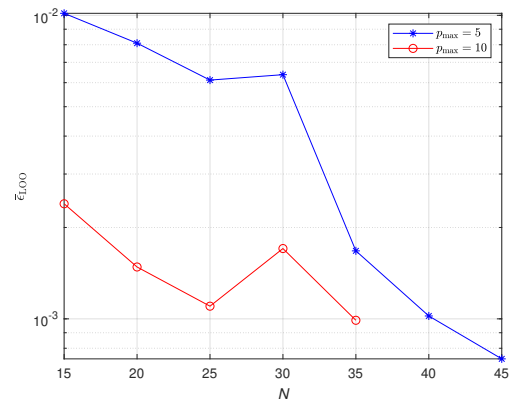
(a) $p_{\max} = 5$ for CB1(b) $p_{\max} = 5$ for CB2(c) $p_{\max} = 5$ for CB3

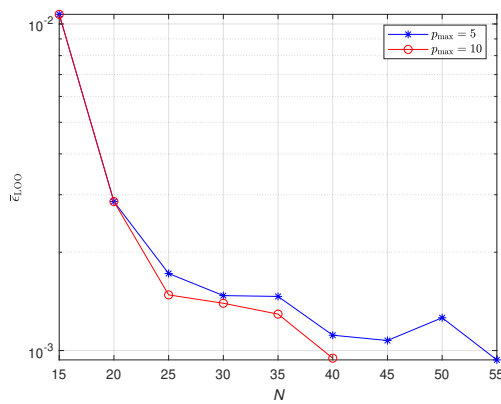
Figure 6.11: Comparison of the impactor displacement predicted by the adaptive POD-SVB-PCE model with the MCS results at 3 samples (the samples were selected randomly)



(a) CB1

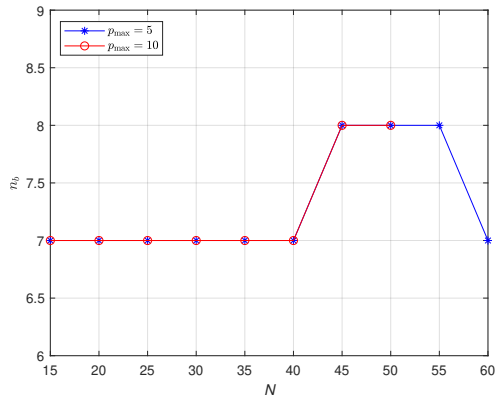


(b) CB2

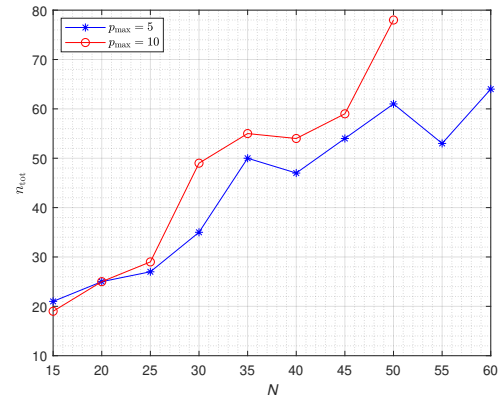


(c) CB3

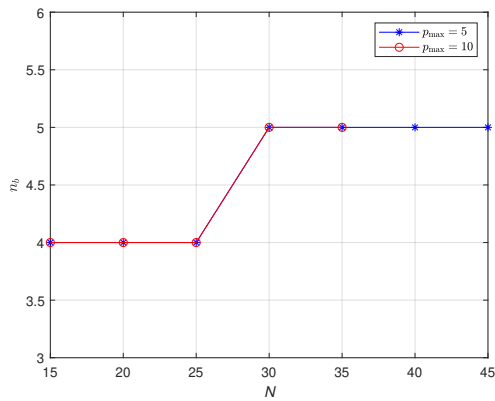
Figure 6.12: Evolution of LOO error for the impactor velocity of crash boxes



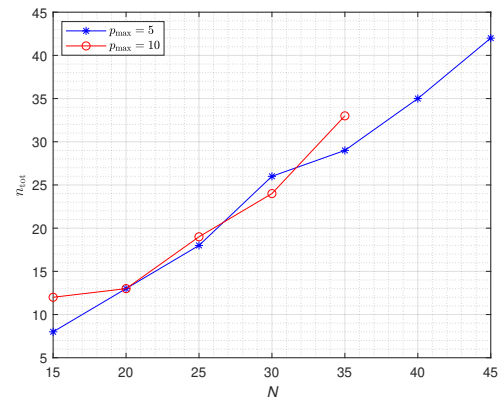
(a) Number of POM for CB1



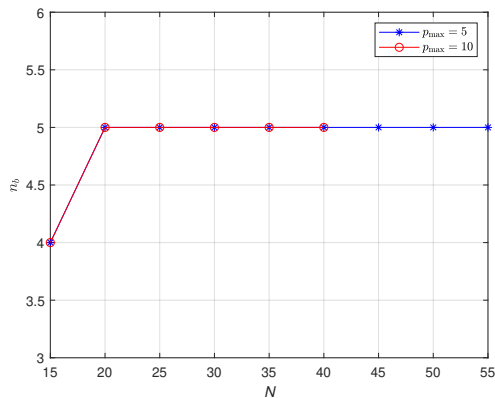
(b) Total number of PCE coefficients for CB1



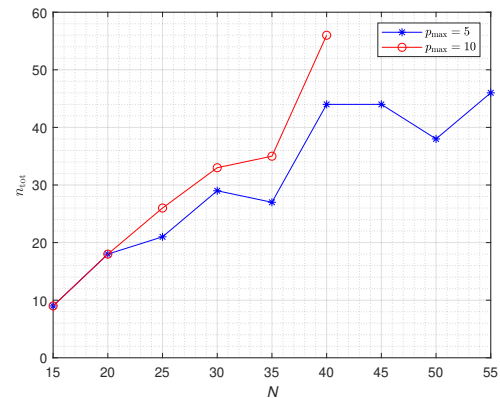
(c) Number of POM for CB2



(d) Total number of PCE coefficients for CB2



(e) Number of POM for CB3



(f) Total number of PCE coefficients for CB3

Figure 6.13: Evolution of the POM number (a)-(c)-(e) and the total number of PCE coefficients (b)-(d)-(f) with the increase of the sample number for the impactor velocity of crash boxes

Table 6.3: Predicted mean relative error $\bar{\epsilon}$ and number of sample points N for the impactor velocity of the crash boxes with the obtained adaptive POD-SVB-PCE model

| ϵ_{tol} | p_{max} | $\bar{\epsilon}(N)$ | | |
|-------------------------|------------------|---------------------------|---------------------------|---------------------------|
| | | CB1 | CB2 | CB3 |
| 1×10^{-2} | 5 | $2.85 \times 10^{-3}(15)$ | $9.87 \times 10^{-3}(20)$ | $5.99 \times 10^{-3}(20)$ |
| 1×10^{-2} | 10 | $2.33 \times 10^{-3}(15)$ | $8.57 \times 10^{-3}(20)$ | $5.99 \times 10^{-3}(20)$ |
| 1×10^{-3} | 5 | $1.81 \times 10^{-3}(60)$ | $1.19 \times 10^{-3}(45)$ | $2.50 \times 10^{-3}(55)$ |
| 1×10^{-3} | 10 | $1.17 \times 10^{-3}(50)$ | $1.13 \times 10^{-3}(35)$ | $2.35 \times 10^{-3}(40)$ |

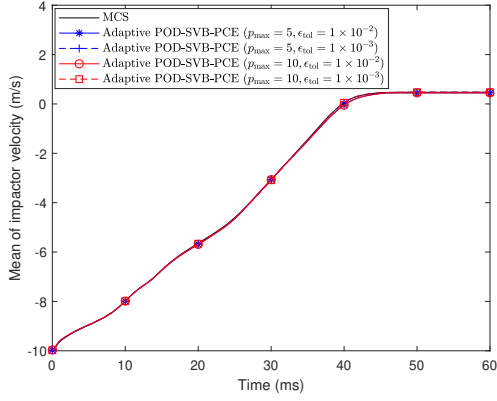
in Figure 6.14. Both statistical moments were predicted quite well by the adaptive POD-SVB-PCE model for all the crash boxes. Impactor velocity for CB2 and CB3 behaves almost similarly. The most accurate standard deviation was predicted with $p_{\text{max}} = 10$ on achieving an accuracy of 1×10^{-3} and at the same time it required less samples than it required with $p_{\text{max}} = 5$: for CB1 and CB2, 10 more samples were required with $p_{\text{max}} = 5$ and for CB3, 15 more samples were required to achieve an accuracy of 1×10^{-3} .

The impactor velocity predicted by the adaptive POD-SVB-PCE model was compared at 3 samples with the LS-Dyna computed results and it is shown in Figure 6.15. The samples were chosen randomly. It is observed that the responses at the 3 samples were predicted quite well with $p_{\text{max}} = 5$ and $p_{\text{max}} = 10$. The predicted responses with $p_{\text{max}} = 10$ are more accurate than with $p_{\text{max}} = 5$ for CB2 and CB3. Furthermore, the obtained adaptive POD-SVB-PCE models were validated using 10^3 samples (MCS results for these samples were obtained). The predicted relative mean errors with 10^3 samples were computed by Equation 3.11 and are listed in Table 6.3. The desired accuracy of 1×10^{-2} was achieved using the same number of samples with $p_{\text{max}} = 5$ and $p_{\text{max}} = 10$. However, some computational cost was reduced for all the crash boxes with $p_{\text{max}} = 10$, with respect to $p_{\text{max}} = 5$ when the requested LOO error was 1×10^{-3} ; the predicted errors are also lower with $p_{\text{max}} = 10$ using lower number of samples.

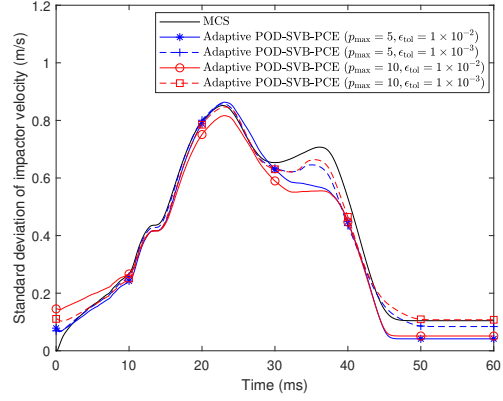
Contact force

The adaptive POD-SVB-PCE model was obtained with the same conditions as the previous responses for the contact force also. The evolution of the LOO error for all the three crash boxes is shown in Figure 6.16. The accuracy is progressively increasing with the increase of the sample number for all the crash boxes. For both maximum polynomial degrees, the minimum desired accuracy (1×10^{-2}) was not achieved even using the maximum number of model evaluations for the CB1 and CB2. However, the minimum desired accuracy of 1×10^{-2} was achieved for the CB3 using $N = 55$ and $p_{\text{max}} = 10$. For that reason, the number of model evaluations was increased further to achieve an accuracy of 1×10^{-3} , however it did not reach 1×10^{-3} . For the CB2, the LOO error achieved with $p_{\text{max}} = 10$ is very close to 1×10^{-2} . From the results of the impact oscillator, it is clear that obtaining a high accuracy for the contact force is more difficult than for the other response quantities and a similar observation is noticed here.

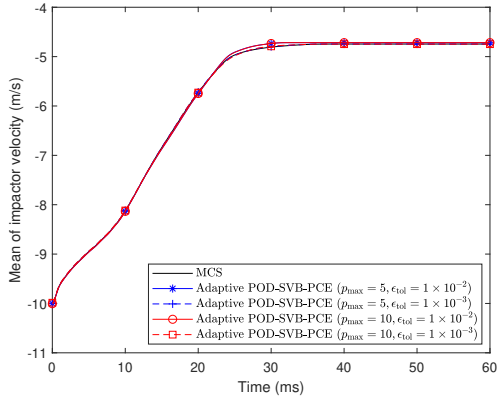
Furthermore, the evolution of the POM number and the evolution of the total number of PCE coefficients with the increase of the sample number are shown in Figure 6.17 for all the crash boxes. It is observed that the POM number was increased with the increase of the sample number and a large number of POM is required to decouple the time-dependent



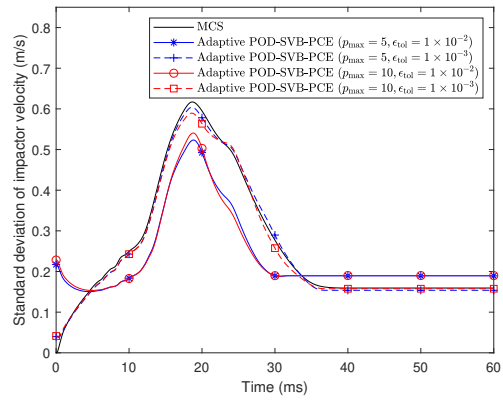
(a) Mean for CB1



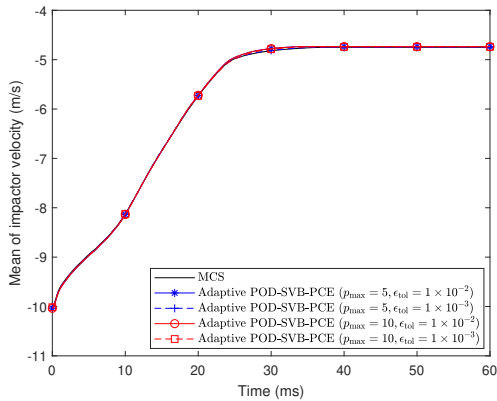
(b) Standard deviation for CB1



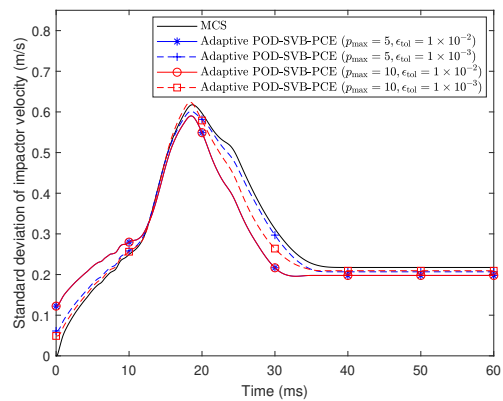
(c) Mean for CB2



(d) Standard deviation for CB2



(e) Mean for CB3



(f) Standard deviation for CB3

Figure 6.14: Comparison of statistical moments for the impactor velocity of crash boxes by different methods

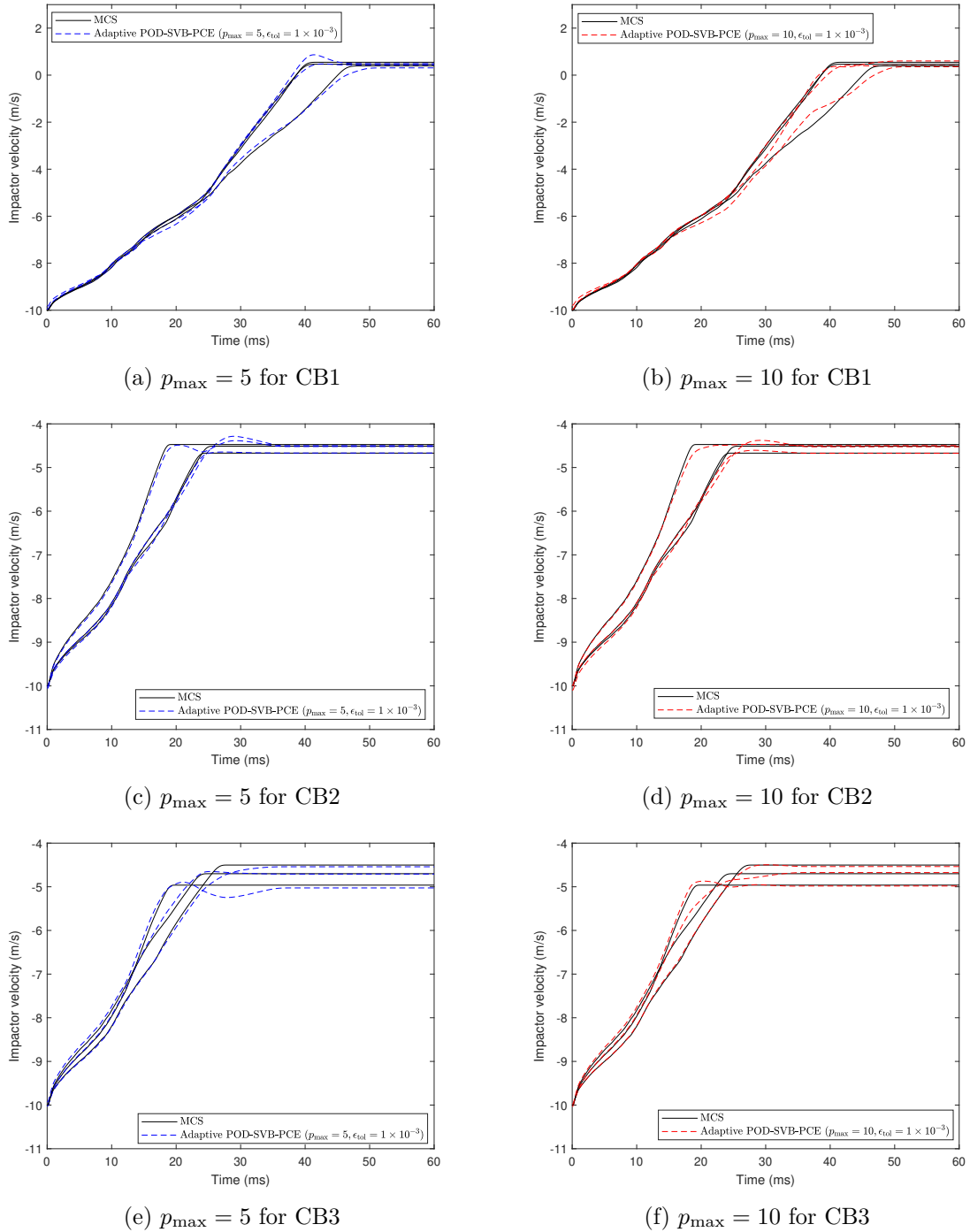
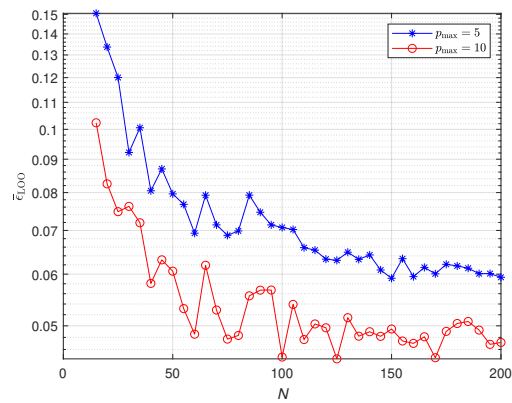
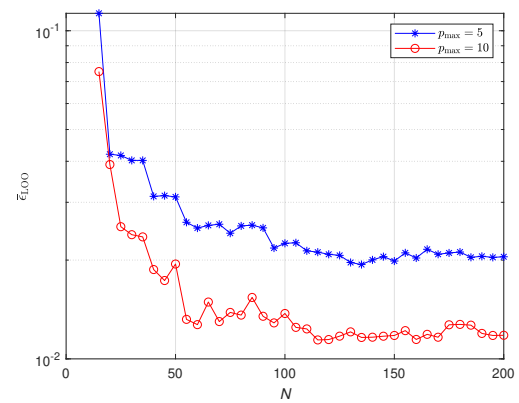


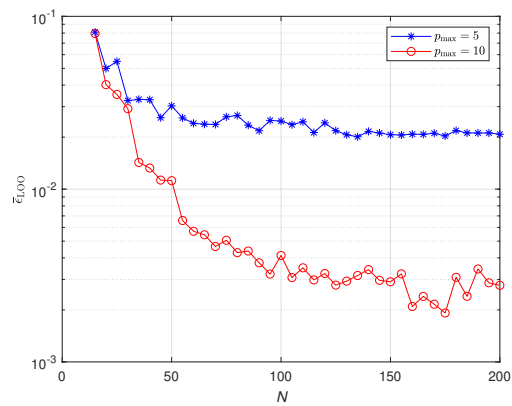
Figure 6.15: Comparison of the impactor velocity predicted by the adaptive POD-SVB-PCE model with the MCS results at 3 samples (the samples were selected randomly)



(a) CB1



(b) CB2



(c) CB3

Figure 6.16: Evolution of LOO error for the contact force of crash boxes

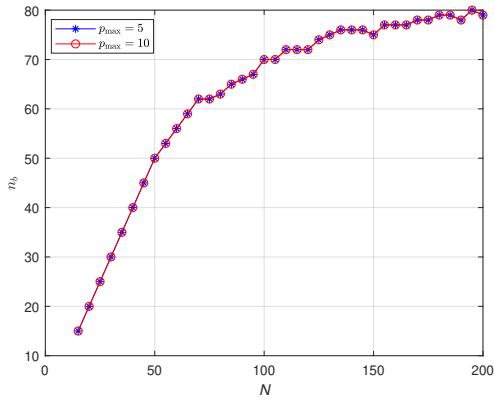
behavior and the randomness. For the CB1, $n_b = 79$ POM was required using $N = 200$ samples to obtain 99.99% of the energy. On the contrary, to obtain the desired energy, a lower number of POM was required for the CB2 and CB3: $n_b = 43$ and $n_b = 44$ POM were required, respectively. The total number of PCE coefficients was also increased with the samples for both maximum degrees in case of all crash boxes. The total number of coefficients is quite small considering the large number of retained POM for CB1 and for CB2. However, n_{tot} is quite large for CB3: it took 3505 PCE coefficients to approximate 44 POM. One of the reasons is that $d = 4$ random variables were there in CB3 whereas it was 3 for the other crash boxes. For $p_{\text{max}} = 10$ and $N = 200$, the adaptive POD-SVB-PCE model detected $n_{\text{tot}} = 483$ and $n_{\text{tot}} = 480$ important PCE coefficients for CB1 and CB2, respectively.

The statistical moments were computed using the $N_{\text{MCS}} = 10^3$ samples and the statistical moments predicted by the adaptive POD-SVB-PCE model were compared with the MCS results: they are shown in Figure 6.18. It is seen that the mean is predicted quite well using both maximum PCE degrees of 5 and 10 for all the crash boxes. However, the standard deviation predicted with $p_{\text{max}} = 10$ is slightly better than that predicted with $p_{\text{max}} = 5$. It is noticeable that the surrogate model results are quite close to the MCS results even without achieving the desired accuracy using a limited number of model evaluations ($N = 200$) for the CB1 and CB2. For the CB3, the minimum desired accuracy of 1×10^{-2} was achieved with $N = 55$ samples and $p_{\text{max}} = 10$. Therefore, the standard deviation with $N = 55$ was also predicted quite well for CB3. A significantly different variation of the statistical moments for all the crash boxes is noticed from the figure. For the CB1, the mean contact force lasts for a longer time than for CB2 and CB3 because the end was fixed for CB1. Further, the statistical moments for CB2 and CB3 almost behave in a similar fashion.

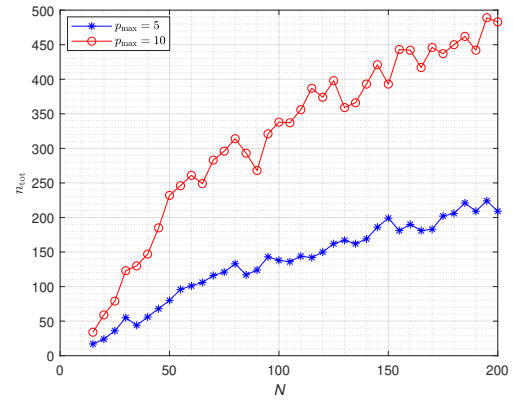
To closely follow the prediction behavior, the surrogate model predicted results were compared with the MCS results at 3 samples (chosen randomly) out of the 10^3 samples for each of the three crash boxes. The comparison is shown in Figure 6.19. The results were predicted with the adaptive POD-SVB-PCE model constructed with $N = 200$ samples for CB1 and CB2 while $N = 55$ samples were used for the prediction of the contact force of CB3 with $p_{\text{max}} = 10$ and threshold value 1×10^{-2} . It is seen from the figures that the prediction accuracies are quite good with both polynomial degrees for all the crash boxes. However, some non-physical negative forces were predicted in a similar way to the impact oscillator and these non-physical forces were minimized with $p_{\text{max}} = 10$. Furthermore, the adaptive POD-SVB-PCE model predicted results were validated with the MCS results at 10^3 samples and the mean relative error was computed for the 10^3 samples by Equation 3.11: the mean relative error is given in Table 6.4. The highest prediction accuracy was obtained in case of CB2 with $p_{\text{max}} = 10$. It is also noticeable that the prediction accuracies are very close to the obtained LOO errors in Figure 6.16. It has been observed from this study that predicting the contact force with the adaptive POD-SVB-PCE model is very challenging. Although some discrepancies were noticed by the surrogate model results, the results are quite good using only $N = 200$ model evaluations.

Maximum contact force

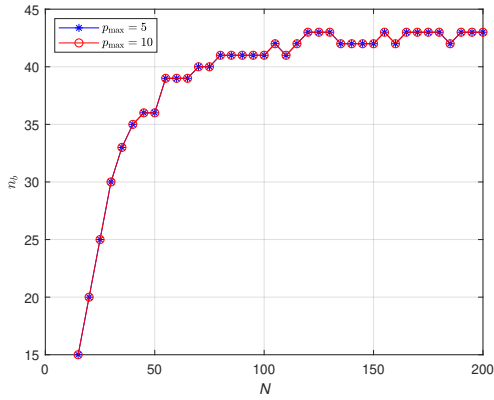
UQ was performed for the maximum contact force. As the maximum contact force is time-independent, UQ was performed by the adaptive SVB-PCE model (Algorithm 6.1). The domain of the PCE polynomial degree for the maximum contact force was set as $p \in \{1, 15\}$. The initial number of model evaluations was $N_{\text{ini}} = 10$. The number of samples is increased



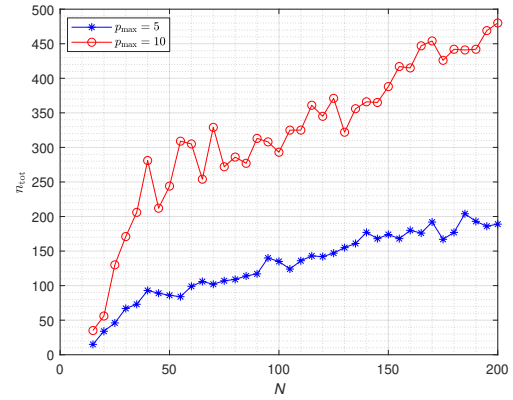
(a) Variation of POM for CB1



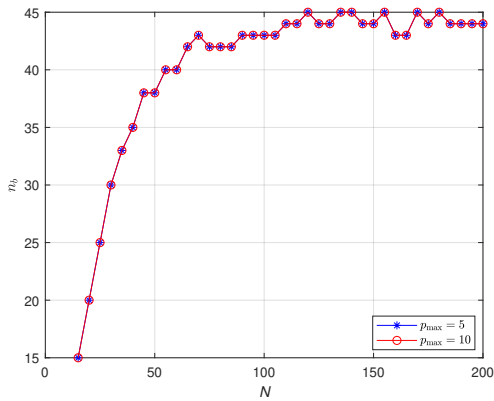
(b) Total PCE coefficients for CB1



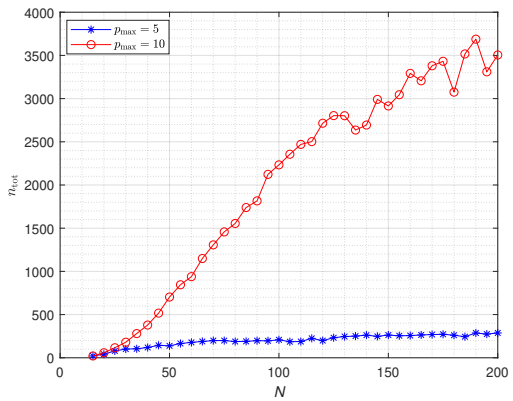
(c) Variation of POM for CB2



(d) Total PCE coefficients for CB2

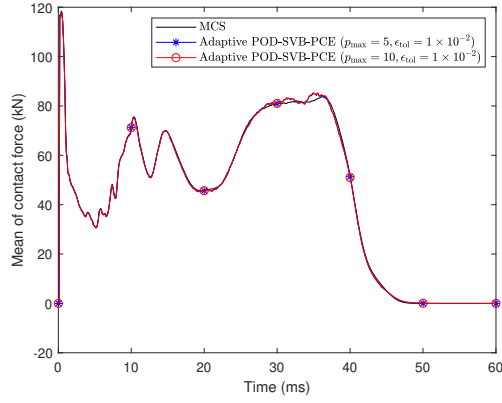


(e) Variation of POM for CB3

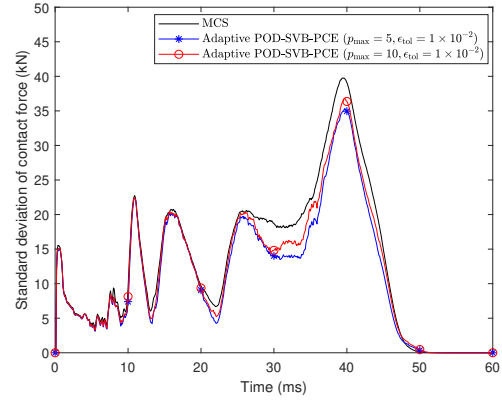


(f) Total PCE coefficients for CB3

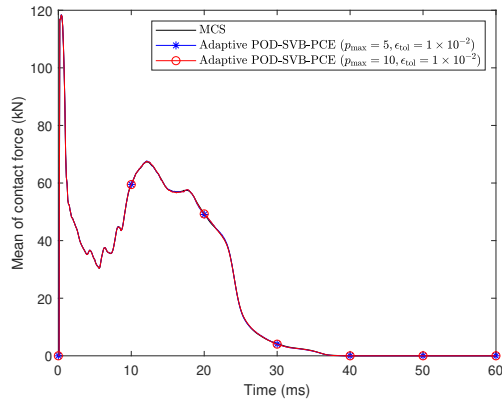
Figure 6.17: Evolution of the POM number (a)-(c)-(e) and the total number of PCE coefficients (b)-(d)-(f) with the increase of the sample number for the contact force of crash boxes



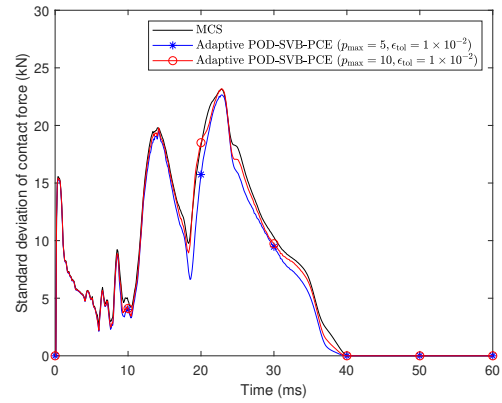
(a) Mean for CB1



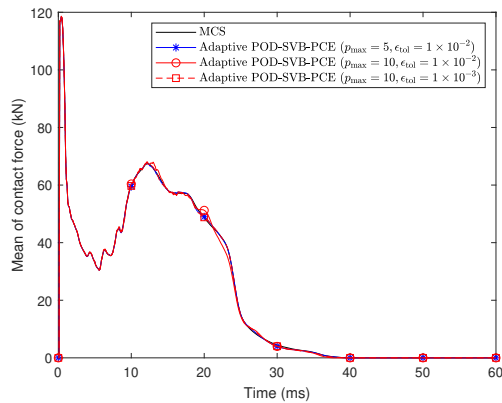
(b) Standard deviation for CB1



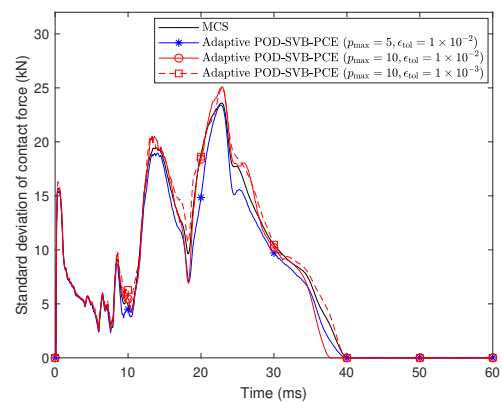
(c) Mean for CB2



(d) Standard deviation for CB2



(e) Mean for CB3



(f) Standard deviation for CB3

Figure 6.18: Comparison of statistical moments of the contact force for all crash boxes by different methods

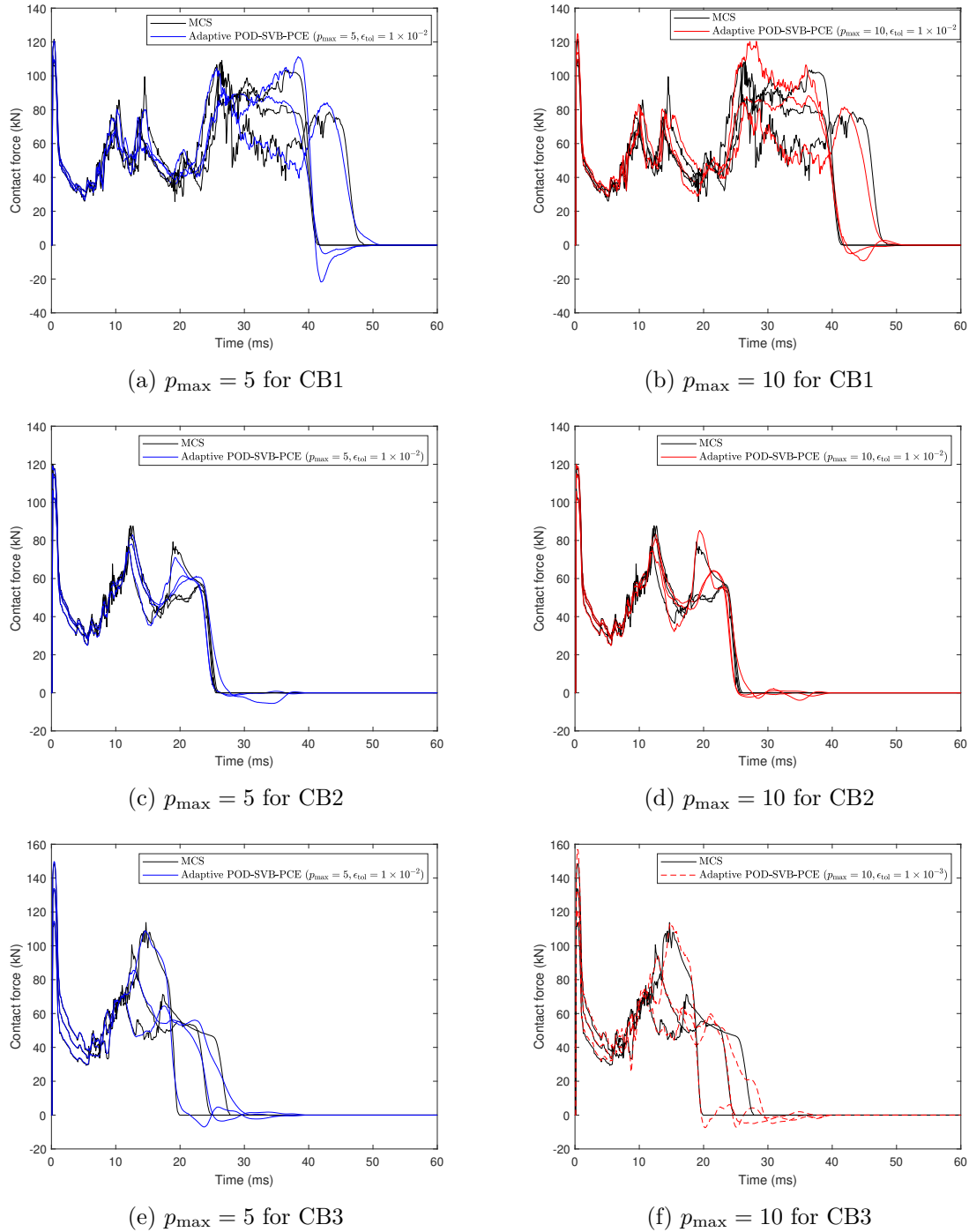


Figure 6.19: Comparison of the contact force predicted by the adaptive POD-SVB-PCE model with the MCS results at 3 samples (the samples were chosen randomly)

Table 6.4: Predicted mean relative error $\bar{\epsilon}$ and number of sample points N for the contact force of the crash boxes with the obtained adaptive POD-SVB-PCE model

| | | $\bar{\epsilon}(N)$ | | |
|-------------------------|------------------|----------------------------|----------------------------|----------------------------|
| ϵ_{tol} | p_{max} | CB1 | CB2 | CB3 |
| 1×10^{-2} | 5 | $6.06 \times 10^{-2}(200)$ | $1.88 \times 10^{-2}(200)$ | $5.05 \times 10^{-2}(200)$ |
| 1×10^{-2} | 10 | $5.60 \times 10^{-2}(200)$ | $1.71 \times 10^{-2}(200)$ | $8.03 \times 10^{-2}(55)$ |
| 1×10^{-3} | 10 | - | - | $2.34 \times 10^{-2}(200)$ |

Table 6.5: Predicted percentage error (PE) for the maximum contact force of the crash boxes by the obtained adaptive SVB-PCE model with $p_{\text{max}} = 15$

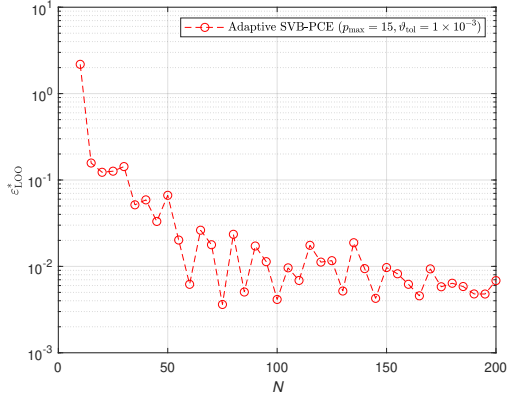
| | | PE(N) | | |
|-------------------------|--|------------|-----------|-----------|
| ϵ_{tol} | | CB1 | CB2 | CB3 |
| 1×10^{-3} | | 5.06%(200) | 0.90%(20) | 0.87%(20) |

by step of $N_{\text{incr}} = 5$ and the maximum number of model evaluations was fixed as $N_{\text{max}} = 200$. The adaptive SVB-PCE model was constructed only for one threshold value $\vartheta_{\text{tol}} = 1 \times 10^{-3}$ for all the crash boxes. The variation of the modified LOO error ϵ_{LOO}^* with the increase of sample number is shown in Figure 6.20 along with the variation of the PCE coefficient number. It is observed that the desired accuracy was not achieved even with N_{max} for CB1 while the desired accuracy was achieved for CB2 and CB3 using much less samples ($N = 20$). The number of PCE coefficients increased with the increase of the sample number: the number of important terms for CB1 is quite high as compared to the others. However, the number of terms in CB1 is quite small as compared to the total terms in the full PCE model ($n = 816$ for $p = 15$). On the contrary, CB2 and CB3 required only $p = 3$ and $p = 4$ to achieve the desired accuracy.

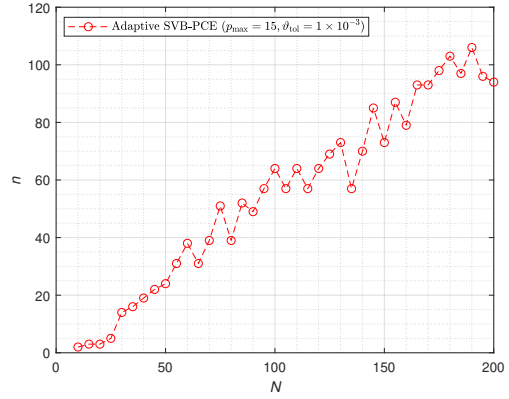
The PDF was computed by the adaptive SVB-PCE model with 10^3 samples and it is compared with the MCS results in Figure 6.21 for all the crash boxes. The reason of the high number of model evaluations for CB1 is quite clear from the PDF. The right side tail of the PDF for CB1 is quite long and obtaining a good result at this position is quite difficult with a low number of model evaluations. The PDF for CB2 and CB3 are almost the same and it is one of the reasons to achieve the desired accuracy using the same number of model evaluations. For all the crash boxes, the PDFs predicted by the adaptive SVB-PCE model are well in line with the reference PDFs from MCS. The percentage error (PE) was also computed using Equation 5.42 for the 10^3 samples, it is listed in Table 6.5 for all the crash boxes. As the desired accuracy was not achieved for CB1, the predicted error is higher for CB1 than for the other two cases. On the other hand, the accuracy at the predicted samples is quite good for CB2 and CB3.

Total dissipated energy

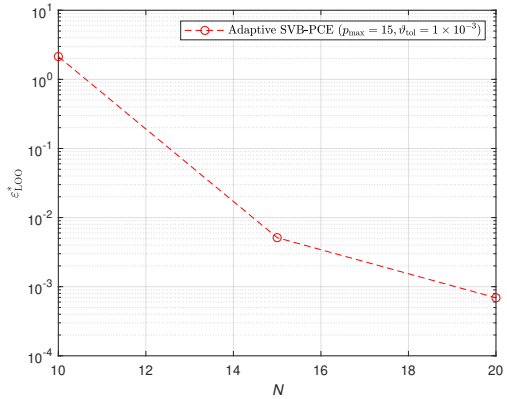
The total energy dissipated during the crash was computed by integrating the force-displacement curve and UQ was performed for the dissipated energy using the adaptive SVB-PCE model. All the parameters for the adaptive SVB-PCE model were the same as the ones for the maximum contact force study. The initial number of model evaluations was $N_{\text{ini}} = 10$. The



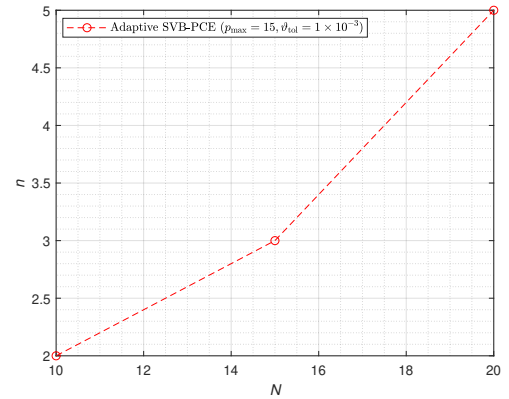
(a) Variation of LOO error for CB1



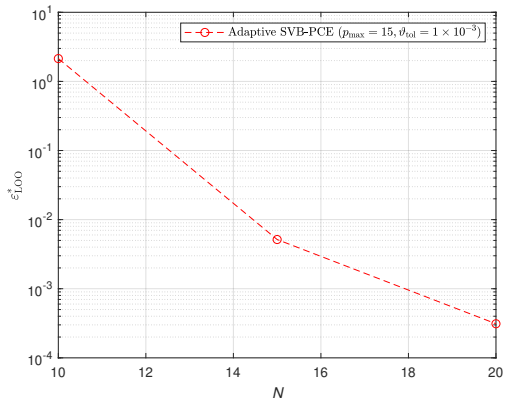
(b) Variation of the PCE coefficients for the CB1



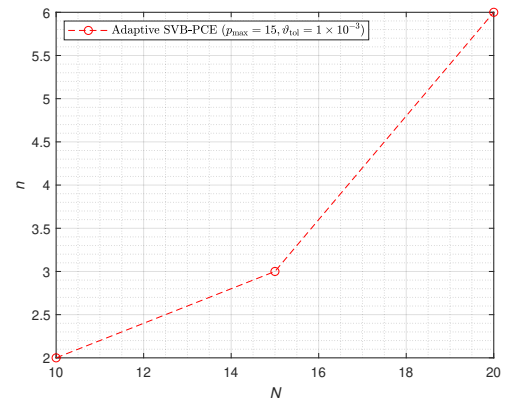
(c) Variation of LOO error for CB2



(d) Variation of the PCE coefficients for the CB2



(e) Variation of LOO error for CB3



(f) Variation of the PCE coefficients for the CB3

Figure 6.20: Evolution of the modified LOO error and the number of selected PCE coefficients with the increase of the sample number for the maximum contact force of all the crash boxes

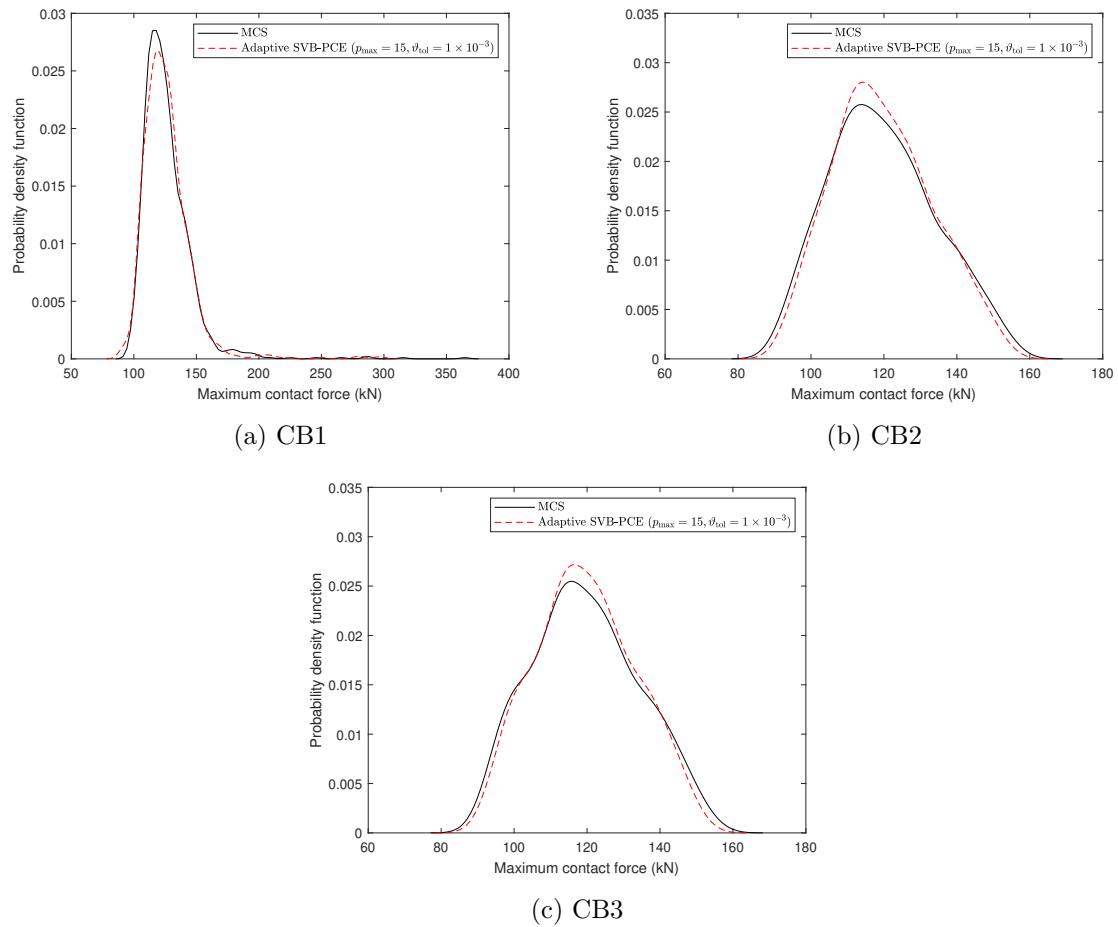


Figure 6.21: PDF of the maximum contact force for all the crash boxes by different approaches

Table 6.6: Predicted percentage error (PE) for the dissipated energy of the crash boxes by the obtained adaptive SVB-PCE model with $p_{\max} = 15$

| ϵ_{tol} | PE(N) | | |
|-------------------------|-----------|-----------|-----------|
| | CB1 | CB2 | CB3 |
| 1×10^{-3} | 0.34%(15) | 0.48%(60) | 0.80%(40) |

evolution of the LOO error and the selected PCE coefficients is shown in Figure 6.22 for all the crash boxes. Unlike the maximum contact force, a low number of model evaluations was required for CB1 here whereas much higher model evaluations was required for CB2 and CB3 to achieve the desired accuracy of 1×10^{-3} . For CB1, the required number of terms was only $n = 2$ with maximum degree $p = 1$ while the required number of terms for CB2 and CB3 was $n = 34$ and $n = 22$ with maximum degree $p = 13$ and $p = 10$, respectively.

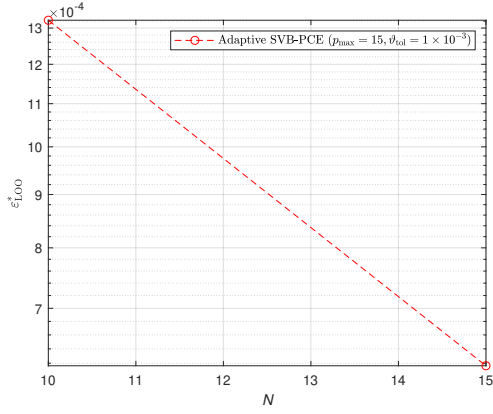
The PDF was also determined on obtaining the desired accuracy with the adaptive SVB-PCE model and it is shown in Figure 6.23 for all the crash boxes. It is seen that the distribution pattern is almost uniform for CB1 and it is narrow for CB2 and CB3. The adaptive SVB-PCE model has predicted quite good result for all the crash boxes. Further, The PE for the predicted response at 10^3 samples was computed and are listed in Table 6.6. All the PE are less than 1% which can be regarded as quite a good results.

6.6 Global sensitivity analysis of the crash box model

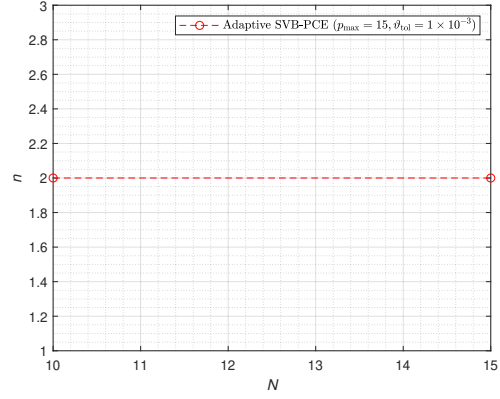
6.6.1 Adaptive POD-SVB-PCE model for time-dependent sensitivity analysis

Sensitivity analysis (SA) measures the effect of the uncertain parameters on a QoI for a system (Saltelli et al., 2008). SA is globally divided in two distinct categories: local SA (Borgonovo and Plischke, 2016) and global SA (GSA) (Sobol, 2001). The former measures the local effect of an uncertain parameter on the QoI through the derivative of the QoI with respect to the uncertain parameter (Helton, 1993). On the other hand, GSA measures the effect of the whole input space on the QoI considering uncertainties (Borgonovo and Plischke, 2016; Sobol, 2001). Various approaches are available in the literature for GSA such as regression based approach (Helton, 1993), variance based approach (Iman and Hora, 1990; Sobol, 1993) and moment independent approach (Borgonovo, 2007; Chakraborty and Chowdhury, 2017). Out of all, the variance based approach has attained more popularity than the others.

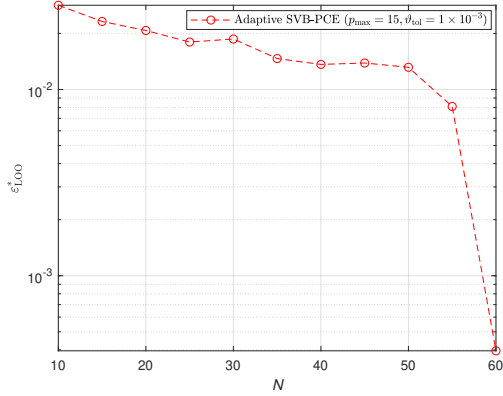
The variance based approach for GSA was proposed by Iman and Hora (1990); Sobol (1993) for the first time. The main idea of the variance based approach came from Efron and Stein (1981), which is the computation of the contribution of variance in the output quantity for a single or a combined effect of inputs. According to Sobol' (Sobol, 1993), the variance based approach is performed by decomposing the output variance into the single and the combine effect of the inputs. Often this method is known as the ANalysis Of VAriance (ANOVA) (Saltelli et al., 2010). The approach proposed by Sobol' (Sobol, 1993, 2001) is widely acknowledged to compute the sensitivity indices (SI), and derived from the decomposition of the variance. To perform GSA for an uncertain system, multidimensional integrals over the input space can be computed by MCS (Sobol, 1990) technique. The computation procedure of Sobol' sensitivity indices is described in Appendix D. Sobol (2001) proposed



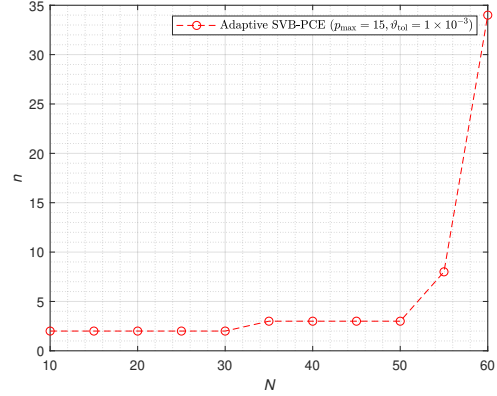
(a) Variation of LOO error for CB1



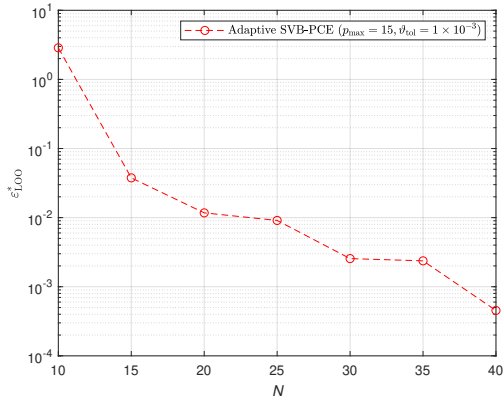
(b) Variation of the PCE coefficients for the CB1



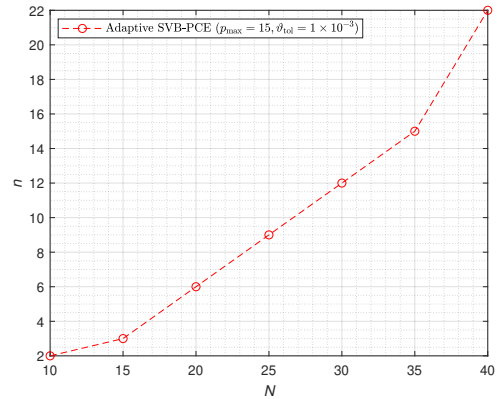
(c) Variation of LOO error for CB2



(d) Variation of the PCE coefficients for the CB2



(e) Variation of LOO error for CB3



(f) Variation of the PCE coefficients for the CB3

Figure 6.22: Evolution of the modified LOO error and the number of selected PCE coefficients with the increase of sample number for the dissipated energy of all the crash boxes

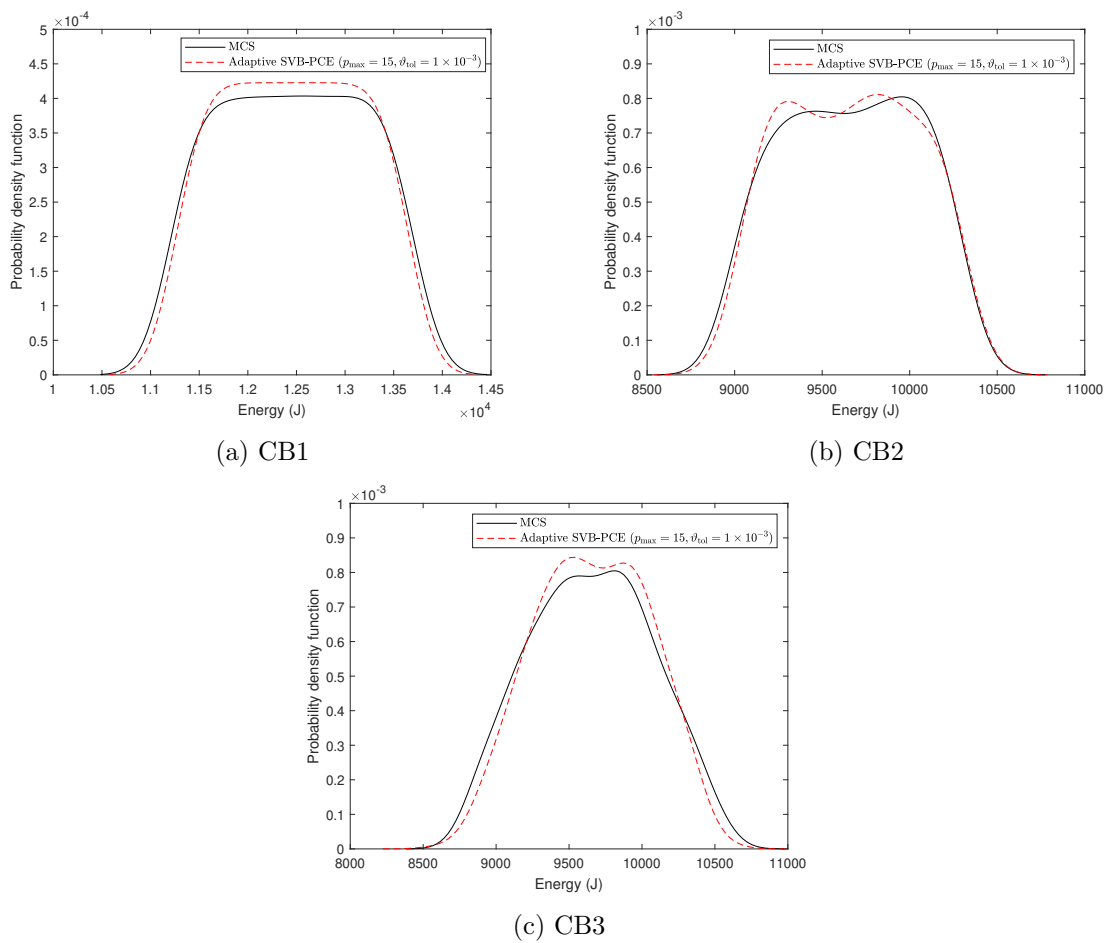


Figure 6.23: PDF of the dissipated energy for all the crash boxes by different approaches

two different types of sensitivity indices: partial sensitivity indices (PSI) (also known as the main effect SI or the first order SI) and total sensitivity indices (TSI). The former only takes care of the variance contribution due to a particular term in the Sobol' decomposition (See Appendix D) whereas the later considers the total sensitivity of a random variable including the interaction terms involving this variable.

In the present research work, the sensitivity analysis is performed considering the uncertain parameters independent.

The main difficulty with the MCS approach is that it requires a large number of model evaluations and it is not possible to obtain such large number of model evaluations for the crash problem. To address this issue, several surrogate models have been developed in the literature (Sudret, 2008; Blatman and Sudret, 2010a; Shao et al., 2017; Ge et al., 2015; Park and Sandberg, 1991; Wu et al., 2019). The PSI and the TSI are computed here by post-processing the PCE coefficients as explained by Sudret (2008). Therefore, after obtaining the adaptive SVB-PCE model using Algorithm 6.1, $\text{var}(y)$ can be computed from Equation 2.15. For computing the PSI, the variance of the conditional expectation in Equation D.7 can be obtained as:

$$\text{var}_{\xi_i} (\mathbb{E}_{\xi_{\sim i}} (y|\xi_i)) = \sum_{\substack{j=1 \\ p_{\xi_{i,j}} \neq 0 \& p_{\xi_{\sim i,j}} = 0}}^n a_j^{*2} \quad (6.11)$$

where $p_{\xi_{i,j}} \neq 0 \& p_{\xi_{\sim i,j}} = 0$ indicates that the j -th multivariate polynomial corresponding to the j -th coefficient has a degree equal to zero for all the univariate polynomials except the one related to the i -th variable, which one must not have a degree equal to zero. Therefore, the PSI can be computed by directly substituting Equation 6.11 and the square of Equation 2.15 in Equation D.7. For the TSI, the conditional expectation in Equation D.8 is given by post-processing of the PCE coefficients:

$$\mathbb{E}_{\xi_{\sim i}} (\text{var}_{\xi_i} (y|\xi_{\sim i})) = \sum_{\substack{j=1 \\ p_{\xi_{i,j}} \neq 0}}^n a_j^{*2} \quad (6.12)$$

The above-mentioned expressions can easily be extended to for a time-dependent response, by defining time-dependent indices. The PSI and the TSI for time-dependent QoI are given by:

$$S_i(t) = \frac{\text{var}_{\xi_i} (\mathbb{E}(y(t) |\xi_i))}{\text{var}(y(t))} \quad (6.13)$$

$$S_{Ti}(t) = \frac{\mathbb{E}(\text{var}_{\xi_i}(y(t) |\xi_{\sim i}))}{\text{var}(y(t))} \quad (6.14)$$

The time-dependent variance $\text{var}(y(t))$ can be computed easily from Equation 4.14 after obtaining the adaptive POD-SVB-PCE model. In a similar way to the time-dependent mean and variance, the time-dependent sensitivity indices can also be computed using the PCE coefficients and the POM. To compute the time-dependent PSI, the variance of the conditional expectation in Equation 6.13 is given by:

$$\text{var}_{\xi_i} (\mathbb{E}(y(t) |\xi_i)) = \sum_{i_1=1}^{n_b} \sum_{i_2=1}^{n_b} \text{cov} [\mathbb{E}(b_{i_1}|\xi_i), \mathbb{E}(b_{i_2}|\xi_i)] \mathbf{V}_{i_1}(t) \mathbf{V}_{i_2}(t) \quad (6.15)$$

where $\mathbf{V}(t)$ is the POM obtained from the POD approach. $\text{cov}[\mathbb{E}(b_{i_1}|\xi_i), \mathbb{E}(b_{i_2}|\xi_i)]$ is the conditional covariance given by:

$$\text{cov}[\mathbb{E}(b_{i_1}|\xi_i), \mathbb{E}(b_{i_2}|\xi_i)] = \sum_{\substack{j=1 \\ p_{i,j} \neq 0 \& p_{\sim i,j} = 0}}^n a_{j,i_1}^* a_{j,i_2}^* \quad (6.16)$$

For the time-dependent TSI, the expectation of the variance is given by:

$$\mathbb{E}(\text{var}_{\xi_i}(y(t)|\xi_{\sim i})) = \sum_{i_1=1}^{n_b} \sum_{i_2=1}^{n_b} \left[\sum_{\substack{j=1 \\ p_{\xi_{i,j}} \neq 0}}^n a_{j,i_1}^* a_{j,i_2}^* \right] \mathbf{V}_{i_1}(t) \mathbf{V}_{i_2}(t) \quad (6.17)$$

Substituting Equation 6.17 in Equation 6.14, the time-dependent TSI can be computed without any additional computational cost.

6.6.2 Global sensitivity analysis of the quarter crash boxes

Global sensitivity analysis for contact force

As discussed in the previous sub-section, a time-dependent GSA was performed using the obtained adaptive POD-SVB-PCE result without any additional computational cost. The GSA was performed using the adaptive POD-SVB-PCE model with $N = 200$ and $p_{\max} = 10$ even if the minimum accuracy of 1×10^{-2} was not obtained for CB1 and CB2. Therefore, the GSA results obtained from the adaptive POD-SVB-PCE model for CB1 and CB2 may not be accurate. PSI for the three crash boxes are shown in Figure 6.24 for all the uncertain parameters. It is noticeable from the figure that PSI after some times are not plotted for all the crash boxes because the variance is zero beyond the contact region. Along with the PSI, a sensitivity index ratio (SIR) for all the uncertain parameters is also plotted in Figure 6.24, which is defined as:

$$\text{Sensitivity index ratio (SIR)} = \frac{\text{PSI}}{\text{TSI}} \quad (6.18)$$

SIR measures the influence of the interaction terms and it varies between 0 and 1 i.e. $0 \leq \text{SIR} \leq 1$. The influence of the interaction terms is low when SIR is close to 1. However, when SIR is close to zero, the TSI value must be checked to decide whether the influence of the interactions is high or not: indeed, SIR may be close to zero when PSI is (almost) equal to zero even with a low TSI value.

As the MCS results were unavailable, it was not possible to compare these results with the actual results. It is observed from Figure 6.24 that the contact force is less sensitive to the impactor mass than the other random variables for CB1. The PSI for H and c_σ up to about $t = 15$ ms behaves almost similarly. Afterwards, the crash box thickness is more influential than the other parameters for most of the times. The SIR for H and c_σ almost behaves similarly up to $t = 23$ ms: a similar influence of the interaction terms is noticed for both parameters. In this time period, the SIR is quite high for most of the times, therefore a low influence of the interaction terms is noticed. The SIR for c_σ is quite low after this time period, therefore an influence of the interaction terms is noticed. However, an opposite behavior is noticed for H and c_σ around $t = 40$ ms. SIR for the impactor mass is quite low up to $t = 8$ ms. However, in that particular case, this is due to the very low (almost zero) value of PSI: TSI is about 0.05 and then the influence of m_I through the interaction terms is low.

For CB2 also, the contact force is less sensitive to the impactor mass than H and c_σ . The variation of the PSI for H and c_σ is almost similar with time. It is seen from Figure 6.24d that the influence of the interaction terms behaves similarly with time for H and c_σ . For both of these parameters, SIR is quite high (close to 1) during the initial time. Therefore, the influence of the interaction terms is quite low during the initial times. SIR for the impactor mass is between 0 and 0.4 from 11 ms to the end of the crash: it indicates a quite high influence of the interaction terms during this time period. The influence of m_I is very low for CB2 and CB3.

The time-dependent PSI and SIR for CB3 are shown in Figure 6.24e and Figure 6.24f. It is noticed that the material property and the crash box thickness are the most influential for the contact force of CB3. PSI for the impactor mass and for the end mass is very low during the crash: both masses have no influence on the contact force. SIR for both masses is quite low but it is due to the fact that the PSI is very low: in fact, TSI is quite low as well (between 0 and 0.3). Therefore, the interaction terms don't have a strong influence on the contact force for m_I and m_E . Similar to CB2, SIR for H and c_σ is quite high during the initial period of the crash: it indicates a very low influence of the interaction terms for both of these parameters. SIR for H and c_σ gets lower as the crash progresses which means the influence of the interaction terms is increasing with time for both of these parameters.

Global sensitivity analysis for impactor velocity

In a similar way to the contact force, time-dependent GSA was also performed considering impactor velocity as the QoI. The results were obtained with the adaptive POD-SVB-PCE model after reaching the lowest threshold error i.e. $\epsilon_{\text{tol}} = 1 \times 10^{-3}$ and with $p_{\text{max}} = 10$. Therefore, GSA was performed for CB1, CB2 and CB3 with the adaptive POD-SVB-PCE model obtained with $N = 50$, $N = 35$ and $N = 40$, respectively.

The sensitivity indices on the impactor velocity are shown in Figure 6.25. The PSI of H and c_σ is higher as compared to the impactor mass PSI for all the crash boxes during the crash. It is noticeable that the PSI for m_I , H and c_σ are very close to zero at the initial time, and the initial SIR for these three uncertain parameters are very low. It suggests that the interaction between these parameters is very high at the very beginning of the impact: this is confirmed by a high value of TSI (at least greater than 0.5). Afterwards, SIR for all the parameters of CB1 increases with time during the crash which indicates a low influence of the interaction terms. Further, SIR of H starts decreasing after 30 ms for CB1. The lowest SIR is noticed for the impactor mass of CB1 after the crash and therefore, as TSI is about 0.25, a moderate influence of the interaction terms was found, which is confirmed by a TSI. The PSI of m_I is quite low during the crash for CB2 and CB3 as compared to the other parameters. SIR for m_I is close to 1 for CB2 and CB3. As a result, no such interaction effect is noticed. However, the PSI of m_E is the lowest one for CB3 during the crash. PSI of the impactor mass starts increasing in case of CB2 and CB3 after the crash because the crash boxes were moving freely only due to the impacting mass during this period and therefore, the velocity was only governed by the impactor mass. Indeed it is seen from Figure 6.7 that the crash box starts moving faster after 20 ms, and it happened because the impactor mass was stuck to the crash box after forming two folds. For CB3, an effect is noticed during that period for m_E due to the same reason. The time-dependent sensitivity of the material property (c_σ) is slightly high as compared to the crash box thickness during the crash for CB2 and CB3. On the other hand, the SIR for H and c_σ starts decreasing after the crash, therefore the effect

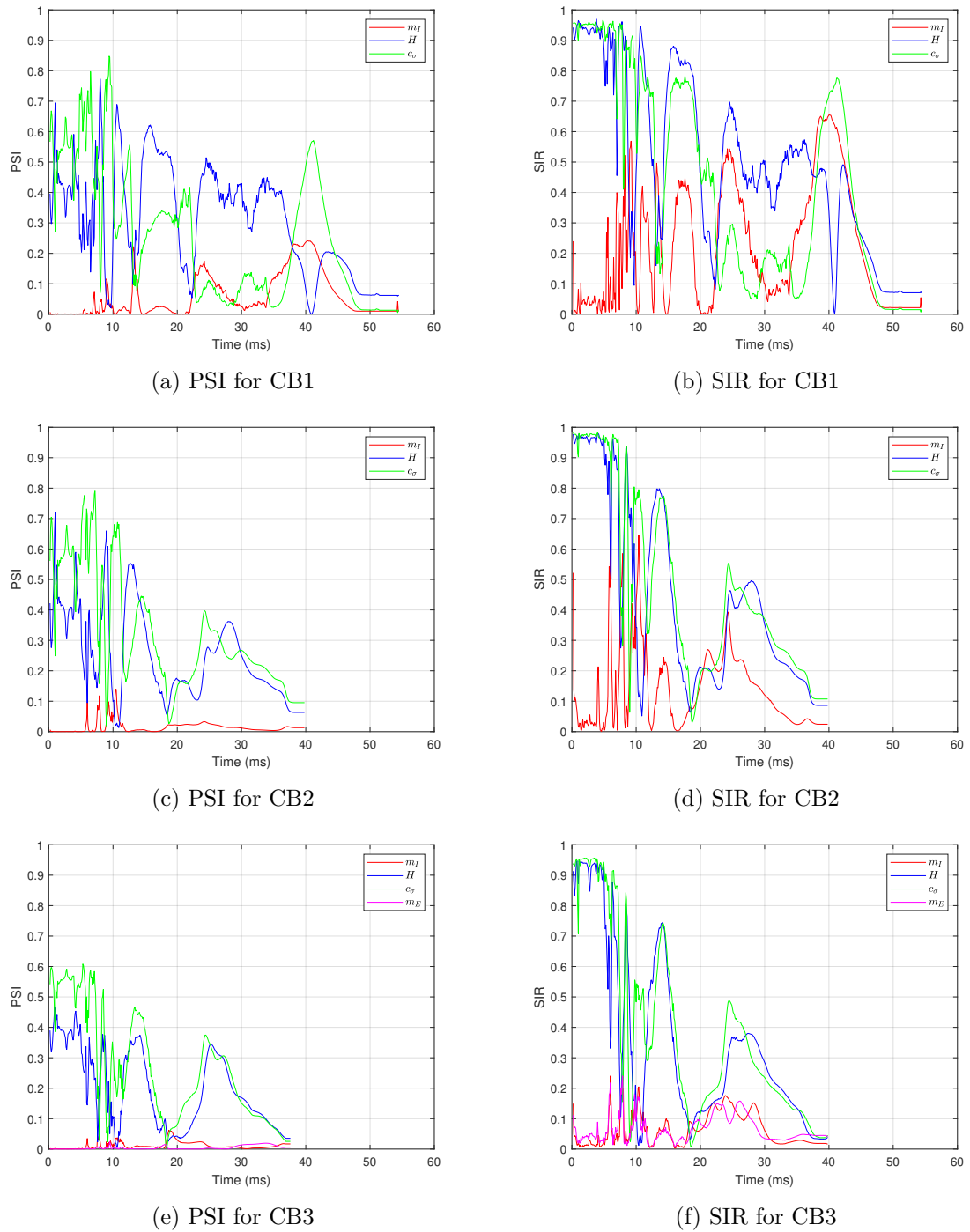


Figure 6.24: Time-dependent GSA results for all the uncertain parameters obtained by the adaptive POD-SVB-PCE model considering contact force as the QoI

of the interaction terms is noticeable after forming the folds, but this effect is low as the TSI values are below 0.1.

Global sensitivity analysis for impacting mass kinetic energy

The sensitivity analysis was also performed considering the time-dependent kinetic energy of the impactor mass. The adaptive POD-SVB-PCE model was constructed using the maximum polynomial degree as $p_{\max} = 10$. The initial number of model evaluations was set to $N_{ini} = 15$. The threshold value for the LOO error was set as $\epsilon_{tol} = 1 \times 10^{-3}$. The evolution of the LOO error with the sample number is shown in Figure 6.26. The adaptive POD-SVB-PCE model was obtained using $N = 20$, $N = 20$ and $N = 25$ with $n_b = 5$, $n_b = 3$ and $n_b = 3$ POM for CB1, CB2 and CB3, respectively. The required corresponding maximum polynomial degrees were 8, 4 and 3, respectively. Furthermore, the adaptive POD-SVB-PCE models were validated with 10^3 MCS results. The relative LOO error for CB1, CB2 and CB3 was found as 5.01×10^{-4} , 1.03×10^{-3} and 1.15×10^{-3} , respectively.

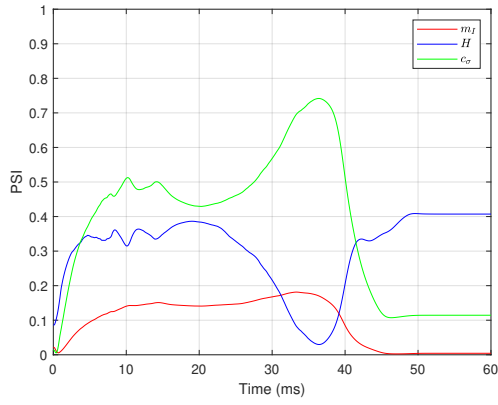
GSA results for all the crash boxes were computed by post-processing the adaptive POD-SVB-PCE models and are shown in Figure 6.27. At the beginning of the crash, the impactor mass is the most influential for the kinetic energy of CB1 because the kinetic energy mainly developed due to the mass at rest. As the crash progresses, the velocity starts decreasing and the folds were started in CB1. Therefore, the PSI for H and c_σ starts increasing with time. PSI for all the three parameters is almost same at 16.5 ms and the SIR for all the parameters is almost 1 at this time. Therefore, no effect of the interaction terms is noticed. SIR for all the variables is almost 1 up to around 25 ms and afterwards, the influence of the interaction terms is noticeable for all the parameters.

For CB2 and CB3, PSI for m_I , H and c_σ behaves almost similarly. As one end is free for both these crash boxes, the kinetic energy was mostly governed by the impactor mass for all the time. The PSI for m_I is very close to 1 for most of the times, which also means that no influence of the interaction terms is noticeable. For CB2, SIR for H and c_σ almost behaves similarly with time. SIR for these two parameters starts decreasing after 20 ms when the folds were already occurred (Figure 6.7) and the crash box was moved under the impacting mass only. For the same reason, SIR for H of CB3 is also quite low after 20 ms. SIR for the end mass is quite low during the initial time of the crash; however, as TSI is about 0.1, a small influence of the interaction terms is noticeable for m_E .

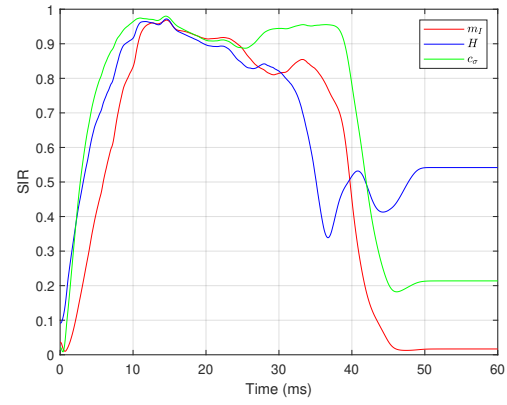
Global sensitivity analysis for maximum contact force

GSA was performed for two time-independent QoI which are the maximum of the contact force and the total dissipated energy.

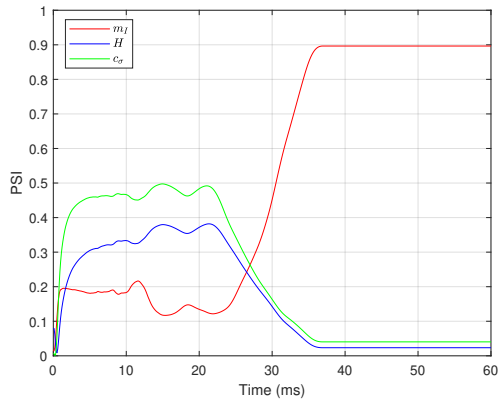
For the maximum contact force, the adaptive SVB-PCE model obtained with the maximum accuracy was considered for GSA. Therefore, it was already shown in Figure 6.20 that the LOO error for CB1 did not achieved the lowest desirable accuracy of 1×10^{-3} using maximum number of model evaluations. Therefore, the SVB-PCE model with $N_{\max} = 200$ was considered for GSA in case of CB1. As a result, the sensitivity indices for CB1 may be less reliable than CB2 and CB3. For CB2 and CB3, the accuracy of 1×10^{-3} was achieved with $N = 20$, therefore, the corresponding adaptive SVB-PCE models were considered for GSA. The PSI and the TSI for all the uncertain parameters (m_I , H , c_σ , m_E) are given in Table 6.7. It is observed that the TSI for all the uncertain parameters of CB1 is quite high as compared



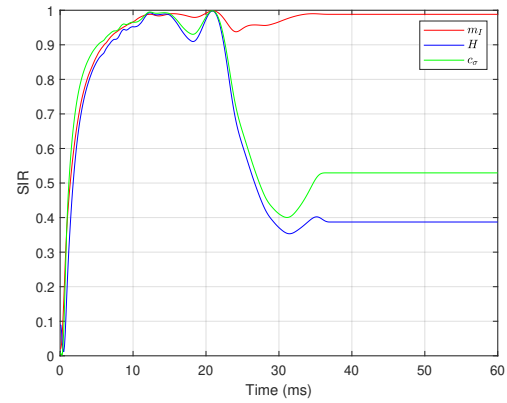
(a) PSI for CB1



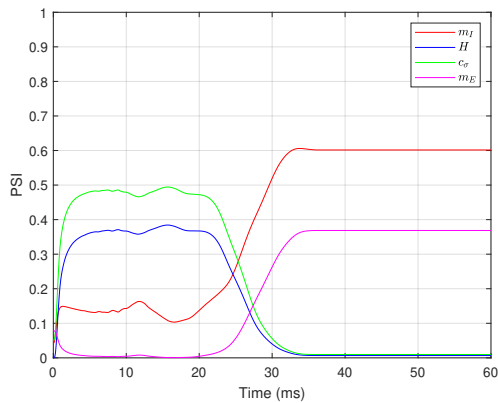
(b) SIR for CB1



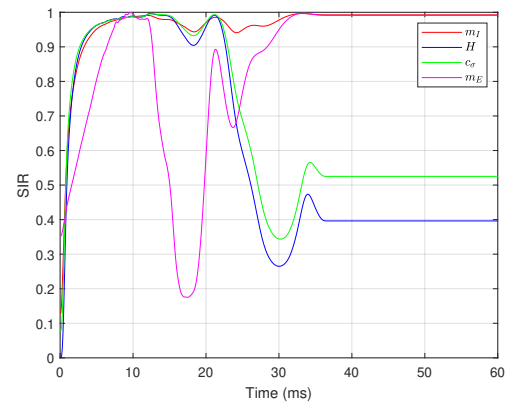
(c) PSI for CB2



(d) SIR for CB2



(e) PSI for CB3



(f) SIR for CB3

Figure 6.25: Time-dependent GSA results for all the uncertain parameters obtained by the adaptive POD-SVB-PCE model considering impactor velocity as the QoI

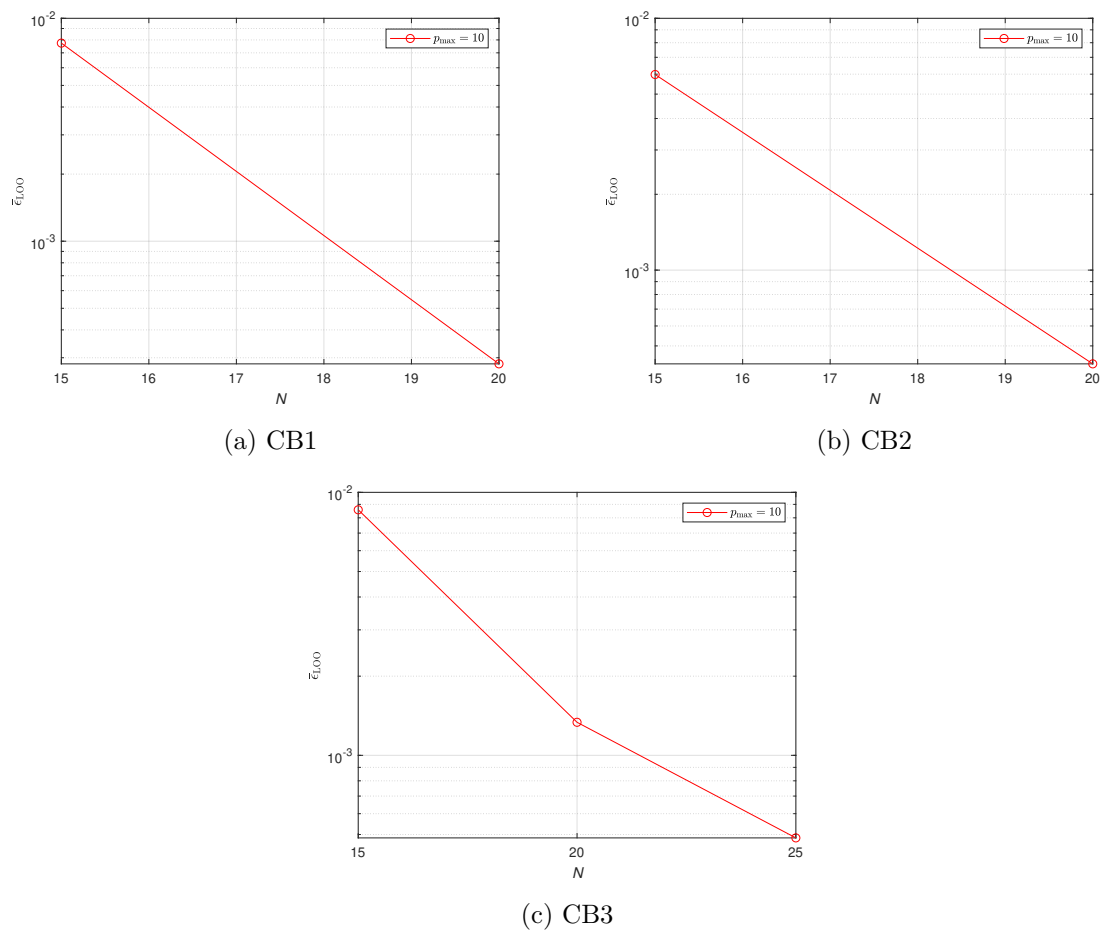


Figure 6.26: Evolution of LOO error for the kinetic energy

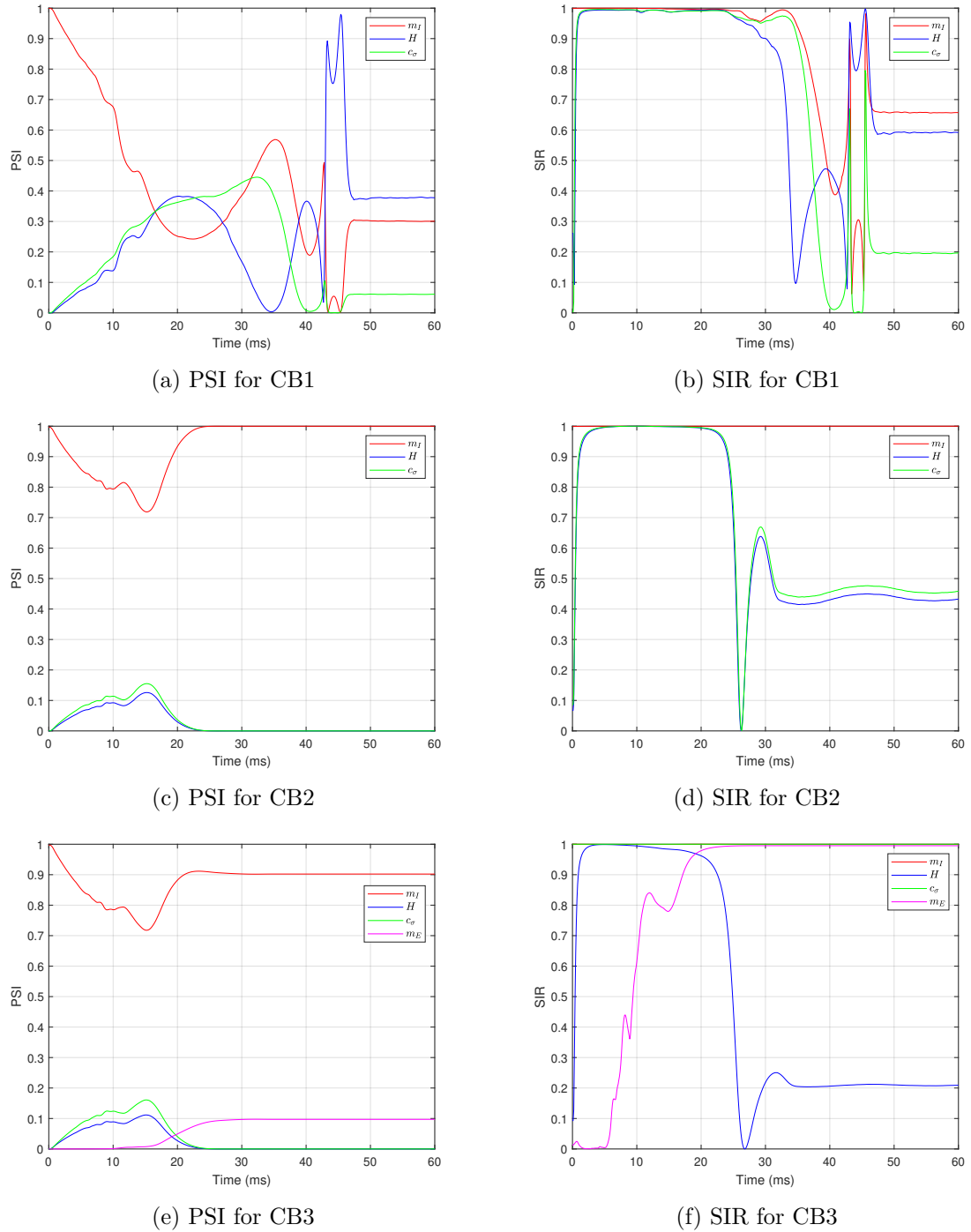


Figure 6.27: Time-dependent GSA results for all the uncertain parameters obtained by the adaptive POD-SVB-PCE model considering kinetic energy as the QoI

Table 6.7: Time-independent GSA results for the maximum of the contact force obtained by the adaptive SVB-PCE model

| Uncertain parameter | PSI | | | TSI | | |
|---------------------|------|------|------|------|------|------|
| | CB1 | CB2 | CB3 | CB1 | CB2 | CB3 |
| m_I | 0.06 | 0.00 | 0.00 | 0.45 | 0.00 | 0.00 |
| H | 0.04 | 0.33 | 0.33 | 0.59 | 0.33 | 0.33 |
| c_σ | 0.18 | 0.67 | 0.67 | 0.82 | 0.67 | 0.67 |
| m_E | - | - | 0.00 | - | - | 0.00 |

to the corresponding PSI: it indicates a strong interaction between the parameters for CB1. Out of all the uncertain parameters, stress multiplying factor (c_σ) is the most influential for CB1. For the two other crash boxes, a different behavior is noticed, as the interactions have no influence on the QoI. For the time-dependent contact force, m_I had a noticeable effect during the crash through interactions (see Figure 6.24): on the contrary, for CB2 and CB3, m_I has no influence on the maximum contact force. For all the crash boxes, the material property and the crash box thickness are the main influential parameters for the maximum contact force. The main reason is that the maximum contact force mostly occurred during the initial strike and therefore the force generated depends mostly on the material property and the crash box geometry.

Global sensitivity analysis for total dissipated energy

Finally, GSA was also performed considering the total dissipated energy as the time-independent QoI. The adaptive SVB-PCE model was obtained using $N = 15$, $N = 60$ and $N = 40$ model evaluations for CB1, CB2 and CB3, respectively. The GSA results for all the uncertain parameters (m_I, H, c_σ, m_E) are listed in Table 6.8. It is seen that for all the crash boxes, the only influential parameter is the impactor mass (m_I), which may indicate that the total dissipated energy is mainly sensitive to the energy that can be dissipated, but is not sensitive to the way the energy is dissipated. On the contrary, the TSI for the material property (c_σ) and for the crash box thickness (H) is very low, which means that both parameters could be set to their nominal values. Furthermore, for CB3, the PSI and the TSI of the end mass (m_E) were found as 0.13 and 0.15, respectively: these values are also very low and therefore, the influence of the end mass on the total dissipated energy is very low. The PSI and the TSI of the impactor mass are very close for all the crash boxes. Therefore, no significant effect of the interaction terms is noticed. A similar behavior is also noticed for the other uncertain parameters. Therefore, almost no sensitivity of the interaction terms is observed for the total dissipated energy.

6.7 Concluding remarks

To adaptively select the number of model evaluations and the polynomial degree, two adaptive surrogate models have been developed in this chapter, both for time-independent and time-dependent QoI. A variance based LOO error was utilized to formulate the adaptive SVB-PCE model for a time-independent QoI. For time-dependent QoI, the addition of the proper orthogonal decomposition gave the adaptative POD-SVB-PCE model.

Table 6.8: Time-independent GSA results for the total dissipated energy obtained by the adaptive SVB-PCE model

| Uncertain parameter | PSI | | | TSI | | |
|---------------------|------|------|------|------|------|------|
| | CB1 | CB2 | CB3 | CB1 | CB2 | CB3 |
| m_I | 1.00 | 0.99 | 0.85 | 1.00 | 0.99 | 0.86 |
| H | 0.00 | 0.00 | 0.00 | 0.00 | 0.01 | 0.02 |
| c_σ | 0.00 | 0.00 | 0.00 | 0.00 | 0.01 | 0.01 |
| m_E | - | - | 0.13 | - | - | 0.15 |

UQ of several time-dependent QoI (impactor displacement, impactor velocity and contact force) was performed for a quarter crash box by the adaptive POD-SVB-PCE model. Due to the high computational cost, it was not possible to compare the results of the surrogate model with the MCS results at a large number of samples. Nevertheless, MCS was performed with 10^3 samples. Furthermore, UQ of some time-independent response quantities (maximum contact force, total dissipated energy) was performed with the adaptive SVB-PCE model.

The POD-SVB-PCE and the SVB-PCE models were also used to perform GSA on the crash box model for time-dependent and time-independent QoI, respectively.

Several important outcomes were observed during the study in this chapter, they are listed below in three main categories namely general remarks on the surrogate models, remarks on UQ of crash box and remarks on the GSA of the crash box.

1. The following remarks are drawn on the surrogate models developed in this chapter:
 - The adaptive surrogate models were useful to select the number of model evaluations and the number of PCE terms adaptively such that a good surrogate model can be obtained without any over-fitting.
 - The threshold LOO error of 1×10^{-3} was found to be sufficient to achieve a good surrogate model. All the obtained surrogate models in this chapter were validated with 10^3 samples and the predicted accuracies were very close to the obtained LOO error in most of the cases when the surrogate models achieved a LOO error less than 1×10^{-3} .
2. The following remarks are drawn from the UQ study of the crash box.
 - For the time-dependent contact force of the crash boxes, it was very difficult to achieve the lowest desired accuracy of 1×10^{-3} using maximum number of model evaluations ($N_{\max} = 200$). However, an acceptable accuracy was achieved for the contact force which was demonstrated by predicting the contact force at three randomly chosen samples.
 - For the other responses (impactor displacement and impactor velocity), it was possible to achieve the accuracy of 1×10^{-3} using much lower model evaluations than the maximum samples. Therefore, the prediction accuracies were very good for these responses.
 - For the maximum contact force, it was not possible to achieve the LOO error of 1×10^{-3} by the adaptive SVB-PCE model for CB1. On the other hand, the same accuracy was achieved for CB2 and CB3 using very low samples.

- For the dissipated energy, the required number of model evaluations was quite less than the maximum number of samples (N_{\max}) to achieve an accuracy of 1×10^{-3} .
3. The conclusions drawn from the GSA are listed below.
- A time-dependent GSA was performed only by post-processing the PCE coefficients and the POM obtained from an adaptive POD-SVB-PCE model.
 - The time-dependent sensitivity indices of the material property and the crash box thickness were found higher for the contact force as compared to the impactor mass during the crash. The same behavior was also noticed for the impactor velocity. On the contrary, the impactor mass was influential for the time-dependent kinetic energy of CB2 and CB3.
 - GSA for the maximum contact force and the total dissipated energy was performed. For CB2 and CB3, the impactor mass did not have any effect on the maximum contact force. All the other parameters have significant effect on the maximum contact force. A different scenario was observed for the total dissipated energy: the impactor mass was the only significant parameter for all the crash boxes.

Chapter 7

Conclusions and future perspectives

The time-dependent uncertainty quantification (UQ) of a crash problem has been investigated in the present research work. A crash problem is very much related to a dynamical system. For that reason, it is important to investigate a suitable approach for UQ of dynamical systems. UQ of a time-dependent dynamical response is often quite a challenging task. The most conventional way for UQ of such problems is the MCS approach. However, the large computational cost of crash simulations prohibits to apply the MCS approach for crash problems. To address this problem, surrogate modeling approaches have been proposed in the literature which makes a trade-off between the accuracy and the efficiency. Therefore, proposing a suitable surrogate model for a crash problem was the main objective of this thesis. The main conclusions drawn from the present study are discussed in this chapter.

7.1 Conclusions of the research

For achieving the first objective of the research, several available surrogate modeling approaches have been reviewed and it was found that most of the surrogate modeling approaches can describe some specific classes of problems but cannot be used for a crash problem. The most versatile surrogate modeling approach found from the review was the sparse PCE-NARX model where the time-dependent behavior and the randomness were decoupled using the NARX model and the PCE model, respectively. Therefore, it was possible to propagate efficiently the uncertain parameters for the nonlinear dynamical systems by the sparse PCE-NARX model.

Inspired by the sparse PCE-NARX model, a similar kind of surrogate model was proposed to increase its efficiency with respect to the number of model evaluations, which is called sparse KNARX model. The sparse KNARX model was used for UQ of several nonlinear dynamical systems. It was found that UQ of nonlinear dynamical systems (Duffing oscillator, Bouc-Wen oscillator and a 2-DOF dynamical system with cubic nonlinearity) can be performed by the sparse KNARX model using much a less number of model evaluations as compared to the sparse PCE-NARX model without losing accuracy. However, it was not possible to identify the response of the impact oscillator using the available NARX models and it is the main drawback of the sparse KNARX model.

Therefore, a different approach was investigated, based on the combined use of the POD and the PCE: the objective was also to uncouple the time and the randomness, as did the sparse PCE-NARX model or the sparse KNARX model. UQ of the time-dependent response

can also be performed by the PCE model. However, the main issue with the PCE model is that the PCE coefficients must be computed at each time-step. On the contrary, the uncertain response quantity was projected on very low number of POD modes (POM) as compared to the number of time-steps. UQ was performed for an impact oscillator using the POD-PCE model with two different conditions: single impact and multiple impacts between a structure and a projectile. It was possible to quantify the time-dependent uncertainty for the responses of the projectile by the POD-PCE model which fulfill the first part of the first and second objectives. For the projectile displacement and velocity, the POD-PCE model required a very low number of POM. The contact force required the highest number of POM among all the responses. The accuracy of the contact force was also a little lower than the other responses. Furthermore, negative values of the contact force were predicted at some moments by the POD-PCE model. It was possible to reduce these non-physical forces to some extent by increasing the number of sample points. However, it was not possible to fully mitigate the non-physical forces because it is much difficult to predict accurately a non-smooth response (e.g. contact force) by a smooth function (PCE): that is why the same problem occurs with the PCE model. Accordingly, this problem is not related to the use of the POD.

For the POD-PCE model, sometimes the required polynomial degree for the PCE model may be high. As a result, the number of terms in the PCE model would also be high. Therefore, a sparse variational Bayesian inference (SVB) based PCE model was proposed. The PCE coefficients were computed using the VB inference and the necessary PCE terms were selected using the automatic relevance determination (ARD) approach. The applicability of the SVB-PCE model was checked using some examples and it was found that it is a very useful alternative way to propagate the uncertain parameters. Furthermore, the SVB-PCE model was coupled with the POD approach for UQ of the impact oscillator. It was found that the required number of terms in a PCE model was quite low as compared to the full PCE model. At the same time, it was possible to reduce the non-physical negative contact forces using high degree polynomials and a low number of model evaluations.

An adaptive framework for the SVB-PCE and the POD-SVB-PCE has been proposed, which was the ultimate goal of the first objective of the thesis. The main motivation behind formulating these adaptive surrogate models was that the polynomial degree and the number of model evaluations should be selected adaptively for a specific response quantity. Two different kinds of leave-one-out (LOO) errors were utilized to measure the accuracies of the surrogate models. Finally, an elasto-plastic crash box FE model under an impact loading was investigated considering several uncertain parameters with different end conditions and it was the final objective of the study. The adaptive surrogate models have been obtained for different responses of the crash boxes and further, the adaptive surrogate models were validated with 10^3 model evaluations. It was found that the adaptive POD-SVB-PCE model predicted very good results when it reached a LOO error of less than 1×10^{-3} for the impactor displacement and for the impactor velocity. However, it was not possible to achieve a LOO error of 1×10^{-3} for the contact force using a limited number of model evaluations. As a result, the adaptive POD-SVB-PCE model obtained for the contact force was less accurate than the other responses. UQ of the time-independent responses was performed by the adaptive SVB-PCE model and a LOO error of 1×10^{-3} was sufficient to achieve a good result at the validated samples. Furthermore, a global sensitivity analysis was performed by post-processing the results of the adaptive surrogate models. It should be noted that the sensitivity analysis results have not been compared with the MCS results due to the high computational cost. The sensitivity analysis results for the contact force may be less accurate than the others

because a LOO error of 1×10^{-3} was not achieved for the surrogate models. The influence of the material property and the crash box thickness was found to be high for the contact force and for the impactor velocity whereas the impactor mass was found as the most influential parameter for the kinetic energy. For the maximum contact force also, the material property and the crash box thickness are the most influential parameters whereas the impactor mass was the most influential parameter for the total absorbed energy.

The main achievement of this thesis is the proposed surrogate model (adaptive POD-SVB-PCE model) for the UQ of time-dependent response. The proposed approach can also be utilized for a sensitivity analysis of the uncertain parameters without any additional computational cost.

7.2 Limitations of the research

Although the approaches developed in this thesis have given good results for the UQ of impact problems, there are some limitations to apply the proposed approach for UQ.

The developed POD-PCE model can be used for UQ of any time-dependent stochastic response. However, it has been noticed from the results of chapter 4 that some non-physical negative contact forces were always predicted by the POD-PCE model or the PCE model. It has been shown that increasing the number of model evaluations may improve the results but some non-physical negative forces have still been predicted by the POD-PCE model. Although the non-physical results were minimized to some extent with the sparse PCE (SVB-PCE) model, it was not possible to mitigate totally the issue. The main reason is that the developed adaptive POD-SVB-PCE model remains a smooth function and predicting a non-smooth function (e.g. a contact force) using the developed approach is very difficult. However, assessing the statistical moments (mean and standard deviation) by the adaptive POD-SVB-PCE model gave more accurate results than the prediction of the individual time-dependent response. This is the main limitation of the adaptive POD-SVB-PCE model for the non-smooth dynamical systems investigated in this thesis.

7.3 Future scope of research

In the present research work, several parts of the drawbacks as pointed out in chapter 2 have been addressed. However, still several things related the current research should be investigated in the future. The future research may include the following:

- As pointed out in the limitations, the present research cannot address fully the non-smooth stochastic behavior of the contact force. Therefore, a suitable surrogate model can be investigated, which can account the non-smooth behavior of the contact force and mitigate the issue with the present research work.
- An adaptive surrogate model has been proposed in this thesis. However, the conventional sample points generation strategy has been used in the current research work. The new sample points can also be generated based on the information from the responses at the previous samples which is called adaptive experimental design technique (Busby, 2009; Picheny et al., 2010; Zhou et al., 2019a). Therefore, an adaptive sampling scheme can be investigated, which would increase the accuracy of the surrogate model more efficiently.

- The rectangular crash box has been investigated in the present thesis. However, some recent research works have shown that the energy absorption is much better for the tailored crash boxes (Lu et al., 2018b) or for the origami shaped crash boxes (Yuan et al., 2019). Therefore, UQ of the other different kinds of crash boxes should also be performed.
- It is evident from the previous researches that the stochastic modeling of full car crash is very difficult. For that reason, only the crash box is investigated in the present thesis. However, with a high performance computing facility, stochastic modeling of a car crash can be investigated at least considering some parts of a car: this investigation would give much better understanding about the stochastic behavior of the responses for several crash conditions (e.g. oblique impact).

Appendix A

Investigation of a dynamical system by TDgPCE

The accuracy of the TDgPCE (Gerritsma et al., 2010) has already been proved for time-dependent ODE having some uncertain parameters (refer section 2.5.1). The TDgPCE model was utilized for UQ of a single degree of freedom (SDOF) dynamical system and the results are presented here.

A.1 Problem definition

In this section, the response characteristics of a SDOF linear dynamical system is studied. The system considered for the present study is shown in Figure A.1. The governing differential equation of the system is:

$$\begin{aligned} m\ddot{y}(t) + c\dot{y}(t) + ky(t) &= F(t) \\ y(0) = 0 \quad \dot{y}(0) &= 0 \end{aligned} \tag{A.1}$$

The uncertain parameter is the stiffness, and it is given by:

$$k = \bar{k}(1 + \delta_k \xi) \tag{A.2}$$

In Equation A.2, \bar{k} is the deterministic stiffness of the dynamical system. The problem will be solved for three different values of \bar{k} (150 N m^{-1} , 1500 N m^{-1} , $15\,000 \text{ N m}^{-1}$). The uncertainty

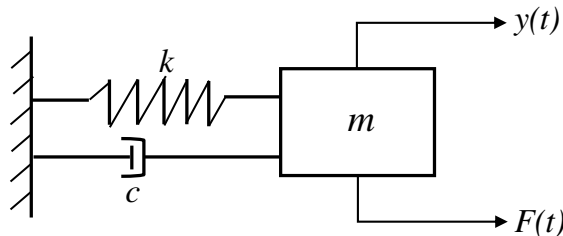


Figure A.1: SDOF dynamical system

Table A.1: Different parameters used for the SDOF dynamical system

| Parameter | Value | Unit |
|------------|-------|---------------------------------|
| m | 1 | kg |
| c | 1 | $\text{N m}^{-1} \text{s}^{-1}$ |
| δ_k | 5 | % |
| F_0 | 10 | N |
| ω | 10 | rad s^{-1} |

in the stiffness was incorporated through the parameter ξ . The problem has been solved by Jacquelin et al. (2015c) using PCE for the steady-state response characteristics in the frequency domain. However, it has already been shown by Mai and Sudret (2017) that PCE cannot predict well the statistical response characteristics in time domain. For this reason, TDgPCE will be utilized to assess the time dependent response characteristics under the uncertain parameter. Note that, in Equation A.2, $\delta_k = 0$ denotes deterministic system. ξ , the uncertain parameter of the system, is supposed to be uniformly distributed in $[-1, 1]$. The system is excited by an external force $F(t)$ which is given by:

$$F(t) = F_0 \cos(\omega t) \quad (\text{A.3})$$

where F_0 is the constant amplitude of the force and ω is the excitation frequency. All the parameters used for this problem are listed in Table A.1.

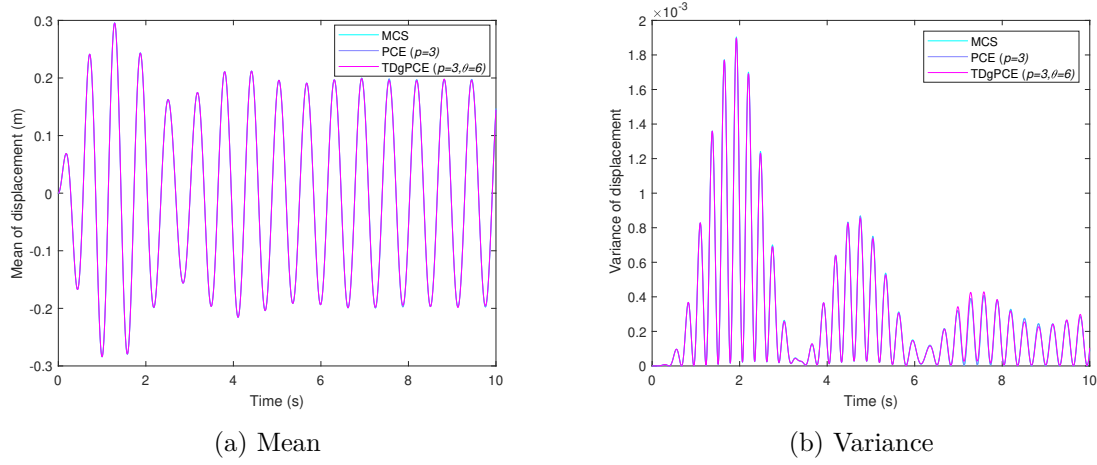
A.2 Case 1: $\bar{k} = 150 \text{ N m}^{-1}$

The uncertain SDOF dynamical system as given in Equation A.1 was solved by the TDgPCE. This problem was also solved using a PCE model to check the performance of TDgPCE over PCE. Here, $\bar{k} = 150 \text{ N m}^{-1}$ and the deterministic natural frequency of the system $\bar{\omega}_n = 12.25 \text{ rad s}^{-1}$. In this case, $\bar{\omega}_n$ is quite close to the excitation frequency ω . The deterministic damping ratio of the system is 4.08%. The differential equation has been solved using the explicit fourth order *Runge-Kutta* method (Runge, 1895; Kutta, 1901) with a time step of $\Delta t = 0.001 \text{ s}$ up to time $T = 10 \text{ s}$ to get the solution. As this is an intrusive approach, the time-integration is performed with the PCE based differential equation.

The QoI for this problem was the displacement of the system. Legendre polynomials were used for the uniformly distributed random variable ξ with polynomial degree $p = 3$. For the TDgPCE model, the stopping parameter $\theta = 6$ was considered (Gerritsma et al., 2010). Furthermore, MCS was also performed on 5×10^4 sample points to check the accuracy of the surrogate model.

The time-dependent mean and variance of the displacement are plotted in Figure A.2. It is seen clearly from Figure A.2 that the mean and the variance are predicted very well by PCE and TDgPCE with low degree polynomials compared to the MCS, which is the reference method.

A more precise comment can be made by investigating the PDF of the response at some certain instances of time. For that reason, the PDFs of the response quantity are plotted in Figure A.3 at 2.5s, 5s and 7.8s. It is seen from the Figure A.3 that the PDFs are in line with the MCS predicted results in the early time, however it starts deviating from the MCS

Figure A.2: Statistical response characteristics of the linear SDOF system for $\bar{k} = 150 \text{ N m}^{-1}$

predicted results in the later time for TDgPCE, which depicts the inability of the method in capturing the PDF. It is also noticeable that the PDF of the displacement is bimodal in the later time which is almost unimodal in the early time.

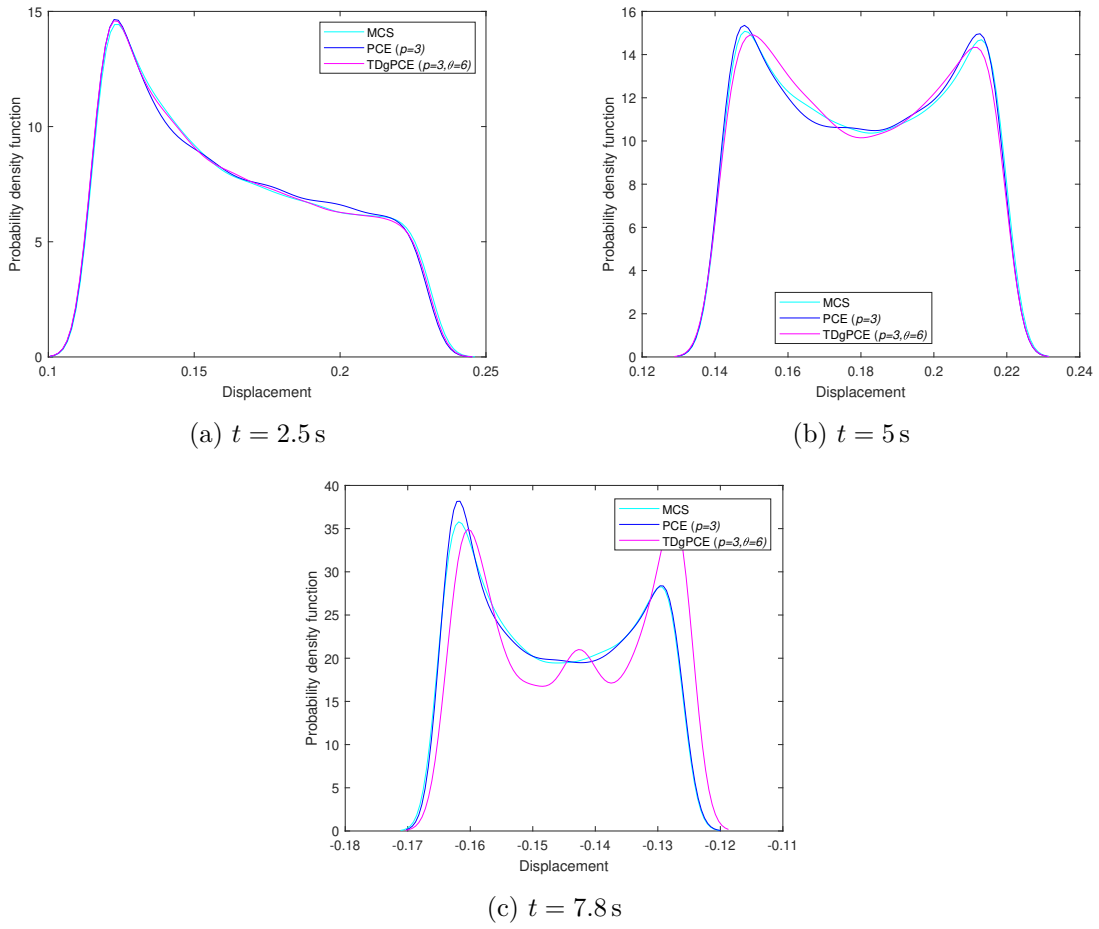
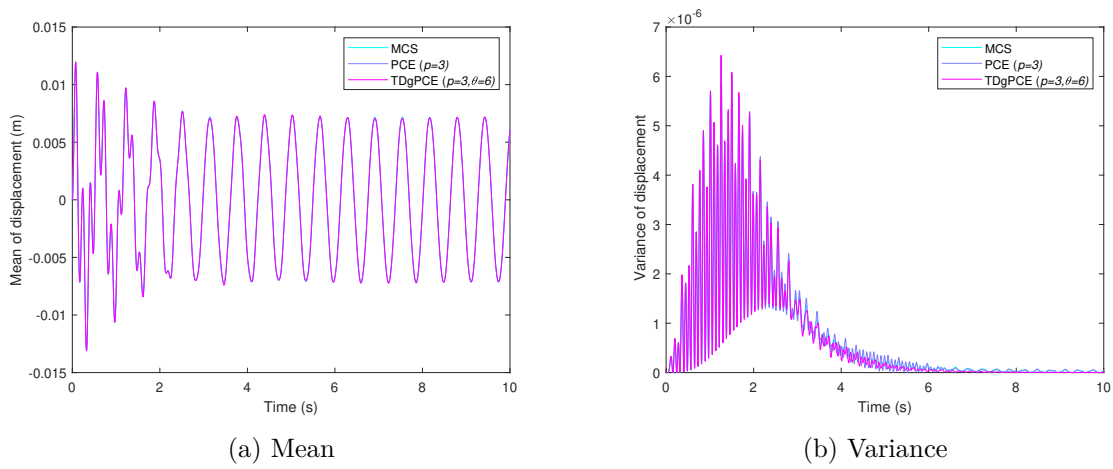
A.3 Case 2: $\bar{k} = 1500 \text{ N m}^{-1}$

In this section, the deterministic stiffness $\bar{k} = 1500 \text{ N m}^{-1}$ is considered and ξ is also uniformly distributed in $[-1, 1]$. Here, the deterministic natural frequency ($\bar{\omega}_n = 38.73 \text{ rad s}^{-1}$) is not so close to the excitation frequency ($\omega = 10 \text{ rad s}^{-1}$) and the deterministic damping ratio is 1.29%. This problem was also solved by PCE and TDgPCE with degree of the polynomial $p = 3$ to get the statistical response characteristics. The mean and the variance of the system are plotted in Figure A.4 by all the three approaches. It seems that the mean predicted by PCE and TDgPCE are in line with the MCS results, however, a small discrepancy is noticed towards the later time.

In order to investigate the results more clearly, the PDFs are plotted at the similar time instances as the previous case in Figure A.5. It is seen that the PDF is not predicted quite well at 5 s and the worst PDF is noticed at 7.8 s, which represents the incapability of capturing the dynamic behavior of the response in the later time.

A.4 Case 3: $\bar{k} = 15000 \text{ N m}^{-1}$

The statistical response characteristics of the linear SDOF dynamical system has also been studied for $\bar{k} = 15000 \text{ N m}^{-1}$. For this case, the deterministic natural frequency ($\bar{\omega}_n = 122.47 \text{ rad s}^{-1}$) is much higher than the excitation frequency (ω). Statistical response parameters are presented in Figure A.6. Note that TDgPCE yields the results upto 9.27 s and beyond this, TDgPCE did not converge. The incapability is more prominent from the PDF plots (Figure A.7) of the response characteristic at the similar time instances like the previous two cases. It is seen from Figure A.7 that the PDFs started deviating from the early time instances and are not capable to capture the stochastic dynamic response behavior by the TDgPCE model.

Figure A.3: PDF of displacement at different time instances for $\bar{k} = 150 \text{ N m}^{-1}$ Figure A.4: Statistical response characteristics of the linear SDOF system for $\bar{k} = 1500 \text{ N m}^{-1}$

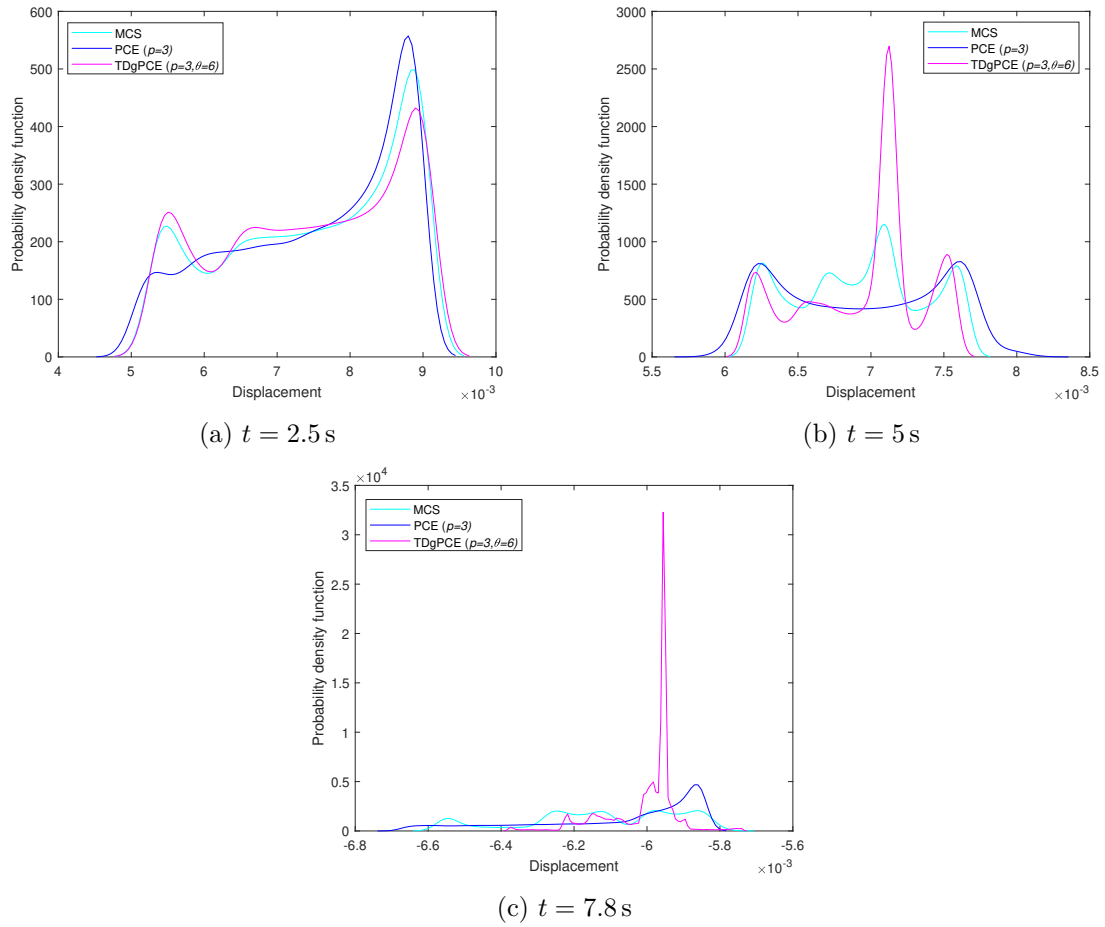


Figure A.5: PDF of displacement at different time instances for $\bar{k} = 1500 \text{ N m}^{-1}$

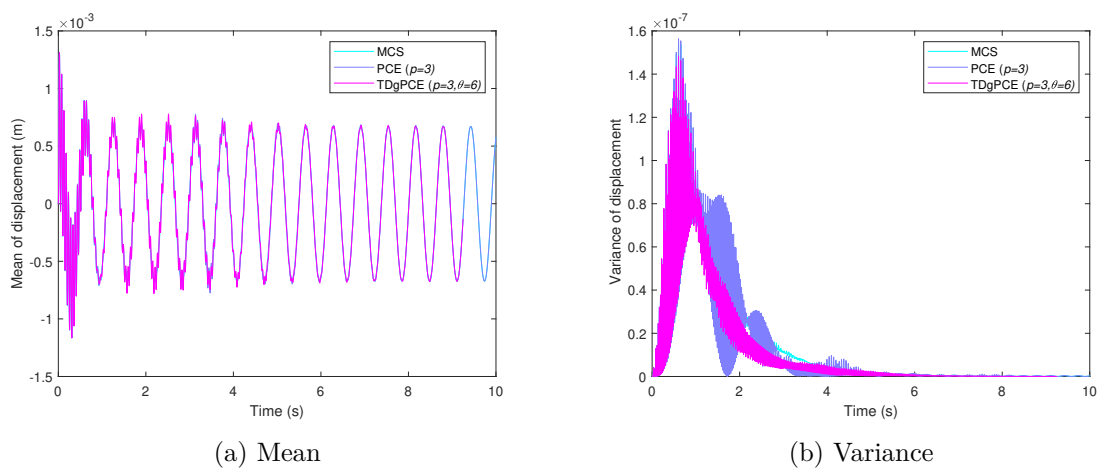


Figure A.6: Statistical response characteristics of the linear SDOF system for $\bar{k} = 15\,000 \text{ N m}^{-1}$

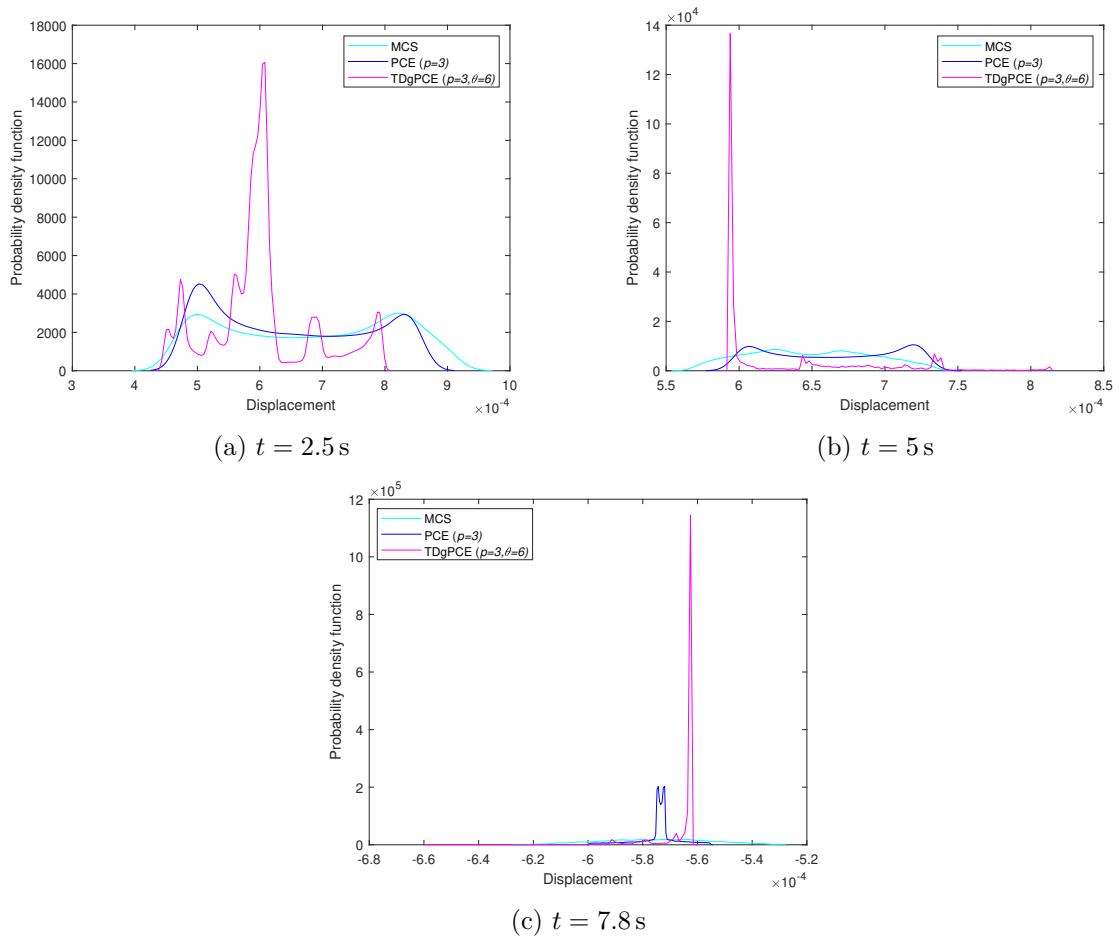


Figure A.7: PDF of displacement at different time instances for $\bar{k} = 15000 \text{ N m}^{-1}$

A.5 Discussion on failure of TDgPCE

At first glance, the TDgPCE model seemed to be very effective as the polynomial basis function is updated with respect to time to get an optimal PCE basis, i.e. a PCE basis that corresponds to the statistical distribution of the response. However, it has been observed from the above study that the time-dependent stochastic response characteristics has not always been predicted quite well by the TDgPCE model. Although the basis function is updated, the nonlinear PCE coefficients may be too sensitive to the criterion of updating the basis function for the time dependent response quantity. Hence, it was not possible to track the time varying PDF properly by using the specified stopping criterion. Consequently, the predicted response quantity has already become erroneous when it satisfied the specified stopping criterion. Afterwards, the erroneous results have been predicted even with the updated polynomial basis function because the polynomial basis function was constructed with the erroneous predicted response quantity. Therefore, to capture the dynamics of the system by TDgPCE properly, the required time-step might be small enough and the stopping parameter θ might be higher than what was considered in the current study. Under these circumstances, the polynomial basis functions might be updated at each time step (with a smaller time step) such that the PDF of the system can be tracked properly. However, one concern about this strategy is that the computational cost would be much higher if the polynomial basis function is constructed frequently during the time-integration procedure. Hence, the high computational cost limits the TDgPCE procedure to be applied in a much complex dynamical system having nonlinear behavior and multiple uncertain input parameters.

Appendix B

Distribution for the prior and likelihood function

The distribution of the generalized Bayesian inference functions in section 5.2.1 are discussed here. The likelihood function is formulated in the following way:

$$p(Y|\Phi, a, \varsigma) = \prod_{i=1}^N p(Y_i|\Phi_i, a, \varsigma) \quad (\text{B.1})$$

$$= \prod_{i=1}^N \mathcal{N}(Y_i|\Phi_i a, \varsigma^{-1}) \quad (\text{B.2})$$

$$= \left(\frac{\varsigma}{2\pi}\right)^{\frac{N}{2}} \exp\left(-\frac{\varsigma}{2} \sum_{i=1}^N (Y_i - \Phi_i a)^2\right) \quad (\text{B.3})$$

where Y_i are independent and identically distributed. In Equation B.2, $\mathcal{N}(Y_i|\Phi_i a, \varsigma^{-1})$ denotes the PDF of the normal distribution of Y_i with mean $\Phi_i a$ and variance ς^{-1} . Φ_i represents the i -th row of the multivariate polynomial matrix. Considering Y as the random parameter, the likelihood function shown in Equation B.3 belongs to the exponential family. As the likelihood function is normally distributed, a conjugate normal-gamma distribution (Griffin and Brown, 2010) is chosen for the prior which is given by (Jacobs et al., 2018):

$$p(a, \varsigma|\alpha) = p(a|\varsigma, \alpha) p(\varsigma) \quad (\text{B.4})$$

$$= \mathcal{N}(a|0, (\varsigma\Lambda)^{-1}) \text{Gam}(\varsigma|A_0, B_0) \quad (\text{B.5})$$

$$= (2\pi)^{-\frac{n}{2}} |\Lambda|^{\frac{1}{2}} \frac{B_0^{A_0}}{\Gamma(A_0)} \varsigma^{\frac{n}{2}+A_0-1} \exp\left(-\frac{\varsigma}{2} (a^T \Lambda a + 2B_0)\right) \quad (\text{B.6})$$

In Equation B.5, $\text{Gam}(\bullet)$ stands for the PDF of the gamma distribution and A_0, B_0 are the parameters of the Gamma distribution. In a similar way to the likelihood function, the normal distribution in the prior has been further parametrized by Λ , which is a diagonal matrix such that $\alpha = \{\alpha_1, \alpha_2, \dots, \alpha_{N_p}\}^T = \text{diag}(\Lambda)$ (see Equation B.5). The determinant of Λ is given by:

$$|\Lambda| = \prod_{i=1}^{N_p} \alpha_i \quad (\text{B.7})$$

To keep the continuity in the formulation and conjugacy in the prior, the hyper-prior is given by the independent gamma distribution:

$$p(\alpha) = \prod_{j=1}^n \frac{D_0^{C_0}}{\Gamma(C_0)} \alpha_j^{C_0-1} \exp(-D_0 \alpha_j) \quad (\text{B.8})$$

where C_0 and D_0 are the parameters of the gamma distribution for α .

Appendix C

Computation of variational lower bound

The convergence of the variational distribution $q(\Theta)$ is checked by the variational lower bound (VLB) in section 5.3. The VLB has already been formulated by the factorized distribution in Equation 5.18. Expanding both the terms of the equation, the VLB is given by:

$$\mathcal{L}[q(\Theta)] = \mathbb{E}_{\Theta} [\ln p(Y, \Theta)] - \mathbb{E}_{\Theta} [\ln q(\Theta)] \quad (\text{C.1})$$

$$\begin{aligned} &= \mathbb{E}_{a, \varsigma} [\ln p(y|\Phi, a, \varsigma)] + \mathbb{E}_{a, \varsigma, \alpha} [\ln p(a, \varsigma|\alpha)] + \mathbb{E}_{\alpha} [\ln p(\alpha)] \\ &\quad - \mathbb{E}_{a, \varsigma} [\ln q(a, \varsigma)] - \mathbb{E}_{\alpha} [\ln q(\alpha)] \end{aligned} \quad (\text{C.2})$$

All the terms of Equation C.2 can be found by taking the expectations over the previous derivations. Therefore, taking the expectation of Equation B.3 (Bishop, 2006), the first term is given by:

$$\begin{aligned} \mathbb{E}_{a, \varsigma} [\ln p(Y|\Phi, a, \varsigma)] &= \frac{N}{2} (g(A_k) - \ln B_k - \ln 2\pi) \\ &\quad - \frac{1}{2} \sum_{i=1}^N \left(\frac{A_k}{B_k} (Y_i - \Phi_i a)^2 + \Phi_i V_k \Phi_i^T \right) \end{aligned} \quad (\text{C.3})$$

where $g(\bullet)$ represents the Digamma function. The second term of Equation C.2 (Bishop, 2006) is computed taking expectation on Equation B.6:

$$\begin{aligned} \mathbb{E}_{a, \varsigma, \alpha} [\ln p(a, \varsigma|\alpha)] &= \frac{n}{2} (g(A_k) - \ln B_k + g(C_k) - \ln 2\pi) - B_0 \frac{A_k}{B_k} \\ &\quad - \frac{1}{2} \sum_{j=1}^n \left(\ln D_{k_j} + \frac{C_k}{D_{k_j}} \left(\frac{A_k}{B_k} a_{k_j}^2 + V_{k_{jj}} \right) \right) \\ &\quad - \ln \Gamma(A_0) + A_0 \ln B_0 + (A_0 - 1) (g(A_k) - \ln B_k) \end{aligned} \quad (\text{C.4})$$

Similarly, the later terms of the VLB are computed by taking expectations on Equation B.8, 5.21 and 5.30 and are given by (Bishop, 2006):

$$\begin{aligned} \mathbb{E}_{\alpha} [\ln p(\alpha)] &= -n (\ln \Gamma(C_0) + C_0 \ln D_0) \\ &\quad + \sum_{j=1}^n \left((C_0 - 1) (g(C_k) - \ln D_{k_j}) - D_0 \frac{C_k}{D_{k_j}} \right) \end{aligned} \quad (\text{C.5})$$

$$\begin{aligned} \mathbb{E}_{a,\varsigma} [\ln q_k(a, \varsigma)] &= \frac{n}{2} (g(A_k) - \ln B_k - \ln 2\pi - 1) - \frac{1}{2} \ln |V_k| - \ln \Gamma(A_k) \\ &\quad + A_k \ln B_k + (A_k - 1)(g(A_k) - \ln B_k) - A_k \end{aligned} \quad (\text{C.6})$$

$$\mathbb{E}_\alpha [\ln q_k(\alpha)] = \sum_{j=1}^n \left((C_k - 1) g(C_k) + \ln D_{k_j} \right) - n (\ln \Gamma(C_k) + C_k) \quad (\text{C.7})$$

The final expression for the VLB is given by substituting Equation C.3 to C.7 in Equation C.2:

$$\begin{aligned} \mathcal{L}[q(\Theta)] &= -\frac{N}{2} \ln 2\pi + \frac{1}{2} \ln |V_k| - B_0 \frac{A_k}{B_k} - \frac{1}{2} \sum_{i=1}^N \left(\frac{A_k}{B_k} (Y_i - \Phi_i a_k)^2 + \Phi_i V_k \Phi_i^T \right) \\ &\quad + \ln \Gamma(A_k) - A_k \ln B_k + A_k - \ln \Gamma(A_0) + A_0 \ln B_0 \\ &\quad - \sum_{j=1}^n \left(C_k \ln D_{k_j} \right) + n \left(\frac{1}{2} - \ln \Gamma(C_0) + C_0 \ln D_0 + \ln \Gamma(C_k) \right) \end{aligned} \quad (\text{C.8})$$

At each iteration in the optimization procedure, the VLB is computed numerically using Equation C.8.

Appendix D

Sobol' sensitivity indices

Global sensitivity analysis in section 6.6.1 has been performed using Sobol' sensitivity index. According to Sobol (1993, 2001), the response can be decomposed into the main effect and the interaction effect of the input variables (considering all the random variables independent) as:

$$\begin{aligned}
 y = g(\xi) = & g_0 + \sum_{i=1}^d g_i(\xi_i) + \sum_{1 \leq i < j \leq d} g_{i,j}(\xi_i, \xi_j) + \cdots \\
 & + \sum_{1 \leq i_1 < \dots < i_s \leq d} g_{i_1, \dots, i_s}(\xi_{i_1}, \dots, \xi_{i_s}) + \cdots + g_{1, \dots, d}(\xi_1, \dots, \xi_d) \quad (D.1)
 \end{aligned}$$

where g_0 is the constant of the expansion which is also the mean of y . One of the important properties of the decomposition is that the summand of the decomposition must satisfy:

$$\begin{aligned}
 \int_{\Omega_{\xi_k}} g_{i_1, \dots, i_s}(\xi_{i_1}, \dots, \xi_{i_s}) f_{\xi_k}(\xi_k) d\xi_k = 0 \\
 1 \leq i_1 < \dots < i_s \leq d; k \in \{i_1, \dots, i_s\} \quad (D.2)
 \end{aligned}$$

where Ω_{ξ_k} is the support of random variable ξ_k . Along with this, the orthogonality condition must be satisfied by all the terms, except the constant one. It is given by:

$$\begin{aligned}
 \int_{\Omega} g_{i_1, \dots, i_s}(\xi_{i_1}, \dots, \xi_{i_s}) g_{j_1, \dots, j_t}(\xi_{j_1}, \dots, \xi_{j_t}) d\xi = 0 \\
 \forall \{i_1, \dots, i_s\} \neq \{j_1, \dots, j_t\} \quad (D.3)
 \end{aligned}$$

Each term in Equation D.1 can be found by:

$$\begin{aligned}
 g_0 &= \mathbb{E}(Y) \\
 g_i(\xi_i) &= \mathbb{E}_{\xi_{\sim i}}(Y|\xi_i) - \mathbb{E}(Y) \\
 g_{i,j}(\xi_i, \xi_j) &= \mathbb{E}_{\xi_{\sim i,j}}(Y|\xi_i, \xi_j) - \mathbb{E}(Y) \\
 &\vdots
 \end{aligned} \quad (D.4)$$

where $\mathbb{E}_{\xi_{\sim i}}$ is the expectation with respect to all the variables except ξ_i , and similarly, $\mathbb{E}_{\xi_{\sim i,j}}$ is the expectation with respect to all the variables except ξ_i and ξ_j . Due to the orthogonal property between the model terms in Equation D.1, the corresponding variance can be represented as:

$$\text{var}(y) = \sum_{i=1}^d \text{var}_i + \sum_{1 \leq i < j \leq d} \text{var}_{i,j} + \cdots + \text{var}_{1, \dots, d} \quad (D.5)$$

where $\text{var}(y)$ is the total variance of the response quantity y . var_i is the partial variance of the response due to the i -th variable and so on. Therefore, after dividing both sides of Equation D.5 by the total variance, the sensitivity indices are given by:

$$\sum_{i=1}^d S_i + \sum_{1 \leq i < j \leq d} S_{i,j} + \cdots + S_{1,\dots,d} = 1 \quad (\text{D.6})$$

where S_i is the partial sensitivity index (PSI) for the i -th variable and $S_{1,\dots,d}$ is the combined PSI for the interaction of the corresponding variables. Often the variance contribution of a single variable is computed (S_i) which is also known as the first order sensitivity index or the main effect sensitivity index. More explicitly, S_i can be written as (Saltelli et al., 2010):

$$S_i = \frac{\text{var}_{\xi_i}(\mathbb{E}_{\xi_{\sim i}}(y|\xi_i))}{\text{var}(y)} \in [0, 1] \quad (\text{D.7})$$

where $\text{var}_{\xi_i}(\mathbb{E}_{\xi_{\sim i}}(y|\xi_i))$ measures the partial contribution of the variance on the output due to variable ξ_i . On the other hand, the total sensitivity index (TSI) measures the whole effect of a variable on the output quantity (Homma and Saltelli, 1996). TSI considers the PSI along with the interaction terms for a particular variable. The TSI for the i -th variable is given by:

$$S_{Ti} = \frac{\mathbb{E}_{\xi_{\sim i}}(\text{var}_{\xi_i}(y|\xi_{\sim i}))}{\text{var}(y)} = 1 - \frac{\text{var}_{\xi_{\sim i}}(\mathbb{E}_{\xi_i}(y|\xi_{\sim i}))}{\text{var}(y)} \quad (\text{D.8})$$

where $\text{var}_{\xi_{\sim i}}(\mathbb{E}_{\xi_i}(y|\xi_{\sim i}))$ is the variance contribution of all the terms other than ξ_i . PSI and TSI are investigated in the present work. For the MCS computation, the procedure proposed by Saltelli et al. (2010) can be utilized. Several other approaches can be found in the literature (Sobol, 1993; Homma and Saltelli, 1996; Jansen, 1999; Sobol, 2007).

Appendix E

Long summary in French

E.1 Introduction

Les accidents de voiture sont l'une des questions majeures concernant la sécurité routière. En 2018, plus de 25 000 décès ont été signalés (Commission, 2019) dans l'Union européenne à la suite d'accidents de la route. Dans le cas d'un accident, l'une des façons d'atténuer le nombre de morts est de concevoir correctement la structure du véhicule. C'est pourquoi la conception sûre des composants de la voiture est une problématique très importante.

Lors d'un accident, la principale préoccupation est la sécurité des occupants. La sécurité d'un occupant d'une voiture dépend de plusieurs paramètres tels que les paramètres de conception de la structure de la voiture, la configuration des ceintures de sécurité lors d'un accident, le nombre d'occupants et la direction du choc. Lors d'un accident, une partie de l'énergie cinétique initiale est dissipée par des dispositifs de protection du véhicule. Les passagers sont blessés lorsqu'ils subissent des décélérations trop importantes. Le pare-chocs installé à l'avant d'une voiture est le premier à être touché par un accident frontal. Les protections les plus touchées après le pare-chocs sont les *crash boxes* (longerons dissipateurs d'énergie). L'énergie cinétique se dissipe à travers ces *crash boxes* lors d'un accident frontal. C'est pourquoi la conception des longerons est l'une des tâches importantes pour concevoir une voiture sûre.

L'analyse d'une *crash box* en tenant compte de tous les paramètres de conception possibles est un critère important pour la conception d'une voiture sûre. Parmi les paramètres de conception des *crash boxes*, on trouve les propriétés des matériaux, la forme, l'épaisseur des tôles, la vitesse de la voiture, la masse totale de la voiture (y compris celle des occupants). En général, une analyse dynamique de l'impact est effectuée en tenant compte de ces paramètres de manière déterministe (Abramowicz, 1983; Dirgantara et al., 2013). On constate souvent une certaine variabilité dans les paramètres de conception mentionnés ci-dessus en raison du processus de fabrication, de l'épaisseur non uniforme des plaques et du nombre d'occupants. Par conséquent, l'analyse déterministe peut produire des résultats non robustes qui peuvent finalement conduire à la défaillance de la *crash box* lors d'un accident frontal. C'est pourquoi une analyse appropriée de la *crash box* doit être effectuée en tenant compte de la variabilité des paramètres de conception.

Le phénomène dynamique produit par un impact est complexe, non linéaire et dépend du temps. Par conséquent, pour obtenir la variabilité réelle de la grandeur étudiée, la variabilité des paramètres de conception doit être propagée à travers le système dynamique et le comportement des variables d'intérêt en fonction du temps doit être étudié. Les paramètres de

conception sont des paramètres incertains et la propagation de ces paramètres à travers un système dynamique impacté est le principal défi de cette thèse. De plus, tous les paramètres de conception peuvent ne pas contribuer de manière égale à la variable d'intérêt, ce qui peut être mesuré par la sensibilité d'une variable d'intérêt vis à vis des paramètres de conception (Saltelli et al., 2008). Pour un système dynamique, la sensibilité aux paramètres de conception peut varier dans le temps. Par conséquent, une analyse de sensibilité en fonction du temps est également nécessaire pour connaître la contribution d'un paramètre de conception à la sensibilité d'une variable d'intérêt.

Les principaux objectifs de cette thèse sont les suivants :

1. Examiner les techniques de quantification de l'incertitude (UQ) disponibles dans la littérature et applicables aux systèmes dynamiques.
2. Rechercher un métamodèle efficace pour traiter l'UQ des systèmes dynamiques impactés.
3. Effectuer l'UQ et une analyse de sensibilité sur des systèmes dynamiques impactés (par exemple, problème de type *crash box*) en utilisant l'approche développée dans l'étape précédente.

E.2 Examen de l'état de l'art

Les approches disponibles pour l'UQ des systèmes dynamiques sont examinées dans ce chapitre. L'approche la plus conventionnelle pour l'UQ est la simulation de Monte Carlo (MCS). Elle nécessite un grand nombre d'évaluations du modèle, ce qui empêche l'application de l'approche MCS à un système complexe tel qu'un problème de crash. Pour résoudre ce problème, des métamodèles ont été proposés par plusieurs chercheurs, tels que le développement en chaos polynomiaux (PCE) (Xiu and Karniadakis, 2002), le krigeage (Santner et al., 2003), la méthode *Support Vector Machine* (SVM) (Collobert and Bengio, 2001), la méthode *Radial Basis Function* (RBF) (Deng, 2006).

Parmi tous les métamodèles, le chaos polynomial est celui le plus utilisé pour l'UQ des systèmes dynamiques. Dans la littérature, le PCE a été utilisée pour l'UQ de deux manières, à savoir l'approche intrusive et l'approche non intrusive. Dans l'approche intrusive, les équations différentielles régissant le système considéré sont utilisées et la réponse stochastique est généralement calculée par une projection de Galerkin (Gerritsma et al., 2010). En revanche, l'approche non intrusive ne nécessite pas de connaître les équations différentielles, mais plutôt la réponse obtenue pour certains échantillons prédéfinis (souvent appelés points du plan d'expérience) ; le modèle PCE est généralement résolu par une approche de régression (Blatman and Sudret, 2011). L'intérêt du modèle PCE est que les deux premiers moments statistiques peuvent être calculés simplement en post-traitant les coefficients de l'expansion polynomiale. Les modèles PCE intrusifs et non intrusifs développés pour les systèmes dynamiques dans le domaine temporel sont abordés dans ce chapitre.

Pour les systèmes dynamiques, le modèle PCE a surtout été étudié de manière intrusive. Les bases du modèle PCE ont été posées par Ghanem et Spanos (Ghanem and Spanos, 1991) dans le domaine de la dynamique des vibrations. Le modèle PCE a ensuite été amélioré pour sélectionner la base polynomiale de manière adaptative (Li and Ghanem, 1998). En outre, un modèle PCE multi-éléments a été proposé (Wan and Karniadakis, 2005) pour prendre en compte correctement la dynamique d'un système dynamique dans le domaine temporel.

Les coefficients du PCE ont été obtenus pour cette approche par la projection de Galerkin. Par la suite, d'autres types de fonction de base ont été étudiés. Ainsi, les fonctions de Haar se sont avérées plus efficaces pour évaluer une classe spécifique de systèmes dynamiques (Le Maître et al., 2004). En outre, un PCE qui change avec le temps a été proposé (Gerritsma et al., 2010); ainsi les fonctions de la base sont mises à jour au cours du temps pour avoir en permanence une base polynomiale optimale pour une variable d'intérêt donnée.

Dans le cas de l'approche non intrusive, l'approche la plus utilisée pour obtenir les coefficients du PCE est la méthode des moindres carrés ordinaires. De manière similaire à l'approche intrusive, les fonctions de Haar ont également été utilisées dans le modèle PCE non intrusif (Pettit and Beran, 2006). Un PCE à déformation temporelle a été développé (Mai and Sudret, 2017) en redimensionnant le domaine temporel afin de saisir avec précision la dynamique d'un système.

Plusieurs autres métamodèles, telles que le krigeage, les méthodes SVM et RBF, sont également abordés dans ce chapitre. Cependant, pour un système dynamique, la plupart des métamodèles doivent être construits à chaque pas de temps et c'est leur principal inconvénient. C'est pourquoi un métamodèle a été développé en combinant le modèle PCE avec le modèle NARX (*Nonlinear Auto-Regressive with exogenous input*), appelé modèle PCE-NARX creux (Spiridonakos and Chatzi, 2015). Ce modèle est très intéressant car le modèle NARX traite de l'aspect temporel alors que le modèle PCE est fonction des paramètres incertains. Par conséquent, le nombre de métamodèles construits est réduit.

L'UQ de systèmes dynamiques stochastiques avec impact est très limité dans la littérature. Dans la plupart des cas, la fonction de densité de probabilité (PDF) stationnaire a été obtenue pour des oscillateurs de type vibro-impact. Très peu de travaux de recherche ont été menés sur l'UQ de systèmes dynamiques avec impact en utilisant un métamodèle. Toutefois cette approche a été utilisée pour les problèmes de contact glissant dans le cas du crissement, qui sont des problèmes mettant en jeu des non-linéarités non régulières, comme pour les problèmes d'impact.

Le principal inconvénient observé dans la revue de littérature est que les utilisations de métamodèles pour un problème dynamique avec impact sont restreintes. Un autre problème lié aux approches disponibles est que les métamodèles doivent être construits à chaque pas de temps, ce qui est coûteux en temps de calcul. Bien que cette question ait été traitée par le modèle PCE-NARX, la pertinence de ce modèle doit être étudiée pour un système dynamique avec impact. Par ailleurs, les métamodèles autres que le modèle PCE n'ont pas beaucoup servi à l'UQ des systèmes dynamiques. Ces problématiques sont abordées dans cette thèse.

E.3 Modèle Kriging-NARX pour les systèmes dynamiques

Comme indiqué précédemment, le PCE a été utilisé dans la plupart des cas dans l'étude de systèmes dynamiques incertains. Toutefois le krigeage est utilisé dans ce chapitre pour formuler un métamodèle. Par analogie avec le modèle PCE-NARX, un modèle KNARX a été construit dans ce chapitre, combinant le krigeage et le modèle NARX. Le modèle NARX est très utilisé pour l'identification des systèmes dynamiques non linéaires. Par conséquent, le comportement non linéaire dépendant du temps a été modélisé à l'aide du modèle NARX. Le modèle NARX a été formulé avec un modèle de type polynomial (presque similaire au modèle PCE). L'utilité du modèle NARX est que la réponse à tout moment est prédite à partir de la réponse aux pas de temps précédents et à partir de l'excitation au pas de temps présent et

aux pas de temps précédents. Le modèle NARX est rendu creux à l'aide de l'approche LARS (*least angle regression*). Il est donc possible d'identifier un système dynamique non linéaire en utilisant un faible nombre de termes dans le modèle NARX. Comme le modèle NARX est déterministe, le krigeage a été utilisé pour prendre en compte l'aspect stochastique. Un modèle de krigeage a été construit pour chaque terme du modèle NARX creux. En conséquence, le nombre de construction de modèles de krigeage reste faible par rapport au nombre total de pas de temps pour le système dynamique.

Le modèle KNARX creux a été appliqué à plusieurs systèmes dynamiques non linéaires, dont l'oscillateur de Duffing, l'oscillateur de Bouc-Wen et un système dynamique à deux degrés de liberté. Les résultats ont été comparés aux simulations de Monte-Carlo et au modèle PCE-NARX creux. Le modèle KNARX creux a prédit avec précision les moments statistiques dépendant du temps pour tous les exemples en utilisant moins d'appels au modèle initial que le modèle PCE-NARX creux. En outre, la PDF déterminée à différents instants a également été assez bien prédite par le modèle KNARX creux.

Bien qu'il soit possible de propager assez bien les paramètres incertains grâce au modèle KNARX creux, le modèle NARX n'a pas réussi à estimer la réponse d'un oscillateur soumis à un impact. Plusieurs autres types de modèles auto-régressifs ont alors été étudiés : modèles auto-régressifs linéaires, non linéaires et en ondelettes. Cependant, aucun de ces modèles auto-régressifs n'a permis d'estimer de façon satisfaisante les différentes réponses de l'oscillateur impacté. Par conséquent, il est clair, d'après l'étude de ce chapitre, que le modèle KNARX ne peut pas être utilisé pour modéliser un système dynamique impacté, car les réponses sont non linéaires et surtout non régulières.

E.4 Modèle PCE reposant sur une décomposition orthogonale en modes propres de type POD

Comme les modèles autorégressifs n'ont pas permis d'estimer les réponses d'un système dynamique impacté, le modèle KNARX creux ne peut pas être utilisé pour l'UQ des systèmes dynamiques impactés. Pour cette raison, un autre type de métamodèle est étudié dans ce chapitre. Le comportement temporel et le caractère aléatoire ont été découplés en utilisant le modèle KNARX creux : cette procédure est également possible en utilisant une technique de réduction de modèle (MOR, *Model Order Reduction*) (Chatterjee, 2000; Chinesta et al., 2011). Les techniques de MOR comprennent la PGD (*Proper Generalized Decomposition*), la POD (*Proper Orthogonal Decomposition*), la décomposition en mode propres. La POD a été utilisée pour la réduction de la dimensionnalité des équations différentielles ordinaires et des équations aux dérivées partielles. La POD a été utilisée dans (Higdon et al., 2008) pour la réduction de la dimensionnalité des sorties à haute dimension. La POD a été largement utilisée pour les problèmes de dynamique des fluides pour étudier la structure cohérente de l'écoulement (Christensen et al., 1999; Zimmermann and Görtz, 2010). La plupart du temps, la structure cohérente de l'écoulement des fluides a été étudiée par l'approche POD. La POD permet de décomposer la réponse spatio-temporelle d'un système, en projetant la réponse sur une base qui dépend du domaine spatial. L'approche POD a été utilisée dans plusieurs recherches pour la réduction de la dimensionnalité (Guo and Hesthaven, 2019; Raisee et al., 2015).

L'approche POD a été utilisée en combinaison avec le modèle PCE pour proposer une nouvelle approche appelée approche POD-PCE. Si l'on considère chaos polynomiaux, les

coefficients du développement doivent être calculés à chaque pas de temps pour un système dynamique. Par conséquent, pour éviter la répétition des calculs des coefficients du PCE, la réponse du système dynamique incertain, dépendante du temps, est projetée sur les modes POD (POM, *Proper Orthogonal Modes*), qui dépendent également du temps : les coefficients ne dépendent donc que des variables aléatoires. Ainsi, le comportement dépendant du temps et le caractère aléatoire ont été découplés : la POD traduit l'évolution temporelle de la réponse alors que les incertitudes sont prises en compte par le PCE. La méthodologie développée dans ce chapitre a été publiée dans (Jacquelin et al., 2019).

Un oscillateur non linéaire soumis à un impact a été étudié dans deux configurations différentes : premièrement avec un seul contact entre la structure et le projectile, puis avec des contacts multiples. L'UQ a été réalisée pour le déplacement du projectile, la vitesse du projectile et la force de contact. Les réponses stochastiques ont été estimées de façon satisfaisante par les modèles PCE et POD-PCE. Pour le modèle POD-PCE, le plus grand nombre de coefficients identifiés était d'environ 100 fois plus faible que le nombre de coefficients du modèle PCE (pour la force de contact de l'oscillateur à impacts multiples) tout en ayant une précision similaire pour ces deux modèles. Il est évident que le temps nécessaire au calcul des modes POM doit être pris en compte. Cependant, comme le nombre d'évaluations du modèle est faible, le nombre de POM est également faible. Par conséquent, le coût numérique pour calculer les POM est faible et le coût numérique total pour obtenir le modèle POD-PCE est beaucoup plus faible que celui pour obtenir le modèle PCE à chaque pas de temps.

Bien que ces deux métamodèles aient prédit de bons résultats, certaines forces de contact non physiques car négatives ont été parfois prédites pour l'oscillateur ayant des impacts multiples. Pour éliminer ce problème, le nombre d'évaluations du modèle et le degré polynomial du PCE ont été augmentés. La force de contact non physique a pu être réduite dans une certaine mesure grâce à ces modifications ; cependant, il n'a pas été possible d'éliminer complètement la prédiction de forces de contact négatives par les deux métamodèles. Les forces non physiques peuvent également être la conséquence d'un sur-ajustement et peuvent être minimisées en utilisant un modèle PCE creux en sélectionnant les termes importants dans la base polynomiale du PCE. Par conséquent, une approche PCE creux est étudiée dans le chapitre suivant.

E.5 Modèle PCE creux basé sur l'inférence bayésienne variationnelle

Il a été constaté dans le chapitre précédent que le modèle POD-PCE est efficace pour propager l'incertitude à travers un oscillateur impacté. Bien que le nombre d'estimations des coefficients du PCE soit beaucoup plus faible pour le modèle POD-PCE que pour le modèle PCE, le nombre de coefficients est élevé si un degré polynomial élevé est utilisé. Il a souvent été constaté dans la littérature que tous les polynômes du modèle PCE ne contribuent pas à la réponse (Blatman and Sudret, 2008, 2011; Jakeman et al., 2015). De plus, l'utilisation de tous les polynômes peut ne pas être optimale pour une réponse donnée. Par conséquent, la sélection des termes les plus appropriés du PCE et le calcul des coefficients correspondants sont les principaux défis à relever pour formuler un modèle PCE creux. En effet, le choix des termes importants dans la base du PCE réduit les risques de sur-ajustement et augmente la précision du modèle de PCE. C'est la raison pour laquelle un modèle PCE creux a été étudié.

Un modèle PCE creux basé sur l'inférence bayésienne a été formulé. L'inférence bayési-

enne variationnelle (VB, *Variational Bayesian Inference*) (Ghahramani and Beal, 2001) a été utilisée pour calculer les coefficients du PCE. En outre, les termes importants de la base polynomiale du PCE ont été sélectionnés en utilisant l’approche de détermination automatique de la pertinence (ARD, *Automatic Relevance Determination*) (Jacobs et al., 2018; Wipf and Nagarajan, 2008); l’approche résultante est appelée modèle PCE basé sur l’inférence VB creux (SVB-PCE). L’utilité de l’inférence VB est qu’elle prend en compte l’erreur résiduelle du modèle PCE tronqué lors du calcul des coefficients du PCE. L’inférence VB est entièrement liée à l’ARD, c’est pourquoi les termes importants ont été sélectionnés en utilisant les résultats de l’inférence VB.

Tout d’abord, la pertinence du modèle SVB-PCE a été testée sur deux fonctions test mathématiques, à savoir la fonction d’Ishigami et une fonction non linéaire à vingt dimensions. Les résultats calculés par le modèle SVB-PCE ont été comparés avec les simulations de Monte Carlo et le modèle PCE creux (Blatman and Sudret, 2011) basé sur l’approche LARS (LARS-PCE). Il a été constaté que le modèle SVB-PCE nécessitait un nombre de termes inférieur à celui du modèle LARS-PCE pour atteindre le même niveau de précision pour les deux fonctions mathématiques. En même temps, le nombre d’évaluations du modèle était inférieur à celui du modèle LARS-PCE pour atteindre un pourcentage d’erreur de 2% par rapport au résultat de la MCS. En conséquence, l’algorithme SVB peut être utilisé comme un outil alternatif à la méthode LARS pour obtenir un modèle PCE creux.

Le modèle SVB-PCE a été couplé avec l’approche POD pour développer le modèle POD-SVB-PCE. L’oscillateur à impacts multiples étudié dans le chapitre précédent avec le modèle POD-PCE a été étudié ici par le modèle POD-SVB-PCE et les résultats ont été comparés avec le modèle POD-PCE. Les réponses stochastiques ont été assez bien prédites par le modèle POD-SVB-PCE avec un très faible nombre de coefficients. Pour la force de contact, il a été possible de réduire dans une certaine mesure les forces négatives non physiques ; cependant, la prédiction d’une fonction non régulière par une fonction régulière (PCE ou SVB-PCE) est toujours une tâche difficile. Le principal avantage du modèle SVB-PCE est qu’il a été capable de prédire la réponse stochastique avec un polynôme de haut degré et avec un faible nombre d’évaluations du modèle car il a sélectionné peu de termes dans le modèle PCE. Au contraire, le modèle POD-PCE n’a pas pu prédire correctement les réponses stochastiques avec l’augmentation du degré polynomial car le nombre de coefficients était supérieur au nombre d’évaluations du modèle qui avait été imposé. Pour cette raison, un modèle PCE creux est toujours utile lorsqu’une base polynomiale à degré élevé est requise et, en même temps, lorsque le nombre d’évaluations du modèle doit être réduit au minimum.

E.6 Application aux simulations de dynamique rapide

L’objectif principal de cette thèse étant l’UQ d’un problème de crash, une telle étude a été finalement menée. Pour un problème réel, le nombre possible d’appels au modèle est souvent limité. Il est donc très difficile d’obtenir un métamodèle de bonne qualité avec un faible nombre d’évaluations de modèle. Un métamodèle approprié doit être formulé en fonction du comportement de la variable d’intérêt, il est important d’utiliser un métamodèle adaptatif. Un modèle PCE adaptatif a été formulé dans (Blatman and Sudret, 2011) afin de sélectionner le nombre d’évaluations du modèle et le degré polynomial de manière adaptative. Ce modèle a également été utilisé dans (Ni et al., 2017) pour un problème de flux de puissance probabiliste. Bien que les modèles PCE disponibles puissent être utilisés pour formuler un

métamodèle adaptatif pour un système dynamique impacté dans le domaine temporel, le principal problème est que le métamodèle doit alors être formulé à chaque pas de temps : c'est sa principale limitation. C'est pourquoi un nouveau métamodèle adaptatif a été proposé dans ce chapitre.

Tout d'abord, un modèle SVB-PCE adaptatif a été formulé pour une réponse indépendante du temps et ensuite, un modèle POD-SVB-PCE adaptatif a été formulé en utilisant le modèle SVB-PCE adaptatif et un critère d'erreur de type *leave-one-out* (LOO). Le métamodèle adaptatif a finalement été appliqué à l'UQ d'une *crash box* percutée par une masse rigide. Un quart de *crash box* est considéré pour la présente étude. Elle est percutée par une masse (impacteur) qui est considérée comme incertaine. En outre, la loi de comportement de la *crash box* et l'épaisseur de la *crash box* sont considérées comme des paramètres incertains. Pour le quart de *crash box*, trois conditions différentes ont été étudiées: (i) l'extrémité de la *crash box* est encadrée, (ii) l'extrémité de la *crash box* est libre mais une masse est attachée à l'extrémité, et (iii) l'extrémité de la *crash box* est libre et attachée à une masse incertaine. Par conséquent, pour la troisième condition, quatre paramètres incertains sont présents. En raison du coût élevé des calculs, il n'a pas été possible de comparer les résultats du métamodèle avec les résultats de la MCS pour un grand nombre d'échantillons. Néanmoins, la méthode de Monte Carlo a été réalisée avec 1000 tirages. Trois réponses ont été prises en compte, à savoir le déplacement de l'impacteur, la vitesse de l'impacteur et la force de contact.

En outre, la sensibilité temporelle aux paramètres incertains des variables d'intérêt a été quantifiée en utilisant le modèle adaptatif POD-SVB-PCE développé. L'utilité du modèle adaptatif POD-SVB-PCE est la possibilité de pouvoir calculer les moments statistiques dépendant du temps et les indices de sensibilité simplement en post-traitant les coefficients du modèle POD-SVB-PCE.

Les métamodèles adaptatifs ont été utiles pour sélectionner le nombre d'évaluations de modèles et le nombre de termes du PCE de manière adaptative, de sorte qu'un bon métamodèle puisse être obtenu sans sur-ajustement. L'erreur seuil LOO de 1×10^{-3} a été jugée suffisante pour obtenir un bon métamodèle. Tous les métamodèles obtenus dans ce chapitre ont été validés avec 1000 échantillons et les précisions prévues étaient très proches de l'erreur LOO obtenue, lorsque les métamodèles ont obtenu une erreur LOO inférieure à 1×10^{-3} .

Le modèle POD-SVB-PCE adaptatif pour le déplacement et la vitesse de la masse rigide a été obtenu avec une erreur LOO valant 1×10^{-3} et utilisant moins d'échantillons que le nombre maximum d'échantillons alloués ($N_{\max} = 200$). En ce qui concerne la force d'impact appliquée sur les *crash boxes*, il a été très difficile d'obtenir la précision souhaitée de 1×10^{-3} pour l'erreur LOO, même en utilisant le nombre maximum alloué d'évaluations du modèle. Cependant, une précision acceptable a été obtenue pour la force de contact, ce qui a été illustré en prédisant la force de contact sur trois échantillons choisis au hasard. L'UQ sur la force de contact maximale et sur l'énergie dissipée totale a été réalisée avec le modèle adaptatif SVB-PCE. La précision des prédictions du modèle adaptatif SVB-PCE était assez bonne avec un nombre d'échantillons relativement faible.

L'analyse de sensibilité globale a été réalisée pour le quart de *crash box* avec le modèle adaptatif POD-SVB-PCE obtenu pour la propagation d'incertitude. Les propriétés du matériau et l'épaisseur de la *crash box* sont les paramètres les plus influents sur la force de contact alors que la masse de l'impacteur est le paramètre le moins influent. Le même comportement a également été observé pour la vitesse de l'impacteur. Au contraire, la masse de l'impacteur a une forte influence sur l'évolution de l'énergie cinétique de l'impacteur dans le cas de la *crash box* avec extrémité libre. Les indices de sensibilité du maximum de la force

de contact et de l'énergie totale dissipée ont été calculés en post-traitant les coefficients du modèle SVB-PCE adaptatif. Pour la *crash box* avec extrémité libre, la masse de l'impacteur n'a pas d'influence sur le maximum de la force de contact. Les autres paramètres (épaisseur, matériau et masse attachée à la *crash box*) ont un effet significatif sur la force de contact maximale. Un scénario différent a été observé pour l'énergie totale dissipée : la masse de l'impacteur était le seul paramètre significatif pour l'ensemble des *crash boxes*.

E.7 Conclusions

L'objectif principal de la thèse était l'UQ pour un système dynamique incertain impacté. Plusieurs métamodèles ont été développés dans cette thèse pour simuler le système dynamique aléatoire. Tout d'abord, le modèle KNARX creux a été développé de manière similaire au modèle PCE-NARX creux pour l'UQ des systèmes dynamiques non linéaires. Il a été possible de propager les paramètres incertains avec le modèle KNARX creux de manière appropriée et avec un faible nombre d'appels au modèle par rapport au modèle PCE-NARX creux. Cependant, un modèle NARX approprié n'a pas été trouvé pour l'oscillateur impacté et c'est le principal inconvénient du modèle KNARX creux dans le contexte de l'objectif de la thèse.

Par conséquent, une approche différente a été étudiée, basée sur l'utilisation combinée de la POD et du PCE : l'objectif était de découpler le temps et le caractère aléatoire, comme l'ont fait le modèle PCE-NARX ou le modèle KNARX creux. L'UQ de la réponse en fonction du temps peut également être réalisée par le modèle PCE. Cependant, le principal problème du modèle PCE est que les coefficients PCE doivent être calculés à chaque pas de temps. Au contraire, la variable d'intérêt a été projetée sur un très petit nombre de modes POD (POM) par rapport au nombre de pas de temps. L'UQ a été réalisée pour un oscillateur avec impact en utilisant le modèle POD-PCE. Pour le déplacement et la vitesse du projectile, le modèle POD-PCE a nécessité un très faible nombre de POM. La force de contact a nécessité le plus grand nombre de POM parmi toutes les réponses. La précision de la force de contact était également un peu plus faible que celle des autres réponses. De plus, des valeurs négatives de la force de contact ont été prédites à certains moments par le modèle POD-PCE. Il n'a pas été possible d'atténuer complètement le problème des valeurs négatives des forces de contact, car il est très difficile de prédire avec précision une réponse non régulière (par exemple une force de contact) par une fonction régulière (PCE) : c'est pourquoi le même problème se pose avec le modèle PCE. Par conséquent, ce problème n'est pas lié à l'utilisation de la POD.

Pour utiliser des termes polynomiaux de degré élevé avec un faible nombre d'évaluations du modèle, un modèle creux PCE basé sur l'inférence bayésienne variationnelle (SVB) a été proposé. Les coefficients du PCE ont été calculés en utilisant l'inférence VB et les termes du PCE ont été sélectionnés en utilisant l'approche ARD. L'applicabilité du modèle SVB-PCE a été vérifiée à l'aide de quelques exemples et il s'est avéré qu'il s'agit d'un moyen alternatif très utile pour obtenir un modèle creux. En outre, le modèle SVB-PCE a été couplé à l'approche POD pour l'UQ de l'oscillateur avec impact. Il a été constaté que le nombre de termes réellement nécessaires dans un modèle PCE était assez faible par rapport au modèle PCE complet. En même temps, il a été possible de réduire les forces de contact négatives, non physiques, en utilisant des polynômes de degré élevé tout en conservant un faible nombre d'évaluations du modèle.

Un cadre adaptatif pour les modèles SVB-PCE et POD-SVB-PCE a été proposé. La principale motivation derrière la formulation de ces métamodèles adaptatifs était que le degré

polynomial et le nombre d'évaluations du modèle doivent être sélectionnés de manière adaptative pour chaque réponse étudiée. Deux différentes erreurs de type "leave-one-out" (LOO) ont été utilisées pour mesurer la précision des métamodèles. Enfin, un modèle éléments finis de *crash box* élasto-plastique soumis à un chargement de type d'impact a été étudié en considérant plusieurs paramètres incertains et pour différentes conditions aux limites. Il a été constaté que les modèles adaptatifs POD-SVB-PCE pour le déplacement et la vitesse de l'impacteur prévoyaient de très bons résultats lorsqu'ils atteignaient une erreur LOO inférieure à 1×10^{-3} . Cependant, il n'a pas été possible d'atteindre ce seuil pour la force de contact en utilisant un nombre limité d'évaluations du modèle. En outre, une analyse de sensibilité globale a été réalisée en post-traitant les résultats des métamodèles adaptatifs.

La principale réalisation de cette thèse est le métamodèle proposé (modèle adaptatif POD-SVB-PCE) pour l'UQ de la réponse temporelle d'un système dynamique impacté. L'approche proposée peut également être utilisée pour une analyse de sensibilité des paramètres incertains sans coût de calcul supplémentaire.

Bibliography

- Abdo, M., Elzohery, R., and Roberts, J. A. (2019). Modeling isotopic evolution with surrogates based on dynamic mode decomposition. *Annals of Nuclear Energy*, 129:280–288.
- Abraham, S., Tsirikoglou, P., Miranda, J., Lacor, C., Contino, F., and Ghorbaniasl, G. (2018). Spectral representation of stochastic field data using sparse polynomial chaos expansions. *Journal of Computational Physics*, 367:109–120.
- Abramowicz, W. (1983). The effective crushing distance in axially compressed thin-walled metal columns. *International Journal of Impact Engineering*, 1(3):309–317.
- Abramowicz, W. and Jones, N. (1984). Dynamic axial crushing of square tubes. *International Journal of Impact Engineering*, 2(2):179–208.
- Al-Anazi, A. F. and Gates, I. D. (2010). Support vector regression for porosity prediction in a heterogeneous reservoir: A comparative study. *Computers and Geosciences*, 36(12):1494–1503.
- Alexander, J. M. (1960). An approximate analysis of the collapse of thin cylindrical shells under axial loading. *The Quarterly Journal of Mechanics and Applied Mathematics*, 13(1):10–15.
- Attias, H. (1999). A variational Bayesian framework for graphical models. In *12th International Conference on Neural Information Processing Systems*, pages 209–215. MIT Press.
- Azeez, M. and Vakakis, A. (2001). Proper orthogonal decomposition (POD) of a class of vibroimpact oscillations. *Journal of Sound and Vibration*, 240(5):859–889.
- Berkooz, G., Holmes, P., and Lumley, J. L. (1993). The Proper Orthogonal Decomposition in the Analysis of Turbulent Flows. *Annual Review of Fluid Mechanics*, 25(1):539–575.
- Beylkin, G. and Mohlenkamp, M. J. (2002). Numerical operator calculus in higher dimensions. *Proceedings of the National Academy of Sciences of the United States of America*, 99(16):10246–10251.
- Beylkin, G. and Mohlenkamp, M. J. (2005). Algorithms for numerical analysis in high dimensions. *SIAM Journal on Scientific Computing*, 26(6):2133–2159.
- Bhattacharyya, B. (2018). A Critical Appraisal of Design of Experiments for Uncertainty Quantification. *Archives of Computational Methods in Engineering*, 25(3):727–751.

- Bhattacharyya, B., Jacquelin, E., and Brizard, D. (2019). Uncertainty quantification of nonlinear stochastic dynamic problem using a Kriging-NARX surrogate model. In *3rd International Conference on Uncertainty Quantification in Computational Sciences and Engineering*, pages 34–46, Crete, Greece.
- Bhattacharyya, B., Jacquelin, E., and Brizard, D. (2020). A Kriging-NARX model for uncertainty quantification of nonlinear stochastic dynamical systems in time domain. *Journal of Engineering Mechanics*.
- Bhusal, R. and Subbarao, K. (2019). Uncertainty Quantification Using Generalized Polynomial Chaos Expansion for Nonlinear Dynamical Systems With Mixed State and Parameter Uncertainties. *Journal of Computational and Nonlinear Dynamics*, 14(2).
- Billings, S. and Wei, H.-L. (2005). A New Class of Wavelet Networks for Nonlinear System Identification. *IEEE Transactions on Neural Networks*, 16(4):862–874.
- Billings, S. A. (2013). *Nonlinear System Identification: NARMAX Methods in the Time, Frequency, and Spatio-Temporal Domains*.
- Billings, S. A. and Wei, H. L. (2008). An adaptive orthogonal search algorithm for model subset selection and non-linear system identification. *International Journal of Control*, 81(5):714–724.
- Bishop, C. M. (2006). *Pattern recognition and machine learning*. Springer.
- Bishop, C. M. and Tipping, M. (2000). Variational Relevance Vector Machines. In *Sixteenth Conference on Uncertainty in Artificial Intelligence (UAI2000)*, pages 46–53.
- Blatman, G. and Sudret, B. (2008). Sparse polynomial chaos expansions and adaptive stochastic finite elements using a regression approach. *Comptes Rendus Mécanique*, 336(6):518–523.
- Blatman, G. and Sudret, B. (2010a). An adaptive algorithm to build up sparse polynomial chaos expansions for stochastic finite element analysis. *Probabilistic Engineering Mechanics*, 25(2):183–197.
- Blatman, G. and Sudret, B. (2010b). Efficient computation of global sensitivity indices using sparse polynomial chaos expansions. *Reliability Engineering & System Safety*, 95(11):1216–1229.
- Blatman, G. and Sudret, B. (2011). Adaptive sparse polynomial chaos expansion based on least angle regression. *Journal of Computational Physics*, 230(6):2345–2367.
- Blatman, G. and Sudret, B. (2013). Sparse polynomial chaos expansions of vector-valued response quantities. In *ICOSSAR*, New York, USA.
- Borgonovo, E. (2007). A new uncertainty importance measure. *Reliability Engineering & System Safety*, 92(6):771–784.
- Borgonovo, E. and Plischke, E. (2016). Sensitivity analysis: A review of recent advances. *European Journal of Operational Research*, 248(3):869–887.
- Bouc, R. (1967). Forced vibration of mechanical systems with hysteresis. In *Proceedings of the Fourth Conference on Nonlinear Oscillation*, page 315.

- Bourinet, J. M. (2016). Rare-event probability estimation with adaptive support vector regression surrogates. *Reliability Engineering and System Safety*, 150:210–221.
- Bourinet, J.-M., Deheeger, F., and Lemaire, M. (2011). Assessing small failure probabilities by combined subset simulation and Support Vector Machines. *Structural Safety*, 33(6):343–353.
- Bowman, A. W. and Azzalini, A. (1997). *Applied Smoothing Techniques for Data Analysis*. Oxford University Press Inc.
- Box, G. E. P., Jenkins, G. M., and Reinsel, G. C. (1994). *Time series analysis: Forecasting and Control*. Prentice Hall, 3rd edition.
- Boyd, S. and Vandenberghe, L. (2004). *Convex Optimization*. Cambridge University Press.
- Bratley, P. (1988). ALGORITHM 659: Implementing Sobol’s Quasirandom Sequence Generator. *ACM Transaction on Mathematical Software*, 14(1):88–100.
- Brezinski, C. (1996). Extrapolation algorithms and Padé approximations: A historical survey. *Applied Numerical Mathematics*, 20(3):299–318.
- Buezas, F. S., Rosales, M. B., and Sampaio, R. (2013). Propagation of uncertainties and multimodality in the impact problem of two elastic bodies. *International Journal of Mechanical Sciences*, 75:145–155.
- Burden, F. R., Ford, M. G., Whitley, D. C., and Winkler, D. A. (2000). Use of Automatic Relevance Determination in QSAR Studies Using Bayesian Neural Networks. *Journal of Chemical Information and Modelling*, 40(6):1423–1430.
- Burrus, C. S., Gopinath, R. A., and Guo, H. (1998). *Introduction to Wavelets and Wavelet Transforms A Primer*. Prentice Hall.
- Busby, D. (2009). Hierarchical adaptive experimental design for Gaussian process emulators. *Reliability Engineering and System Safety*, 94(7):1183–1193.
- Cafisch, R. E. (1998). Monte Carlo and quasi-Monte Carlo methods. *Acta Numerica*, 7:1–49.
- Cantelmo, C. and Piroddi, L. (2010). Adaptive model selection for polynomial NARX models. *IET Control Theory & Applications*, 4(12):2693–2706.
- Chai, W., Dostal, L., Naess, A., and Leira, B. J. (2018). A comparative study of the stochastic averaging method and the path integration method for nonlinear ship roll motion in random beam seas. *Journal of Marine Science and Technology (Japan)*, 23(4):854–865.
- Chakraborty, S. and Chowdhury, R. (2017). A hybrid approach for global sensitivity analysis. *Reliability Engineering & System Safety*, 158:50–57.
- Chapelle, O., Vapnik, V., and Bengio, Y. (2002). Model selection for small sample regression. *Machine Learning*, 48(1-3):9–23.
- Chatterjee, A. (2000). An introduction to the proper orthogonal decomposition. *Current Science*, 78(7):808–817.

- Chatterjee, T. and Chowdhury, R. (2017). An efficient sparse Bayesian learning framework for stochastic response analysis. *Structural Safety*, 68:1–14.
- Chen, S. and Billings, S. A. (1989). Modelling and analysis of non-linear time series. *International Journal of Control*, 50(6):2151–2171.
- Cheng, K. and Lu, Z. (2018a). Adaptive sparse polynomial chaos expansions for global sensitivity analysis based on support vector regression. *Computers & Structures*, 194:86–96.
- Cheng, K. and Lu, Z. (2018b). Sparse polynomial chaos expansion based on D-MORPH regression. *Applied Mathematics and Computation*, 323:17–30.
- Cheng, K., Lu, Z., and Zhen, Y. (2019). Multi-level multi-fidelity sparse polynomial chaos expansion based on Gaussian process regression. *Computer Methods in Applied Mechanics and Engineering*, 349:360–377.
- Cheng, K., Lu, Z., Zhou, Y., Shi, Y., and Wei, Y. (2017). Global sensitivity analysis using support vector regression. *Applied Mathematical Modelling*, 49:587–598.
- Cheng, Y., Wang, L., Yu, M., and Hu, J. (2011). An efficient identification scheme for a nonlinear polynomial NARX model. *Artificial Life and Robotics*, 16(1):70–73.
- Chinesta, F., Ladeveze, P., and Cueto, E. (2011). A Short Review on Model Order Reduction Based on Proper Generalized Decomposition. *Archives of Computational Methods in Engineering*, 18(4):395–404.
- Christensen, E. A., Brøns, M., and Sørensen, J. N. (1999). Evaluation of proper orthogonal decomposition-based decomposition techniques applied to parameter-dependent nonturbulent flows. *SIAM Journal of Scientific Computing*, 21(4):1419–1434.
- Collobert, R. and Bengio, S. (2001). SVM-Torch: Support Vector Machines for large-scale regression problems. *Journal of Machine Learning Research*, 1(2):143–160.
- Commission, E. (2019). 2018 road safety statistics: what is behind the figures?
- Cortes, C. and Vapnik, V. (1995). Support-vector networks. *Machine Learning*, 20(3):273–297.
- Crank, J. and Nicolson, P. (1996). A practical method for numerical evaluation of solutions of partial differential equations of the heat-conduction type. *Advances in Computational Mathematics*, 6(1):207–226.
- Dai, H. Z., Zhao, W., Wang, W., and Cao, Z. G. (2011). An improved radial basis function network for structural reliability analysis. *Journal of Mechanical Science and Technology*, 25(9):2151–2159.
- De Vuyst, F. and Villon, P. (2019). Identification of nonlinear dynamical system equations using dynamic mode decomposition under invariant quantity constraints.
- Deng, J. (2006). Structural reliability analysis for implicit performance function using radial basis function network. *International Journal of Solids and Structures*, 43(11-12):3255–3291.

- Denimal, E., Nechak, L., Sinou, J. J., and Nacivet, S. (2018). A novel hybrid surrogate model and its application on a mechanical system subjected to friction-induced vibration. *Journal of Sound and Vibration*, 434:456–474.
- Dick, J. and Pillichshammer, F. (2010). *Digital nets and sequences: discrepancy theory and quasi-Monte Carlo Integration*.
- Dimentberg, M. F. and Iourtchenko, D. V. (2004). Random Vibrations with Impacts: A Review. *Nonlinear Dynamics*, 36(2-4):229–254.
- Dirgantara, T., Gunawan, L., Putra, I. S., Sitompul, S. A., and Jusuf, A. (2013). Numerical and Experimental Impact Analysis of Square Crash Box Structure with Holes. *Applied Mechanics and Materials*, 393:447–452.
- Doi, M. and Imamura, T. (1969). The Wiener-Hermite Expansion with Time-Dependent Ideal Random Function. *Progress of Theoretical Physics*, 41(2):358–366.
- Doostan, A. and Iaccarino, G. (2009). A least-squares approximation of partial differential equations with high-dimensional random inputs. *Journal of Computational Physics*, 228(12):4332–4345.
- Doostan, A., Validi, A., and Iaccarino, G. (2013). Non-intrusive low-rank separated approximation of high-dimensional stochastic models. *Computer Methods in Applied Mechanics and Engineering*, 263:42–55.
- Drugowitsch, J. (2013). Variational Bayesian inference for linear and logistic regression.
- Dubourg, V., Sudret, B., and Bourinet, J.-M. (2011). Reliability-based design optimization using kriging surrogates and subset simulation. *Structural and Multidisciplinary Optimization*, 44(5):673–690.
- Durantini, C., Marzat, J., and Balesdent, M. (2016). Analysis of multi-objective Kriging-based methods for constrained global optimization. *Computational Optimization and Applications*, 63(3):903–926.
- Echard, B., Gayton, N., and Lemaire, M. (2011). AK-MCS: An active learning reliability method combining Kriging and Monte Carlo Simulation. *Structural Safety*, 33(2):145–154.
- Efron, B., Hastie, T., Johnstone, I., and Tibshirani, R. (2004). Least angle regression. *The Annals of Statistics*, 32(2):407–499.
- Efron, B. and Stein, C. (1981). The Jackknife Estimate of Variance. *The Annals of Statistics*, 9(3):586–596.
- Elanayar, S. and Shin, Y. C. (1994). Radial Basis Function Neural Network for Approximation and Estimation of Nonlinear Stochastic Dynamic Systems. *IEEE Transactions on Neural Networks*, 5(4):594–603.
- Fan, Z., Lu, G., and Liu, K. (2013). Quasi-static axial compression of thin-walled tubes with different cross-sectional shapes. *Engineering Structures*, 55:80–89.
- Feeny, B. and Kappagantu, R. (1998). On the physical interpretation of proper orthogonal modes in vibrations. *Journal of Sound and Vibration*, 211(4):607–616.

- Feeny, B. F. (2002). On proper orthogonal co-ordinates as indicators of modal activity. *Journal of Sound and Vibration*, 255(5):805–817.
- Feng, J., Xu, W., Rong, H., and Wang, R. (2009). Stochastic responses of Duffing-Van der Pol vibro-impact system under additive and multiplicative random excitations. *International Journal of Non-Linear Mechanics*, 44(1):51–57.
- Feng, J., Xu, W., and Wang, R. (2008). Stochastic responses of vibro-impact duffing oscillator excited by additive Gaussian noise. *Journal of Sound and Vibration*, 309(3-5):730–738.
- Fishman, G. S. (1996). *Monte Carlo : concepts, algorithms, and applications*. Springer-Verlag.
- Fox, C. W. and Roberts, S. J. (2012). A tutorial on variational Bayesian inference. *Artificial Intelligence Review*, 38(2):85–95.
- Franck, I. M. and Koutsourelakis, P. (2016). Sparse Variational Bayesian approximations for nonlinear inverse problems: Applications in nonlinear elastography. *Computer Methods in Applied Mechanics and Engineering*, 299:215–244.
- Gaspar, B., Teixeira, A., and Soares, C. G. (2014). Assessment of the efficiency of Kriging surrogate models for structural reliability analysis. *Probabilistic Engineering Mechanics*, 37:24–34.
- Ge, Q., Ciuffo, B., and Menendez, M. (2015). Combining screening and metamodel-based methods: An efficient sequential approach for the sensitivity analysis of model outputs. *Reliability Engineering & System Safety*, 134:334–344.
- Gerritsma, M., Steen, J.-b. V. D., Vos, P., and Karniadakis, G. (2010). Time-dependent generalized polynomial chaos. *Journal of Computational Physics*, 229(22):8333–8363.
- Gerstner, T. and Griebel, M. (1998). Numerical integration using sparse grids. *Numerical Algorithms*, 18(3/4):209–232.
- Ghahramani, Z. and Beal, M. J. (2001). Propagation Algorithms for Variational Bayesian Learning. In *Advances in Neural Information Processing Systems*, pages 507–513.
- Ghanem, R. and Spanos, P. (1991). *Stochastic finite elements-A spectral approach*.
- Ghanem, R. and Spanos, P. D. (1993). A stochastic Galerkin expansion for nonlinear random vibration analysis. *Probabilistic Engineering Mechanics*, 8(3-4):255–264.
- Ghosh, D. and Ghanem, R. (2008). Stochastic convergence acceleration through basis enrichment of polynomial chaos expansions. *International Journal for Numerical Methods in Engineering*, 73(2):162–184.
- Ghosh, D. and Iaccarino, D. G. (2007). Applicability of the spectral stochastic finite element method in time-dependent uncertain problems. Technical report.
- Gibbs, J. W. (1898). Fourier’s Series. *Nature*, 59:200.
- Gibbs, J. W. (1899). Fourier’s series. *Nature*, 59:606.

- Gilks, W. R. W. R., Richardson, S. S., and Spiegelhalter, D. J. (1996). *Markov chain Monte Carlo in practice*. Chapman & Hall.
- Giner, E., Bognet, B., Ródenas, J. J., Leygue, A., Fuenmayor, F. J., and Chinesta, F. (2013). The Proper Generalized Decomposition (PGD) as a numerical procedure to solve 3D cracked plates in linear elastic fracture mechanics. *International Journal of Solids and Structures*, 50(10):1710–1720.
- Green, P. (2015). Bayesian system identification of a nonlinear dynamical system using a novel variant of Simulated Annealing. *Mechanical Systems and Signal Processing*, 52-53:133–146.
- Griffin, J. E. and Brown, P. J. (2010). Inference with normal-gamma prior distributions in regression problems. *Bayesian Analysis*, 5(1):171–188.
- Gu, X. and Zhu, W. (2014). A stochastic averaging method for analyzing vibro-impact systems under Gaussian white noise excitations. *Journal of Sound and Vibration*, 333(9):2632–2642.
- Gunzburger, M., Jiang, N., and Schneier, M. (2017). An ensemble-proper orthogonal decomposition method for the nonstationary Navier-Stokes equations. *SIAM Journal on Numerical Analysis*, 55(1):286–304.
- Guo, L., Narayan, A., and Zhou, T. (2018). A gradient enhanced ℓ_1 -minimization for sparse approximation of polynomial chaos expansions. *Journal of Computational Physics*, 367:49–64.
- Guo, M. and Hesthaven, J. S. (2019). Data-driven reduced order modeling for time-dependent problems. *Computer Methods in Applied Mechanics and Engineering*, 345:75–99.
- Hardy, R. L. (1971). Multiquadric equations of topography and other irregular surfaces. *Journal of Geophysical Research*, 76(8):1905–1915.
- Helton, J. and Davis, F. (2003). Latin hypercube sampling and the propagation of uncertainty in analyses of complex systems. *Reliability Engineering & System Safety*, 81(1):23–69.
- Helton, J. C. (1993). Uncertainty and sensitivity analysis techniques for use in performance assessment for radioactive waste disposal. *Reliability Engineering & System Safety*, 42(2-3):327–367.
- Heuveline, V. and Schick, M. (2014). A hybrid generalized polynomial chaos method for stochastic dynamical systems. *International Journal for Uncertainty Quantification*, 4(1):37–61.
- Higdon, D., Gattiker, J., Williams, B., and Rightley, M. (2008). Computer Model Calibration Using High-Dimensional Output. *Journal of the American Statistical Association*, 103(482):570–583.
- Holmes, P., Lumley, J. L., Berkooz, G., and Rowley, C. W. (2012). *Turbulence, Coherent Structures, Dynamical Systems and Symmetry*. Cambridge University Press.
- Homma, T. and Saltelli, A. (1996). Importance measures in global sensitivity analysis of nonlinear models. *Reliability Engineering & System Safety*, 52(1):1–17.

- Hosni Elhewy, A., Mesbahi, E., and Pu, Y. (2006). Reliability analysis of structures using neural network method. *Probabilistic Engineering Mechanics*, 21(1):44–53.
- Huan, X., Safta, C., Sargsyan, K., Vane, Z. P., Lacaze, G., Oefelein, J. C., and Najm, H. N. (2018). Compressive Sensing with Cross-Validation and Stop-Sampling for Sparse Polynomial Chaos Expansions. *SIAM/ASA Journal on Uncertainty Quantification*, 6(2):907–936.
- Hurtado, J. E. and Barbat, A. H. (1998). Monte Carlo techniques in computational stochastic mechanics. *Archives of Computational Methods in Engineering*, 5(1):3–30.
- Iman, R. L. and Conover, W. J. (1980). Small sample sensitivity analysis techniques for computer models with an application to risk assessment. *Communications in Statistics - Theory and Methods*, 9(17):1749–1842.
- Iman, R. L. and Hora, S. C. (1990). A Robust Measure of Uncertainty Importance for Use in Fault Tree System Analysis. *Risk Analysis*, 10(3):401–406.
- Iourtchenko, D. V. and Song, L. L. (2006). Numerical investigation of a response probability density function of stochastic vibroimpact systems with inelastic impacts. *International Journal of Non-Linear Mechanics*, 41(3):447–455.
- Jacobs, W. R., Baldacchino, T., Dodd, T. J., and Anderson, S. R. (2018). Sparse Bayesian Nonlinear System Identification using Variational Inference. *IEEE Transactions on Automatic Control*, 63(12):4172–4187.
- Jacquelin, E., Adhikari, S., Sinou, J.-J., and Friswell, M. (2015a). Polynomial chaos expansion in structural dynamics: Accelerating the convergence of the first two statistical moment sequences. *Journal of Sound and Vibration*, 356:144–154.
- Jacquelin, E., Adhikari, S., Sinou, J.-J., and Friswell, M. (2015b). Polynomial chaos expansion in structural dynamics: Accelerating the convergence of the first two statistical moment sequences. *Journal of Sound and Vibration*, 356:144–154.
- Jacquelin, E., Adhikari, S., Sinou, J.-J., and Friswell, M. I. (2015c). Polynomial Chaos Expansion and Steady-State Response of a Class of Random Dynamical Systems. *Journal of Engineering Mechanics*, 141(4):04014145.
- Jacquelin, E., Baldanzini, N., Bhattacharyya, B., Brizard, D., and Pierini, M. (2019). Random dynamical system in time domain: A POD-PC model. *Mechanical Systems and Signal Processing*, 133:106251.
- Jacquelin, E., Dessombz, O., Sinou, J. J., Adhikari, S., and Friswell, M. I. (2017). Polynomial chaos-based extended Padé expansion in structural dynamics. *International Journal for Numerical Methods in Engineering*, 111(12):1170–1191.
- Jakeman, J. D., Eldred, M. S., and Sargsyan, K. (2015). Enhancing ℓ_1 -minimization estimates of polynomial chaos expansions using basis selection. *Journal of Computational Physics*, 289:18–34.
- Jansen, M. J. (1999). Analysis of variance designs for model output. *Computer Physics Communications*, 117(1-2):35–43.

- Jing, H.-S. and Young, M. (1990). Random response of a single-degree-of-freedom vibro-impact system with clearance. *Earthquake Engineering & Structural Dynamics*, 19(6):789–798.
- Johnson, K. L. (1985). *Contact Mechanics*. Cambridge University Press.
- Jolliffe, I. T. (2002). *Principal component analysis*. Springer.
- Kang Li, Jian-Xun Peng, and Irwin, G. (2005). A fast nonlinear model identification method. *IEEE Transactions on Automatic Control*, 50(8):1211–1216.
- Karagiannis, G. and Lin, G. (2014). Selection of polynomial chaos bases via Bayesian model uncertainty methods with applications to sparse approximation of PDEs with stochastic inputs. *Journal of Computational Physics*, 259:114–134.
- Kaymaz, I. (2005). Application of kriging method to structural reliability problems. *Structural Safety*, 27(2):133–151.
- Kersaudy, P., Sudret, B., Varsier, N., Picon, O., and Wiart, J. (2015). A new surrogate modeling technique combining Kriging and polynomial chaos expansions - Application to uncertainty analysis in computational dosimetry. *Journal of Computational Physics*, 286:103–117.
- Koekoek, R. and Swarttouw, R. F. (1996). The Askey-scheme of hypergeometric orthogonal polynomials and its q-analogue.
- Kopsaftopoulos, F. P. and Fassois, S. D. (2013). A functional model based statistical time series method for vibration based damage detection, localization, and magnitude estimation. *Mechanical Systems and Signal Processing*, 39(1-2):143–161.
- Kostova-Vassilevska, T. and Oxberry, G. M. (2018). Model reduction of dynamical systems by proper orthogonal decomposition: Error bounds and comparison of methods using snapshots from the solution and the time derivatives. *Journal of Computational and Applied Mathematics*, 330:553–573.
- Krige, D. (1951). A Statistical Approach to Some Basic Mine Valuation Problems on the Witwatersrand. *Journal of the Chemical, Metallurgical and Mining Society of South Africa*, 52(6):119 – 139.
- Kumar, D. and Budman, H. (2014). Robust nonlinear MPC based on Volterra series and polynomial chaos expansions. *Journal of Process Control*, 24(1):304–317.
- Kumar, P., Narayanan, S., and Gupta, S. (2016). Stochastic bifurcations in a vibro-impact Duffing–Van der Pol oscillator. *Nonlinear Dynamics*, 85(1):439–452.
- Kundu, A. and Adhikari, S. (2013). A Novel Reduced Spectral Function Approach for Finite Element Analysis of Stochastic Dynamical Systems. In *Computational Methods in Stochastic Dynamics*, volume 26, pages 31–54. Springer Netherland.
- Kundu, A. and Adhikari, S. (2014). Transient Response of Structural Dynamic Systems with Parametric Uncertainty. *Journal of Engineering Mechanics*, 140(2):315–331.

- Kundu, A. and Adhikari, S. (2015). Dynamic analysis of stochastic structural systems using frequency adaptive spectral functions. *Probabilistic Engineering Mechanics*, 39:23–38.
- Kundu, A., DiazDelaO, F. A., Adhikari, S., and Friswell, M. I. (2014). A hybrid spectral and metamodeling approach for the stochastic finite element analysis of structural dynamic systems. *Computer Methods in Applied Mechanics and Engineering*, 270:201–219.
- Kunisch, K. and Volkwein, S. (1999). Control of the Burgers Equation by a Reduced-Order Approach Using Proper Orthogonal Decomposition. *Journal of Optimization Theory and Applications*, 102(2):345–371.
- Kunisch, K. and Volkwein, S. (2002). Galerkin Proper Orthogonal Decomposition Methods for a General Equation in Fluid Dynamics. *SIAM Journal on Numerical Analysis*, 40(2):492–515.
- Kutta, M. (1901). *Beitrag zur näherungsweise Integration totaler Differentialgleichungen*.
- Lancaster, P. and Salkauskas, K. (1981). Surfaces Generated by Moving Least Squares Methods. *Mathematics of Computation*, 37(155):141.
- Langseth, M., Hopperstad, O. S., and Berstad, T. (1999). Crashworthiness of aluminum extrusions: Validation of numerical simulation, effect of mass ratio and impact velocity. *International Journal of Impact Engineering*, 22(9):829–854.
- Le Maître, O. P., Knio, O. M., Najm, H. N., and Ghanem, R. G. (2004). Uncertainty propagation using Wiener-Haar expansions. *Journal of Computational Physics*, 197(1):28–57.
- Le Maître, O. P., Najm, H. N., Pébay, P. P., Ghanem, R. G., and Knio, O. M. (2007). Multi-Resolution-Analysis Scheme for Uncertainty Quantification in Chemical Systems. *SIAM Journal on Scientific Computing*, 29(2):864–889.
- Le Maître, O. P., Knio, O. M., Najm, H. N., and Ghanem, R. G. (2001). A stochastic projection method for fluid flow. I. Basic formulation. *Journal of Computational Physics*, 173(2):481–511.
- Lelièvre, N., Beaurepaire, P., Mattrand, C., and Gayton, N. (2018). AK-MCSi: A Kriging-based method to deal with small failure probabilities and time-consuming models. *Structural Safety*, 73:1–11.
- Leon, A., Barasinski, A., Abisset-Chavanne, E., Cueto, E., and Chinesta, F. (2018). Wavelet-based multiscale proper generalized decomposition. *Comptes Rendus - Mécanique*, 346(7):485–500.
- Leontaritis, I. J. and Billings, S. A. (1985). Input-output parametric models for non-linear systems Part II: stochastic non-linear systems. *International Journal of Control*, 41(2):329–344.
- Li, G. and Rabitz, H. (2010). D-MORPH regression: Application to modeling with unknown parameters more than observation data. *Journal of Mathematical Chemistry*, 48(4):1010–1035.

- Li, J. and Zhao, F. (2006). Identification of dynamical systems using radial basis function neural networks with hybrid learning algorithm. In *1st International Symposium on Systems and Control in Aerospace and Astronautics*, volume 2006, pages 1115–1118.
- Li, R. and Ghanem, R. (1998). Adaptive polynomial chaos expansions applied to statistics of extremes in nonlinear random vibration. *Probabilistic Engineering Mechanics*, 13(2):125–136.
- Li, X., Gong, C., Gu, L., Gao, W., Jing, Z., and Su, H. (2018). A sequential surrogate method for reliability analysis based on radial basis function. *Structural Safety*, 73:42–53.
- Li, Y., Campbell, C., and Tipping, M. (2002). Bayesian automatic relevance determination algorithms for classifying gene expression data. *Bioinformatics*, 18(10):1332–1339.
- Liao, M., Liu, Y., Páez Chávez, J., Chong, A. S., and Wiercigroch, M. (2018). Dynamics of vibro-impact drilling with linear and nonlinear rock models. *International Journal of Mechanical Sciences*, 146-147:200–210.
- Lu, C., Feng, Y.-W., Liem, R. P., and Fei, C.-W. (2018a). Improved Kriging with extremum response surface method for structural dynamic reliability and sensitivity analyses. *Aerospace Science and Technology*, 76:164–175.
- Lu, G. and Yu, T. (2003). *Energy Absorption of Structures and Materials*. Woodhead Publishing Limited.
- Lu, R., Gao, W., Hu, X., Liu, W., Li, Y., and Liu, X. (2018b). Crushing analysis and crashworthiness optimization of tailor rolled tubes with variation of thickness and material properties. *International Journal of Mechanical Sciences*, 136:67–84.
- Luchtenburg, D. M., Brunton, S. L., and Rowley, C. W. (2014). Long-time uncertainty propagation using generalized polynomial chaos and flow map composition. *Journal of Computational Physics*, 274:783–802.
- Lucor, D. and Karniadakis, G. E. (2004). Adaptive Generalized Polynomial Chaos for Non-linear Random Oscillators. *SIAM Journal on Scientific Computing*, 26(2):720–735.
- Lucor, D., Su, C. H., and Karniadakis, G. E. (2004). Generalized polynomial chaos and random oscillators. *International Journal for Numerical Methods in Engineering*, 60(3):571–596.
- Ma, X., Azeez, M. F., and Vakakis, A. F. (2000). Non-linear normal modes and non-parametric system identification of non-linear oscillators. *Mechanical Systems and Signal Processing*, 14(1):37–48.
- Mai, C. V. (2016). *Polynomial chaos expansions for uncertain dynamical systems – Applications in earthquake engineering*. PhD thesis, ETH Zurich, Switzerland.
- Mai, C. V., Spiridonakos, M. D., Chatzi, E. N., and Sudret, B. (2016). Surrogate modeling for stochastic dynamical systems by combining nonlinear autoregressive with exogenous input models and polynomial chaos expansions. *International Journal for Uncertainty Quantification*, 6(4):313–339.

- Mai, C. V. and Sudret, B. (2017). Surrogate models for oscillatory systems using sparse polynomial chaos expansions and stochastic time warping. *SIAM/ASA Journal on Uncertainty Quantification*, 5(1):540–571.
- Maitre, O. P. L., Mathelin, L., Knio, O., and Hussaini, M. (2010). Asynchronous Time Integration for Polynomial Chaos Expansion of Uncertain Periodic Dynamics. *Discrete Continuum Dynamic Systems - Series A*, 28(1):199–226.
- Mamalis, A. G., Manolakos, D. E., Ioannidis, M. B., Kostazos, P. K., and Dimitriou, C. (2003). Finite element simulation of the axial collapse of metallic thin-walled tubes with octagonal cross-section. *Thin-Walled Structures*, 41(10):891–900.
- Marelli, S. and Sudret, B. (2014). UQLab: A Framework for Uncertainty Quantification in Matlab. In *Second International Conference on Vulnerability and Risk Analysis and Management (ICVRAM)*, pages 2554–2563, Liverpool, UK. American Society of Civil Engineers.
- Marple, S. L., J. (1987). *Digital spectral analysis with applications*. Prentice Hall.
- Matheron, G. (1963). Principles of geostatistics. *Economic Geology*, 58(8):1246–1266.
- Matos, A. C. (1996). Some convergence results for the generalized Padé-type approximants. *Numerical Algorithms*, 11(1-4):255–269.
- McFarland, J., Mahadevan, S., Romero, V., and Swileir, L. (2008). Calibration and uncertainty analysis for computer simulations with multivariate output. *AIAA Journal*, 46(5):1253–1265.
- McKay, M. D., Beckman, R. J., and Conover, W. J. (1979). A Comparison of Three Methods for Selecting Values of Input Variables in the Analysis of Output from a Computer Code. *Technometrics*, 21(2):239–245.
- Mohammadi, A. and Raisee, M. (2019). Stochastic field representation using bi-fidelity combination of proper orthogonal decomposition and Kriging. *Computer Methods in Applied Mechanics and Engineering*, 357.
- Mohebujjaman, M., Rebholz, L. G., Xie, X., and Iliescu, T. (2017). Energy balance and mass conservation in reduced order models of fluid flows. *Journal of Computational Physics*, 346:262–277.
- Moore, R. E. (1979). *Methods and Applications of Interval Analysis*. Society for Industrial and Applied Mathematics.
- Moustapha, M., Bourinet, J.-M., Guillaume, B., and Sudret, B. (2018). Comparative Study of Kriging and Support Vector Regression for Structural Engineering Applications. *ASCE-ASME Journal of Risk and Uncertainty in Engineering Systems, Part A: Civil Engineering*, 4(2):04018005.
- Moustapha, M., Sudret, B., Bourinet, J.-M., and Guillaume, B. (2016). Quantile-based optimization under uncertainties using adaptive Kriging surrogate models. *Structural and Multidisciplinary Optimization*, 54(6):1403–1421.

- Mukhopadhyay, T., Chakraborty, S., Dey, S., Adhikari, S., and Chowdhury, R. (2016). A Critical Assessment of Kriging Model Variants for High-Fidelity Uncertainty Quantification in Dynamics of composite Shells. *Archives of Computational Methods in Engineering*, pages 1–24.
- Muscolino, G., Ricciardi, G., and Cacciola, P. (2003). Monte Carlo simulation in the stochastic analysis of non-linear systems under external stationary Poisson white noise input. *International Journal of Non-Linear Mechanics*, 38(8):1269–1283.
- Muscolino, G., Ricciardi, G., and Vasta, M. (1997). Stationary and Non-Stationary Probability Density Function for Non-Linear Oscillators. *Int. J. Non-Linear Mechanics*, 32(6):1051–1064.
- Nair, P. B. and Keane, A. J. (2002). Stochastic reduced basis methods. *AIAA Journal*, 40(8):1653–1664.
- Namachchivaya, N. S. and Park, J. H. (2005). Stochastic Dynamics of Impact Oscillators. *Journal of Applied Mechanics*, 72(6):862.
- Nechak, L., Berger, S., and Aubry, E. (2011). A polynomial chaos approach to the robust analysis of the dynamic behaviour of friction systems. *European Journal of Mechanics - A/Solids*, 30(4):594–607.
- Nechak, L., Berger, S., and Aubry, E. (2012). Prediction of random self friction-induced vibrations in uncertain dry friction systems using a multi-element generalized polynomial chaos approach. *Journal of Vibration and Acoustics, Transactions of the ASME*, 134(4).
- Nechak, L., Berger, S., and Aubry, E. (2013). Non-intrusive generalized polynomial chaos for the robust stability analysis of uncertain nonlinear dynamic friction systems. *Journal of Sound and Vibration*, 332(5):1204–1215.
- Nechak, L., Besset, S., and Sinou, J. J. (2018). Robustness of stochastic expansions for the stability of uncertain nonlinear dynamical systems – Application to brake squeal. *Mechanical Systems and Signal Processing*, 111:194–209.
- Nechak, L. and Sinou, J. J. (2017). Hybrid surrogate model for the prediction of uncertain friction-induced instabilities. *Journal of Sound and Vibration*, 396:122–143.
- Newmark, N. M. (1959). A Method of Computation for Structural Dynamics. *Journal of the Engineering Mechanics Division*, 85(3):67–94.
- Ni, F., Nguyen, P. H., and Cobben, J. F. G. (2017). Basis-Adaptive Sparse Polynomial Chaos Expansion for Probabilistic Power Flow. *IEEE Transactions on Power Systems*, 32(1):694–704.
- Niederreiter, H. (1992). *Random Number Generation and Quasi-Monte Carlo Methods*.
- Orszag, S. A. and Bissonnette, L. R. (1967). Dynamical properties of truncated Wiener-Hermite expansions. *Physics of Fluids*, 10(12):2603–2613.
- Ozen, H. C. and Bal, G. (2016). Dynamical polynomial chaos expansions and long time evolution of differential equations with random forcing. *SIAM-ASA Journal on Uncertainty Quantification*, 4(1):609–635.

- Ozen, H. C. and Bal, G. (2017a). A dynamical polynomial chaos approach for long-time evolution of SPDEs. *Journal of Computational Physics*, 343:300–323.
- Ozen, H. C. and Bal, G. (2017b). A Dynamical Sparse Grid Collocation Method for Differential Equations Driven by White Noise.
- Palar, P. S., Tsuchiya, T., and Parks, G. T. (2016). Multi-fidelity non-intrusive polynomial chaos based on regression. *Computer Methods in Applied Mechanics and Engineering*, 305:579–606.
- Papadrakakis, M. and Papadopoulos, V. (1996). Robust and efficient methods for stochastic finite element analysis using Monte Carlo simulation. *Computer Methods in Applied Mechanics and Engineering*, 134(3-4):325–340.
- Parisi, G. (1988). *Statistical field theory*. Addison-Wesley.
- Park, J. and Sandberg, I. W. (1991). Universal Approximation Using Radial-Basis-Function Networks. *Neural Computation*, 3(2):246–257.
- Peierls, R. (1938). On a Minimum Property of the Free Energy. *Physical Review*, 54(11):918–919.
- Peng, J., Hampton, J., and Doostan, A. (2014). A weighted ℓ_1 -minimization approach for sparse polynomial chaos expansions. *Journal of Computational Physics*, 267:92–111.
- Peng, J., Hampton, J., and Doostan, A. (2016). On polynomial chaos expansion via gradient-enhanced ℓ_1 -minimization. *Journal of Computational Physics*, 310:440–458.
- Peng, L. and Mohseni, K. (2016). Nonlinear model reduction via a locally weighted POD method. *International Journal for Numerical Methods in Engineering*, 106(5):372–396.
- Pettit, C. and Beran, P. (2006). Spectral and multiresolution Wiener expansions of oscillatory stochastic processes. *Journal of Sound and Vibration*, 294(4-5):752–779.
- Picheny, V., Ginsbourger, D., Roustant, O., Haftka, R. T., and Kim, N.-H. (2010). Adaptive Designs of Experiments for Accurate Approximation of a Target Region. *Journal of Mechanical Design*, 132(7):071008.
- Pradlwarter, H. J. and Schuëller, G. I. (1997). On advanced Monte Carlo simulation procedures in stochastic structural dynamics. *International Journal of Non-Linear Mechanics*, 32(4):735–744.
- Pryse, S. E., Adhikari, S., and Kundu, A. (2018). Sample-based and sample-aggregated based Galerkin projection schemes for structural dynamics. *Probabilistic Engineering Mechanics*, 54:118–130.
- Qiao, S. and Ibrahim, R. (1999). Stochastic dynamics of systems with friction-induced vibration. *Journal of Sound and Vibration*, 223(1):115–140.
- Qinghua Zhang (1997). Using wavelet network in nonparametric estimation. *IEEE Transactions on Neural Networks*, 8(2):227–236.

- Raisee, M., Kumar, D., and Lacor, C. (2015). A non-intrusive model reduction approach for polynomial chaos expansion using proper orthogonal decomposition. *International Journal for Numerical Methods in Engineering*, 103(4):293–312.
- Rasmussen, C. E. and Williams, C. K. I. (2006). *Gaussian Processes for Machine Learning*. MIT Press.
- Rubinstein, R. and Kroese, D. (2008). *Simulation and the Monte Carlo method*.
- Runge, C. (1895). Ueber die numerische Auflösung von Differentialgleichungen. *Mathematische Annalen*, 46(2):167–178.
- Sacks, J., Welch, W. J., Mitchell, T. J., and Wynn, H. P. (1989). Design and Analysis of Computer Experiments. *Statistical Science*, 4(4):409–423.
- Sakellariou, J. S. and Fassois, S. D. (2016). Functionally Pooled models for the global identification of stochastic systems under different pseudo-static operating conditions. *Mechanical Systems and Signal Processing*, 72-73:785–807.
- Salehi, S., Raisee, M., Cervantes, M. J., and Nourbakhsh, A. (2018). An efficient multifidelity ℓ_1 -minimization method for sparse polynomial chaos. *Computer Methods in Applied Mechanics and Engineering*, 334:183–207.
- Saltelli, A., Annoni, P., Azzini, I., Campolongo, F., Ratto, M., and Tarantola, S. (2010). Variance based sensitivity analysis of model output. Design and estimator for the total sensitivity index. *Computer Physics Communications*, 181(2):259–270.
- Saltelli, A., Ratto, M., Andres, T., Campolongo, F., Cariboni, J., Gatelli, D., Saisana, M., and Tarantola, S. (2008). *Global Sensitivity Analysis: The Primer*. John Wiley & Sons, Ltd.
- Sampaio, R. and Soize, C. (2007). On measures of nonlinearity effects for uncertain dynamical systems—Application to a vibro-impact system. *Journal of Sound and Vibration*, 303(3-5):659–674.
- Santner, T., Williams, B., and Notz, W. (2003). *The design and analysis of computer experiments*.
- Sarrouy, E., Dessombz, O., and Sinou, J.-J. (2013). Piecewise polynomial chaos expansion with an application to brake squeal of a linear brake system. *Journal of Sound and Vibration*, 332(3):577–594.
- Schmid, P. J. (2010). Dynamic mode decomposition of numerical and experimental data. *Journal of Fluid Mechanics*, 656:5–28.
- Shaik Dawood, M. S., Ghazilan, A. L., and Shah, Q. H. (2017). Finite element analysis of a composite crash box subjected to low velocity impact. In *IOP Conference Series: Materials Science and Engineering*, volume 184. Institute of Physics Publishing.
- Shao, Q., Younes, A., Fahs, M., and Mara, T. A. (2017). Bayesian sparse polynomial chaos expansion for global sensitivity analysis. *Computer Methods in Applied Mechanics and Engineering*, 318:474–496.

- Sirovich, L. (1987). Turbulence and the dynamics of coherent structures part I: coherent structures. *Quarterly of Applied Mathematics*, 45(3):561–571.
- Sjöberg, J., Zhang, Q., Ljung, L., Benveniste, A., Delyon, B., Glorennec, P.-Y., Hjalmarsson, H., and Juditsky, A. (1995). Nonlinear black-box modeling in system identification: a unified overview. *Automatica*, 31(12):1691–1724.
- Sobol, I. M. (1967). On the distribution of points in a cube and the approximate evaluation of integrals. *USSR Computational Mathematics and Mathematical Physics*, 7(4):86–112.
- Sobol, I. M. (1990). Quasi-Monte Carlo methods. *Progress in Nuclear Energy*, 24(1-3):55–61.
- Sobol, I. M. (1993). Sensitivity analysis for nonlinear mathematical models. *Mathematical Modelling Computational Experiments*, 1(4):407–414.
- Sobol, I. M. (2001). Global sensitivity indices for nonlinear mathematical models and their Monte Carlo estimates. *Mathematics and Computers in Simulation*, 55(1–3):271–280.
- Sobol, I. M. (2007). Global sensitivity indices for the investigation of nonlinear mathematical models. *Matematicheskoe Modelirovanie*, 19(11):23–24.
- Song, J., Zhou, Y., and Guo, F. (2013). A relationship between progressive collapse and initial buckling for tubular structures under axial loading. *International Journal of Mechanical Sciences*, 75:200–211.
- Spiridonakos, M. and Chatzi, E. (2015). Metamodeling of dynamic nonlinear structural systems through polynomial chaos NARX models. *Computers & Structures*, 157:99–113.
- Stein, M. (1987). Large Sample Properties of Simulations Using Latin Hypercube Sampling. *Technometrics*, 29(2):143.
- Steiner, M., Bourinet, J.-M., and Lahmer, T. (2019). An adaptive sampling method for global sensitivity analysis based on least-squares support vector regression. *Reliability Engineering & System Safety*, 183:323–340.
- Strang, G. and Nguyen, T. (1996). *Wavelets and Filter Banks*. Wellesley-Cambridge Press.
- Sudret, B. (2008). Global sensitivity analysis using polynomial chaos expansions. *Reliability Engineering & System Safety*, 93(7):964–979.
- Sun, S. (2013). A review of deterministic approximate inference techniques for Bayesian machine learning. *Neural Computing and Applications*, 23(7-8):2039–2050.
- Tibshirani, R. (1996). Regression Shrinkage and Selection via the Lasso. *Journal of the Royal Statistical Society. Series B (Methodological)*, 58(1):267–288.
- Tripathy, M. (2010). Power transformer differential protection using neural network Principal Component Analysis and Radial Basis Function Neural Network. *Simulation Modelling Practice and Theory*, 18(5):600–611.
- Tripathy, R. K. and Bilonis, I. (2018). Deep UQ: Learning deep neural network surrogate models for high dimensional uncertainty quantification. *Journal of Computational Physics*.

- Tsiolakis, V., Giacomini, M., Sevilla, R., Othmer, C., and Huerta, A. (2019). Nonintrusive proper generalised decomposition for parametrised incompressible flow problems in OpenFOAM. *Computer Physics Communications*.
- Tsungnan Lin, Horne, B., Tino, P., and Giles, C. (1996). Learning long-term dependencies in NARX recurrent neural networks. *IEEE Transactions on Neural Networks*, 7(6):1329–1338.
- Wan, X. and Karniadakis, G. E. (2005). An adaptive multi-element generalized polynomial chaos method for stochastic differential equations. *Journal of Computational Physics*, 209(2):617–642.
- Wan, X. and Karniadakis, G. E. (2006). Long-term behavior of polynomial chaos in stochastic flow simulations. *Computer Methods in Applied Mechanics and Engineering*, 195(41-43):5582–5596.
- Wei, H. and Billings, S. (2009). Improved parameter estimates for non-linear dynamical models using a bootstrap method. *International Journal of Control*, 82(11):1991–2001.
- Wen, Y.-K. (1976). Method for Random Vibration of Hysteretic Systems. *Journal of the Engineering Mechanics Division*, 102(2):249–263.
- Wiener, N. (1938). The homogeneous chaos. *American Journal of Mathematics*, 60(4):897–936.
- Wierzbicki, T. and Abramowicz, W. (1983). On the crushing mechanics of thin-walled structures. *Journal of Applied Mechanics, Transactions ASME*, 50(4):727–734.
- Wipf, D. and Nagarajan, S. (2008). A New View of Automatic Relevance Determination. In *Advances in neural information processing systems*, pages 1625–1632.
- Witteveen, J. A. and Bijl, H. (2008a). An alternative unsteady adaptive stochastic finite elements formulation based on interpolation at constant phase. *Computer Methods in Applied Mechanics and Engineering*, 198(3-4):578–591.
- Witteveen, J. A. and Bijl, H. (2008b). An unsteady adaptive stochastic finite elements formulation for rigid-body fluid-structure interaction. *Computers and Structures*, 86(23-24):2123–2140.
- Wold, H. O. A. (1938). *A Study in the Analysis of Stationary Time Series*. Almqvist & Wiksell.
- Wu, Z., Wang, D., Okolo N, P., Hu, F., and Zhang, W. (2016). Global sensitivity analysis using a Gaussian Radial Basis Function metamodel. *Reliability Engineering and System Safety*, 154:171–179.
- Wu, Z., Wang, W., Wang, D., Zhao, K., and Zhang, W. (2019). Global sensitivity analysis using orthogonal augmented radial basis function. *Reliability Engineering & System Safety*, 185:291–302.
- Xiu, D. and Karniadakis, G. E. (2002). The Wiener-Askey polynomial chaos for stochastic differential equation. *SIAM Journal on Scientific Computing*, 24(2):619–644.

- Yuan, L., Shi, H., Ma, J., and You, Z. (2019). Quasi-static impact of origami crash boxes with various profiles. *Thin-Walled Structures*, 141:435–446.
- Yun, W., Lu, Z., Jiang, X., and Zhang, L. (2018). Borgonovo moment independent global sensitivity analysis by Gaussian radial basis function meta-model. *Applied Mathematical Modelling*, 54:378–392.
- Zakian, P. (2017). An efficient stochastic dynamic analysis of soil media using radial basis function artificial neural network. *Frontiers of Structural and Civil Engineering*, 11(4):470–479.
- Zarei, H., Kröger, M., and Albertsen, H. (2008). An experimental and numerical crashworthiness investigation of thermoplastic composite crash boxes. *Composite Structures*, 85(3):245–257.
- Zhang, L. and Li, K. (2015). Forward and backward least angle regression for nonlinear system identification. *Automatica*, 53:94–102.
- Zhang, X., Cheng, G., You, Z., and Zhang, H. (2007). Energy absorption of axially compressed thin-walled square tubes with patterns. *Thin-Walled Structures*, 45(9):737–746.
- Zhang, X. and Zhang, H. (2012). Experimental and numerical investigation on crush resistance of polygonal columns and angle elements. *Thin-Walled Structures*, 57:25–36.
- Zhang, Z., Tretyakov, M. V., Rozovskii, B., and Karniadakis, G. E. (2014). A recursive sparse grid collocation method for differential equations with white noise. *SIAM Journal on Scientific Computing*, 36(4):A1652–A1677.
- Zhao, W., Beach, T. H., and Rezgui, Y. (2017). Efficient least angle regression for identification of linear-in-the-parameters models. *Proceedings of the Royal Society A*, 473(2198):1–22.
- Zhao, X., Xu, W., Yang, Y., and Wang, X. (2016). Stochastic responses of a viscoelastic-impact system under additive and multiplicative random excitations. *Communications in Nonlinear Science and Numerical Simulation*, 35:166–176.
- Zhou, C., Wang, B., Ma, J., and You, Z. (2016). Dynamic axial crushing of origami crash boxes. *International Journal of Mechanical Sciences*, 118:1–12.
- Zhou, C., Zhou, Y., and Wang, B. (2017). Crashworthiness design for trapezoid origami crash boxes. *Thin-Walled Structures*, 117:257–267.
- Zhou, Y., Lu, Z., Cheng, K., and Ling, C. (2019a). An efficient and robust adaptive sampling method for polynomial chaos expansion in sparse Bayesian learning framework. *Computer Methods in Applied Mechanics and Engineering*, 352:654–674.
- Zhou, Y., Lu, Z., Cheng, K., and Shi, Y. (2019b). An expanded sparse Bayesian learning method for polynomial chaos expansion. *Mechanical Systems and Signal Processing*, 128:153–171.
- Zhu, H. (2014a). Stochastic response of vibro-impact Duffing oscillators under external and parametric Gaussian white noises. *Journal of Sound and Vibration*, 333(3):954–961.

- Zhu, H. T. (2014b). Probabilistic solution of vibro-impact stochastic Duffing systems with a unilateral non-zero offset barrier. *Physica A: Statistical Mechanics and its Applications*, 410:335–344.
- Zhu, H. T. (2015). Stochastic response of a vibro-impact Duffing system under external Poisson impulses. *Nonlinear Dynamics*, 82(1-2):1001–1013.
- Zimmermann, R. and Görtz, S. (2010). Non-linear reduced order models for steady aerodynamics. In *Procedia Computer Science*, volume 1, pages 165–174. Elsevier B.V.